

Understanding and Controlling the Optoelectronic
Properties of $\text{Cs}_2\text{AgBiBr}_6$ Double Perovskite

Zewei Li

Department of Physics

Downing College, University of Cambridge

This thesis is submitted for the degree of

Doctor of Philosophy

September 2021

Declaration

I declare that the contents of this thesis are the result of my own work, except where specific reference is made to the work of others. This thesis has not been submitted in whole or in part for consideration for any other degree or qualification in this, or any other university. This dissertation contains fewer than 60,000 words including appendices, bibliography, footnotes, tables and equations.

Zewei Li

September 2021

Acknowledgement

The works in this thesis were conducted with fundings from China Scholarship Council and Cambridge Trust. I would like to thank for their financial supports.

I would like to express all my gratitude to my supervisor: Robert Hoye and Richard Friend. They have provided me with endless support and valuable guidance. They have motivated me to always devote more to work. Their sharp eyes, logics of thinking and enthusiasm for work will be my life-long examples. I would like to thank all my collaborators. Without their help and discussions, my projects will never be complete. I also want to thank my colleagues and staffs in the OE group for making it a supportive environment.

Also, Downing College has always been my home in Cambridge since the first day I arrived. Although I sometimes live off-site, walking on the grounds of the college can always relax my mind and give me pleasure. Sprouting and perishing of its shrubs witness my time in Cambridge, which I know I will always miss.

Finally, my family and my friends, thank you for all your love. It is my greatest honour to have you in my life.

List of Publications

- **Li, Z.**; Kavanagh, S. R.; Napari, M.; Palgrave, R.; Abdi-Jalebi, M.; Andaji-Garmaroudi, Z.; Davies, D.; Laitinen, M.; Julin, J.; Isaacs, M. A.; Friend, R.; Scanlon, D. O.; Walsh, A.; Hoye, R. L. Z. Bandgap Lowering in Mixed Alloys of $\text{Cs}_2\text{Ag}(\text{Sb}_x\text{Bi}_{1-x})\text{Br}_6$ Double Perovskite Thin Films. *J. Mater. Chem. A* **2020**, *8* (41), 21780–21788. <https://doi.org/10.1039/d0ta07145e>.
- **Li, Z.**; Senanayak, S. P.; Dai, L.; Kusch, G.; Shivanna, R.; Zhang, Y.; Pradhan, D.; Ye, J.; Huang, Y.; Sirringhaus, H.; Oliver, R. A.; Greenham, N. C.; Friend, R. H.; Hoye, R. L. Z. Understanding the Role of Grain Boundaries on Charge-Carrier and Ion Transport in $\text{Cs}_2\text{AgBiBr}_6$ Thin Films. *Adv. Funct. Mater.* **2021**, 2104981. <https://doi.org/10.1002/adfm.202104981>.
- Raninga, R. D.; Jagt, R. A.; Béchu, S.; Huq, T. N.; Li, W.; Nikolka, M.; Lin, Y. H.; Sun, M.; **Li, Z.**; Li, W.; Bouttemy, M.; Frégnaux, M.; Snaith, H. J.; Schulz, P.; MacManus-Driscoll, J. L.; Hoye, R. L. Z. Strong Performance Enhancement in Lead-Halide Perovskite Solar Cells through Rapid, Atmospheric Deposition of n-Type Buffer Layer Oxides. *Nano Energy* **2020**, *75*, 104946. <https://doi.org/10.1016/j.nanoen.2020.104946>.

Abstract

Halide double perovskites have gained significant attention, owing to their composition of low-toxicity elements, stability in air and long charge-carrier lifetimes. In particular, $\text{Cs}_2\text{AgBiBr}_6$ has been the subject of many investigations in photovoltaic devices. This thesis focuses on understanding and controlling the optoelectronic properties of $\text{Cs}_2\text{AgBiBr}_6$ double perovskite thin films, focusing on three main areas: 1) understanding the role of grain boundaries on device performance, 2) lowering the bandgap through alloying with Sb^{3+} , and 3) understanding the potential and limitations of bismuth-antimony double perovskite alloys for photovoltaic applications.

For the first area, I show through cathodoluminescence measurements that grain boundaries are the dominant non-radiative recombination sites. I also demonstrate through field-effect transistor and temperature-dependent transient current measurements that grain boundaries act as the main channels for ion transport. Interestingly, I find a positive correlation between carrier mobility and temperature, which resembles the hopping mechanism often seen in organic semiconductors. These findings account for the discrepancy between the long diffusion lengths found in $\text{Cs}_2\text{AgBiBr}_6$ single crystals versus the limited performance achieved in their thin film counterparts, where the diffusion length of the minority carrier (electrons) can be as low as 30 nm.

For the second area, I show through photothermal deflection spectroscopy measurements that mixed alloys of $\text{Cs}_2\text{Ag}(\text{Sb}_x\text{Bi}_{1-x})\text{Br}_6$ (x between 0.5 and 0.9) demonstrate smaller bandgaps than the pure Sb- or Bi-based compounds. The reduction in the bandgap of $\text{Cs}_2\text{AgBiBr}_6$ achieved through alloying (170 meV) is larger than if the mixed alloys had obeyed Vegard's law (70 meV). Through in-depth computations, I propose that bandgap lowering arises from the type II band alignment between $\text{Cs}_2\text{AgBiBr}_6$ and $\text{Cs}_2\text{AgSbBr}_6$. The energy mismatch between the Bi and Sb s and p atomic orbitals, coupled with their non-linear mixing, results in the alloys adopting a smaller bandgap than the pure compounds.

For the third area, I show that despite Sb alloying lowering the bandgap, there is a strong decrease in the power conversion efficiency in photovoltaic devices. Through photothermal deflection spectroscopy and steady-state photoluminescence measurements, I demonstrate that Sb alloying introduces sub-bandgap states, especially a weak luminescent state at 1.55 eV, thus deteriorating the performances of the mixed alloy films in solar cells, especially by causing a substantial reduction in the open-circuit voltage.

These results indicate that addressing the effects of grain boundaries of $\text{Cs}_2\text{AgBiBr}_6$ double perovskite and mitigating the sub-bandgap states in $\text{Cs}_2\text{Ag}(\text{Sb}_x\text{Bi}_{1-x})\text{Br}_6$ alloy are essential to improve their optoelectronic properties and further facilitate their application in optoelectronic devices.

Table of Contents

1 Introduction	9
2 Background	11
2.1 Physics of semiconductors	11
2.1.1 Fundamentals of semiconductors.....	11
2.1.2 p-n junction	20
2.1.3 Solar cell	23
2.1.4 Thin film transistor	25
2.2 Lead-halide perovskite	27
2.2.1 Optoelectronic properties.....	27
2.2.2 Electronic structure and defect tolerance.....	30
2.2.3 Stability and toxicity	33
2.3 Cs ₂ AgBiBr ₆ double perovskite.....	34
2.3.1 Overview of halide double perovskites.....	34
2.3.2 Optoelectronic properties and electronic structure	35
2.3.3 Defects in Cs ₂ AgBiBr ₆	37
2.3.4 Carrier localization.....	39
2.3.5 Ion migration.....	43
2.3.6 Bandgap engineering	47
2.4 Research objectives.....	48
3 Experimental Methods	50
3.1 Film deposition	50
3.1.1 Cs ₂ AgBiBr ₆ thin films with different grain sizes.....	50
3.1.2 Cs ₂ Ag(Sb _x Bi _{1-x})Br ₆ thin films.....	50
3.2 Device fabrication	51
3.2.1 Solar cell fabrication	51
3.2.2 Thin film transistor fabrication	53
3.3 Material characterization.....	53
3.3.1 XRD	53
3.3.2 SEM	54
3.3.3 UV–Visible Spectrophotometry.....	54
3.3.4 Photothermal Deflection Spectroscopy.....	55
3.3.5 Photoluminescence	56
3.3.6 Transient Absorption Spectroscopy.....	56
3.3.7 Cathodoluminescence	57
3.3.8 Rutherford Backscattering Spectrometry.....	58
3.3.9 Photoemission Spectroscopy (XPS and UPS)	59
3.3.10 Transient current measurement.....	62
3.4 Device characterization.....	63
3.4.1 Solar cell characterization.....	63
3.4.2 Thin film transistor characterization.....	64

4 Understanding the Role of Grain Boundaries on Charge-Carrier and Ion Transport in Cs₂AgBiBr₆ Thin Films	65
4.1 Introduction	65
4.2 Phase purity and grain size.....	67
4.3 Charge-carrier recombination	70
4.4 Charge-carrier and ion transport	76
4.5 Conclusions	84
Contributions.....	85
5 Bandgap Lowering in Mixed Alloys of Cs₂Ag(Sb_xBi_{1-x})Br₆ Double Perovskite Thin Films	86
5.1 Introduction	86
5.2 Synthesis and verification of composition	87
5.3 Crystal structure and phase purity.....	91
5.4 Absorption, bandgap and band positions	93
5.5 Electronic structure and bandgap lowering mechanism	101
5.6 Conclusions	111
Contributions.....	111
6 Investigating the Limiting Factors for the Performance of Cs₂Ag(Sb_xBi_{1-x})Br₆ Double Perovskite Solar Cell.....	112
6.1 Introduction	112
6.2 Morphology optimization and device performance	113
6.3 Absorption, photoluminescence and transient absorption	116
6.4 Conclusions and future work	121
6.4.1 Characterization of the sub-bandgap states.....	121
6.4.2 Identification of the sub-bandgap states	121
6.4.3 Mitigation of the sub-bandgap states	122
Contributions.....	122
7 Conclusions and Outlook	123
References	126

1 Introduction

Following the momentous decisions made at the COP21 talks in Paris, where 196 parties agreed to keep the increase in global average temperatures below 2°C above pre-industrial levels, the world's attention is turning to renewable energy sources to curb and reduce the emission of greenhouse gases. Solar energy, perhaps the most reliable form of renewable energy, can be used in virtually every part of the planet, since solar is a ubiquitous and reliable energy source that is more than adequate for meeting the world's energy needs. Specifically, the past decade has seen substantial cost reductions and greatly increased uptake of photovoltaics (PV), particularly in silicon-based modules, which accounts for 94.5% of the global PV market.¹ The growth of the PV market is being driven by ongoing improvements in both silicon solar cell costs and performance,² because each doubling of accumulated production volume resulted in a 20% reduction in the price of modules.³ The positive feedback between production volume and the cost will continue to help PV energy production to grow in future.

PV reaching 'grid parity' (meaning that the projected cost of electricity for a PV project is comparable to local grid electricity prices) denotes a useful milestone, but this is just the first step. For higher penetration of the market, PV systems must cost even less to cover the additional costs of storage or transmission so that solar generation can be dispatched to cost-effectively meet electricity demand more broadly in both time and space.⁴ Policy-driven fixed-price long-term contracts have protected renewables from both lower demand and wholesale electricity prices. "The time" comes when its pure commercial nighttime 'price at the outlet' is lower than that of grid electricity. Dramatic reductions in the capital costs of PV manufacturing, along with significant increases in efficiency are required.⁵

With the increasing dominance of silicon-based modules in the PV market, it is more difficult for other materials to compete against it. Therefore, applying a wider bandgap material on top of the silicon PV to work together in tandem solar cells can avoid the direct competition with the silicon PV industries, whilst also increasing the module efficiency, which helps to reduce the levelized cost of energy further.⁶

One potential material is hybrid organic-inorganic perovskites, with certified efficiencies now surpassing 25% in single junction solar cells.⁷ However, the solar cells with the highest efficiency have all been made with lead-based perovskites. The toxicity of lead could be problematic when accidentally released to the environment, and the solvents used to produce the most efficient lead-halide perovskite solar cells (such as *N,N*-dimethyl formamide) are also

highly toxic.⁸ Currently, solar cells are exempt from EU regulations limiting the usage of lead in electrical components, yet this could change in the future.^{9,10} This has motivated the investigation of lead-free alternatives to the conventional lead-halide perovskites, among which the double perovskite $\text{Cs}_2\text{AgBiBr}_6$ has been a popular candidate.

In this thesis, I aim to identify and address the factors limiting the suitability of $\text{Cs}_2\text{AgBiBr}_6$ for photovoltaic applications.

Chapter 2 discusses the key background relevant to this thesis. Some fundamental principles of semiconductor physics are introduced, as well as the working principles of solar cells and thin film transistors (TFTs). The properties of both the conventional lead halide perovskites and double perovskites are discussed.

Chapter 3 introduces the synthesis methodology for the materials investigated in this thesis. The principles and experimental details of various characterization methods are also given.

Chapter 4 investigates the effects of grain boundaries on charge-carrier and ion transport in $\text{Cs}_2\text{AgBiBr}_6$ thin films. Transient absorption and cathodoluminescence measurements are used to characterize the lifetime and carrier recombination in $\text{Cs}_2\text{AgBiBr}_6$ thin films with different grain boundary densities. The first p-type TFT with $\text{Cs}_2\text{AgBiBr}_6$ as the semiconductor layer is demonstrated, together with capacitance and transient current measurements to explore charge-carrier and ion transport.

Chapter 5 investigates the bandgap lowering mechanism in $\text{Cs}_2\text{Ag}(\text{Sb}_x\text{Bi}_{1-x})\text{Br}_6$ alloys. Through photothermal deflection spectroscopy (PDS), it was found that the Sb-Bi mixed double perovskite alloys could have smaller bandgap than either of the pure compounds. The electronic structure and band positions are calculated by Density Functional Theory (DFT) to provide insight in the origins of the bandgap lowering.

Chapter 6 presents research that builds on the work in Chapter 5. Since the bandgap of $\text{Cs}_2\text{AgBiBr}_6$ could be reduced by alloying with Sb, making it a better candidate for solar absorbers, the performance of $\text{Cs}_2\text{Ag}(\text{Sb}_x\text{Bi}_{1-x})\text{Br}_6$ double perovskite solar cells are investigated. The underlying limiting factors are analysed by transient absorption and photoluminescence measurements.

Chapter 7 discusses the key conclusions of this thesis and the main areas of future work opened up, as well as the possible impact in a broader context.

2 Background

2.1 Physics of semiconductors

2.1.1 Fundamentals of semiconductors

Energy band and bandgap

The electrons of an isolated atom occupy atomic orbitals with discrete energy levels. When two identical atoms are brought together, their atomic orbitals overlap. Each atomic orbital would split into two orbitals, one slightly higher and one slightly lower than their original energy level (Figure 2.1). The atomic orbital with lower energy results from constructive interference of orbitals, with higher electron density between the two atoms, and is called bonding state. The atomic orbital with higher energy results from destructive interference of orbitals, with higher electron density besides the two atoms, and is called antibonding state. When a large number of atoms are brought together, their atomic orbitals would split into a very large number of levels. These levels are so close in energy that they form a continuum band of allowed energies. The highest occupied band that contains the valence electrons is called the valence band (VB). The lowest unoccupied band is called the conduction band (CB). If the valence band is partially full or it overlaps with the conduction band, it is a metal. If the valence band is completely full and separated with the conduction band, it is a semiconductor or an insulator. The separation between the energy of the conduction band minimum and valence band maximum is the bandgap. Normally, a semiconductor has a bandgap of 0.5-3 eV (wide bandgap semiconductors need to be doped to be conductive). At room temperature, semiconductors in the dark will have a small conductivity because a small number of the valence band electrons will be activated thermally into the conduction band. More detailed backgrounds of semiconductors can be found in the books by Sze *et al.*¹¹ and Würfel *et al.*¹²

The band structure of a crystalline solid, that is, the energy-momentum relationship, is obtained by solving the Schrödinger equation. This is usually represented by a band structure diagram as shown in Figure 2.2. The bottom of the conduction band is designated E_C , and the top of the valence band is designated E_V . If the conduction band minimum and the valence band maximum occur at the same momentum (value of k), it is called a direct bandgap. A photon with energy no less than the bandgap is sufficient to create an electron-hole pair. If the conduction band minimum and the valence band maximum occur at different k values, it is an

indirect bandgap. A phonon with correct momentum difference is needed for the creation of electron-hole pair in addition to the photon.

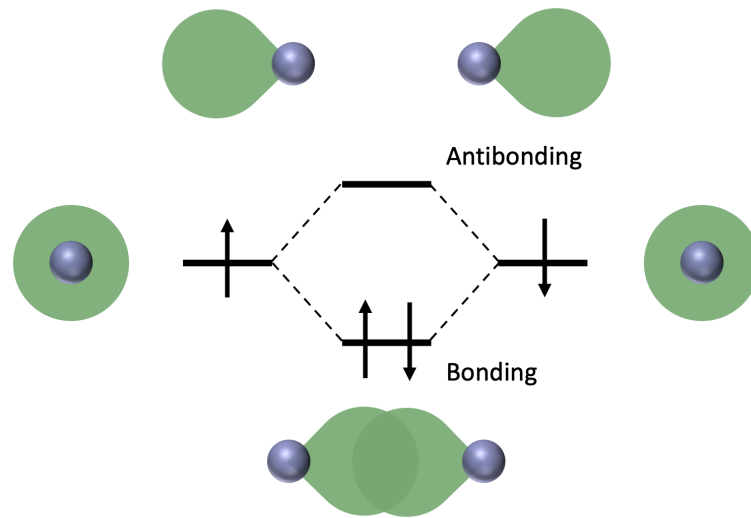


Figure 2.1 Schematic representation of the bonding orbital and the antibonding orbital of the two atomic molecular.

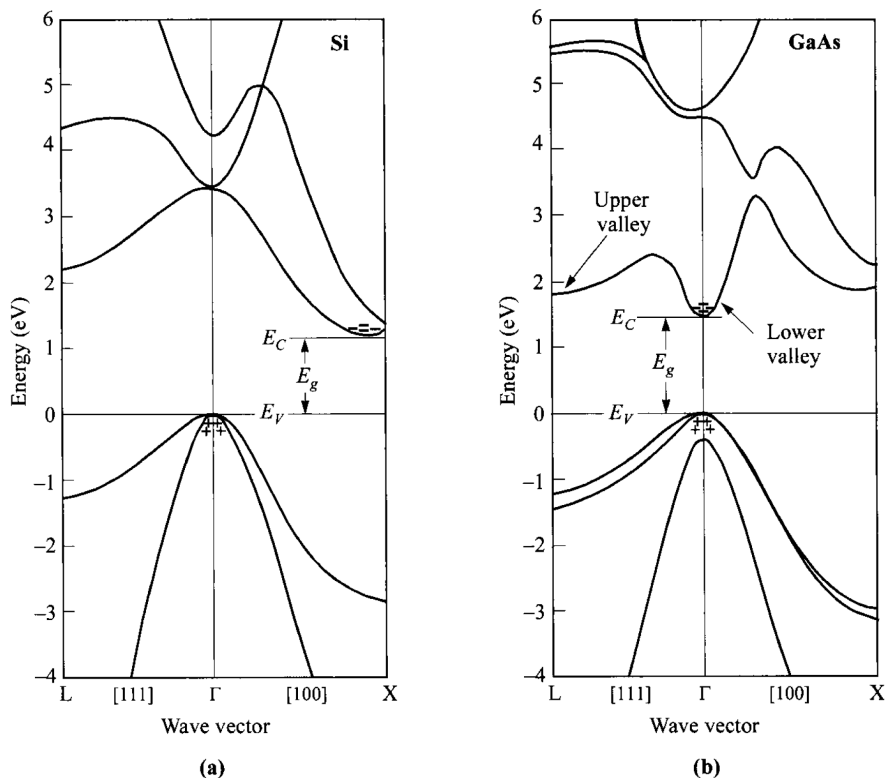


Figure 2.2 Energy-band structures of (a) Si and (b) GaAs, where E_g is the energy bandgap. Plus signs (+) indicate holes in the valence bands and minus signs (-) indicate electrons in the conduction bands.¹¹ Adapted with permission. Copyright 2006, John Wiley and Sons

Near the band edges, i.e., bottom of E_C and top of E_V , the $E-k$ relationship can be approximated by parabolic equation for some traditional semiconductors, such as Si or GaAs.

$$E(k) = \frac{\hbar^2 k^2}{2m_{eff}} \quad (2.1)$$

where m_{eff} is the effective mass. The effective mass is related to the curvature of the $E-k$ curve as,

$$\frac{1}{m_{eff}} = \frac{1}{\hbar^2} \frac{\partial^2 E(k)}{\partial k^2} \quad (2.2)$$

Carriers in motion can also be characterized by group velocity

$$v_g = \frac{1}{\hbar} \frac{dE}{dk} \quad (2.3)$$

Therefore, carriers in flat bands are always heavier and move slower, whereas carriers in less dispersed band are lighter and move faster.

Carrier concentration at thermal equilibrium

Semiconductors can be doped with different type of impurities to vary their conductivity. For example, intrinsic Si can be doped with donors like phosphorus (introduce electrons) to be n type semiconductors or doped with acceptors like boron (introduce holes) to be p type semiconductors.

The number of electrons (n in the conduction band) is obtained by the total number of states $N(E)$ multiplied by the probability of occupation $F(E)$, integrated over the conduction band

$$n = \int_{E_C}^{\infty} N(E)F(E)dE \quad (2.4)$$

The occupancy is represented by Fermi-Dirac distribution

$$F(E) = \frac{1}{1 + \exp [(E - E_F)/kT]} \quad (2.5)$$

where E_F is the Fermi energy level. For nondegenerate semiconductors where doping concentration are smaller than N_c and Fermi levels are several kT below E_C (Boltzmann approximation apply), equation 2.4 becomes

$$n = N_C \exp\left(-\frac{E_C - E_F}{kT}\right) \quad (2.6)$$

where N_C is the effective density of states in the conduction band. Equation 2.6 is equivalent to

$$E_C - E_F = kT \ln\left(\frac{N_C}{n}\right) \quad (2.7)$$

Similarly, for p type semiconductors, we can get the hole density in the valence band and the Fermi energy level near the top of the valence band

$$p = N_V \exp\left(-\frac{E_F - E_V}{kT}\right) \quad (2.8)$$

$$E_F - E_V = kT \ln\left(\frac{N_V}{p}\right) \quad (2.9)$$

For intrinsic semiconductors at finite temperature, thermal generation of electron-hole pairs is balanced by thermal recombination of electrons with holes. The net result is $n=p=n_i$, where n_i is the intrinsic carrier density. The Fermi level for intrinsic semiconductors can be obtained by equating equation 2.7 and 2.9,

$$E_F = E_i = \frac{E_C + E_V}{2} + \frac{kT}{2} \ln\left(\frac{N_V}{N_C}\right) \quad (2.10)$$

Therefore, the Fermi energy level for intrinsic semiconductors lies very close to the middle of the bandgap. The last part of this equation is usually very small that we normally take E_i as in the centre of the bandgap. Hence, the intrinsic carrier density is given by

$$n_i = N_C \exp\left(-\frac{E_C - E_i}{kT}\right) = N_V \exp\left(-\frac{E_i - E_V}{kT}\right) = \sqrt{N_C N_V} \exp\left(-\frac{E_g}{2kT}\right) \quad (2.11)$$

We find that the product of the majority carrier density and the minority carrier density is fixed to be

$$np = N_C N_V \exp\left(-\frac{E_g}{kT}\right) = n_i^2 \quad (2.12)$$

which is also applicable for both n type and p type semiconductors at thermal equilibrium. Rearranging equation 2.6 with 2.11, we have the following alternative equations for carrier densities for n type materials

$$n = n_i \exp\left(\frac{E_F - E_i}{kT}\right) \quad (2.13)$$

$$E_F - E_i = kT \ln\left(\frac{n}{n_i}\right) \quad (2.14)$$

and for p type materials

$$p = n_i \exp\left(\frac{E_i - E_F}{kT}\right) \quad (2.15)$$

$$E_i - E_F = kT \ln\left(\frac{p}{n_i}\right) \quad (2.16)$$

Therefore, E_F will move closer to the conduction band for higher electron density and will move closer to the valence band for higher hole density.

Carrier transport

At low electric field, the drift velocity under an applied electric field is given by

$$v_d = \mu E \quad (2.17)$$

where μ is defined as mobility of the carriers and E is the electric field. μ can be related to the mean free time τ_m and mean free path λ_m of scattering by

$$\mu = \frac{q\tau_m}{m_{eff}} = \frac{q\lambda_m}{\sqrt{3kTm_{eff}}} \quad (2.18)$$

because we have

$$\lambda_m = v_{th}\tau_m \quad (2.19)$$

$$v_{th} = \sqrt{\frac{3kT}{m_{eff}}} \quad (2.20)$$

where v_{th} is the thermal velocity. For semiconductors with both electrons and holes, the general current density under an applied electric field is given by

$$J = \sigma E = q(\mu_n n + \mu_p p)E \quad (2.21)$$

where σ is the conductivity. Mobility always decreases with increasing effective mass. It is related to carrier scattering which is influenced by acoustic phonon and ionic impurities.

Whenever there is a gradient of carrier concentration, the carriers tend to diffuse from the high concentration region to the low concentration region. This flux of carriers follows Fick's law

$$\frac{d\Delta n}{dt} = -D_n \frac{d\Delta n}{dx} \quad (2.22)$$

where D_n is diffusion coefficient or diffusivity. Therefore, the diffusion current of electrons and holes will be

$$J_n = qD_n \frac{d\Delta n}{dx} \quad (2.23)$$

$$J_p = -qD_p \frac{d\Delta n}{dx} \quad (2.24)$$

The relationship between diffusivity and mobility is given by

$$D_n = \frac{kT}{q} \mu_n \quad (2.25)$$

$$D_p = \frac{kT}{q} \mu_p \quad (2.26)$$

Carrier recombination

There are normally three kinds of recombination mechanisms in a semiconductor (Figure 2.3). Radiative recombination happens when an electron in the conduction band recombines with a hole in the valence band and releases energy equal to the bandgap as a photon. For Auger recombination, the released energy is transferred to a third carrier which is subsequently activated to higher energy levels within the same band. It is important for low bandgap materials with higher carrier densities and indirect bandgaps, such as silicon solar cells. The third mechanism is trap-assisted recombination (Shockley Read Hall Recombination). It is a multiple-step relaxation process where an electron and a hole are sequentially captured and recombine to release energy as heat. It is strongest for deep trap states and particularly important at surfaces. In real materials, trap assisted recombination is dominant.

The net radiative recombination rate is given by

$$U_{rad} = R_{rad}(pn - n_i^2) \quad (2.27)$$

where $R_{rad}n_i^2$ is equal to thermal generation rate.

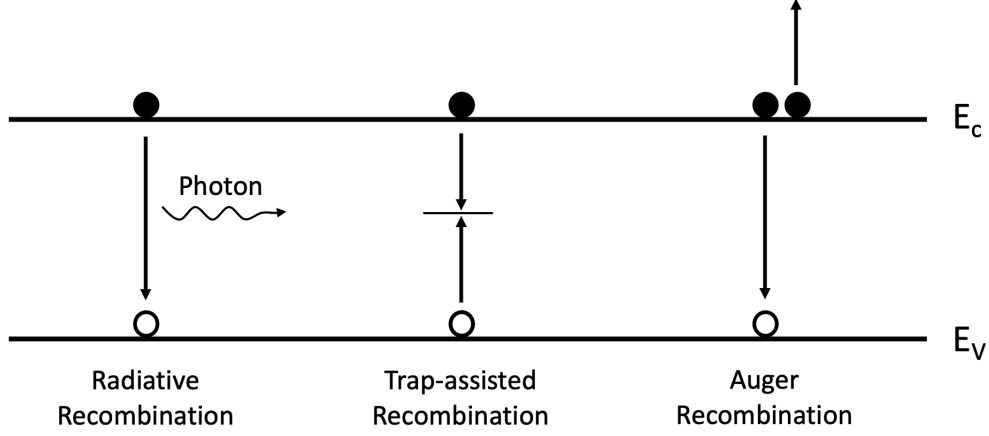


Figure 2.3 Schematic representation of the three kinds of recombination mechanisms.

Net trap assisted recombination rate is

$$U_{trap} = \frac{\sigma_n \sigma_p v_{th} N_t (pn - n_i^2)}{\sigma_n \left[n + n_i \exp\left(\frac{E_t - E_i}{kT}\right) \right] + \sigma_p \left[p + n_i \exp\left(\frac{E_i - E_t}{kT}\right) \right]} \quad (2.28)$$

where σ_n and σ_p are the electron and hole capture cross sections, and N_t and E_t is the trap density and trap energy state respectively. U_{trap} is maximized when E_t equals E_i . Considering only these traps, the recombination rate is

$$U_{trap} = \frac{\sigma_n \sigma_p v_{th} N_t (pn - n_i^2)}{\sigma_n [n + n_i] + \sigma_p [p + n_i]} \quad (2.29)$$

The net Auger recombination rate when two electrons and a hole (usually in n type material) are involved is

$$U_{Aug} = A_p (n^2 p - n_0^2 p_0) \quad (2.30)$$

When two holes and an electron are involved (usually in p type material), the recombination rate is

$$U_{Aug} = A_n (p^2 n - p_0^2 n_0) \quad (2.31)$$

Under completely ionization condition (intermediate temperature range and doping concentration), n equals to N_D for n type material and p equals to N_A for p type material. Under low level injection where the excess carrier density is far more than the minority carrier density and far fewer than the majority carrier density, i.e.

$$p_0 \ll \Delta p = \Delta n \ll n_0 \text{ (n type)}$$

$$n_0 \ll \Delta p = \Delta n \ll p_0 \text{ (} p \text{ type)}$$

The net radiative recombination rate can be simplified to be

$$U_{rad} = \frac{\Delta p}{\tau_p} \text{ (} n \text{ type)} \quad (2.32)$$

$$\tau_p = \frac{1}{R_{rad} N_D} \text{ (} n \text{ type)} \quad (2.33)$$

$$U_{rad} = \frac{\Delta n}{\tau_n} \text{ (} p \text{ type)} \quad (2.34)$$

$$\tau_n = \frac{1}{R_{rad} N_A} \text{ (} p \text{ type)} \quad (2.35)$$

The net trap assisted recombination rate can be simplified to be

$$U_{trap} = \frac{\Delta p}{\tau_p} \text{ (} n \text{ type)} \quad (2.36)$$

$$\tau_p = \frac{1}{\sigma_p v_{th} N_t} \text{ (} n \text{ type)} \quad (2.37)$$

$$U_{trap} = \frac{\Delta n}{\tau_n} \text{ (} p \text{ type)} \quad (2.38)$$

$$\tau_n = \frac{1}{\sigma_n v_{th} N_t} \text{ (} p \text{ type)} \quad (2.39)$$

The net Auger recombination rate can be simplified to be

$$U_{Aug} = \frac{\Delta p}{\tau_p} \text{ (} n \text{ type)} \quad (2.40)$$

$$\tau_p = \frac{1}{A_p N_D^2} \text{ (} n \text{ type)} \quad (2.41)$$

$$U_{Aug} = \frac{\Delta n}{\tau_n} \text{ (} p \text{ type)} \quad (2.42)$$

$$\tau_n = \frac{1}{A_n N_A^2} \text{ (p type)} \quad (2.43)$$

Therefore, we found that under low injection approximation, all expressions of U follow the form

$$U = \frac{\text{excess minority carrier density}}{\text{minority carrier lifetime}} \quad (2.44)$$

If all recombination processes are independent, the general expression can be combined to equation 2.44, where the minority carrier lifetime is

$$\frac{1}{\tau_p} = \sum \frac{1}{\tau_i} = R_{rad}n + A_p n^2 + \sigma_p v_{th} N_t \text{ (n type)} \quad (2.45)$$

$$\frac{1}{\tau_n} = \sum \frac{1}{\tau_i} = R_{rad}p + A_n p^2 + \sigma_n v_{th} N_t \text{ (p type)} \quad (2.46)$$

The one with the shortest lifetime will be the dominant recombination mechanism.

In high level injection where the excess charge carrier generation is far more than the majority carrier density, we will have n approximately equals to p in either n type or p type material. And the recombination equations will develop as

$$U_{trap} = \frac{n}{\tau_p + \tau_n} \quad (2.47)$$

$$U_{rad} = R_{rad}n^2 \quad (2.48)$$

$$U_{Aug} = R_{Aug}n^3 \quad (2.49)$$

The lifetime for each kind of recombination still holds the same dependence on carrier density. Normally, as the carrier density increase, the dominant recombination type change from SRH to radiative to Auger recombination.

Surface recombination is a kind of trap assisted recombination in two dimensions ($\text{cm}^{-2} \text{s}^{-1}$). If a surface or interface have a density N_s traps per unit area, we have

$$U_s = S_p \Delta p \text{ (n type)} \quad (2.50)$$

$$U_s = S_n \Delta n \text{ (p type)} \quad (2.51)$$

Where S_n and S_p , proportional to N_s , are surface recombination velocity for electrons and holes, respectively.

2.1.2 p-n junction

When an n type material and a p type material are brought together, they form a junction with a potential barrier between the regions. The junction acts as a selective barrier for carriers, thus providing asymmetric resistance when applied a bias. Therefore, it only allows current in one direction. By control of the doping levels, large potential barrier can be established to generate large photovoltaics.

Depletion region

When the two types of semiconductors are brought together, due to the carrier concentration gradient, electrons flow from the n type material to the p type, leaving fixed positive charges, and holes flow from the p type material to n type, leaving fixed negative charges behind (Figure 2.4). The fixed charges build in an electric field that tend to prevent diffusion of carriers. Thermal equilibrium is reached when the built-in electric field is just sufficient to prevent further carrier flow. In thermal equilibrium condition, the net electron and hole current will be zero

$$J_n = q\mu_n nE + qD_n \nabla n = \mu_n n \nabla E_F = 0 \quad (2.52)$$

$$J_p = q\mu_p pE + qD_p \nabla p = \mu_p p \nabla E_F = 0 \quad (2.53)$$

Therefore, the Fermi level must be constant throughout the whole sample. As the Fermi level line up, all the bands at a certain distance from the *p-n* junction, together with the vacuum level, shift by the same energy. This is called band bending. For electrons, a higher band position means higher electrostatic potential energy and the associated electric field always points upwards. Hence, electrons will tend to move downwards without other force, and vice versa for holes. The built-in potential is given by the difference in original Fermi level divided by *q*

$$V_{bi} = \frac{kT}{q} \exp\left(\frac{N_D N_A}{n_i^2}\right) \quad (2.54)$$

From Poisson's equation, we obtain

$$-\frac{d^2\psi_i}{dx^2} = \frac{\rho(x)}{\epsilon_s} = \frac{q}{\epsilon_s} [N_D^+(x) + p(x) - n(x) - N_A^-(x)] \quad (2.55)$$

We assume that there are no free carriers in the depletion region and the region in each side has a rectangular shape. By integrating the above Poisson's equation and using boundary

conditions, we get the electric field distribution and potential distribution in the depletion region. The depletion width for each side could also be calculated then. The majority of the potential variation and depletion region will fall into the lightly doped region.

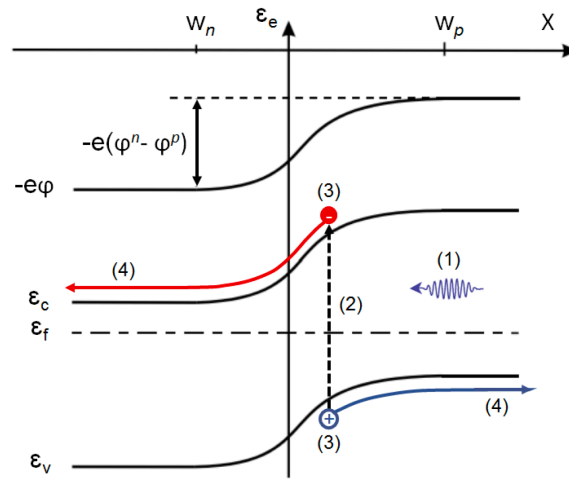


Figure 2.4 Schematic representation of a p-n junction. ϵ_c , ϵ_f , ϵ_v , ϕ and W stand for the conduction band minimum, Fermi level, valence maximum, electrical potential and the depletion width. The subscripts indicate the n-type (left) and p-type semiconductor (right).¹² Adapted with permission. Copyright 2007, John Wiley and Sons

I-V characteristics

The ideal I-V Shockley equation (given below) is based on the abrupt depletion approximation (abrupt p-n junction), Boltzmann approximation ($f(E) = \frac{1}{1 + \exp(\frac{E - \mu}{k_B T})} \approx \exp(\frac{\mu - E}{k_B T})$), low-level injection assumption (the number of minority carriers generated is small compared to the majority carriers of the material.) and no generation-recombination current in the depletion region. In non-equilibrium conditions, if we have a small or intermediate steady disturbance, the population of electrons and holes each relax to a state of quasi-Fermi equilibrium where the Fermi level is split to a quasi-Fermi level E_{Fn} for electrons and quasi-Fermi level E_{Fp} for holes. When an external bias is applied (non-equilibrium), pn is no longer equal to n_i^2 and we have

$$n = n_i \exp\left(\frac{E_{Fn} - E_i}{kT}\right) \quad (2.56)$$

$$p = n_i \exp\left(\frac{E_i - E_{Fp}}{kT}\right) \quad (2.57)$$

$$E_{F_n} - E_i = kT \ln \left(\frac{n}{n_i} \right) \quad (2.58)$$

$$E_i - E_{F_p} = kT \ln \left(\frac{p}{n_i} \right) \quad (2.59)$$

$$pn = n_i^2 \exp \left(\frac{E_{F_n} - E_{F_p}}{kT} \right) \quad (2.60)$$

Therefore, for forward bias, $E_{F_n} > E_{F_p}$ and $pn > n_i^2$; for reverse bias, $E_{F_n} < E_{F_p}$ and $pn < n_i^2$. Similar to equation 2.52 and 2.53, we now have

$$J_n = q\mu_n nE + qD_n \nabla n = \mu_n n \nabla E_{F_n} \quad (2.61)$$

$$J_p = q\mu_p pE + qD_p \nabla p = \mu_p p \nabla E_{F_p} \quad (2.62)$$

Thus, electrons and holes flow according to the gradient of their quasi-Fermi levels: electrons move downwards, and holes move upwards (holes have lower energy in higher position). The quasi-Fermi levels of electrons and holes are split by the external applied voltage,

$$qV = E_{F_n} - E_{F_p} \quad (2.63)$$

Following the continuity equations that deal with time-dependent phenomena, such as low-level injection, recombination and generation

$$\frac{\partial n}{\partial t} = G_n - U_n + \frac{1}{q} \nabla J_n \quad (2.64)$$

$$\frac{\partial p}{\partial t} = G_p - U_p - \frac{1}{q} \nabla J_p \quad (2.65)$$

where G_n and G_p are the generation rate of electrons and holes caused by external factor such as optical absorption and applied bias. The total ideal I-V Shockley equation is

$$J = J_p + J_n = J_0 \left[\exp \left(\frac{qV}{kT} \right) - 1 \right] \quad (2.66)$$

$$J_0 = \frac{qD_p n_i^2}{L_p N_D} + \frac{qD_n n_i^2}{L_n N_A} \quad (2.67)$$

where J_0 is the saturation current at reverse direction. L_p and L_n is the minority diffusion length. If considering the current J_{re} due to the recombination process in the depletion region under forward bias,

$$J = J_p + J_n + J_{re} = J_0 \left[\exp\left(\frac{qV}{mkT}\right) - 1 \right] \quad (2.68)$$

where m varies between 1 and 2.

2.1.3 Solar cell

Fundamentals of solar cells

A photovoltaic cell consists of a light absorbing material connected to the external circuit in an asymmetric manner. Charge carriers are generated in the material by the absorption of light, separated and driven towards opposite terminals by the built-in potential. When a load is connected, the cell outputs voltage and current at the same time at the operating point, doing electric work. The solar cell is equivalent to a circuit where a current generator is in parallel with a diode, and two parasitic resistances, one in series and one in parallel with the cell, as shown in Figure 2.5.

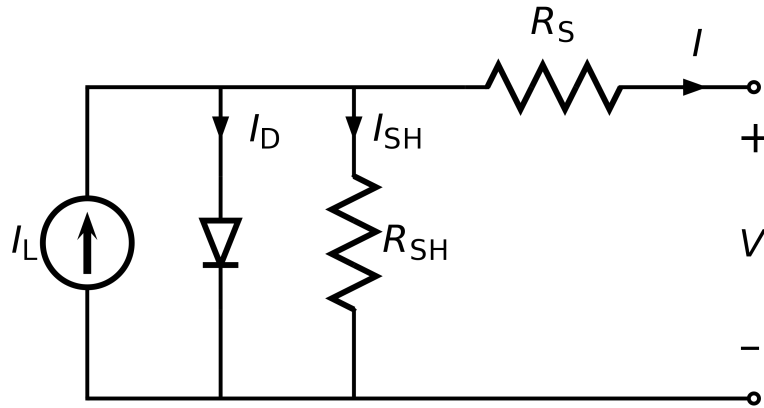


Figure 2.5 Equivalent circuit of solar cells including series and shunt resistances

The current output of the solar cells is

$$J = J_{sc} - J_0 \left(e^{\frac{q(V+JAR_S)}{mkT}} - 1 \right) - \frac{V + JAR_S}{R_{sh}} \quad (2.69)$$

The Shockley-Queisser limit in efficiency is calculated according to thermodynamic detailed balance where the spontaneous radiative recombination is an unavoidable loss mechanism, and where the absorption profile is taken to be a step function.¹³ Any additional non-radiative recombination will reduce the quasi-level splitting and thus reduce the open circuit voltage. Additional recombination reduces photocurrent through the less efficient carrier collection, and the voltage by increasing the dark current.

Design principles

To have an efficient solar cell, charge-carrier generation and transport need to be efficient. For good light absorption, we need a high absorption coefficient or thick absorbing layer. Reflection and shading, such as from the top electrodes, should be minimized, and an appropriate bandgap is needed according to the Shockley-Queisser limit. For better charge separation, a large built-in bias and low recombination rate in the junction are desired. In terms of charge transport, low effective mass and thus high mobility, as well as long minority carrier lifetimes are required. Low series resistance and high shunt resistance are required for efficient majority carrier transport.

Commercial inorganic solar cells

There are generally two categories of inorganic photovoltaics used commercially: crystalline Si-based solar cells (c-Si) and thin film solar cells. Silicon has an indirect bandgap. Therefore, the absorption coefficient is low, and a thick absorption layer (usually hundreds of microns) is needed. The emitter layer should be thin to let more light pass to the base region, but at the same time thick enough to maintain high conductivity. The emitter is doped heavily to achieve high conductivity and allow the base to be lightly doped in order to achieve long minority carrier lifetimes and diffusion lengths. Reflection losses can be minimized by texturing the front surface and adding an anti-reflection coating. Shading could be minimized by using thin conducting fingers and burying them into the emitter. The series resistance can be reduced through differential doping near the metal contact (higher doping near the metal electrodes to increase conductivity). Surface recombination could be reduced by passivating the surface with an oxide layer to reduce the active recombination centres. For the front surface, we can add a window layer with wider bandgap to drive minority carriers back to the junction. For the rear surface, we normally adopt a heavier doping layer at the back to create a back-surface field which also works to block minority carriers, together with the oxide layer and point contacts.

Thin film solar cells normally include amorphous silicon, polycrystalline cadmium telluride (CdTe) and polycrystalline copper indium gallium selenide (CIGS) solar cells, where CdTe solar cell is the most common, and its levelized cost of energy is now lower than c-Si PV. “Thin film” refers to an absorber with thickness less than one micron and deposited onto a substrate. In these amorphous or polycrystalline materials, the defect densities are much higher than the monocrystalline materials, leading to shorter diffusion lengths and higher trap assisted recombination. The high defect densities make a material harder to dope. Conductivity and

carrier transport characteristics become carrier density dependent, especially at low doping and low light intensity. Passivating the amorphous silicon with hydrogen could saturate the dangling bonds and reduce the trap densities. Because of the short diffusion lengths of carriers, p-i-n device structures are used rather than simple p-n junctions. Amorphous silicon solar cells have low light stability because photons could break the connection between hydrogen and the dangling bond. High defect densities reduce the majority carrier mobility and enhance minority carrier recombination. These solar cells thus perform better in high light intensity for saturation of the traps.

Limitations of existing PV

Today the global PV market is dominated by wafer-based crystalline Si solar modules, with a total market share of >90% (65% multicrystalline Si represents and 35% monocrystalline Si of this market segment).^{14,15} Combined with other mature technologies (CdTe and CIGS thin film solar cells), the current line of sight growth of the PV market is far from satisfying the required capacity to maintain the global temperature below 2 °C above preindustrial levels. It is also capital-intensive to build new factories to achieve a sufficiently high PV capacity. Reductions in capex (factory cost) and increases in efficiency are desired to accelerate a growth in capacity and ease demand at the same time.¹⁶ Therefore, coordinating technology innovation is necessary to reach enough cumulative PV capacities to provide a substantial fraction of world's energy needs in the future.

2.1.4 Thin film transistor

A thin-film transistor (TFT) is a type of metal–oxide–semiconductor field-effect transistor (MOSFET).¹⁷ Over a supporting (non-conducting) substrate, a thin film semiconductor is deposited on top as the channel for carrier transport, together with a dielectric layer and metallic contacts. TFTs have three terminals: source, drain and gate. With an applied voltage between the source and drain, TFTs control the flow of current by the application of a voltage to the gate, which in turn alters the conductivity between the source and drain. There are usually four types of TFT structures (Figure 2.6). A common substrate is glass because of the primary application of TFTs as switches that control each pixel in liquid-crystal displays (LCDs).

Both MOSFETs and TFTs rely on the application of an electric field to modulate the conductance of the semiconductor channel. However, important differences exist between the two. First, while TFTs use an insulating substrate, in MOSFETs the silicon wafer acts both as

the substrate and the semiconductor in which the conducting channel is created. Thus, the temperatures involved in fabrication of both devices are different: while processing temperatures exceeding 1000 °C are common for MOSFETs, in TFTs temperatures are limited by parameters such as the softening point of the substrates.¹⁷ In addition, MOSFETs are inversion type of device, in which the polarity of the gate voltage is set so that the surface of the semiconductor layer is in inversion (*i.e.*, the carrier in the conduction channel is opposite to that of the bulk). By contrast, TFTs operate in accumulation mode, in which the conducting channel is formed by the accumulation of the majority charge carriers of the bulk (Figure 2.7).

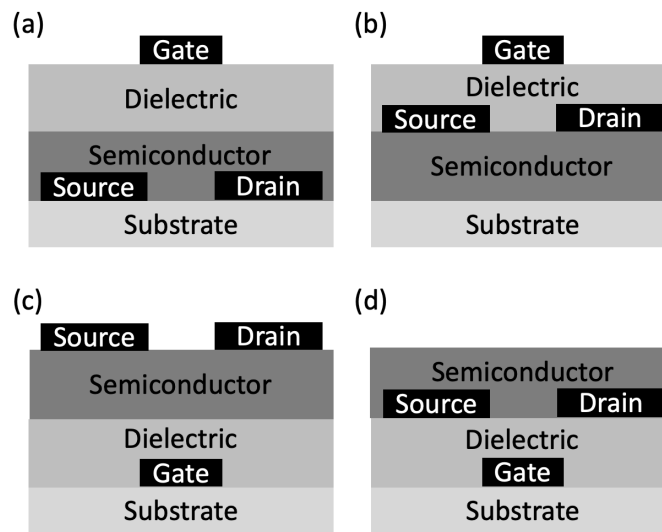


Figure 2.6 Schematic representation of TFT structures. (a) Top-gate bottom-contact, (b) Top-gate top-contact, (c) Bottom-gate top-contact, (d) Bottom-gate bottom-contact.

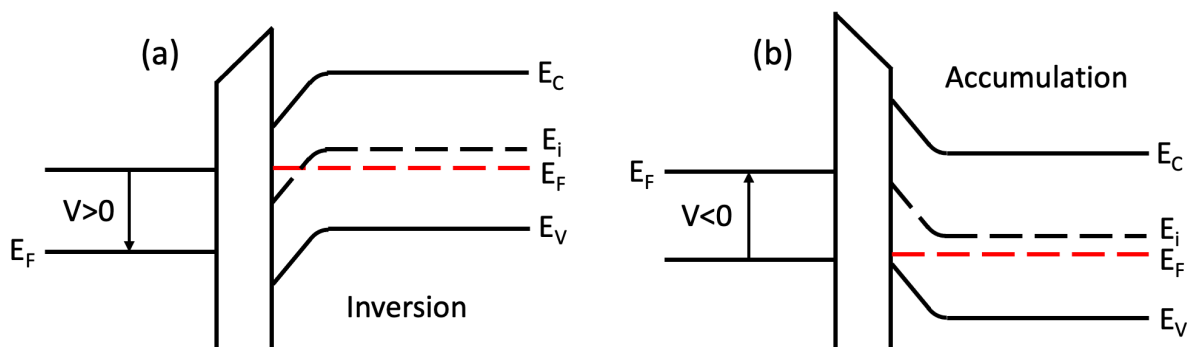


Figure 2.7 Schematic representation of (a) inversion (which occurs in MOSFETs), and (b) accumulation (which occurs in TFTs) for a p-type semiconductor.¹⁸

TFTs provide a versatile platform to study the charge transport mechanism of semiconductors in a controlled manner, macroscopically over the thin film rather than in a localised area.¹⁹ In

addition to determining field-effect mobility, FETs allow precise electrical control of the charge density and have yielded valuable insights into the transport properties of organic^{20,21} and inorganic^{22,23} semiconductors. In this thesis, we fabricated FETs based on the p-type $\text{Cs}_2\text{AgBiBr}_6$ double perovskite. p-type FETs are important for making complementary metal-oxide-semiconductor (CMOS) inverter circuits but have been generally more difficult to achieve than n-type FETs for perovskite semiconductors.¹⁷

2.2 Lead-halide perovskite

Lead-halide perovskites have demonstrated rapid increases in efficiency in photovoltaic devices, with certified efficiencies now surpassing 25% in single junction solar cells after only a decade of their first report.⁷ It has a high absorption coefficient across the entire visible spectrum and also a long carrier diffusion length.²⁴ Its bandgap can be tuned through the composition or dimensionality. In this section, we will take a closer look at the specific properties of lead-halide perovskites.

2.2.1 Optoelectronic properties

The crystal structure of the lead-halide perovskite initially reported in photovoltaics, MAPbI_3 , is depicted in Figure 2.8. Each Pb^{2+} cation is octahedrally coordinated with I^- anions, and each I^- anion is shared with neighbouring octahedra. This corner-sharing octahedral arrangement forms a 3D symmetric lattice. The cuboctahedral voids are filled with the methylammonium molecular cations.

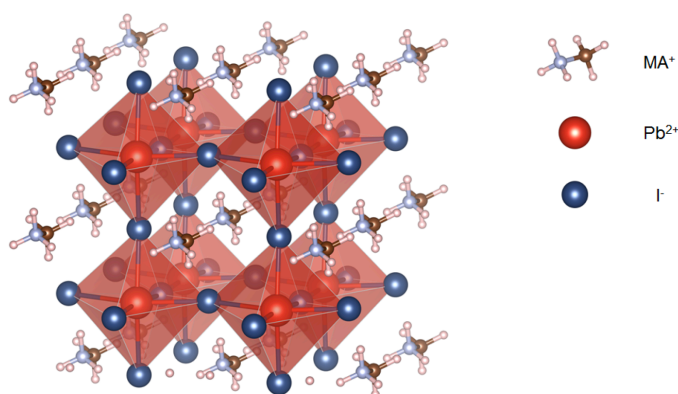


Figure 2.8 MAPbI_3 crystal structure at room temperature with a $Pm\bar{3}m$ space group.

Photoluminescence (PL), which is indicative of the bandgap, electronic quality and charge separation, is an important optical property when studying optoelectronic materials. Lead-

halide perovskites have demonstrated high photoluminescence quantum yield.^{25–27} This indicates that nonradiative recombination is substantially suppressed, which is a prerequisite for achieving the highest performance in light-emitting and photovoltaic applications.²⁸ The PL spectra of some representative organometal halide perovskite materials are shown in Figure 2.9. The narrow PL peak and the sharp absorption onset of $\text{MAPbI}_{3-x}\text{Cl}_x$ in Figure 2.9b reflect its low Urbach energy, and thus high chemical purity and low sub-bandgap defect states. In Figure 2.9d, the sharp emission peak for pure iodide broadens as the bromide ratio increases or vice versa, indicating the formation of solid solutions of iodide and bromide in the lattice. This phenomenon is not obvious for $(\text{MA}_{1-x}\text{FA}_x)\text{PbI}_3$ because the organic cation does not account much for the electronic band structure, and thus the photoluminescence characteristics.

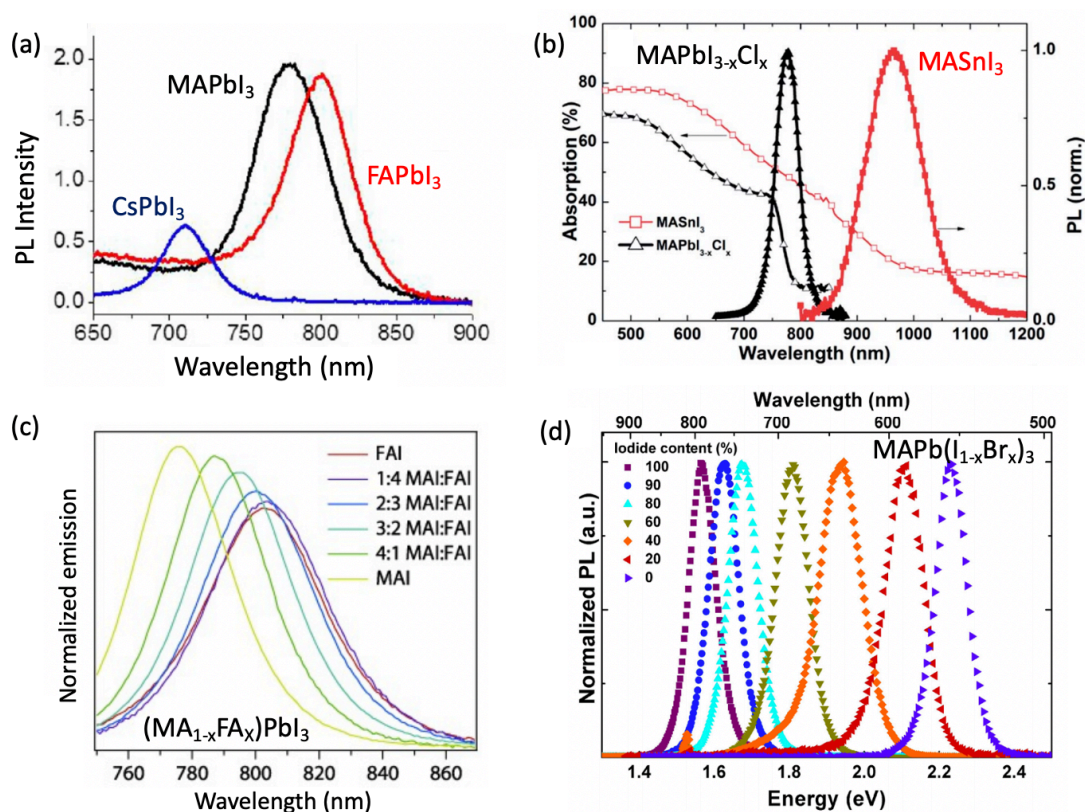


Figure 2.9 Photoluminescence (PL) spectra of some representative organometal halide perovskite materials,²⁹ including (a) lead iodides (Adapted with permission.³⁰ Copyright 2013, American Chemical Society), (b) tin iodide and its lead analogue (Adapted with permission.³¹ Copyright 2014, RSC), (c) MAPbI_3 and FAPbI_3 (Adapted with permission.³² Copyright 2014, John Wiley and Sons), and (d) iodide and bromide mixed halides (Adapted with permission.³³ Copyright 2014, ACS). PL spectra were obtained by photoexcitation at 532 nm for (a), 500 nm for (b), 460 nm for (c) and 400 nm (3.1 eV) for (d).

The transient photoluminescence and photoluminescence quenching experiment conducted by Stranks *et al.*³⁴ reveals balanced electron and hole transport behaviour (Figure 2.10). Using the diffusion coefficient D and recombination lifetime τ_e , where D is estimated from a one-dimensional diffusion mode, and τ_e defined as the time taken to reach $1/e$ of the initial PL intensity, the diffusion length of electrons and holes in MAPbI_3 was estimated to be more than 100 nm, and more than 1000 nm in $\text{MAPbCl}_{1-x}\text{I}_x$. This showed that lead-halide perovskites can be used in a thin film device architecture, rather than being thought of as a sensitiser in solid-state dye-sensitised solar cells, as they were originally conceived.

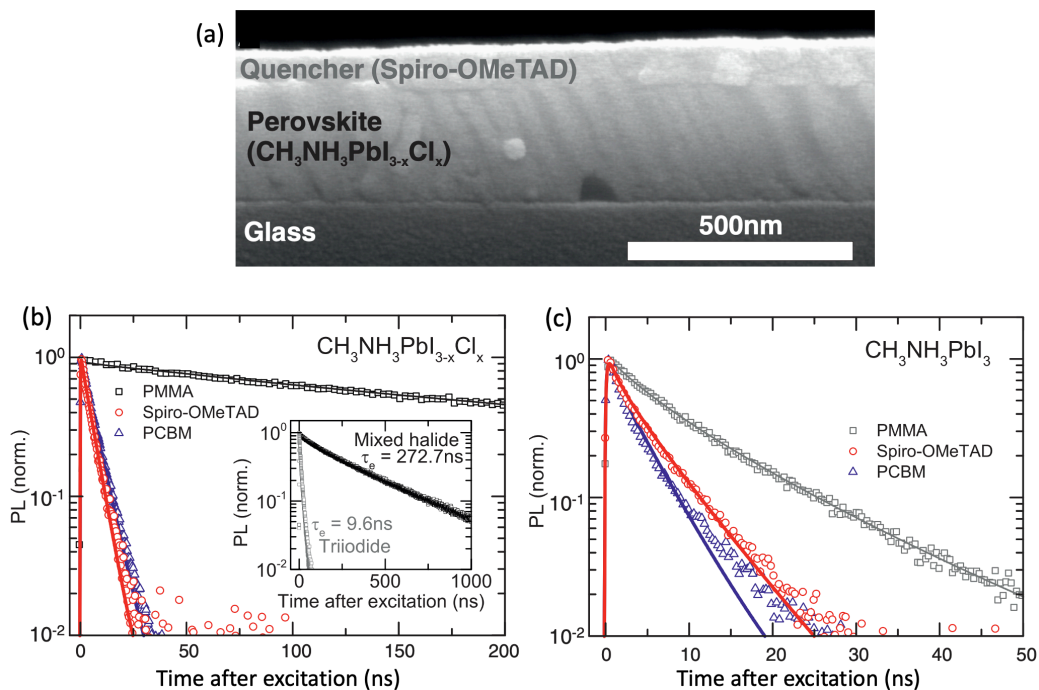


Figure 2.10 (a) Cross-sectional SEM image of 270 nm thick mixed halide absorber layer with hole-quenching layer of Spiro-OMeTAD. Time resolved photoluminescence data taken at the peak emission wavelength of the (b) mixed halide perovskite and (c) triiodide perovskite with an electron (PCBM; blue triangles), hole (Spiro-OMeTAD; red circles) quencher layer or without any quenchers (PMMA). Adapted with permission.³⁴ Copyright 2013, AAAS.

In lead-halide perovskites, the large dielectric constants and disperse band extrema lead to the exciton binding energies being small,^{35,36} and it has been shown that radiative recombination is dominated by efficient free charge carrier recombination instead of exciton recombination, owing to the exciton binding energy being only a few tens of meV at room temperature.^{37,38} The interplay among different recombination mechanisms show that the highest internal photoluminescence quantum yields occur for carrier densities between 10^{15} - 10^{17} cm^{-3} .²⁸ This is

calculated from internal luminescence yields as a function of carrier density and extrinsic Shockley–Read–Hall lifetime using reported values for bimolecular ($1.35 \times 10^{-10} \text{ cm}^3 \text{ s}^{-1}$) and Auger ($1.1 \times 10^{-28} \text{ cm}^6 \text{ s}^{-1}$) recombination constants.^{39,40} Photon recycling will occur if a device has high internal photoluminescence quantum yield and low photon outcoupling, provided that the emission peak is only slightly red-shifted against the absorption onset, which is the case for halide perovskites. In principle, for solar cells, photon recycling could increase the photon and charge carrier concentrations, thus increasing the efficiency. For LEDs, photon recycling has the potential to improve outcoupling in the forward direction. However, Bowman *et al.* showed that photon recycling in lead-halide perovskites has a marginal influence on efficiency.⁴¹ Absorptance and emittance should be maximized when optimizing solar cells and LEDs, even if this reduces the number of photon recycling events.

Cation disorder and stoichiometric deviation can lead to point defects, eventually leading to absent or weak and broad photoluminescence peaks. Correspondingly, in the absorption curve, those low crystalline materials always have long Urbach tails (high absorption below the bandgap) due to the localized states which extend in the bandgap. For halide perovskites, minority carrier lifetime is usually taken as an index to reflect the level of defect states.

2.2.2 Electronic structure and defect tolerance

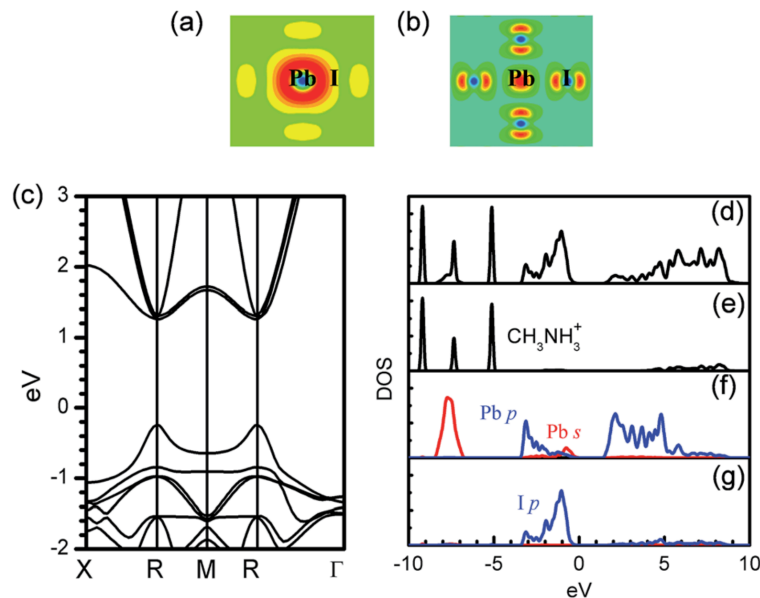


Figure 2.11 (a) partial charge density of the CBM, (b) partial charge density of the VBM, (c) band structure, and (d-g) DOS of $\text{CH}_3\text{NH}_3\text{PbI}_3$ using DFT–PBE calculations. Adapted with permission.⁴² Copyright 2014, AIP Publishing.

The unusual defect properties were attributed to the strong Pb lone-pair s orbital and I p orbital antibonding coupling and the high ionicity of $\text{CH}_3\text{NH}_3\text{PbI}_3$.⁴² From the band structure and density of states (DOS) shown in Figure 2.11, its CBM is derived from Pb p orbitals, and the VBM is a mixture of Pb s and I p orbitals. The fully occupied s orbital of Pb^{2+} has strong antibonding coupling with I p , making the upper valence bands (VBs) dispersive. The disperse bands results in the small hole effective mass which is comparable with the electron effective mass, accounting for the origin of high mobility of both electrons and holes, and thus ambipolar conductivity.⁴² Also, the atomic p orbital of CBM in perovskite exhibits less dispersion than s orbitals of CBM in the second-generation thin film material like GaAs. Therefore, the DOS in the lower CB of the halide perovskites is significantly higher than that of GaAs, leading to a higher density of states, and thus high absorption coefficient.⁴³

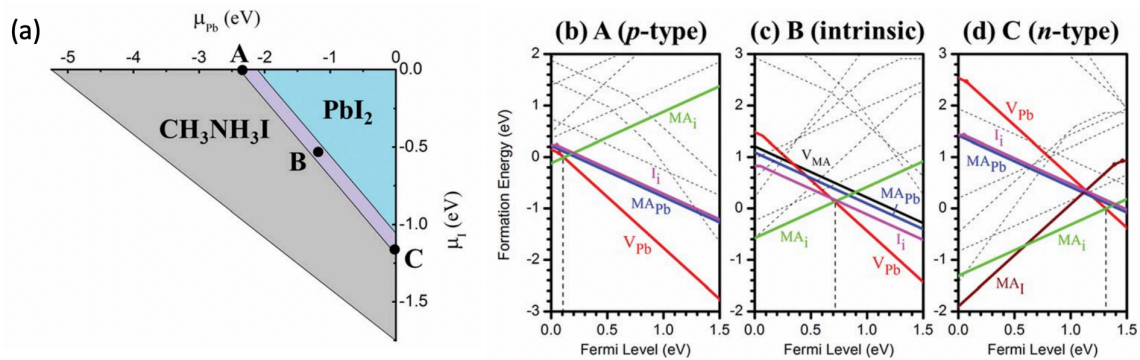


Figure 2.12 The feasible chemical potentials for thermal equilibrium growth of $\text{CH}_3\text{NH}_3\text{PbI}_3$ and the formation energies of intrinsic point defects at different chemical potentials. Defects with much higher formation energies are displayed as dashed lines. Adapted with permission.⁴² Copyright 2014, AIP Publishing.

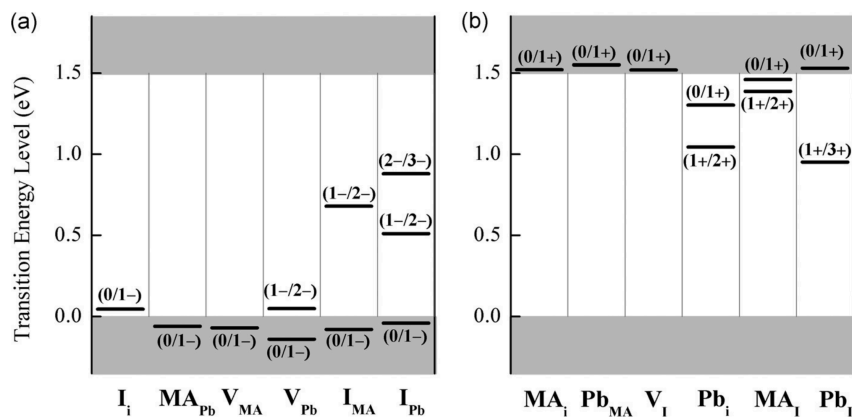


Figure 2.13 The transition energy levels of (a) intrinsic acceptors and (b) intrinsic donors in $\text{CH}_3\text{NH}_3\text{PbI}_3$. Adapted with permission.⁴² Copyright 2014, AIP Publishing.

First principle calculations have been used to study the point defect properties of $\text{CH}_3\text{NH}_3\text{PbI}_3$.⁴² The formation energy for various point defects in three representative chemical potential are shown in Figure 2.12.

The transition level of a defect is the Fermi level position where the defect can donate/accept electrons, with shallow transition levels in the bandgap promoting conductivity and deep transition levels acting as nonradiative recombination centres. The calculated transition levels for different point defects are shown in Figure 2.13. It was found that shallow defect levels normally have low formation energy, providing at least part of explanation for the defect tolerance. This is in correspondence with the reported long electron-hole diffusion lengths.

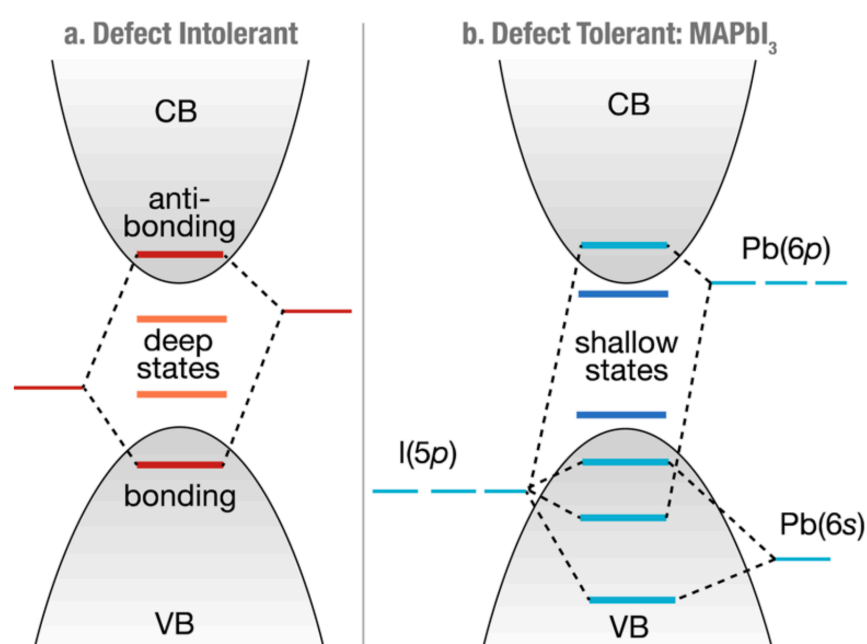


Figure 2.14 Electronic structure of typical ‘defect intolerant’ III–V, II–VI, or group IV semiconductors (a), prone to the formation of deep defect levels, compared to the ‘defect tolerant’ anti-bonding valence band of the lead halide perovskites (b). Adapted with permission.⁴⁴ Copyright 2017, American Chemical Society.

The benign defect tolerant properties of the lead halide perovskites originate mainly from its specific electronic structure. According to the Shockley–Read–Hall (SRH) recombination model, the closer a defect level is to the mid-gap region, the higher the nonradiative recombination rate. In an elementary semiconductor such as Si, there is a bonding state in the VBM and an antibonding state at the CBM. The original Si atomic orbitals are close to the middle of the bandgap. Therefore, a point defect, such as a vacancy, will create a non-bonding state close to these original atomic orbitals (in the middle of the bandgap), leading to fast SRH

recombination (Figure 2.14a). On the other hand, if the VBM originates from antibonding character and CBM from bonding character, such as in Cu_3N ,⁴⁵ non-bonding states would fall in the CBM or VBM instead of the bandgap, thus making the material defect tolerant. For lead halide perovskite (Figure 2.14b), the VBM is from antibonding character. It is therefore able to tolerate the defect states that form from lead vacancies, since these arise from the dangling bonds from the halide. Although the CBM is from antibonding character (instead of the defect tolerant type bonding type), the strong spin orbit coupling from the heavy element can increase the electron affinity, thus also increasing the likelihood that donor defects (e.g., from I vacancies) are shallow as well.⁴⁶ A thorough discussion about defect tolerance can be found in the review by Huang *et al.*⁴⁶

However, the presence of substantial non-radiative losses suggests that deep defect states are present. It is likely that the halide vacancies, particularly at the grain boundaries and interfaces, are playing an important role.²⁸ This is further evidenced by the discoveries that these nonradiative losses can be passivated by variety of agents, such as potassium iodide.⁴⁷ Doherty *et al.* found that traps clusters almost exclusively form at local junctions between grains.⁴⁸ This provides rational strategies for the removal of harmful trap states. Passivation and growth strategies for the removal of these inhomogeneous and distorted grains will be critical to eliminate performance losses and instabilities.

2.2.3 Stability and toxicity

Current perovskite solar cell (PSC) stability is lower than that of traditional silicon solar cells, which have a certified lifetime of 25 years. Device degradation can occur when exposed to moisture, light, heat or oxygen. A challenge with MA-based compounds is their chemical decomposition, releasing gaseous methylamine or methylammonium iodide. The basic degradation mechanism is $\text{CH}_3\text{NH}_3\text{PbI}_3 \rightarrow \text{PbI}_2 + \text{CH}_3\text{NH}_2\uparrow + \text{HI}\uparrow$.⁴⁹⁻⁵¹ Moisture and the ultraviolet part of the solar spectrum were proposed to be particularly detrimental to device stability, especially when using TiO_2 as the electron transport layer, in which TiO_2 can act as a catalyst to accelerate degradation.⁵² The incorporation of phosphonic acid ammonium additives in the perovskite structure of $\text{CH}_3\text{NH}_3\text{PbI}_3$ was reported to increase the moisture resistance.⁵³ Promising results by the addition of Caesium, FA and bromine mixtures, enabling high efficiencies with better thermal stability have been reported.⁵⁴ The ion migration and erosion of the top metal electrode have motivated efforts to develop barrier layers or alternative electrodes, such as carbon.⁵⁵ Perovskite solar cells, with a 2D/3D $(\text{HOOC}(\text{CH}_2)_4\text{NH}_3)_2\text{PbI}_4/\text{CH}_3\text{NH}_3\text{PbI}_3$ structure, have

been reported to remain stable for 12,000 hours under illumination and with exposure to oxygen and moisture.⁵⁶ Perovskite solar cells utilising the standard encapsulation of silicon solar cells (glass and ethyl vinyl alcohol) have been reported to be stable at 85 °C and 85% relative humidity for >1000 h.⁵⁴ However, efforts are still needed to further improve the stability of perovskite solar cells to match those of silicon photovoltaics, as well as develop protocols specifically for accelerated degradation testing of perovskite PV.

Furthermore, it is known that lead in the perovskites is toxic to humans. Lead from perovskites leaking into the ground can enter plants, and consequently the food cycle, ten times more effectively than other lead contaminants already present as the result of the human activities.⁵⁷ Lead is toxic in any concentration and there should be a very low tolerance to its usage in solar cells. Although it is allowed to contain lead in PV modules under the current legislation, light emitting devices and other consumer electronics are not in the list of exemption. Therefore, it is preferred to find lead-free alternatives in the long run.⁵⁸

2.3 Cs₂AgBiBr₆ double perovskite

2.3.1 Overview of halide double perovskites

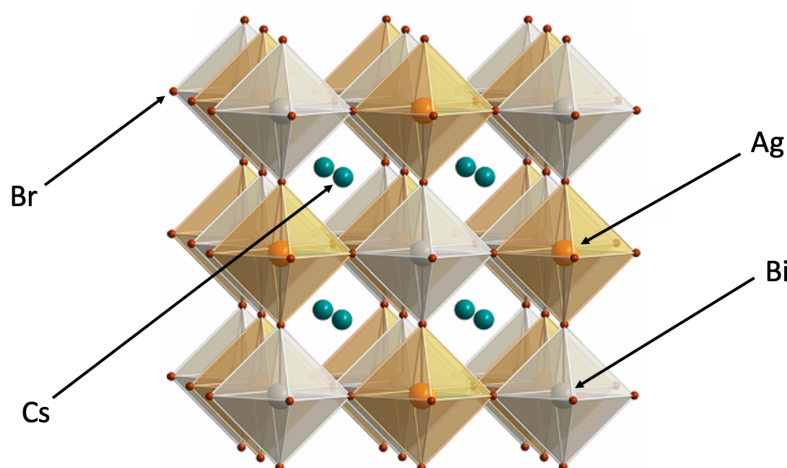


Figure 2.15 X-ray structure of the ordered double perovskite Cs₂AgBiBr₆. Adapted with permission.⁵⁹ Copyright 2016, American Chemical Society.

To address the toxicity of lead in hybrid organic-inorganic halide perovskites, there has been a substantial effort to identify non-toxic alternatives that could replicate the exceptional optoelectronic properties of lead-halide perovskites. This has led to the exploration of halide double perovskites, which have the general formula: A₂B'B''X₆, where A is a monovalent

cation that occupies the cuboctahedral voids, and can be Cs, MA or FA; B' is another monovalent cation that occupy the centre of the metal-halide octahedra, such as K⁺, Cu⁺, Ag⁺ or Au⁺; B'' is a trivalent cation that also occupy the centre of metal-halide octahedra, such as Sb³⁺ or Bi³⁺ and X is Cl⁻, Br⁻ or I⁻.^{59–65} One of the pioneer compounds of lead-free halide double perovskites is Cs₂AgBiBr₆, which exhibits an indirect bandgap of 1.95~2.25 eV and a notably long charge-carrier lifetime of 660 ns~1.4 μs at room temperature.^{59,66,67} In addition, unlike Pb-based perovskites that have to be synthesised in the glovebox, Cs₂AgBiBr₆ shows improved environmental and thermal stability, which allows it to be synthesized under ambient conditions.^{59,65,68} The toxic lead cation is replaced by two more benign cations (*e.g.*, Ag⁺ and Bi³⁺), whilst maintaining the 3D perovskite crystal structure. In order to maintain charge neutrality, the metal-halide octahedra need to alternate between the monovalent and trivalent cations (Figure 2.15).

2.3.2 Optoelectronic properties and electronic structure

At room temperature, Cs₂AgBiBr₆ powder displays weak PL centred at 1.9 eV. The long PL decay time of ~660 ns does not vary significantly between single-crystal and powder samples, as shown in Figure 2.16.⁵⁹ According to Savory *et al.* samples may possess different degrees of cation disorder.⁶¹ This could significantly alter the bandgap and therefore may partly explain the difference in measured bandgaps (1.9~2.25 eV) for the silver–bismuth double perovskites.^{59,66,67}

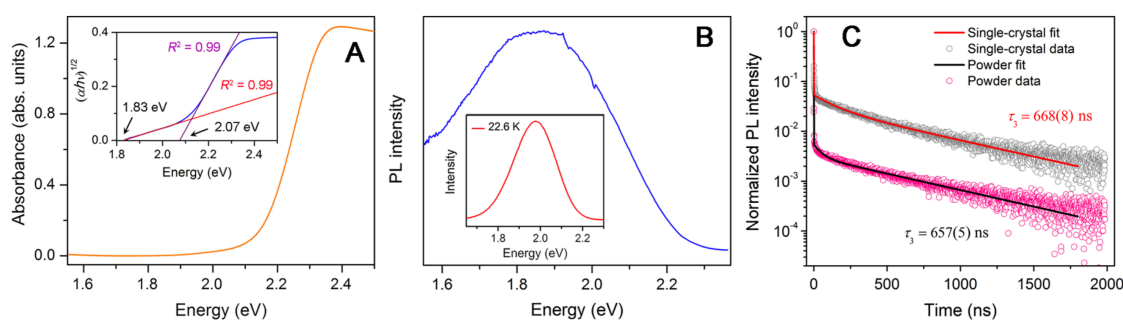


Figure 2.16 (a) Absorbance spectrum of Cs₂AgBiBr₆ powder. Inset: Tauc plot showing the characteristics of an indirect bandgap. (b) Steady-state room temperature photoluminescence (PL) spectrum of a powdered sample upon 500 nm excitation. Inset: low-temperature PL spectrum. (c) Time-resolved room-temperature PL and fits for the PL decay time (τ) in powder and single-crystal samples. Adapted with permission.⁵⁹ Copyright 2016, American Chemical Society.

Spin-orbit coupling (SOC) can have a large impact on the electrical properties, especially for compounds containing heavy elements such as Pb and Bi, which is attributed to relativistic effects. Xiao *et al.* performed electronic structure calculations for $\text{Cs}_2\text{AgBiBr}_6$ using density functional theory with PBE and hybrid HSE functionals, both with and without the effect of SOC.⁶³ The HSE functional predicts an indirect bandgap of 1.97 eV with SOC and 2.21 eV without SOC. Figure 2.17 shows the calculated band structure using PBE non-SOC and HSE+SOC methods.

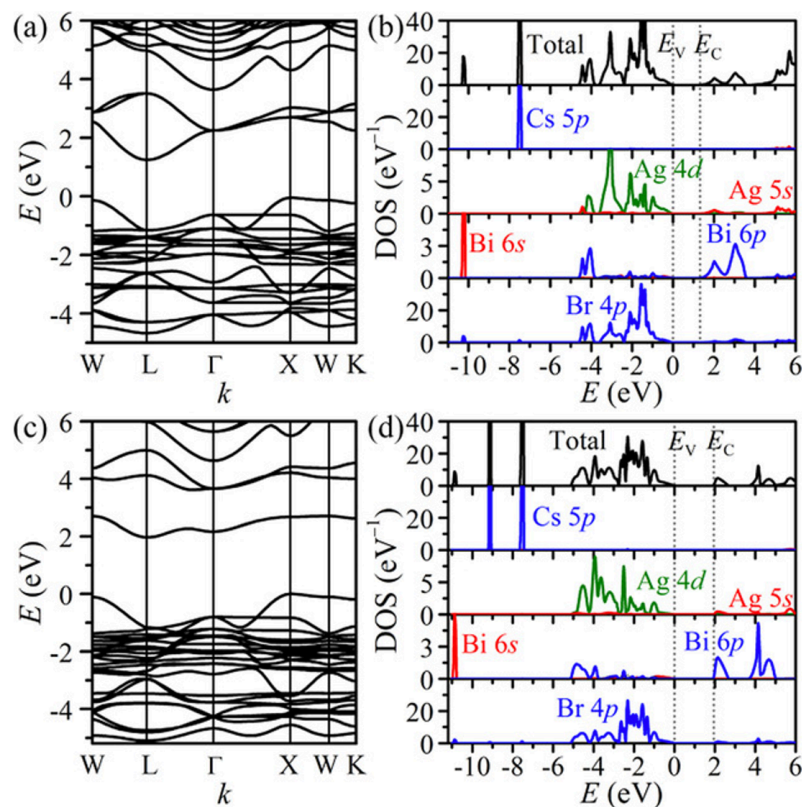


Figure 2.17 (a, c) Band structures and (b, d) total and projected densities of states (DOSs) of $\text{Cs}_2\text{AgBiBr}_6$ calculated with the (a,b) PBE non-SOC and (c, d) HSE+SOC methods. Adapted with permission.⁶³ Copyright 2016, John Wiley and Sons.

From Figure 2.17, we can see the VBM is located at the X point and the CBM is located at the L point. The VBM consists of antibonding states of Br 4p and Ag 4d orbitals. The CBM is mainly composed of Bi 6p orbitals and slightly of Ag 5s and Br 4p orbitals. Enforced by the preferential Ag d interactions at X, the bandgap of $\text{Cs}_2\text{AgBiBr}_6$ becomes indirect. As these features are replicated in the chloride and iodide, it appears that the electronic mismatch between Ag and Bi is the fundamental cause of the large, indirect bandgaps of the $\text{Cs}_2\text{AgBiX}_6$ family.⁶¹ To permit a direct bandgap in a double perovskite structure, silver must be replaced

by an atom with valence s states, for example, the “lone pair” 5s and 6s states in In^+ and Tl^+ .⁶¹ In $\text{Cs}_2\text{AgBiBr}_6$, the VBM-deriving Ag 4d and Br 5p orbitals cannot connect 3-dimensionally because the $[\text{AgBr}_6]$ octahedra are isolated by the adjacent $[\text{BiBr}_6]$ octahedra. Similarly, the CBM-deriving Bi 6p orbitals cannot connect 3-dimensionally because of the isolated $[\text{BiBr}_6]$ octahedra.⁶⁹ Therefore, the confined frontier orbitals lead to more localized, flat band edges and a large bandgap. Although an indirect bandgap need not necessitate weak absorption provided a direct allowed transition exists only slightly higher in energy. In the case of the $\text{Cs}_2\text{AgBiX}_6$ materials, however, the energy level difference between these two conditions is large. This would severely impact the absorption coefficient and photoluminescence quantum yield.

2.3.3 Defects in $\text{Cs}_2\text{AgBiBr}_6$

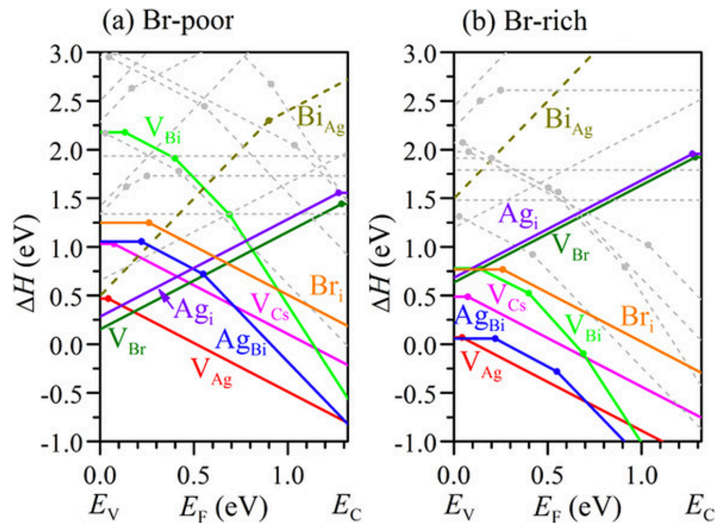


Figure 2.18 Calculated formation enthalpies, ΔH , of intrinsic defects in $\text{Cs}_2\text{AgBiBr}_6$ as a function of the Fermi level, E_F , at two representative chemical potential points: (a) Br-poor and (b) Br-rich. Defects with very high ΔH values are shown by dashed lines. Adapted with permission.⁶³ Copyright 2016, John Wiley and Sons.

Theoretical calculations about defects in $\text{Cs}_2\text{AgBiBr}_6$ have been made by Xiao *et al.*⁶³ Two representative chemical potentials (Br-poor and Br-rich) are chosen, at which the calculated formation enthalpies (ΔH) of the defects as a function of the Fermi energy (E_F) are plotted in Figure 2.18. The calculated transition levels $\varepsilon(q/q')$ of acceptor and donor defects are summarised in Figure 2.19. These defect calculations show that V_{Ag} has the lowest formation energy and acts as a shallow acceptor. $\text{Cs}_2\text{AgBiBr}_6$ would therefore naturally exhibit p-type

conductivity. Although Ag_{Bi} , V_{Bi} and Br_i have deep transition levels in the bandgap, they can be significantly suppressed in the Br-poor Bi-rich growth condition. It is noted that, according to their calculations, V_{Br} is a shallow donor and has much higher formation energies than V_{Ag} . This is in contrast to the calculated result by Li *et al.* that V_{Br} is a deep donor with small formation energy and require Br-rich Bi-poor conditions to suppress.⁷⁰

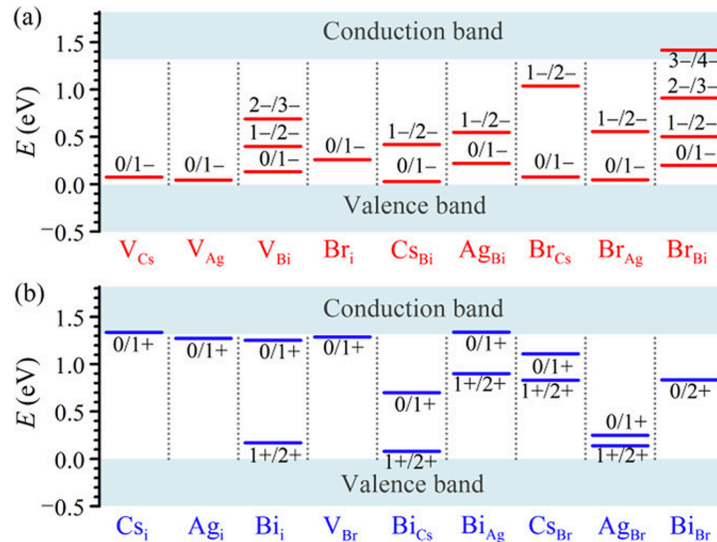


Figure 2.19 Calculated transition energy levels $\varepsilon(q/q')$ for (a) intrinsic acceptors and (b) intrinsic donors in $\text{Cs}_2\text{AgBiBr}_6$. Adapted with permission.⁶³ Copyright 2016, John Wiley and Sons.

Thorough experimental measurements of the defects in $\text{Cs}_2\text{AgBiBr}_6$ have not been made, but there have been reports investigating various aspects of the role of defects on the optoelectronic properties of this material and related compounds. This is in part due to defect formation (and consequently the majority carrier population) being strongly influenced by the material fabrication technique and growth conditions that can substantially alter the semiconductor electronic properties.⁷⁰ Halide vacancies are prime defects for shallow trapping in lead halide perovskites; their formation enthalpies are relatively low, and they typically form shallow traps within a few kT of the conduction band.^{42,71–73} Similarly, halide vacancies are also reported to be the prime defect for $\text{Cs}_2\text{AgBiBr}_6$. Degassing of Br_2 was observed by mass spectrometry from the related $\text{Cs}_2\text{AgTlBr}_6$ double perovskite.⁷⁴ Igbari *et al.* also found that $\text{Cs}_2\text{AgBiBr}_6$ solar cells with a lower Br stoichiometry have lower efficiencies.⁷⁵ Consistently, Longo *et al.* reported a sequentially evaporated n-type $\text{Cs}_2\text{AgBiBr}_6$ and found that surfaces accumulate electron traps by Surface Photovoltage (SPV) measurements, which they attributed to Br vacancies.⁷⁶ They estimated the electron diffusion length to be only 30 nm through External

Quantum Efficiency (EQE) measurements on Cs₂AgBiBr₆ solar cells. Delor *et al.* reported trap densities exceeding 10¹⁷ cm⁻³ within ~20 nm of the surface of Cs₂AgBiBr₆ single crystals. They stated that carrier diffusion lengths can still exceed 1 μm even in the presence of large trap densities and under solar excitation densities where traps are not saturated.⁷⁷ They attributed this to the shallow nature of the halide vacancy defect state that likely form through surface bromine degassing. This is consistent with the results from Time Resolved Microwave Conductance (TRMC) and Transient Absorption Spectroscopy (TAS) measurements which show that at least one type of carrier has lifetimes in the millisecond range.^{67,78,79} It is noted that a large discrepancy exists between carrier diffusion lengths (30 nm in thin films *v.s.* 1 μm in single crystals).

Apart from halide vacancies, the aforementioned Ag vacancy from theoretical calculations could also be possible, as it can lead to a p type conductivity, which has been confirmed experimentally by X-ray photoemission spectroscopy (XPS).^{66,67}

Some works attributed the PL peak with large Stoke shift in Cs₂AgBiBr₆ to originate from a colour centre, but it is not clear whether this arises from defect states, and if they do, where the defect states are from.^{80,81}

2.3.4 Carrier localization

Atoms vibrate around their equilibrium crystallographic positions, and these quantized vibrations are described by phonons. Phonons can be optical (out of phase vibrations) or acoustic (in-phase vibrations). In both cases, the vibrations can either occur perpendicular (transverse mode) or in-plane (longitudinal mode) to the direction of propagation. When a charge carrier moves in a material, it can distort the lattice and drag this distortion field along with it. Thus, the carriers are effectively coupled to the phonons, forming a quasi-particle known as a polaron. Depending on the spatial extent of this polarization cloud, a general classification into small and large polarons can be introduced, which form as a result of coupling to acoustic (small) or optical (large) phonons. While large polarons are viewed as delocalized, with the polaron radius much larger than the lattice constant, small polarons are localized within one unit cell.⁸² Other than size, the most important difference between large and small polarons is in their transport properties: large polarons tend to have band-like transport with the mobility decreasing with increasing temperature, while small polarons usually undergo incoherent hopping transport with mobility increasing with temperature.⁸³

In a polar crystal, Fröhlich interactions are expected, in which charge-carriers couple to longitudinal optical (LO) phonons.⁴⁶ The strength of this electron–phonon coupling is described by a dimensionless coupling constant, α , which is given by equation 2.70⁸²

$$\alpha = e^2 \left(\frac{1}{\epsilon_\infty} - \frac{1}{\epsilon_0} \right) \sqrt{\frac{m^*}{2\omega_0}} \quad (2.70)$$

where ω_0 is the characteristic longitudinal optical phonon frequency (which can be measured by Raman spectroscopy), ϵ_∞ and ϵ_0 the dielectric constants at infinite and zero frequency, respectively, and m^* the effective mass of the electron or hole without phonon coupling. This electron-lattice interaction can also be quantified through the Huang–Rhys factor, S , which indicates the average number of phonons emitted after an optical transition between excited and ground states.⁸⁴

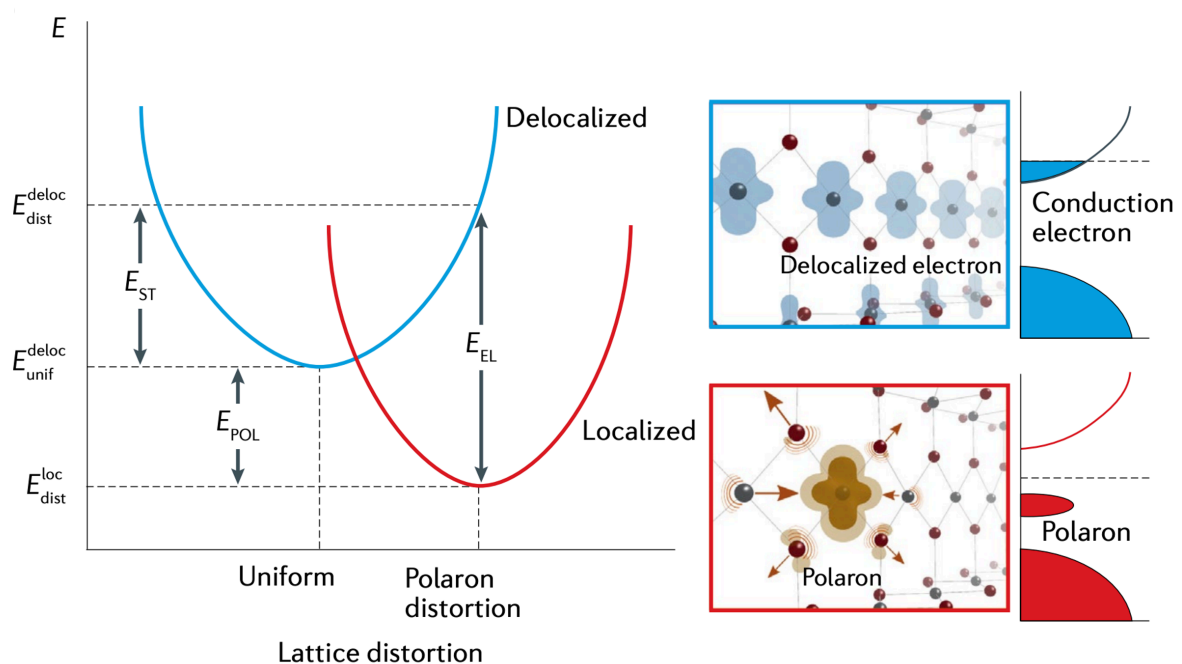


Figure 2.20 Configuration coordinate diagram depicting the energy balance as a function of lattice distortion for a conduction (delocalized) electron and for a localized polaron. E_{ST} is the structural energy, E_{POL} the polaron binding energy and E_{EL} is the electronic energy. The right side of the panel shows charge density isosurfaces and the corresponding schematic band structure of a delocalized conduction electron (upper panel) and a small polaron with the polaron peak localized below the Fermi energy (lower panel). Adapted with permission.⁸² Copyright 2021, Springer Nature.

The Fröhlich interactions described above relate to interactions spanning over dozens of unit cells, without pronounced localization effects, and are therefore large polarons.^{85,86} If the charge-carriers further couple to acoustic phonons, shorter-range, localized interactions can result (small polarons).^{85,87} In the limiting case, the carrier is effectively immobilized, and therefore termed ‘self-trapped’.^{87,88} Carrier localization breaks down the electronic band picture (as depicted in an E vs. k diagram for a periodic structure) replacing it with a local polaronic picture,⁸⁹ which is depicted in the configuration coordinate diagram, represented in Figure 2.20. Configuration coordinate diagrams show how the energy of a lattice in the ground state and excited states changes with local distortions, which can arise from interactions with acoustic or LO phonons.

Excitons (electrons and holes Coulombically bound together) can also couple with phonons. When electrons are initially excited from the ground state to an excited state, they exist as a hot carrier before cooling down, during which process they could couple to LO phonons. The free carrier could lose energy E_b to become a free exciton if E_b is sufficiently high or if the excitation fluence is high. Next, if self-trapping is energetically favored, the free carrier/exciton could relax to the self-trapped state, release energy E_{st} . At the same time, the ground state energy increases due to the deformation of the lattice, and this change in energy is the deformation energy E_d . The localized carrier in the self-trapped state could couple to the ground state and luminescence directly.⁸⁴ This PL peak could therefore be centered at energy $E_{PL} = E_g - E_b - E_{st} - E_d$ (Figure 2.21a). When the coupling strength is very strong, the excited and ground state curves can cross in the configuration coordinate diagram, which means that some excited electrons and holes can recombine via this interaction non-radiatively, emitting phonons (Figure 2.21b).⁸⁴

Self-trapping and trapping are similar processes in many ways. For example, both are multi-phonon emission processes, involve lattice distortions, and result in carrier localization in the lattice.^{90,91} The key difference is that trapping involves a permanent local perturbation, such as a defect or an impurity.⁸⁸ When excitons localize in the lattice in the absence of defects due to distortions in the lattice, This is referred to as intrinsic self-trapping (Figure 2.21c(A)). These self-trapped excitons (STEs) can be considered to be defect states, but unlike lattice defects, STEs are only created after excitation and will recover after relaxation. Moreover, if the exciton occurs in the vicinity of a permanent defect, it will form an extrinsic STE that is trapped at different energies compared to those of intrinsic STEs or bare defect trapping (Figure 2.21c).⁹²

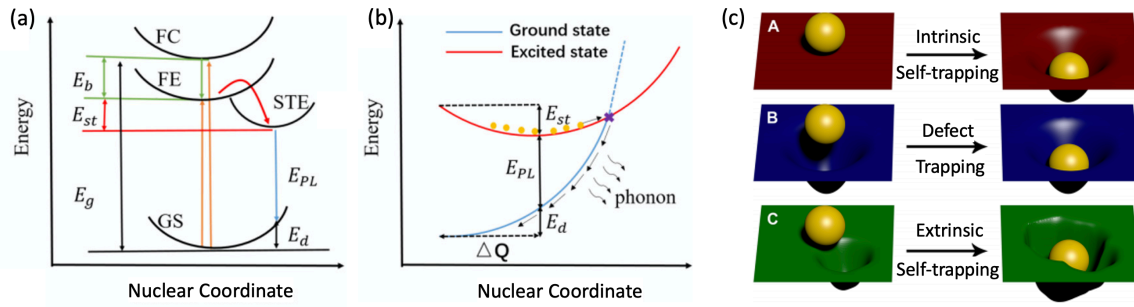


Figure 2.21 (a) Schematic of the energy level structure of STE (GS, ground state; FE, free exciton state; FC, free carrier state; STE, self-trapped exciton state; E_g , bandgap energy; E_b , exciton binding energy; E_{st} , self-trapping energy; E_d , lattice deformation energy; E_{PL} , emission energy). Adapted with permission.⁸⁴ Copyright 2019, American Chemical Society. (b) Schematic of the nonradiative recombination process for strong electron phonon coupling. Orange circles represent excited electrons. Adapted with permission.⁸⁴ Copyright 2019, American Chemical Society. (c) Exciton self-trapping and trapping at permanent defects represented by balls deforming a rubber sheet. Adapted with permission.⁹² Copyright 2019, American Chemical Society.

Early work attributed carrier-phonon coupling in $\text{Cs}_2\text{AgBiBr}_6$ to be primarily Fröhlich (large polaron), which was supported by fits to the temperature dependence of the PL linewidth, which gave a strong coupling factor to LO phonons, and weak acoustic phonon coupling factor.⁹³ This is consistent with the observation based on time-resolved microwave conductance measurements, which showed the sum mobilities of all mobile carriers to increase as temperature decreases.⁷⁹ The dominant LO phonon mode carriers couple to is the A_{1g} symmetric stretching mode of the $[\text{BiBr}_6]^{3-}$ octahedra, which has an energy of $175\text{--}180\text{ cm}^{-1}$ ($\sim 22\text{ meV}$).^{80,89,93,94} This has been found from both Raman measurements as well as Fourier transforms on the periodic of oscillations in the ground state bleach from transient absorption spectroscopy measurements on the picosecond timescale.⁹⁴ However, $\text{Cs}_2\text{AgBiBr}_6$ has much more limited mobilities and broader PL linewidth than MAPbI_3 . Also, large polaron formation has been associated with a reduction in hot carrier cooling rates,⁹⁵ while recent studies have revealed $\text{Cs}_2\text{AgBiBr}_6$ to be characterized by fast hot carrier cooling.⁹⁶

Some recent works, however, proposed that acoustic phonons play an important role, which lead to small polarons or even self-trapped excitons forming.^{81,89,97,98} Wu *et al.* pointed out that fitting the PL linewidth under strong coupling condition would lead to the conclusion that acoustic phonons play a significant role,⁸⁹ as opposed to the conclusion that optical phonons

are dominant when fitting the PL linewidth using equations for weak coupling condition.⁹³ Transient reflectance spectroscopy and optical pump terahertz probe (OPTP) measurements also provide strong evidence in support of self-trapping in Cs₂AgBiBr₆, by showing there to be an initial ultrafast drop in the density of excited state carriers or the mobility of the carriers on a picosecond timescale.^{89,81} The proposed explanation is that hot carriers thermalize *via* LO phonons on a sub-picosecond timescale, before coupling to acoustic phonons within the picoseconds time range, then interacting with defects on longer timescales. In support of this, it was found that changing the defect density of the Cs₂AgBiBr₆ did not influence the kinetics on the <10 ps timescale.⁸⁹ Notably, the localization rate was found to be temperature-independent, which is consistent with self-trapping rather than trapping.⁸¹ Furthermore, it is found that carriers formed immediately after photo-excitation have a negative dependence of mobility with temperature (band-like transport of large polarons), whereas carriers after localization have a positive dependence (thermally-activated hopping of small polarons).⁸¹ It has also been argued that the rapid localization is not due to carrier relaxation directly to color centers because: i) the final mobility of the localized state (1.3 cm² V⁻¹ s⁻¹ at room temperature) exceeds that expected from carriers tightly bound in traps, ii) the picosecond timescale of localization would require the defect density too high, and iii) carrier diffusion to color centers would be temperature-dependent, whereas the localization rate was found to not depend on temperature.⁸¹

2.3.5 Ion migration

Ion migration in lead-halide perovskites

Solid-state diffusion of ions can be mediated by defects, especially vacancies. The concentration of defects depends on the thermodynamic equilibrium of the material which can be described by formation energy of the defect, and the processing history of the material. Therefore, different samples of the same material can have different conductivity and photophysical properties. The total ionic migration process depends on the concentrations of the relative defects and the activation energy for ion migration. For example, the interstitial migration may have low activation energy, but if the concentration of the interstitial species is low, this mechanism would not contribute appreciably to the overall ionic transport.

First-principles calculations agree on that there are a large number of low-energy point defects in lead-halide perovskites, leading to high equilibrium concentrations.^{99–101} Iodine vacancies

(V_i^+) are believed to have the lowest formation energy and thus the highest concentration in MAPbI_3 .¹⁰¹ Eames *et al.* calculated that the activation energy for vacancy mediated ion migration in MAPbI_3 for MA^+ , Pb^{2+} , and I^- were 0.58 eV, 2.31 eV and 0.84 eV, respectively.¹⁰² They further extracted the activation energy for ion migration from photocurrent relaxation, which was measured to be around 0.60~0.68 eV. Therefore, they attribute this to the migration of the iodide anion via vacancies. The method they used to extract the activation energy is to fit the transient photocurrents under different temperatures with exponential function to extract time constants and use these time constants to fit an Arrhenius function to get the activation energy E_a (Figure 2.22). Interestingly, they fit the photocurrent rise after applying a reverse bias with a bi-exponential function and obtained two different set of time constants, but the two different sets of time constants gave similar activation energies. Apart from migration timescales, how easily ions can move can also be seen from the electric field needed to drive them. Yuan *et al.* investigated ion migration in a polycrystalline film along the lateral direction. They found that some ions began to move at a relative smaller electrical field of $\sim 0.1 \text{ V}/\mu\text{m}$ (named “fast ions”) and some ions began to move at electrical field of $>0.3 \text{ V}/\mu\text{m}$ (named “slow ions”). The origins of “fast ions” and “slow ions” may be caused by ion migration through different channels (through the bulk or the grain boundaries or film surface), or by the migration of different species with different E_A , or by the combination of them.^{103,104}

Additional contributions from CH_3NH_3^+ diffusion under “device-like” conditions is also possible as the activation energy is also reasonably small (0.8 eV) compared to that of Pb^{2+} diffusion (2.3 eV).¹⁰² However, identification of the migrating species in many studies is often from indirect evidence, such as the closeness of the activation energy value from experiments and from calculation. Transient ion drift measurement by measuring the device capacitance has been reported to be able to differentiate the positive and negative ionic species.¹⁰⁵ Futscher *et al.* found that the concentration of mobile MA^+ ions is significantly higher than the concentration of mobile I^- ions but the diffusion coefficient of I^- ions is three orders of magnitude higher than the diffusion coefficient of MA^+ ions. They also claimed that the measured capacitance change is due to the migration of ions and not to the migration of vacancies because the diffusion coefficient of the assigned negative ion is similar to I^- ions in literature. To determine whether iodine motion occurs through interstitials or vacancies, Senocrate *et al.* studied ionic conductivity as a function of iodine partial pressure, which revealed iodine vacancies to be responsible for ion conduction.¹⁰⁶

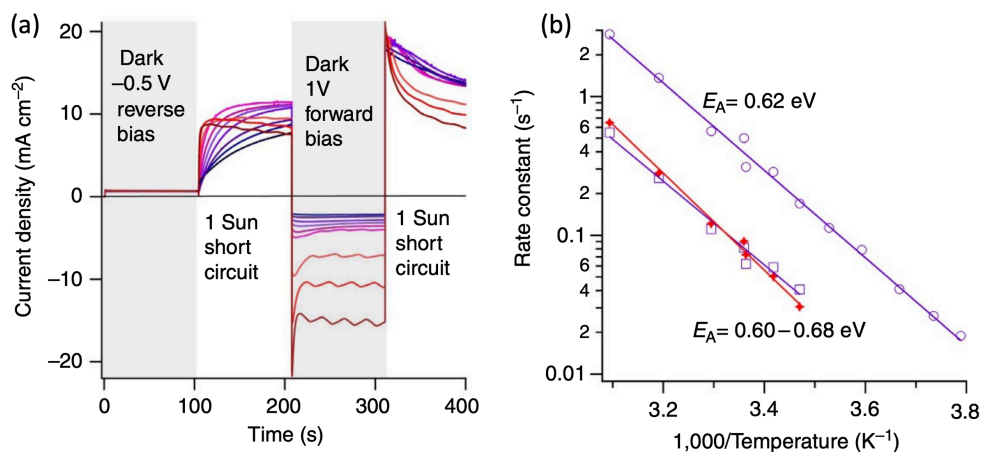


Figure 2.22 (a) The measurement sequence in a $\text{TiO}_2/\text{CH}_3\text{NH}_3\text{PbI}_3/\text{spiro-OMeTAD}/\text{Au}$ cell is indicated; measured temperatures (to the nearest 0.5°C) of the devices were -9.5 (dark blue), -5.5 , 0.5 , 5 , 10.5 , 15 , 19.5 , 24.5 , 30 , 40 and 50°C (dark red). The dark current under forward bias was very sensitive to fluctuations in the controlled temperature; no time constants were taken from the dark current. (b) Arrhenius plot of the rates of photocurrent relaxation. Fits (purple lines) to the fast (k_1) and slow (k_2) components of bi-exponential to the photocurrent rise at 1 sun equivalent light intensity following reverse bias at -0.5 V in the dark (open circles and squares, respectively). The activation energy of the fast component evaluated between -9.5 and 50°C was $E_A = 0.62$ eV. The activation energy for the slow component evaluated between 15 and 50°C was $E_A = 0.60$ eV (the measurement duration was insufficient to reliably estimate the slow component at lower temperatures). The photocurrent rise at 50°C did not reach a stable plateau and started to decline after its peak; we did not fit to this portion of the curve. The red crosses show the rates inferred from a single exponential fit to the tail of the photocurrent decay (k_3) following forward bias at 1 V in the dark; the corresponding activation energy is 0.68 eV (red line) evaluated between 15 and 50°C . Given the spread of points, we consider that the range of activation energies determined is similar to the uncertainty of the estimation. Adapted with permission.¹⁰² Copyright 2015, Springer Nature.

Beyond the bulk processes described above, extended defects, including dislocations (pipe diffusion), surfaces, interfaces, and grain boundaries, can accumulate high concentrations of charged defects and can also provide alternative low-energy diffusion pathways.¹⁰⁷ However, despite the low activation energy, the ion migration cross-section area along interfaces or grain boundaries is usually smaller than that of the bulk migration. Therefore, either bulk migration or migration through extended defects can dominate the ion migration process in polycrystalline films.¹⁰⁴ Grain boundaries have been reported to facilitate fast iodine diffusion

in $\text{CH}_3\text{NH}_3\text{PbI}_3$ from conductive atomic force microscopy.¹⁰⁸ Yun *et al.* found a shorter recovery time from the application of a bias voltage at grain boundaries compared to the bulk using Kelvin probe microscopy.¹⁰⁹ Xing *et al.* also reported a lower activation energy for iodine diffusion with higher grain boundary density.¹¹⁰ It is noted that the measured activation energy for ionic transport may be the result of different diffusing species and pathways rather than a single process. Grain boundaries may accommodate high concentrations of charged point defects, which is consistent with some observations of enhanced charge carrier recombination at these sites.^{107,111,112}

Ion migration in $\text{Cs}_2\text{AgBiBr}_6$

As we have discussed above (2.3.3), there are contradictory results about whether V_{Ag^-} , V_{Br^+} or silver on bismuth anti-sites have the smallest defect formation energy. However, there is agreement in the current literature that for ion migration through vacancies, Br^- anion has the lowest activation energy and the shortest migration distance (followed by Ag^- ion).^{113,114} Pan *et al.* measured the ion migration activation energy of a $\text{Cs}_2\text{AgBiBr}_6$ single crystal to be 348 meV from transient current decay measurements (Figure 2.23).¹¹³ This value is nearly three times that of MAPbBr_3 single crystals, suggesting that the ion migration in $\text{Cs}_2\text{AgBiBr}_6$ single crystals is indeed more difficult.

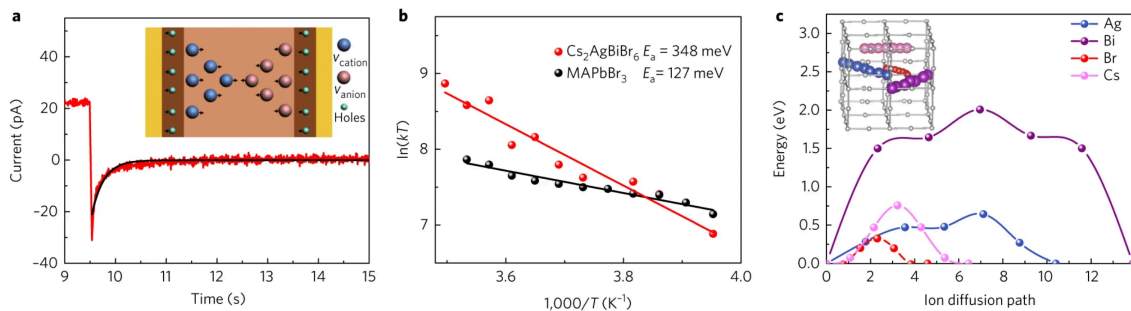


Figure 2.23 (a) A representative temporal response curve of $\text{Cs}_2\text{AgBiBr}_6$ SC device measured at 273 K. Inset: Schematic illustration of the discharging process during the ionic migration measurement when the external bias is off. (b) Arrhenius plots of the temperature dependence of kT versus $1,000/T$. Note k in the y axis is the decay rate (s^{-1}) (c) Calculated energy profile along the ionic migration path for the possible ion vacancies in $\text{Cs}_2\text{AgBiBr}_6$. Inset: Migration path of these ion vacancies. Adapted with permission.¹¹³ Copyright 2017, Springer Nature.

Ghasemi *et al.* reported that Ag and Br in the bulk $\text{Cs}_2\text{AgBiBr}_6$ migrate and consequently accumulate in the Poly(3-hexylthiophene-2,5-diyl) (P3HT) layer and the P3HT/Cu interface

from Energy Dispersive X-Ray Spectroscopy measurements.¹¹⁴ Interestingly, two oppositely charged ions (i.e., Ag^+ and Br^-) can diffuse to the same direction and accumulate between the P3HT layer and the metal contact. They attributed this to the volatility of the halide and its reactivity with metal elements (Ag and Cu). In addition to the formation of AgBr in the Cu and P3HT interface, the migrated Br may react with the Cu metal contact to form copper/cuprous bromide. Yang *et al.* introduced Bismuth Oxybromide (BiOBr) as heteroepitaxial passivation layers to $\text{Cs}_2\text{AgBiBr}_6$. The epitaxial growth of BiOBr onto $\text{Cs}_2\text{AgBiBr}_6$ enables the passivation of grain boundaries and helps to reduce ion migration.¹¹⁵

2.3.6 Bandgap engineering

The wide indirect bandgap of $\text{Cs}_2\text{AgBiBr}_6$ limits its application in photovoltaics. Therefore, people are pursuing methods to reduce the bandgap to improve its absorption of solar energy. By using first-principles calculation, Yang *et al.* showed that by controlling the ordering parameter at the mixed sublattice, the bandgap of $\text{Cs}_2\text{AgBiBr}_6$ can vary continuously from a wide indirect bandgap of 1.93 eV for the fully ordered double perovskite structure to a partially disordered structure with indirect bandgap 1.46 eV and ultimately a small pseudo direct bandgap of 0.44 eV for the fully random alloy.¹¹⁶ The fully disordered (random) state means that there is 50% probability of finding a silver ion in the position which is originally for Bi ion, and vice versa for finding the Bi in the position for Ag. However, the fully disordered material could only be synthesized and quenched from above 3000 K. Even the partially disordered structure with 1.46 eV bandgap needs to be quenched from 1200 K, which is the order-disorder transition temperature. Compared with the limiting stable temperature of 700 K from Thermogravimetric Analysis measurements,⁵⁹ those disorder structures seem to be unrealistic to achieve in experiments. Fortunately, calculations also showed that the energy difference between the ordered and random phase and thus the transition temperature could be reduced by introducing n-type dopants such as Ba or La on Cs site and p-type dopants such as Te on Br site into the alloy.¹¹⁶ Ji *et al.* decreased the bandgap of $\text{Cs}_2\text{AgBiBr}_6$ single crystal from 1.98 eV (growth temperature 150 °C) to 1.72 eV (growth temperature 60 °C).¹¹⁷ They attributed the reduction of bandgap to the higher Ag–Bi disorder. First principles calculations show that a set of defect states progressively emerges from the conduction band edge, and broadens, as the Ag–Bi disorder is increased.

In addition, the phase transition induced by high pressure (15 GPa) leads to the band gap narrowing from the original 2.19 eV to 1.70 eV in $\text{Cs}_2\text{AgBiBr}_6$ single crystals.¹¹⁸ The recovered

$\text{Cs}_2\text{AgBiBr}_6$ after releasing pressure to ambient conditions still possess a bandgap of 2.0 eV, which is 8.2% smaller than the original value.

Cation substitution was also proposed to be an effective way to change the bandgap of perovskites. Past reports showed that the bandgap of $\text{MA}(\text{Sn}_{1-x}\text{Pb}_x)\text{I}_3$ is narrower than both MASnI_3 and MAPbI_3 .¹¹⁹ Im *et al.* proposed that the decrease in bandgap as x increases ($x < 0.5$) is due to the stronger spin orbit coupling by the alloying of the heavier Pb atom and lighter Sn atom, whereas the bandgap increases when $x > 0.5$ is caused by the phase transition from $P4mm$ to $I4cm$.¹²⁰ Snaith and co-workers attributed the lower bandgap of the mixed alloy to be the short range ordering of preferred atomic scale clusters.¹²¹ In contrast, Stevanović and co-workers found that the strong nonlinearity in bandgap was primarily due to the mismatch in energy between s and p atomic orbitals of Pb and Sn.¹²² They found that spin-orbit coupling, structure changes and short-range ordering did not have a significant effect on bandgap bowing and proposed that a homogeneous structure would have improved stability over a structure with short range ordering. Slavney *et al.* showed that dilute Tl substitution could decrease the bandgap of $\text{Cs}_2\text{AgBiBr}_6$ by approximately 0.5 eV.¹²³ In this case, the Tl^{3+} tend to occupy the position of Bi^{3+} . However, since the toxicity of Tl is stronger than Pb, other appropriate substitutions are preferred. It was also reported that using $\text{Cs}_2\text{AgBiBr}_6$ as a host, the bandgap of $\text{Cs}_2\text{Ag}(\text{Bi}_{1-x}\text{Sb}_x)\text{Br}_6$ decreases from 2.12 eV to 1.86 eV with x increasing from 0 to 0.375.¹²⁴ However, the substitution could introduce substantial relatively deep defects, which may account for the rapidly suppressed emission intensity. Further band structure and defect state deviation need to be analysed for a comprehensive evaluation of this cation substitution method to reduce the bandgap of double perovskites.

2.4 Research objectives

As a candidate initially proposed to replicate the promising optoelectronic properties of lead-halide perovskite for photovoltaics with benign elements, $\text{Cs}_2\text{AgBiBr}_6$ has not proved its feasibility. Although it demonstrates long charge-carrier lifetimes due to its indirect bandgap, the reported photovoltaic efficiencies are far from ideal. I notice that a large discrepancy exists in the charge-carrier diffusion length between 30 nm in thin films and $1\mu\text{m}$ in single crystals. The underlying reasons remain unexplored, although carrier diffusion length is the key factor for charge-carrier collection in solar cells. One possibility is that grain boundaries which may accumulate point defects may impede carrier transport macroscopically over a long distance. The first aim of this thesis is to explore the role of grain boundaries in $\text{Cs}_2\text{AgBiBr}_6$.

Another key factor limiting the feasibility of $\text{Cs}_2\text{AgBiBr}_6$ for photovoltaic applications is its large bandgap. Alloying with chemically similar elements provides a promising route to tune the bandgap or even change the bandgap nature (indirect to direct). Therefore, the second aim of this thesis is to develop a method to fully alloy Sb into $\text{Cs}_2\text{AgBiBr}_6$ and investigate the effect on the optical bandgap, and thirdly to investigate whether Sb alloying can help to improve the performance of $\text{Cs}_2\text{AgBiBr}_6$ solar cells.

3 Experimental Methods

3.1 Film deposition

3.1.1 Cs₂AgBiBr₆ thin films with different grain sizes

Procedures to deposit Cs₂AgBiBr₆ thin films are shown in Figure 3.1(a). 1.5 mmol CsBr (99.9%, Sigma Aldrich), 0.75 mmol AgBr (99.998%, Alfa Aesar), and 0.75 mmol BiBr₃ (99.998%, Sigma Aldrich) were dissolved in 1.5 mL anhydrous dimethyl sulfoxide (DMSO; 99.9%, Sigma Aldrich) and mixed at 700 rpm at RT inside a N₂ glovebox for an hour to form the 0.5 mol/L Cs₂AgBiBr₆ solution. The solution was then filtered by 0.2 μm PTFE membranes (Sigma Aldrich). 0.5 mL of 0.5 mol/L Cs₂AgSbBr₆ solution was mixed with 0.333 mL DMSO to form the 0.3 mol/L Cs₂AgBiBr₆ solution. Another 0.5 mL of 0.5 mol/L Cs₂AgSbBr₆ solution was mixed with 0.125 mL DMSO to form the 0.4 mol/L Cs₂AgBiBr₆ solution. 12 mm × 12 mm glass substrates were cleaned by ultrasonication in acetone and isopropanol for 15 min sequentially, followed by 10 min O₂ plasma cleaning at 300 W (forward power) and 0 W reverse power in a radio frequency (RF) plasma system. The substrates were subsequently taken into a N₂ glovebox and preheated to 75 °C. Precursor solutions were preheated to 75 °C. To deposit the films, the substrate was placed onto a vacuum-free chuck, and 60 μL solution was immediately dropped onto the substrate, before spinning at 4500 rpm for 45 s. Substrates were then annealed at 250 °C for 5 min. The spin coating and annealing process were undertaken in the N₂ glovebox.

3.1.2 Cs₂Ag(Sb_xBi_{1-x})Br₆ thin films

Figure 3.1 depicts the procedures to synthesize Cs₂Ag(Sb_xBi_{1-x})Br₆ thin films. 1.5 mmol CsBr (99.9%, Sigma Aldrich), 0.75 mmol AgBr (99.998%, Alfa Aesar), and 0.75 mmol SbBr₃ (99.99%, Sigma Aldrich) were dissolved in 1.5 mL anhydrous DMSO (99.9%, Sigma Aldrich) and mixed at 700 rpm at room temperature (RT) inside a N₂ glovebox for an hour. Another 1.5 mmol CsBr (99.9%, Sigma Aldrich), 0.75 mmol AgBr (99.998%, Alfa Aesar), and 0.75 mmol BiBr₃ (99.998%, Sigma Aldrich) were dissolved in 1.5 mL anhydrous DMSO (99.9%, Sigma Aldrich) and mixed at 700 rpm at RT inside a N₂ glovebox for an hour. Both solutions were then filtered by 0.2 μm PTFE membranes (Sigma Aldrich). 0.45 mL Cs₂AgSbBr₆ solution was mixed with 0.05 mL Cs₂AgBiBr₆ solution to form the 90% Sb Sb-Bi solution. 0.35 mL

$\text{Cs}_2\text{AgSbBr}_6$ solution was mixed with 0.15 mL $\text{Cs}_2\text{AgBiBr}_6$ solution to form the 70% Sb Sb-Bi solution. 0.25 mL $\text{Cs}_2\text{AgSbBr}_6$ solution was mixed with 0.25 mL $\text{Cs}_2\text{AgBiBr}_6$ solution to form the 50% Sb Sb-Bi solution. 0.1 mL $\text{Cs}_2\text{AgSbBr}_6$ solution was mixed with 0.4 mL $\text{Cs}_2\text{AgBiBr}_6$ solution to form the 20% Sb Sb-Bi solution. Substrates and the cleaning process are the same as in 3.11. The substrates were subsequently taken into a N_2 glovebox and preheated to 75 °C. Precursor solutions containing Sb were kept at room temperature. Precursor solution with pure $\text{Cs}_2\text{AgBiBr}_6$ was preheated to 75 °C. To deposit the films, the substrate was placed onto a vacuum-free chuck, and 60 μL solution was immediately dropped onto the substrate, before spinning at 4000 rpm for 45 s. Substrates containing Sb were annealed at 135 °C for 5 min. Substrates with pure $\text{Cs}_2\text{AgBiBr}_6$ were annealed at 250 °C for 5 min. The spin coating and annealing process were undertaken in the N_2 glovebox.

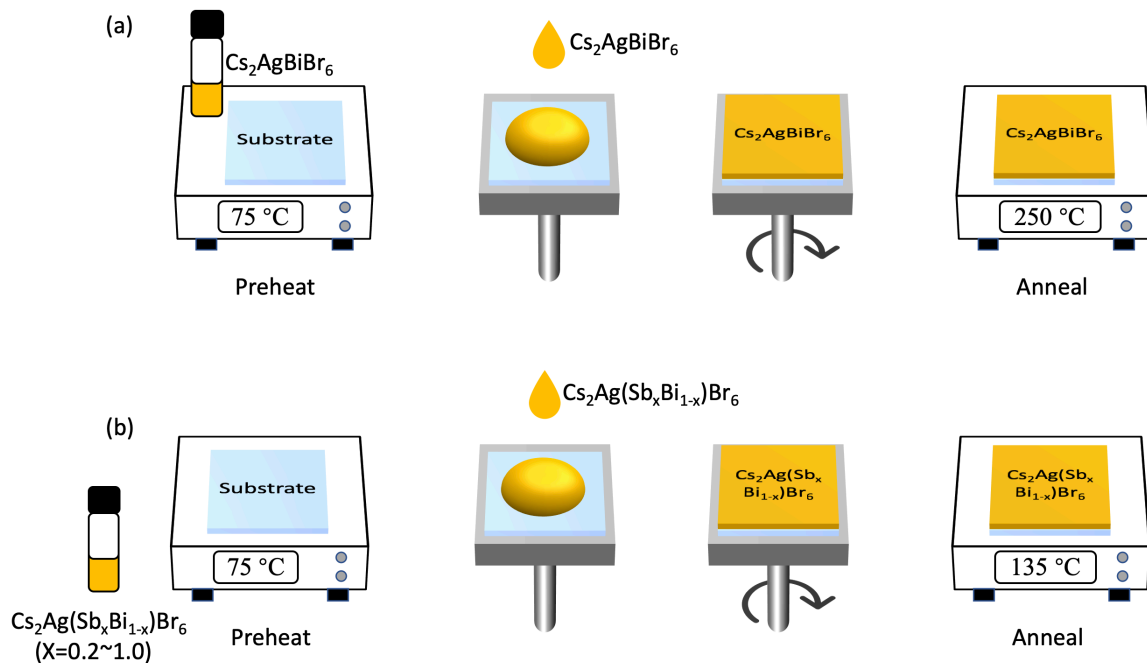


Figure 3.1 Schematic diagram illustrating the deposition steps for $\text{Cs}_2\text{Ag}(\text{Sb}_x\text{Bi}_{1-x})\text{Br}_6$ thin films. (a) Pure $\text{Cs}_2\text{AgBiBr}_6$ thin films. (b) $\text{Cs}_2\text{Ag}(\text{Sb}_x\text{Bi}_{1-x})\text{Br}_6$ ($x=0.2\sim 1.0$) thin films.

3.2 Device fabrication

3.2.1 Solar cell fabrication

The solar cell structure I studied in this thesis is glass/FTO/compact TiO_2 /mesoporous TiO_2 /double perovskite/PTAA/gold (Figure 3.2). Fluorine-doped tin oxide (FTO)-coated glass sheets were patterned by etching with zinc powder (98%, Sigma Aldrich) and 2 M HCl (diluted

from 37%, Fisher Chemical). They were subsequently cleaned with a 2% Hellmanex solution and rinsed with deionized water and ethanol. They were then sonicated with Acetone and IPA, each for 15 min. Directly before applying the blocking layer, remaining organic residues were removed by an oxygen plasma treatment for 5 min at 300 W (forward power) and 0 W reverse power in a radio frequency (RF) plasma system.

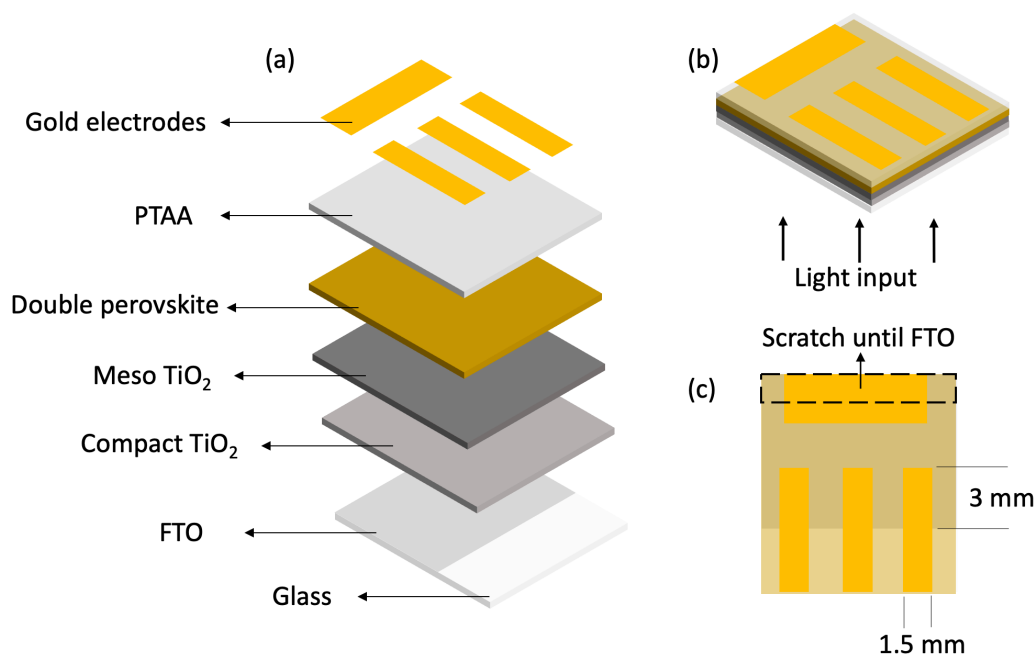


Figure 3.2 Schematic figure of the glass/FTO/compact TiO₂/mesoporous TiO₂/double perovskite/PTAA/gold structure solar cell. (a) Components of the solar cell device. (b) A complete device. (c) Dimensions of the device (the red area indicates the active area).

To deposit the compact TiO₂ layer, the cleaned FTO substrates were put on the hotplate and heat up to 450 °C. 0.4 mL acetylacetone (99%, Alfa Aesar) and 0.6 mL titanium diisopropoxide bis(acetylacetonate) (75 wt.% in isopropanol, Sigma Aldrich) were dissolved in 9 mL ethanol. The dissolved solutions were put into a spray pyrolysis glass container and sprayed in air over the whole hot plate, which had already reached 450 °C. The ideal position is 20 cm distance from the hotplate with 45° angle. The hotplate was then cooled down to 150 °C. To deposit the mesoporous TiO₂ layer, 150 mg/mL TiO₂ paste (Dyesol) was dissolved in ethanol. Substrates were transferred from the hotplate to Al foil to cool down and put on the vacuum chuck in spin coater. 30 μL TiO₂ paste solution (150 mg/mL in ethanol) was immediately dropped onto the substrate, before spinning at 4000 rpm for 10 s, with 2000 rpm ramp. After spin coating, substrates were transferred to the hotplate and anneal for five steps: 125 °C (ramp in 5 min and hold for 5 min), 325 °C (ramp in 15 min and hold for 5 min), 375 °C (ramp in 5 min and hold

for 5 min), 450 °C (ramp in 5 min and hold for 30 min), 150 °C (ramp for 0 min and hold until use). $\text{Cs}_2\text{AgSbBr}_6$, $\text{Cs}_2\text{Ag}(\text{Sb}_{0.9}\text{Bi}_{0.1})\text{Br}_6$ and $\text{Cs}_2\text{AgBiBr}_6$ double perovskite thin films were spin coated onto the FTO/compact TiO_2 /mesoporous TiO_2 substrates with the same process as described in 3.1. Poly[bis(4-phenyl)(2,4,6-trimethylphenyl)amine] (PTAA) solution was deposited on the double perovskite layer as hole transporting layer. To make the PTAA solution, 10 mg PTAA, 16 μL Bis(trifluoromethane)sulfonimide lithium salt (Li-TFSI) solution (51.7mg/mL Li-TFSI (99%, Sigma Aldrich) in acetonitrile) and 20 μL 4-tert-butylpyridine (tBP) solution (100 $\mu\text{L}/\text{mL}$ tBP (96%, Sigma Aldrich) in toluene) were dissolved in 964 μL toluene and shook until mixed. 40 μL PTAA solution was dropped onto the sample, before spinning at 4000 rpm for 20 s. Finally, 100 nm thick gold electrodes were thermally deposited under a high vacuum on top of the device.

3.2.2 Thin film transistor fabrication

For the fabrication of TFTs, lithographically patterned Cr/Au source drain electrodes were deposited on Si/SiO₂ substrates. This was followed by introducing the perovskite layer with varied concentration which allowed variation in the perovskite grain size (Figure 3.3).

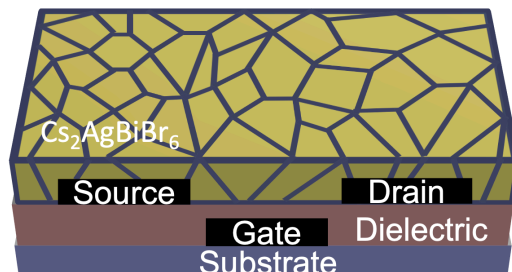


Figure 3.3 Schematic figure of the thin film transistor device.

3.3 Material characterization

3.3.1 XRD

1D X-ray Diffraction (XRD) was carried out on films in air at room temperature with a B3 Bruker D8 DAVINCI instrument employing Cu K_α radiation. (number of steps: 1700, step dwell time: 1s).

2D thin film XRD was measured with a Bruker D8 Davinci diffractometer in reflection geometry. The incident X-ray beam was microfocused and columnated to a 2 mm² spot on the

sample surface. A 2D area detector was used and the sample was held on a Eulerian cradle. Diffraction patterns were obtained over two frames of the 2D detector. Data analysis was carried out using Bruker Multex 3 software.

3.3.2 SEM

Scanning Electron Microscopy (SEM) images were obtained with LEO 1530 VP instrument. Acceleration voltage is 3 keV and the chamber vacuum around 10^{-5} Pa. Before taking SEM images, films were sputtered with Au/Pd source for 7 s at 65 mA using the Emitech sputter coater.

3.3.3 UV–Visible Spectrophotometry

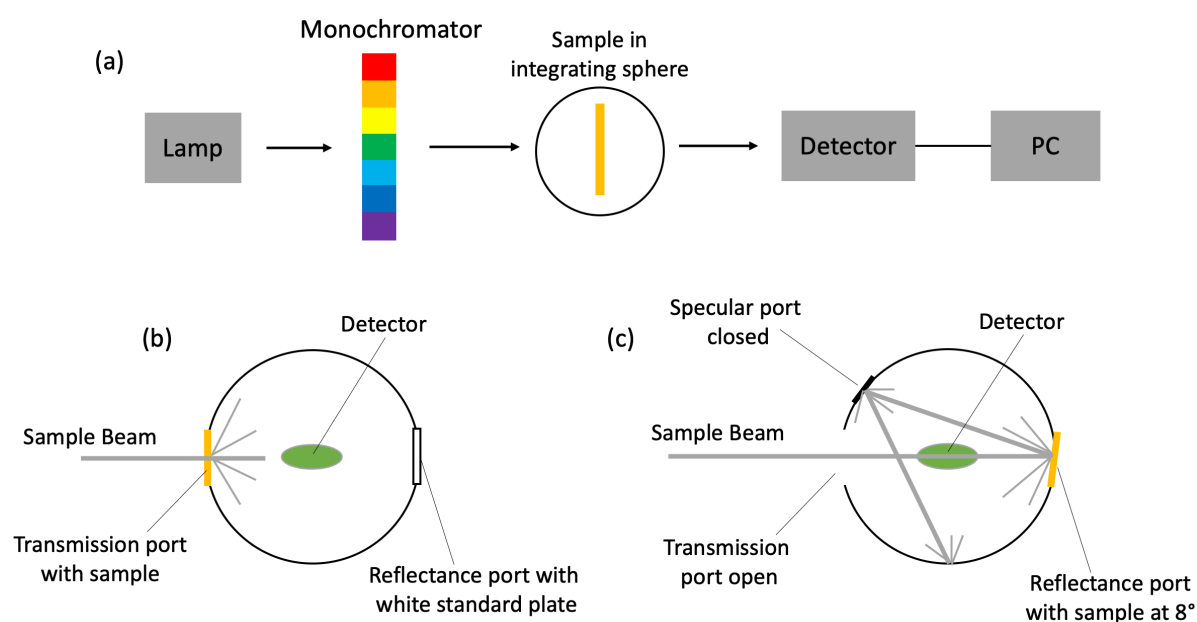


Figure 3.4 (a) Configuration of a UV-Vis spectrophotometer. (b) Total transmittance measurement in an integrating sphere. (c) Total reflectance measurement in an integrating sphere.

UV–Visible Spectrophotometry measurements were performed using a PerkinElmer Lambda 750 spectrometer inside an integrating sphere (Figure 3.3). The reflectance and transmittance of the $\text{Cs}_2\text{AgBiBr}_6$ thin film on glass were separately measured. The instrument was calibrated to 0% and 100% reflectance/transmittance prior to measuring the sample. The measurements were taken from 900 to 300 nm wavelength with an interval of 5 nm. The absorption coefficient was calculated using the equation shown below.

$$\alpha = \frac{\ln\left(\frac{1-R}{T}\right)}{d} \quad 3.1$$

Where α is absorption coefficient, T is transmittance, R is reflectance and d is the measured thickness of the thin film (from Dektak profilometry).

3.3.4 Photothermal Deflection Spectroscopy

Photothermal Deflection Spectroscopy (PDS) is an ultrasensitive absorption measurement technique that detects heating of the sample due to the nonradiative relaxation of absorbed light and is insensitive to reflection and scattering (Figure 3.5). PDS enables the detection of absorbance signals with 5-6 orders of magnitude weaker than the band edge absorption. For the measurements, a monochromated pump light beam is illuminated on the sample (film on quartz substrate), which on absorption produces a thermal gradient near the sample surface via non-radiative relaxation induced heating. This results in a refractive index gradient in the area surrounding the sample surface. This refractive index gradient is further enhanced by immersing the sample in an inert liquid FC-72 Fluorinert® (3M Company) which has a high refractive index change per unit change in temperature. A fixed wavelength CW laser probe beam is passed through this refractive index gradient producing a deflection proportional to the absorbed light at that particular wavelength, which is detected by a photodiode and lock-in amplifier combination. Scanning through different wavelengths gives us the complete absorption spectra. Because this technique makes use of the non-radiative relaxation processes in the sample, it is immune to optical effects like interference and scattering.

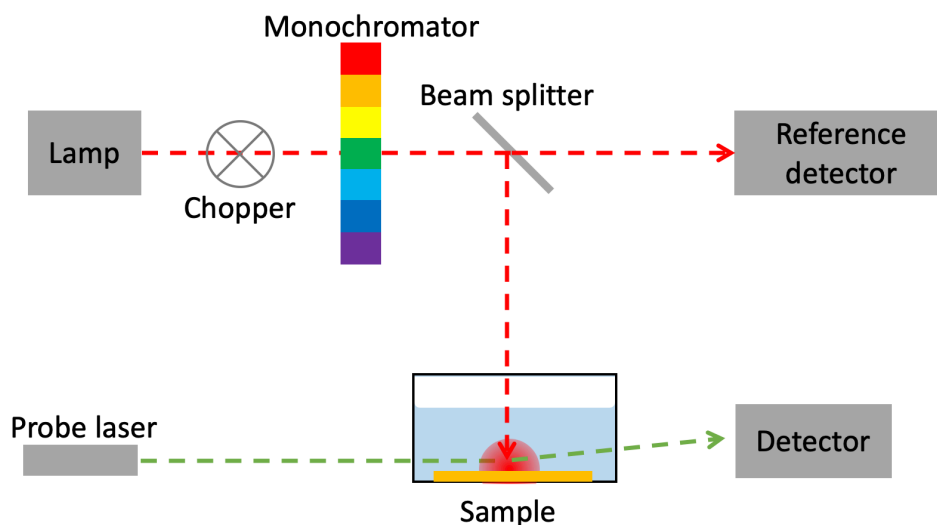


Figure 3.5 Schematic representation of a PDS setup.

3.3.5 Photoluminescence

Photoluminescence measurements using an intensified charge-coupled device camera were measured with an Andor iStar DH740 CCI-010 system connected to a grating spectrometer (Andor SR303i). Excitation was made at 400 nm wavelength from a frequency-doubled Ti:Sapphire laser (Spectra Physics Solstice) with a wavelength of 800 nm, repetition rate of 1 kHz and pulse length of ≈ 100 fs. For measurements of the $\text{Cs}_2\text{Ag}(\text{SbxBi}_{1-x})\text{Br}_6$ thin films, the gate width was 5 ns. The exposure time was 0.3 s, slit width 400 μm and accumulation times 15.

3.3.6 Transient Absorption Spectroscopy

In transient absorption spectroscopy (TAS), a weak white probe pulse (the probe pulse has low intensity that it does not influence the population of the excited state carriers) is sent to the sample with a delay time with respect to the fixed wavelength pump pulse (every other pump pulse is blocked; Figure 3.6a). TAS signal is given by the difference between transmission spectrums of the probe, the transmission spectrum of the excited sample minus the transmission spectrum of the unexcited sample. By changing the delay time between the pump and probe, $\Delta T/T$ signal at each delay time ($\Delta T/T$ as a function of delay time and wavelength) is obtained.

In general, a $\Delta T/T$ spectrum has four contributions (Figure 3.6b and c).¹²⁵ The first one is ground state bleach (GSB). As a fraction of electrons has been promoted to the excited state by the pump pulse, the number of the electrons in the ground state decreases. Hence, the ground state absorption in the excited sample is less than that in the unexcited sample. Consequently, a positive signal in the $\Delta T/T$ is observed. The second contribution is stimulated emission (SE). Upon population of the excited state, stimulated emission to the ground state will occur when the probe pulse passes through the excited sample. Stimulated emission results in an increase of the light intensity in the detector, corresponding to a positive $\Delta T/T$ signal. With the same relationship between absorption and emission, the stimulated emission will be red shifted to the ground state bleach. It is noted that the intensity of the probe pulse is so weak that it does not influence the excited state population (this assumption also applies to the next two contributions). The third contribution is excited state absorption (ESA). This corresponds to the excited carriers being excited again to a higher state. Since probe light is absorbed during this process, a negative $\Delta T/T$ will be observed in the spectrum. The last contribution is called product absorption (PA). The pump pulse may generate some new product or transient states,

such as self-trapped carriers or excitons, that can absorb the probe light. This will again result in less light transmitted through the sample, corresponding to a negative $\Delta T/T$ signal. The third and the last contributions are sometimes not differentiated and are called photoinduced absorption (PIA) together, which also includes some other mechanisms, such as bandgap renormalisation.

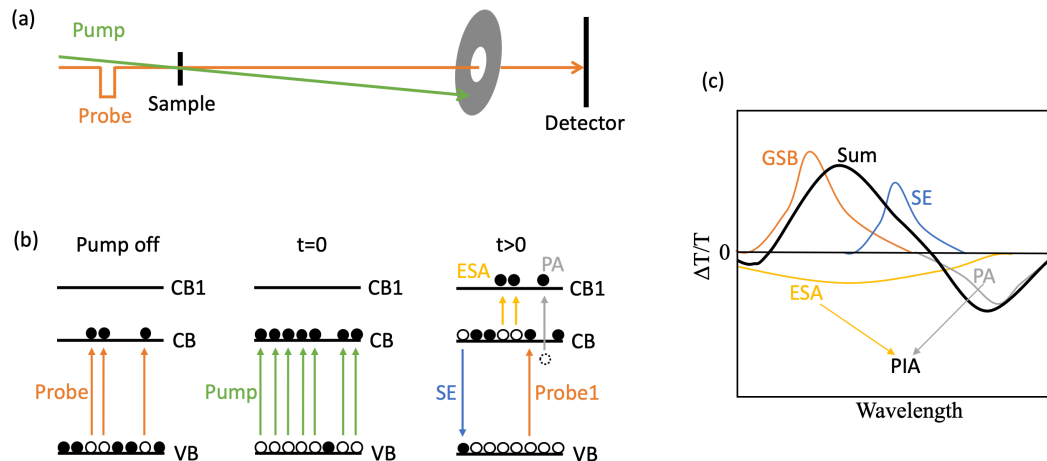


Figure 3.6 Schematic depiction of (a) the transient absorption spectroscopy principle, (b) carrier excitation processes during the TA measurement, and (c) contributions to the $\Delta T/T$ spectrum. GSB (ground state bleach), SE (stimulated emission), ESA (excited state absorption), PA (product absorption), PIA (photoinduced absorption).

For transient absorption measurements in this thesis, the third harmonic of a Nd:YVO₄ laser system (Piccolo-AOT-MOPA 25, InnoLas) at 355 nm with electronically controlled delay was used as pump. For the probe beam, the output of a Ti:sapphire amplifier system (Spectra Physics Solstice Ace) operating at 1 kHz and generating ~100-fs pulses was sent into a mechanical delay stage (Thorlabs DDS300-E/M). The ultraviolet-visible broadband probe beam (330 – 700 nm) was generated by focusing the 800 nm fundamental beam onto a CaF₂ crystal (Eksma Optics, 5 mm) connected to a digital motion controller (Mercury C-863 DC Motor Controller) after passing through the mechanical delay stage. The transmitted pulses were collected with a monochrome line scan camera (JAI SW-4000M-PMCL, spectrograph: Andor Shamrock SR-163) with collected data fed straight into the computer.

3.3.7 Cathodoluminescence

CL measurements were performed in an Attolight Allalin 4027 Chronos scanning electron microscope cathodoluminescence (SEM-CL) system at room temperature (RT).

Measurements were taken using a beam current of 500 pA and an acceleration voltage of 3 kV which corresponds to 90% of the beam energy being deposited in a depth of 67nm according to simulations using Monte Carlo Casino software.¹²⁶ The CL hyperspectral maps were analysed using Hyperspy.¹²⁷

3.3.8 Rutherford Backscattering Spectrometry

Rutherford Backscattering Spectrometry (RBS) is a bulk measurement method to provide information on composition rather than chemical state. RBS uses accelerated ions which have higher depth penetration because they are not readily scattered by electron clouds. It is based on the elastic scattering of ion by the atoms/ions present in the sample. The ratio of the energy of the backscattered ions (E_1) and incident ion (E_0) is given by Equation 3.1. This ratio is the kinematic factor (k) and can be derived through the conservation of energy and momentum.

$$k = \frac{E_1}{E_0} = \left(\frac{\sqrt{m_2^2 - m_1^2 \sin^2 \theta} + m_1 \cos \theta}{m_1 + m_2} \right)^2 \quad 3.1$$

m_1 is the mass of incident ion, m_2 the mass of the atom/ion in the sample and θ the scattering angle of the backscattered ion compared to its original path. The kinematic factor is a function of θ . (Figure 3.7) Typically, the detector is held at 160-170° for optimal mass resolution (i.e., between different m_2 values).

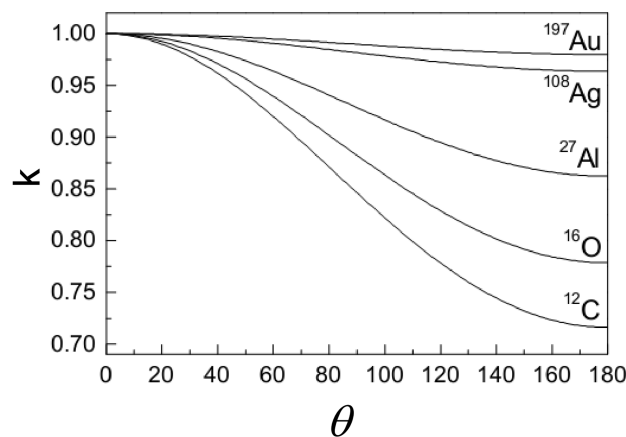


Figure 3.7 Kinematic factor (k) for various elements as a function of incident ion scattering angle θ .¹²⁸

The energy of the back-scattered ion is described by the kinematic factor, and the intensity of backscattered ions depends on the scattering cross-section ($\sigma(\theta)$), given in Equation 3.2, if we neglect the effects of the electron cloud around the nucleus.

$$\sigma = \left(\frac{Z_1 Z_2 e^2}{4E_0 \sin^2(\frac{\theta}{2})} \right)^2 \quad 3.2$$

Equation 3.2 shows that there is more scattering when the atomic number of the incident ion (Z_1) or atom in the material (Z_2) are larger, or when the incident energy of the ion (E_0) is smaller. The area density of atoms (Nt , units: atoms per unit area) is calculated from the area of the peak for each element in the RBS spectrum (A_i) from Equation 3.3

$$A_i = (Nt)_i Q \Omega \frac{\sigma}{\cos \theta} \quad 3.3$$

In Equation 3.3, Q is the ion beam fluence and Ω the solid angle of the detector. A_i is determined through the fitting of the experimental peak.

In this thesis, RBS data were measured with 5.115 MeV ${}^7\text{Li}^{2+}$ ion beam. The incident beam with a spot size of ca. 1.5 mm \times 3 mm was parallel to surface normal (sample tilt 0°) and the backscattering angle was 165° . The beam fluence was normalized with the backscattering counts from the Au-coated chopper and sample substrate. The acquired RBS spectra were analysed using SimNRA simulation software to determine the elemental composition of the films.¹²⁹ The uncertainty of the elemental fractions is in the order of 1%, and is based on the estimated statistical error of the backscattering yield (proportional to $1/\sqrt{N}$), the uncertainty of the simulation parameters for the peak fitting, as well as the uncertainties arising from the detector setup.

3.3.9 Photoemission Spectroscopy (XPS and UPS)

X-ray photoemission spectroscopy (XPS) and Ultraviolet photoemission spectroscopy (UPS) operate based on the photoelectric effect and use X-ray or ultraviolet photons to excite electrons to vacuum, which are then detected and measured. Electrons with kinetic energy are produced from the core-level electrons that have overcome the binding energy (E_{BE} , difference between Fermi level and the core level) and work function (Figure 3.8). Since both the sample and the instrument are grounded, the kinetic energy of the electron measured ($E_{KE \text{ (measured)}}$) is relative to the work function of the instrument ($W_{\text{instrument}}$).

XPS/UPS spectra plot intensity against binding energy on the calibrated scale. This scale is typically shown in reverse so that kinetic energy (which binding energy is calculated from) increases in value from left to right. The photoemission spectrum is comprised of contributions

from photoelectrons that are directly excited and emitted to vacuum (primary electrons), as well as electrons that have undergone multiple inelastic scattering events (secondary electrons).

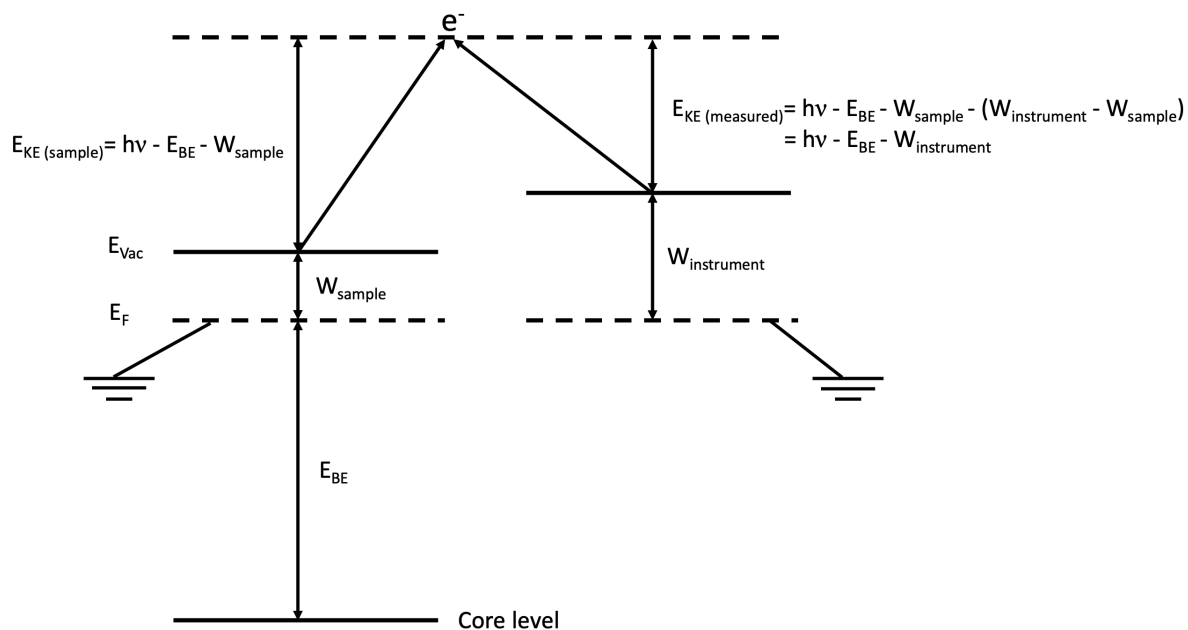


Figure 3.8 Schematic showing the relation between measured kinetic energy, binding energy and working function of the sample and instrument.

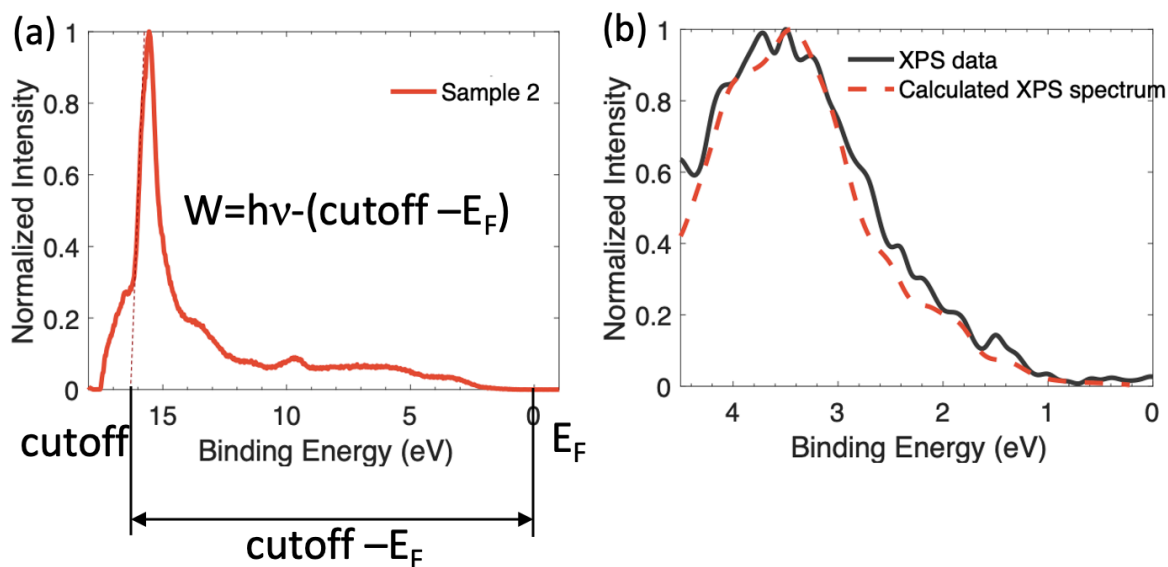


Figure 3.9 (a) UPS spectrum of $\text{Cs}_2\text{AgBiBr}_6$ thin film deposited on ITO/glass. (b) XPS measurements of $\text{Cs}_2\text{AgBiBr}_6$ thin film deposited on ITO/glass. The $E_F - \text{VB}$ value that gave the best fit of the calculated XPS spectrum to the measured data was 1.21 eV.

To a first order, the primary electron intensity reflects the valence density of states. The onset of primary electrons from the Fermi level therefore gives the difference between the valence band maximum and Fermi level ($E_V - E_F$). The intensity of secondary electrons increases with decreasing kinetic energy. This is because the mean free path for secondary electrons is longer when they have less kinetic energy, since they then do not interact with the sample as much. But below a certain kinetic energy, the secondary electrons can no longer overcome the work function of the sample, giving a cut-off. By fitting the secondary electron cut-off from the UPS spectrum, we can get the work function of the sample (Figure 3.9a). To determine the leading edge of the valence spectra ($E_V - E_F$), The most physically-relevant method is to fit the leading edge with the density of states convolved with instrument broadening (Figure 3.9b).

In this thesis, XPS data was acquired using a Kratos Axis SUPRA using monochromated Al K_α (1486.69 eV) X-rays at 12 mA emission and 15 kV HT (180W) and a spot size/analysis area of $700 \times 300 \mu\text{m}$. The instrument was calibrated to gold metal Au 4f core level (83.95 eV) and dispersion adjusted give a BE of 932.6 eV for the Cu $2p_{3/2}$ line of metallic copper. Ag $3d_{5/2}$ line FWHM at 10 eV pass energy was 0.544 eV. Source resolution for monochromatic Al K_α X-rays is ~ 0.3 eV. The instrumental resolution was determined to be 0.29 eV at 10 eV pass energy using the Fermi edge of the valence band for metallic silver. Resolution with charge compensation system on < 1.33 eV FWHM on PTFE. High resolution spectra were obtained using a pass energy of 20 eV, step size of 0.1 eV and sweep time of 60 s, resulting in a line width of 0.696 eV for Au $4f_{7/2}$. Survey spectra were obtained using a pass energy of 160 eV. Charge neutralisation was achieved using an electron flood gun with filament current = 0.38 A, charge balance = 2 V, filament bias = 4.2 V. Successful neutralisation was adjudged by analysing the C 1s region wherein a sharp peak with no lower BE structure was obtained. The spectra were charge corrected to the main line of the carbon 1s spectrum (adventitious carbon) set to 284.8 eV. All data was recorded at a base pressure of below 9×10^{-9} Torr and a room temperature of 294 K. Data was analysed using CasaXPS v2.3.19PR1.0. Peaks were fit with a Shirley background prior to component analysis. UPS measurements were recorded using He(I) (21.22 eV) at an emission of 35 mA. All UPS spectra were recorded at a pass energy of 5 eV. UPS spectra were aligned to the recorded XPS valence bands through peak fitting of the Cs $5p_{3/2}$ species using an LA(1,3,230) lineshape for both sets of spectra.

The work function was determined by linear fitting of the secondary-electron cut-off of the ultraviolet photoemission spectra (Figure 3.10). The valence band to Fermi level offset ($E_F - E_V$) was determined by fitting the leading-edge of the X-ray photoemission spectroscopy (XPS)

data. These were fit by the least-squares method to the leading edge of calculated XPS plots to determine the $E_F - E_v$ value. The ionization potential (the valence band maximum position relative to vacuum level) was determined from the work function and $E_F - E_v$ measurements. The electron affinity (the conduction band minimum position relative to vacuum level) was calculated by subtracting the bandgap measured by PDS from the ionization potential.

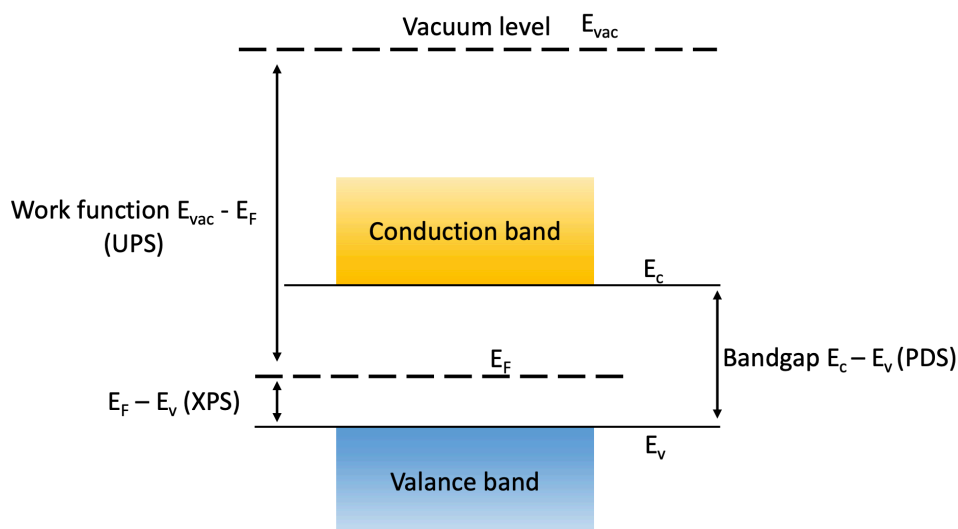


Figure 3.10 Schematic diagram illustrating the relationship among different characterization values.

3.3.10 Transient current measurement

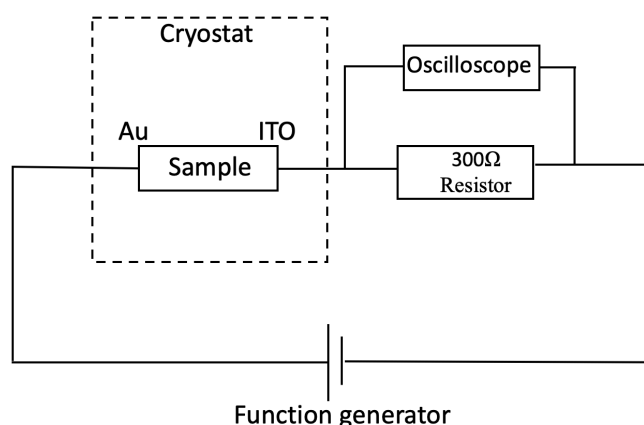


Figure 3.11 Schematic circuit for the temperature dependent transient current measurement.

In the transient current measurements, a pulse voltage generated by a function generator (Hewlett Packard 8116A) was applied to the hole-only device (ITO/NiO_x/Cs₂AgBiBr₆/PTAA/Au). The device was connected in series with a resistor (300

Ω). The voltage across the resistor was measured with an oscilloscope (RS PRO RSDS1304CFL) to monitor the current density kinetics (Figure 3.11). The samples were mounted in a Desert TTP4 Probe Station for temperature-dependent studies in the range of 230 to 300 K. The samples were cooled using liquid nitrogen while kept under a vacuum of 10^{-6} mbar.

3.4 Device characterization

3.4.1 Solar cell characterization

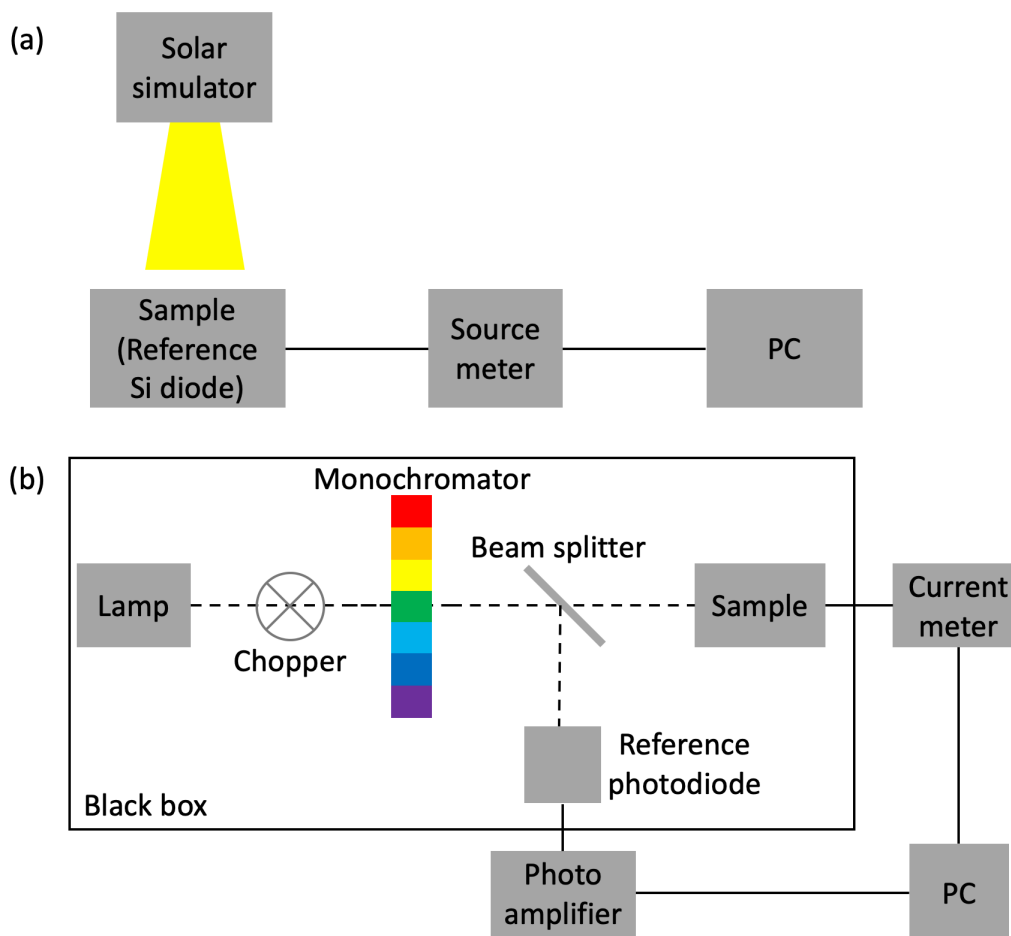


Figure 3.12 Schematic figure of the setup for measuring (a) Power conversion efficiency and (b) External quantum efficiency.

Solar simulations were performed using an ABET Technologies Sun 2000 Solar Simulator and Keithley 2623A source-measure unit (Figure 3.12a). The light source was a 450 W Xenon lamp (Oriol) equipped with a Schott-K113 Tempax sunlight filter (Präzisions Glas & Optik GmbH) to match the emission spectrum of the lamp to the AM1.5G standard. The devices were all

illuminated from the substrate (FTO) side. Before measuring the devices, the solar simulator was calibrated with a silicon reference diode equipped with an infrared cut-off filter (KG-3, Schott). The scan rate was 100 mV s^{-1} . The active area (by placing an aperture on the solar cell device) was 4.1 mm^2 .

External quantum efficiency (EQE) spectra were measured without light-bias, with illumination only from the monochromatic source. Monochromatic light was supplied by a 300W Xenon lamp (ILC Technology) that was focused through a Gemini-180 double monochromator (Jobin Yvon Ltd) and chopped at approximately 2 Hz (Figure 3.12b). The monochromatic light is separated by the beam splitter, with half going to the reference photodiode and the other half going to the sample. The signal was recorded using a Model SR830 DSP lock-in amplifier (Stanford Research Systems).

3.4.2 Thin film transistor characterization

TFT Device Characterization: All the devices were characterized using an Agilent 4155B parameter analyzer operated in pulsed mode. In the pulsed mode of operation, for the transfer (output) measurement, V_g (V_d) was applied over a short impulse of 0.5 ms. The temperature-dependent transport measurements were performed using a Desert Cryogenics low-temperature probe station.

Impedance Spectroscopy: For the impedance measurement, vertical sandwich devices were fabricated with patterned ITO/Au bottom electrode and shadow mask-patterned top Au electrode. Perovskite films were introduced using similar technique as used for FET fabrication. Impedance measurement was performed using Keithley 4200 SCS with an AC voltage of 10 mV while the frequency was varied from 1 kHz to 10 MHz.

4 Understanding the Role of Grain Boundaries on Charge-Carrier and Ion Transport in Cs₂AgBiBr₆ Thin Films

Although Cs₂AgBiBr₆ has gained significant attention, the efficiencies of solar cells based on this double perovskite material are still one third of its theoretical efficiency limit. Together with the discrepancy between the promising optoelectronic properties of single crystals and the much more limited performance in thin films, attentions are brought to the effect of grain boundaries. Therefore, in this chapter, I investigate the role of grain boundaries on the optoelectronic properties of Cs₂AgBiBr₆ thin films. Through cathodoluminescence measurements, I show that grain boundaries are the dominant non-radiative recombination sites. I also demonstrate through field-effect transistor and temperature-dependent transient current measurements that grain boundaries act as the main channels for ion transport. Interestingly, I find a positive correlation between carrier mobility and temperature, which resembles the hopping mechanism often seen in organic semiconductors. These findings explain the discrepancy between the long diffusion lengths >1 μm found in Cs₂AgBiBr₆ single crystals versus the limited performance achieved in their thin film counterparts. This work shows that mitigating the impact of grain boundaries will be critical for these double perovskite thin films to reach the performance achievable based on their intrinsic single-crystal properties.

4.1 Introduction

The best reported power conversion efficiency (PCE) for a planar solar cell device based on Cs₂AgBiBr₆ thin film is only 2.84%,¹³⁰ which is the highest record for any halide double perovskite absorber. But even considering its large and indirect bandgap of 2.25 eV, the current efficiency record is still three times lower than the spectroscopic limited maximum efficiency calculated based on its absorption spectrum.⁶¹ The limited performance, especially the low short-circuit current density, implies a significant impact of defect states, which reduce carrier transport lengths.^{76,130–132}

For single crystals, trap densities of 10¹⁶ - 10¹⁷ cm⁻³ have been reported, and these defects have been attributed predominantly to Br vacancies formed due to surface bromine degassing,^[19] although there are also calculations proposing Ag vacancies to be the most easily formed defects.¹³³ In spite of the high trap densities, charge-carrier lifetimes exceed 600 ns due to the shallow nature of the majority of traps.^{59,79} Furthermore, in single crystals, mobilities of 11.8

$\text{cm}^2 \text{V}^{-1} \text{s}^{-1}$ (from space charge-limited current density measurements)¹¹³ and diffusion lengths exceeding $1 \mu\text{m}$ (from stroboscopic scattering microscopy)⁷⁷ have been reported, despite trap-limited transport.

Although these diffusion lengths in single crystals are reported long, carrier transport in thin films used in photovoltaic devices is significantly lower, with electron diffusion lengths of only 30 nm and mobilities $<1 \text{ cm}^2 \text{V}^{-1} \text{s}^{-1}$.⁷⁶ The discrepancy between the 30 nm carrier diffusion length in thin films and the micron diffusion length in single crystals is often attributed to fast recombination in surface states due to the accumulation of defects on the surface of thin films.⁷⁹ However, despite their likely importance, an effect that has not been directly accounted for is the impact of grain boundaries on the optoelectronic properties of $\text{Cs}_2\text{AgBiBr}_6$. Establishing how charge-carriers and ions interact with grain boundaries is essential for understanding the discrepancies between the transport properties of polycrystalline thin films and single crystals, and how the performance of double perovskite thin films could be improved.

Grain boundaries break the periodicity of single crystals and, with few exceptions, lead to an accumulation of dislocations, vacancies and dangling bonds, as well as other structural and point defects, giving rise to defect states in the band gap.^{134,135} These localized sub-bandgap states can enhance the non-radiative recombination of photogenerated carriers, and therefore reduce photovoltaic performance.⁷ On the other hand, in some cases, the built-in electric field induced by the grain boundary can result in more efficient charge collection.^{136,137} Various spatially-resolved techniques, such as scanning probe microscopy (Kelvin Probe Force Microscopy, Scanning Capacitance Microscopy, Conductive-Probe Atomic Force Microscopy), laser-beam-induced current microscopy and cathodoluminescence, have been used to compare the band bending, charge collection and recombination at the boundaries vs. interiors of grains in polycrystalline solar cells.^{135,138,139}

In this chapter, I investigate the role of grain boundary density by synthesizing and characterizing $\text{Cs}_2\text{AgBiBr}_6$ thin films with three different grain sizes. Through transient absorption spectroscopy (TAS), I measured how the grain boundary density affects charge-carrier lifetimes. I used cathodoluminescence (CL) mapping to determine if grain boundaries act as the dominant non-radiative recombination sites. To understand the role of grain boundaries on carrier transport, I developed thin film transistors using $\text{Cs}_2\text{AgBiBr}_6$ in the active channel and measured the temperature dependence of the field-effect mobility. This also represents the first report of field-effect transistor performance in this material, and one of the

handful reports of *p*-type field-effect behaviour among halide perovskites, especially bulk 3D perovskites. These field-effect transistor measurements and temperature-dependent transient current measurements provide a direct correlation between grain boundary densities and charge-carrier transport, as well as ionic transport.

4.2 Phase purity and grain size

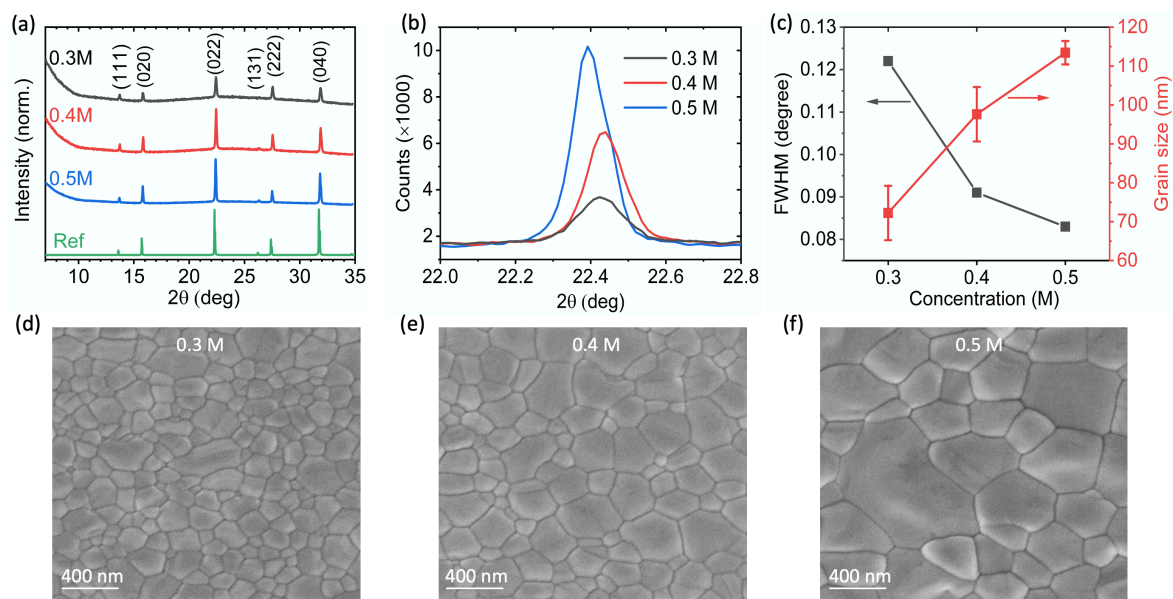


Figure 4.1 (a) XRD patterns of $\text{Cs}_2\text{AgBiBr}_6$ films grown from three different precursor concentrations. The reference pattern is calculated from its crystallographic information file, obtained from Ref.⁶⁵. (b) Close-up of the (022) peak for the $\text{Cs}_2\text{AgBiBr}_6$ films from part (a). (c) Comparison of the full width at half maximum (FWHM) of the (022) peak with the grain size calculated from the Scherrer equation (Table 4.1). Scanning electron micrographs of $\text{Cs}_2\text{AgBiBr}_6$ thin films grown from precursor solutions with concentrations of (d) 0.3 mol L⁻¹, (e) 0.4 mol L⁻¹ and (f) 0.5 mol L⁻¹. The thickness of the 0.3 mol L⁻¹, 0.4 mol L⁻¹ and 0.5 mol L⁻¹ thin films are 118±4 nm, 160±3 nm and 242±6 nm respectively (measured by profilometry). Data taken and analysed by myself.

$\text{Cs}_2\text{AgBiBr}_6$ thin films were synthesized by solution processing, as detailed in Chapter 3. To tune the grain size, the concentration of the precursor solution was adjusted to 0.3, 0.4 and 0.5 mol L⁻¹ (M). The phase-purity of the films was determined through X-ray diffraction (XRD) measurements (Figure 4.1a). The larger peak intensity for the higher concentration films is due to increased film thickness. Only peaks due to the double perovskite phase were present. In particular, the common impurity peak at 8.95° for $\text{Cs}_3\text{Bi}_2\text{Br}_9$ was absent.⁶⁵ Later in Chapter 5,

it is verified that phase impurities in the film would be detectable by 1D linescan measurements (refer also to my paper Ref.⁶⁶). The full width at half maximum (FWHM) of the XRD peaks decreased for films grown from higher concentration solutions, implying an increase in crystallite size (Figure 4.1b, c). The crystallite sizes obtained by fitting the XRD peaks were 72 ± 7 nm (0.3 mol L^{-1}), 98 ± 7 nm (0.4 mol L^{-1}) and 113 ± 3 nm (0.5 mol L^{-1}), as shown in Figure 4.1c.

Table 4.1 Calculation of XRD grain size according to Scherrer equation. Data taken and analysed by myself.

Concentration	2θ (°)	Grain size (nm)	Average grain size (nm)	2*[standard error] (nm)
0.3 M	15.8	75	72	7
	22.4	73		
	27.5	78		
	31.9	62		
0.4M	15.8	104	98	7
	22.4	103		
	27.5	93		
	31.9	90		
0.5 M	15.8	115	113	3
	22.4	116		
	27.5	111		
	31.9	112		

The grain sizes extracted from XRD are calculated with Scherrer equation below,

$$D = \frac{K\lambda}{\beta \cos \theta} \quad (4.1)$$

Where K is the Scherrer constant that depends on the shape of the crystals. For crystallites of cubic symmetry, $K=0.94$. λ is the X-ray wavelength (1.5406 Å for Cu K_α) D is the mean size of the ordered crystalline domains, which may be smaller or equal to the grain size. β is the line broadening at full width half maximum intensity (FWHM), after correcting for instrumental line broadening, in radians. θ is the Bragg angle in radians. To determine the instrumental line broadening, we had the Al_2O_3 standard sample ran on the same instrument and setting. The Cagliotti equation for the instrument broadening is fitted as follows,

$$FWHM_{instrument}^2 = 0.0082 \tan^2 \theta - 0.0032 \tan \theta + 0.0019 \quad (4.2)$$

Where $FWHM_{instrument}$ is in degree and theta is in radians. Therefore, for our angle range from 10° to 35° , the $FWHM_{instrument}$ is taken as 0.04. $FWHM_{measured}$ is the experimental fit from XRD data, in degree. $FWHM_{true}$ (unit in degree) is calibrated as follows,

$$FWHM_{true} = \sqrt{FWHM_{measured}^2 - FWHM_{instrument}^2} \quad (4.3)$$

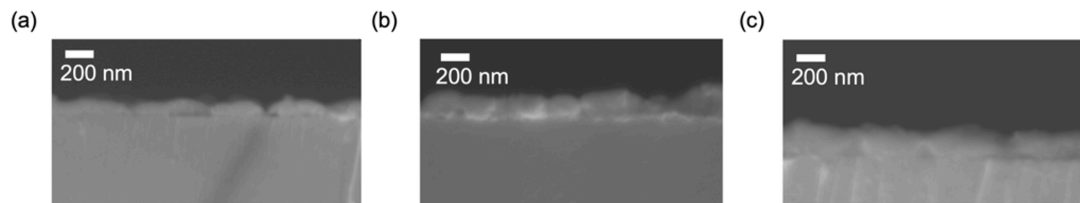


Figure 4.2 Cross-sectional scanning electron micrographs of $\text{Cs}_2\text{AgBiBr}_6$ thin films grown from precursor solutions with concentrations of (a) 0.3 mol L^{-1} , (b) 0.4 mol L^{-1} and (c) 0.5 mol L^{-1} . The thicknesses measured from this figure are $127 \pm 8 \text{ nm}$ (0.3 mol L^{-1}), $173 \pm 23 \text{ nm}$ (0.4 mol L^{-1}) and $220 \pm 18 \text{ nm}$ (0.5 mol L^{-1}). Data taken and analysed by myself.

Consistent with these XRD results, I found from top-down Scanning Electron Microscopy (SEM) micrographs that the microfeature size increased from $160 \pm 10 \text{ nm}$ (0.3 mol L^{-1}) to $200 \pm 20 \text{ nm}$ (0.4 mol L^{-1}) and $370 \pm 40 \text{ nm}$ (0.5 mol L^{-1}), as shown in Figure 4.1d–f (determined using ImageJ). These microfeature sizes are slightly larger than the film thicknesses measured by profilometry, which are $118 \pm 4 \text{ nm}$ (0.3 mol L^{-1}), $160 \pm 3 \text{ nm}$ (0.4 mol L^{-1}) and $242 \pm 6 \text{ nm}$ (0.5 mol L^{-1}). From cross-sectional SEM images (Figure 4.2), there is one grain throughout the thickness of the film, which is consistent with the typical growth of halide perovskites from solution.¹⁴⁰ The differences between the crystallite and microfeature sizes found from XRD vs. SEM measurements may have been due to i) the microfeatures in SEM being composed of

several crystallites, ii) because of a variation in grain size and the narrower XRD peaks from the larger grains being hidden behind the broader peaks from the smaller grains, or iii) because the XRD peaks were broadened due to other factors, such as stacking faults. To avoid ambiguity, we hereafter refer to the films based on the concentration of the precursor solution they were deposited from (rather than their XRD or SEM grain size).

4.3 Charge-carrier recombination

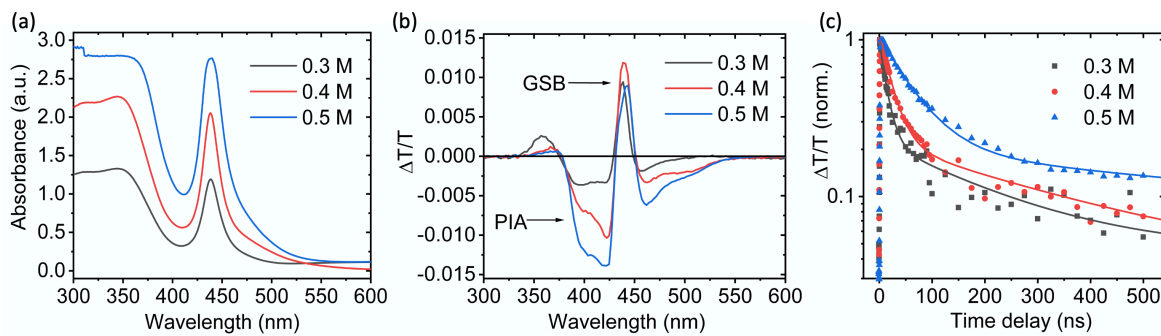


Figure 4.3 Absorption measurements and kinetics of $\text{Cs}_2\text{AgBiBr}_6$ thin films grown from three different precursor solution concentrations. (a) Steady-state absorbance of the thin films grown on glass. (b) $\Delta T/T$ spectra for the integrated time range of 1-10 ns. (c) Normalized kinetics of the ground state bleach (GSB). The $\Delta T/T$ values were integrated over the wavelength range of 437-442 nm. The excitation wavelength was 355 nm for laser pulses with a pulse length less than 1 ns at a repetition rate of 1 kHz and fluence of $50 \mu\text{J cm}^{-2} \text{ pulse}^{-1}$. Data in Figure 4.3(a) taken by myself; data in Figure 4.3(b)(c) taken by Linjie Dai; all analysed by myself.

Figure 4.3a shows the absorbance of the films measured by ultraviolet-visible (UV-vis) spectrophotometry. As expected, the absorbance increased with increasing film thickness. In photovoltaic devices, carrier extraction depends on the drift and diffusion lengths, and the two key components in this regard are the charge-carrier lifetime and mobility. Transient absorption spectroscopy (TAS) was used to measure the charge-carrier lifetime of the films, which were excited with a 355 nm wavelength pump laser incident on the top surface of the films. I found two ground state bleach (GSB) and two photo-induced absorption (PIA) features in the TAS spectra (Figure 4.3b). The GSB peak below 380 nm wavelength is ascribed to a localized state well above the conduction band minimum.^{93,94} However, the explanation for the GSB peak at approximately 440 nm wavelength has been the subject of controversy. Some previous studies attributed this peak to a resonant exciton associated with the first direct transition of $\text{Cs}_2\text{AgBiBr}_6$.^{94,97,141} There are also calculations showing that this peak could be due to a narrow

distribution of states with a direct transition above the indirect band-edges, and which have high oscillator strength.⁶⁶ Consistent with the GSB peak at 440 nm being due to excitons, the two PIA signals on either side of the main GSB peak (440 nm) are attributed to the broadening of the direct exciton transition introduced by carrier-exciton scattering.^{89,94} The origins of these GSB and PIA peaks are beyond the scope of this work, and I do not discuss them further here. However, in either case, the decay of carriers from states at the first direct transition or the decay of excitons provide important information on non-radiative recombination processes, and a comparison can be made between different samples of the non-radiative recombination rate based on these GSB kinetics. I did not observe any GSB at wavelengths longer than 550 nm. This is attributed to a combination of two effects: i) the weak absorption at the indirect bandgap (as seen in the steady-state spectra in Figure 4.3a) and ii) the neighbouring PIA peak covering any weak GSB that may exist here.

Table 4.2 Bi-exponential fitting of transient absorption data in Figure 4.3c. Fit with $y = A_1 \exp\left(-\frac{x}{t_1}\right) + A_2 \exp\left(-\frac{x}{t_2}\right) + y_0$. Data taken by Linjie Dai and analysed by myself.

Parameter fit	0.3 mol L ⁻¹	0.4 mol L ⁻¹	0.5 mol L ⁻¹
y0	0.044±0.003	0.033±0.002	0.032±0.002
A1	0.77±0.02	0.92±0.01	0.863±0.009
t1	13.9±0.8	22.4±0.8	59±1
A2	0.18±0.02	0.19±0.01	0.168±0.009
t2	209±31	332±33	1044±112
R ²	0.989	0.997	0.998

Irrespective of the intrinsic nature of the sharp bleach peak at ~440 nm wavelength, it represents the repopulation of the ground state with time after the absorption of the femtosecond pump laser. I integrated the GSB over the wavelength range of 437–442 nm to characterize the carrier lifetime because this peak has high intensity and a high signal-to-noise ratio. Whilst the GSB kinetics could be fit with a drift-diffusion model to determine the charge-carrier lifetime and surface recombination velocity,¹⁴⁰ this requires a large number of variables to be fit to a single kinetics curve, and it cannot be guaranteed that the fit obtained is the global minimum rather than one of the local minima. I therefore fit the data with a bi-exponential function, which,

whilst not necessarily being physically relevant, provides a numerical comparison between the GSB kinetics of different samples (Figure 4.3c). For the 0.3 mol L⁻¹, 0.4 mol L⁻¹, and 0.5 mol L⁻¹ films, the time constants of the short-lived components of the bi-exponential function are 14±1 ns, 22±1 ns and 59±1 ns, respectively, and long-lived components are 210±30 ns, 330±30 ns and 1000±100 ns, respectively (Table 4.2). Due to the indirect nature of its bandgap and thus the low photoluminescence quantum efficiency (PLQE), most carriers recombine non-radiatively.⁶⁷ We attribute the fast component to trapping of one carrier and the slow component to the subsequent non-radiative recombination process, which would happen if traps are shallow.¹⁴²

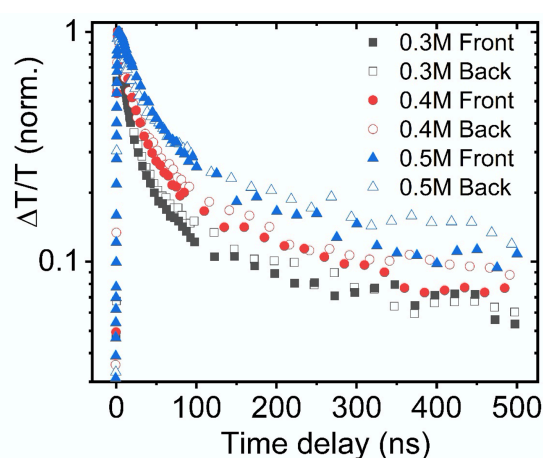


Figure 4.4 Normalized kinetics of Cs₂AgBiBr₆ thin films grown from three different precursor solution concentrations, with 355 nm wavelength laser incident on the front (film surface) and back (substrate) side of the sample. The $\Delta T/T$ values were integrated over the wavelength range of 440-448 nm (GSB). The excitation wavelength was 355 nm for laser pulses with a pulse length less than 1 ns at a repetition rate of 1 kHz and fluence of 50 $\mu\text{J cm}^{-2} \text{ pulse}^{-1}$. Data taken by Linjie Dai and analysed by myself.

An alternative explanation for the change in GSB kinetics is the difference in film thicknesses across the films from 120 nm (0.3 mol L⁻¹) to 240 nm (0.5 mol L⁻¹) leading to different degrees of contribution from surface recombination to the overall GSB kinetics measured. However, the absorption coefficient of the film at the TA excitation wavelength (355 nm) is $2 \times 10^5 \text{ cm}^{-1}$, and therefore the absorption depth is 50 nm. The out-of-plane electron diffusion length in Cs₂AgBiBr₆ thin film is reported to be around 20-30 nm.⁷⁶ Carriers are therefore unlikely to diffuse to the back surface and recombine rapidly there. In addition, when we excited the films from the back (*i.e.*, glass substrate side), we found that the kinetics had the same decay profile (as compared to excitation from the film side), and the change in kinetics with film thickness

follows the same trend (Figure 4.4). Overall, these analyses show that the change in GSB kinetics are due to changes in the bulk carrier lifetime of the films as the grain size changed with film thickness.

The TAS measurements performed above and by others only give carrier kinetics spatially averaged over the measurement spot, which has a diameter of 1.6 mm. To move beyond spatially averaged measurements and directly compare the optoelectronic properties of the grain boundary and interior, I used cathodoluminescence hyperspectral mapping (CL), which takes place inside an SEM and provides spatial resolution beyond the optical limit. CL results from the radiative recombination of excess electrons and holes generated by the incident electron beam (e-beam), with the lateral resolution depending on the electron beam energy (which controls the interaction volume) and the carrier diffusion length. The acceleration voltage used in this study was 3 keV, corresponding to a penetration depth of 67 nm according to Monte Carlo simulations using Monte Carlo Casino (Figure 4.5).¹²⁶ Thus, the interaction volume size in CL is significantly smaller than in confocal PL,¹⁴³ providing sufficient spatial resolution to differentiate between the grain boundary and interior.

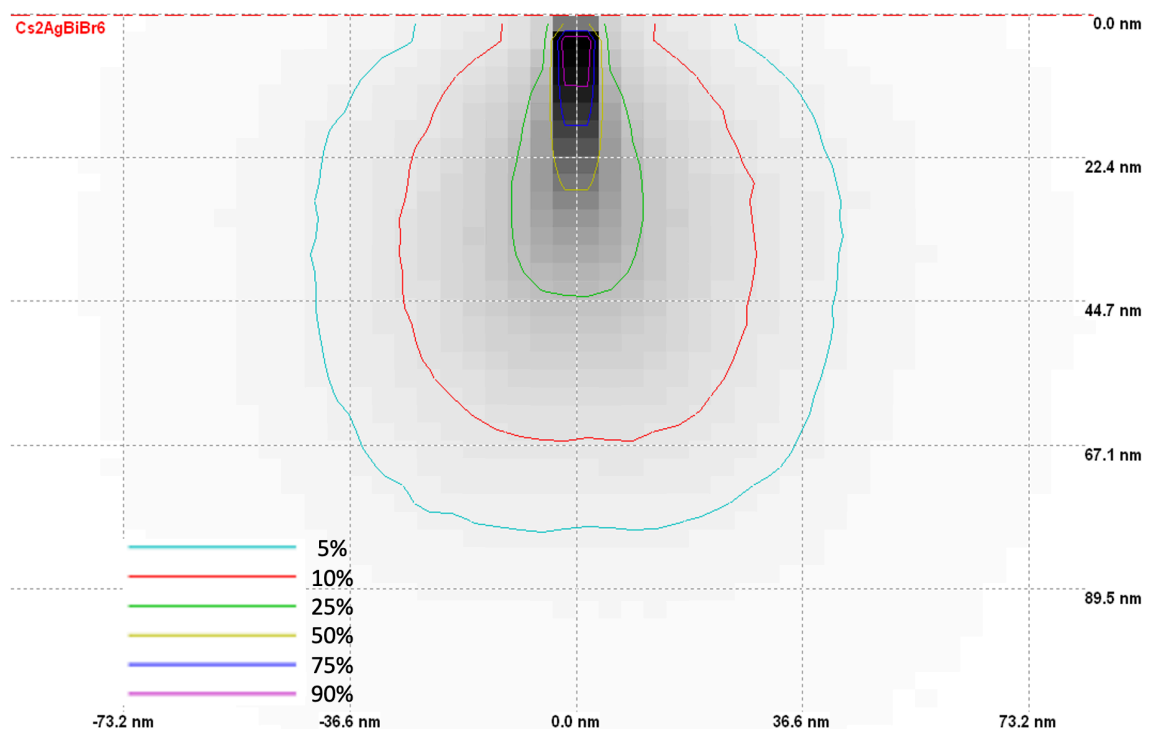


Figure 4.5 Monte Carlo Simulation of the interaction volume in cathodoluminescence measurement. 90% of beam energy lost in a depth of 67nm. (Beam current: 500 pA; Acceleration voltage: 3 kV). Simulation made by Gunnar Kusch.

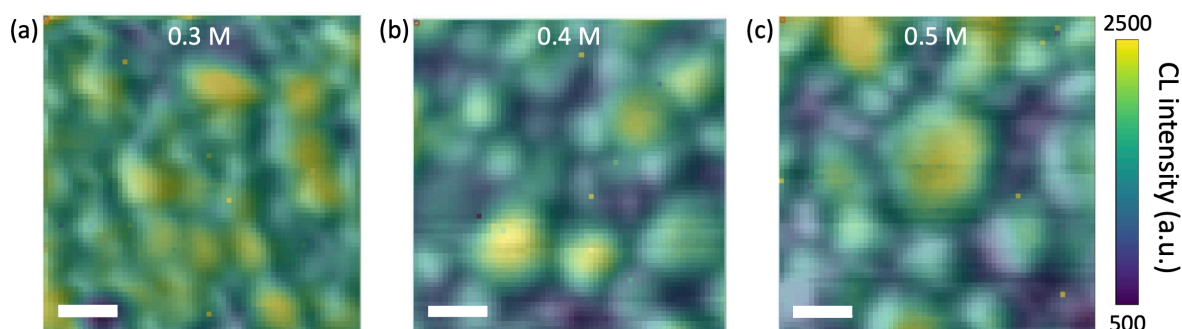


Figure 4.6 Fitted cathodoluminescence intensity maps overlaid on the SE micrographs of the $\text{Cs}_2\text{AgBiBr}_6$ double perovskite thin films grown from precursor solutions with the concentrations (a) 0.3 mol L^{-1} , (b) 0.4 mol L^{-1} and (c) 0.5 mol L^{-1} . Scale bars in the plots are 200 nm . All three measurements were performed with an acceleration energy of 3 keV and a beam current of 500 pA . Note that different acquisition times were used for different CL maps. A comparison of the CL intensity, corrected for the different acquisition times, of the grain interiors between different samples is given in Figure 4.7. Data taken by Gunnar Kusch and analysed by myself.

We were able to compare the CL intensity of the perovskite peak with the secondary electron (SE) image by fitting a Gaussian function to the halide double perovskite signal in each pixel of the map and extracting the fitted intensity using the HyperSpy Python Library, which is given in Ref [127]. By superimposing the perovskite peak intensity map on the SE image, I found a distinct difference between the CL intensity at grain boundaries *versus* grain interiors. For all three samples, I found that the grain interior shows a much higher CL emission intensity than the grain boundary (Figure 4.6). This observation suggests that grain boundaries act as the main non-radiative recombination sites in the investigated samples. This may be due to disorder or dangling bonds at the grain boundary, but could also be due to the accumulation of point defects adjacent to the grain boundary, and is consistent with the GSB kinetics becoming slower with a reduction in the grain boundary density. It explains the correlation between slower GSB kinetics and a reduction in grain boundary density. The origin of luminescence in CL is attributed to be the same as in PL, that is, due to sub-bandgap state emission.⁸⁰

These measurements are consistent with the PL intensity from the film increasing with grain size (Figure 4.7a). I verified that these changes in PL intensity were due to a reduction in grain boundary density by comparing the CL intensity (corrected for acquisition time, *i.e.*, given in counts s^{-1}) in the interior of the grains and finding there to not be a monotonic trend with grain size (Figure 4.7b). These results suggest that non-radiative recombination within each grain

depends on the local defect density, whereas the PL intensity, measured on a millimeter scale, is dominated by non-radiative recombination at grain boundaries.

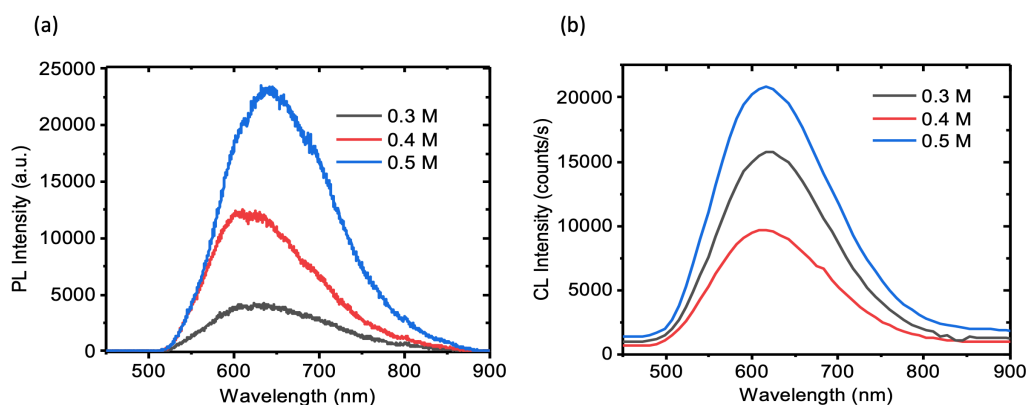


Figure 4.7 (a) PL intensity of the thin films measured using an intensified CCD camera detector. For the PL measurements, the excitation wavelength was 400 nm, with a repetition rate of 1 kHz and fluence of $50 \mu\text{J cm}^{-2} \text{ pulse}^{-1}$. For the detector, the gate width was 5 ns, exposure time 0.3 s, slit width $400 \mu\text{m}$ and the number of accumulations 15. (b) Mean CL intensity of the grain interior corrected for acquisition time.

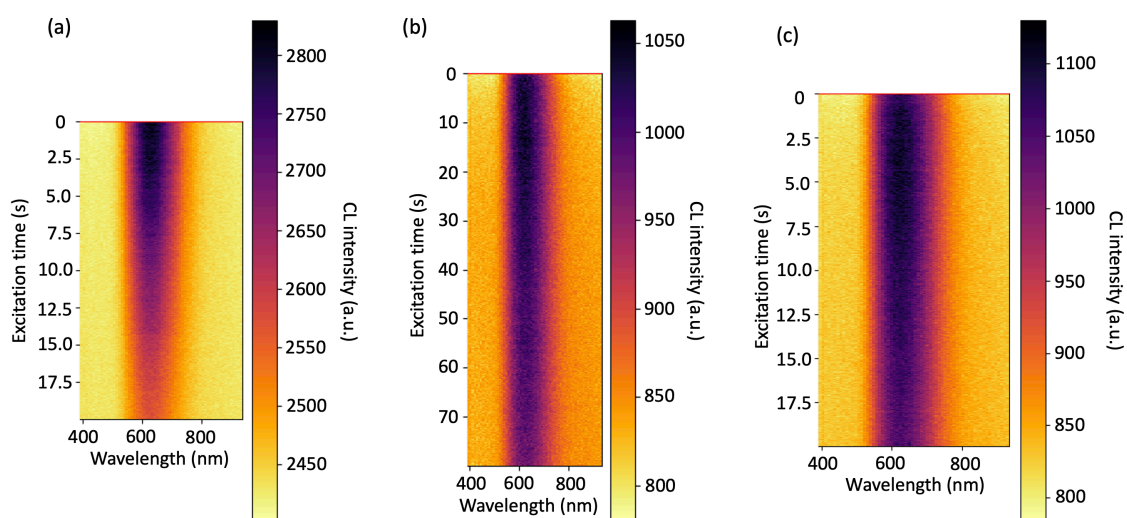


Figure 4.8 Survival traces under continuous exposure to the electron beam on Cs₂AgBiBr₆ thin films deposited from precursor solutions with (a) 0.3 mol L⁻¹, (b) 0.4 mol L⁻¹ and (c) 0.5 mol L⁻¹ concentration. Data taken by Gunnar Kusch and analysed by myself.

A series of spectra recorded at the same point were measured to address variations in CL emission intensity with the amount of exposure to the electron beam. Halide perovskites are

known to be highly beam sensitive, potentially leading to alterations in both the emission wavelength and emission intensity under the continuous electron beam which could have influenced our measurements. All samples were found to show a degradation in the luminescence intensity with increasing excitation time, but the onset of this degradation was at least an order of magnitude larger than the pixel dwell time used in the hyperspectral images (Figure 4.8). It is thus unlikely that our measurements were strongly affected by these effects. Also, no change in the emission energy with excitation time was observed for any of the samples. I further note that morphology can also influence the CL signal. In troughs, such as grain boundaries, the increased scatter of electrons leads to increased electron-hole pair generation and therefore a larger CL signal.^{144,145} But in this case, it is evident from Figure 4.6 that these morphological effects are negligible compared to the effects of non-radiative recombination, since grain boundaries are consistently darker than the interior of the grains.

4.4 Charge-carrier and ion transport

FETs (bottom gate, bottom contact) were fabricated by spin-coating the specific concentration of perovskite on top of lithographically-patterned Au source and drain electrodes. Currently in the broader literature, the demonstration of perovskite FETs has been difficult due to significant ionic defect migration, which screens the gate potential. To the authors' knowledge, this work represents the first report of FETs from halide double perovskites. FETs fabricated from these double perovskites exhibit room temperature p-type field effect transport (accumulation and switch-on occur for negative gate biases), with current modulation in the range of 10^3 (Figures 4.9a). This is consistent with the p-type character of the $\text{Cs}_2\text{AgBiBr}_6$ films previously found from X-ray photoemission spectroscopy measurements.^{66,67} p-type FETs are important for making CMOS complementary inverter circuits but have been generally more difficult to achieve than n-type FETs for perovskite semiconductors.¹⁷ Despite the “anti-clockwise” hysteresis in the device characteristics, it was possible to extract a hole μ_{FET} from the forward scan plot which tend to be a more conservative estimate of mobility. Devices fabricated with 0.3 mol L^{-1} perovskite precursor solution exhibited a room-temperature field effect mobility (μ_{FET}) of $1 \times 10^{-4} \text{ cm}^2 \text{ V}^{-1} \text{ s}^{-1}$, which increased by around 6-15 times upon increasing the precursor concentration to 0.5 mol L^{-1} (Figure 4.9b).

In typical 3D perovskite FETs fabricated from MAPbI_3 , a negative coefficient of mobility with temperature is usually observed, since the ionic screening of gate potential decreases with a decrease in temperature.¹⁹ However in the case of these double perovskite based FETs, I

observed a transition from a positive coefficient of mobility to negative coefficient of mobility as temperature increased for devices fabricated with perovskite precursor concentrations of 0.3 mol L⁻¹ and 0.4 mol L⁻¹. As the grain size increased, I observed a positive coefficient of field-effect mobility, which is typical of a thermally-activated hopping mechanism of transport.¹⁴⁶ These $\mu_{\text{FET}}(T)$ trends are indicative of the fact that upon increasing the grain size it is possible to observe a transport regime where the ionic screening of the gate potential can be minimized to an extent such that a hopping mechanism of transport, which is likely intrinsic to the material, is observed.

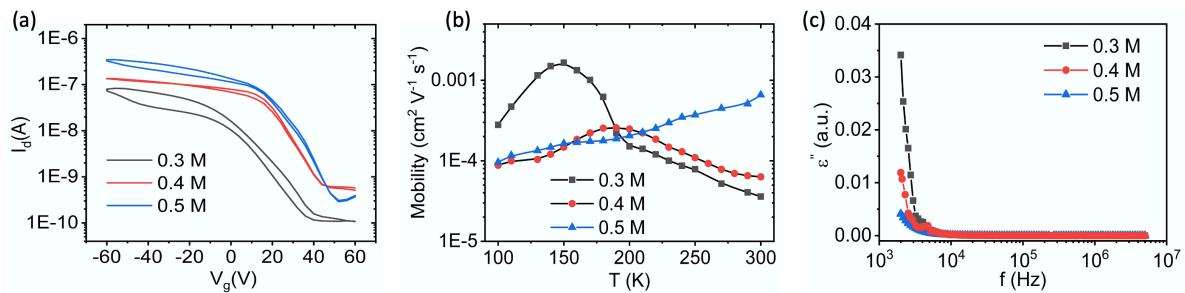


Figure 4.9 (a) Transfer curves of $\text{Cs}_2\text{AgBiBr}_6$ thin films grown from precursor solutions with 0.3 mol L⁻¹, 0.4 mol L⁻¹ and 0.5 mol L⁻¹ concentrations. The measurements were conducted on bottom contact bottom gate field-effect transistors at 300 K (FETs with $L = 20 \mu\text{m}$, $W = 1 \text{mm}$), $V_d = -60 \text{V}$. (b) Temperature-dependent FET mobility and (c) dielectric loss for $\text{Cs}_2\text{AgBiBr}_6$ thin films grown from three different concentrations. Data taken by Satyaprasad P. Senanayak and Dipika Pradhan; analysed by Satyaprasad P. Senanayak and myself.

To verify our proposal that the negative coefficient of mobility in double perovskite films with small- and medium-sized grains in the high temperature regime is due to the stronger screening effect induced by ion motion, we estimated the ionic conductivity in the perovskite films through impedance measurements on perovskite devices with the capacitor structure: ITO/Au/ $\text{Cs}_2\text{AgBiBr}_6$ /Au. The dielectric loss spectroscopy measurements showed that perovskite devices fabricated with 0.3 mol L⁻¹ precursor concentration had a significantly higher ionic conductivity, which then decreased by an order of magnitude as the precursor concentration increased to 0.5 mol L⁻¹ (Figure 4.9c).

It should be noted that although it was possible to observe field effect modulation at room temperature, the transfer characteristics exhibit features that are non-ideal (Figure 4.9a). Similarly, the output characteristics measured on these FETs exhibit clear signatures of ionic migration without a clean saturation regime (Figure 4.10 and 4.11). Even for devices fabricated

with 0.5 mol L^{-1} precursor solutions (which correspond to a grain size of $113 \pm 3 \text{ nm}$, as calculated from XRD), the output characteristics exhibit an injection-limited concave shape ($\sim V_d^2$; refer to Figure 4.10). This is likely due to the associated space charge that accumulates and creates a parallel channel for conduction, as observed in earlier reports on perovskite FETs.¹⁹ Furthermore, there is a significant mismatch between the channel currents of transfer and output characteristics when the devices were measured under the same S-D (V_d) and gate (V_g) potentials, reflecting an instability in the device current depending on different measurement sequences. Similar effects were observed in some early MAPbI₃ FETs and possible future routes to reduce these non-idealities in the output characteristics include: (a) using suitable interlayers, such as MoO₃, PEDOT:PSS or PFBT treated Au electrode;¹⁴⁷ (b) increasing the channel length, which would effectively decrease the contact resistance.¹⁴⁸

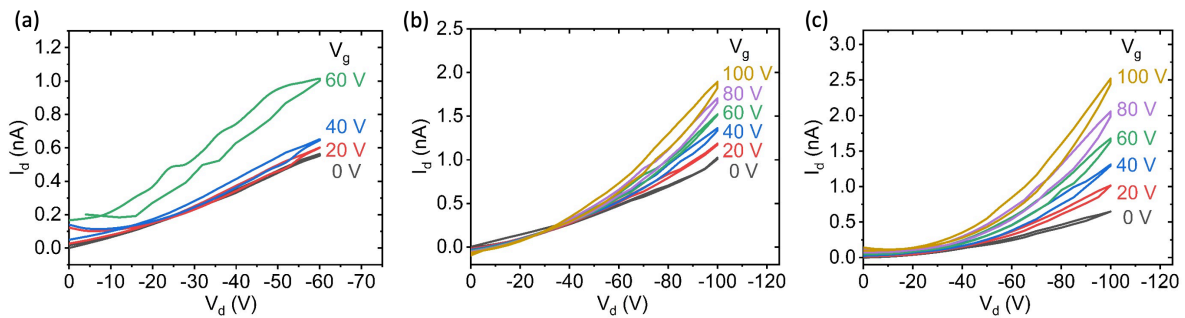


Figure 4.10 Output characteristics measured on bottom-contact bottom-gate field-effect transistors at 300 K (FETs with $L = 20 \mu\text{m}$, $W = 1 \text{ mm}$), with the perovskite layer fabricated from (a) 0.3 mol L^{-1} , (b) 0.4 mol L^{-1} , (c) 0.5 mol L^{-1} precursor solutions. Data taken by Satyaprasad P. Senanayak; analysed by Satyaprasad P. Senanayak and myself.

Output characteristics on these perovskite FETs at $T = 100 \text{ K}$ where the ionic defects do not play a significant role were also measured (Figure 4.11). The FETs with double perovskites grown from 0.4 mol L^{-1} precursor solution exhibited clean saturation (Figure 4.11b). However, the FETs based on double perovskites grown from 0.3 mol L^{-1} and 0.5 mol L^{-1} precursor solutions still exhibited non-ideal output characteristics. Possibly this can be attributed to the presence of trap states in the double perovskite thin films, which is consistent with the thermally activated transport behaviour shown in the main text. Overall, from these measurements, we attribute the non-ideal output characteristics of the double perovskite FETs to the effects of electronic traps and ionic defects, which would need to be addressed in future to improve the performance of Cs₂AgBiBr₆ FETs.

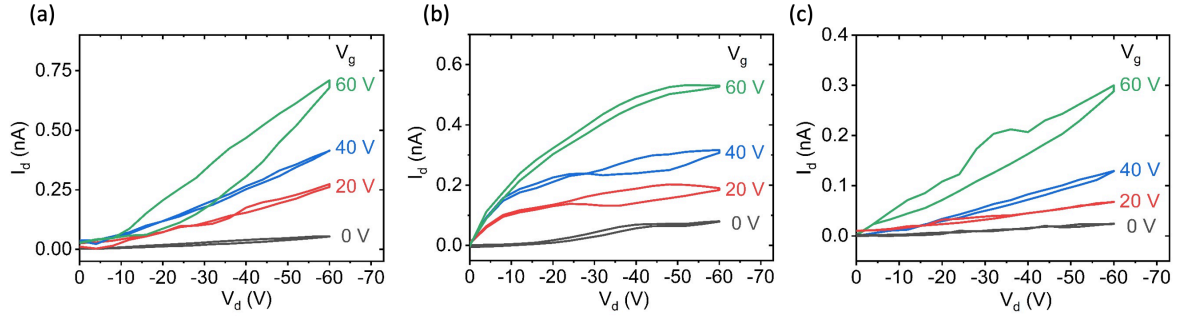


Figure 4.11 Output characteristics measured on bottom contact bottom gate field-effect transistors at 100 K (FETs with $L = 20 \mu\text{m}$, $W = 1 \text{ mm}$), with the perovskite layer fabricated from (a) 0.3 mol L^{-1} , (b) 0.4 mol L^{-1} , (c) 0.5 mol L^{-1} precursor solutions. Data taken by Satyaprasad P. Senanayak; analysed by Satyaprasad P. Senanayak and myself.

The observed non-ideal transistor characteristics complicate the understanding of the underlying transport physics. However, we have been able to mitigate the possible factors to an extent such that meaningful $\mu_{\text{FET}}(T)$ can be extracted by linear fit to $I_d^{0.5}$ versus V_g (Figure 4.12), and the mobilities extracted from the forward and reverse sweeps differ no more than by 12%. Based on Ref.,¹⁴⁹ we estimated the reliability of mobility estimation to be in the range of 55% - 79% across all devices and the entire temperature range considered, comparable to other non-ideal FETs.¹⁴⁷ This reliability calculation takes into account the non-idealities of the FET characteristics to the model fit, among other factors.

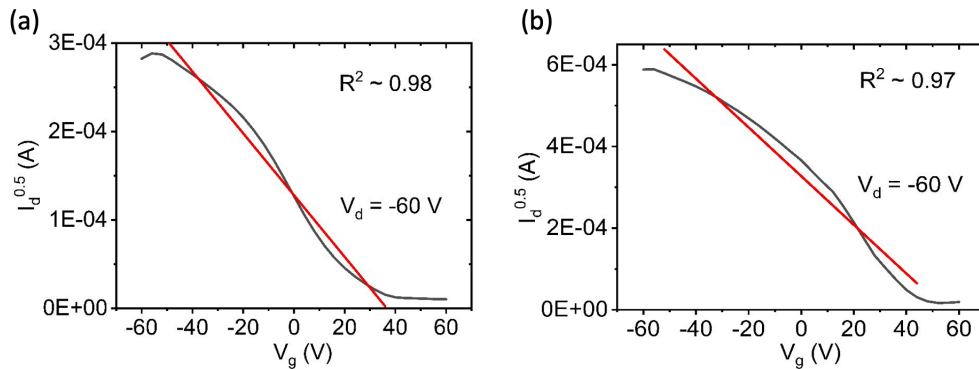


Figure 4.12 Typical Linear fit to $I_d^{0.5}$ versus V_g used for estimating the mobility values, with the perovskite FETs measured at 300 K. Linear fits with R^2 values greater than 0.96 was utilized for the estimation of mobility. Data taken by Satyaprasad P. Senanayak; analysed by Satyaprasad P. Senanayak and myself.

To further verify if ionic transport increases with grain boundary density, I conducted temperature-dependent transient current measurements. For these measurements, I used hole-

only devices due to the aforementioned p-type character of the films. Mobile ions in perovskites with an electric field applied can migrate to the contact layers.^{150,151} In a typical MAPbI₃ perovskite, when applying a bias, halide anions migrate to the anode (where holes are being injected), while MA⁺ cations migrate to the cathode (where electrons are being injected),¹⁵² due to the low formation energy of halide and MA⁺ vacancies.¹⁰¹

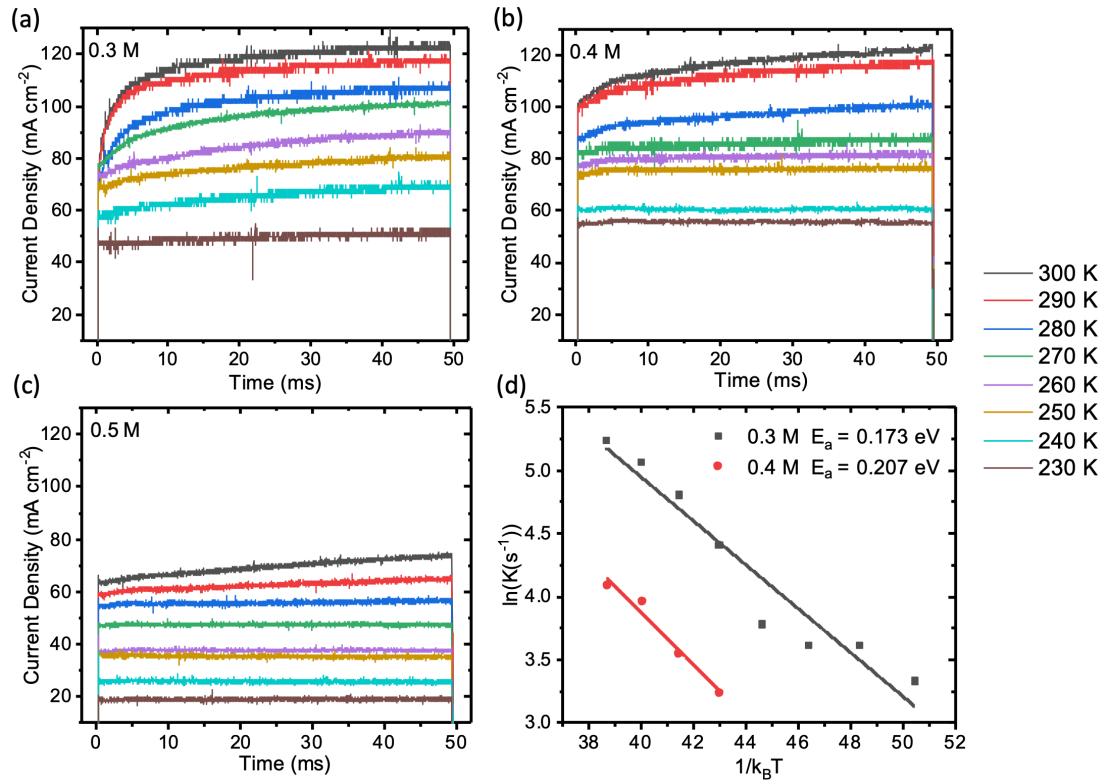


Figure 4.13 Temperature-dependent transient current measurements of hole-only devices with Cs₂AgBiBr₆ thin films deposited from precursor solutions with (a) 0.3 mol L⁻¹, (b) 0.4 mol L⁻¹ and (c) 0.5 mol L⁻¹ concentration. The device structure was ITO/NiO_x/Cs₂AgBiBr₆/PTAA/Au. (pulse voltage = 3.0 V, reference voltage = 0 V, frequency = 4 Hz, and pulse width = 50 ms). (d) Arrhenius plots of the temperature dependence of the natural logarithm of K against the inverse of k_BT. Note K in the y axis is the decay rate (s⁻¹), as obtained from Equation 4.5. The activation energy for ion migration (E_a) was extracted by linear fitting. Data taken and analysed by myself.

I noticed that there is a temporal increase in the hole current density in all three films (Figure 4.13a, b and c). The increase in current is due to enhanced hole injection by the accumulation of anions at the anode interface,¹⁵² most likely Br⁻, since bromine vacancies (V_{Br}) have been calculated to be the donor defect with lowest formation energy in Cs₂AgBiBr₆.¹³³ This agrees with calculations showing that V_{Br} has the lowest activation energy for vacancy-assisted

diffusion among the four constituent vacancies.¹¹³ In principle, hole transport should also be impeded by the screening effect (accumulation of ions on the gate interface) which will lead to a current decay. However, the enhanced hole injection at the anode interface due to ion migration plays a dominant role, so we mainly observed a current rise.¹⁵² It was observed that the stabilized current decreased with higher precursor concentrations (*i.e.*, increased film thickness and grain size). The temperature dependence in all three films further confirms that the transient increase in current is due to the drift of mobile ions, which are arrested at lower temperatures. It is noticed that the transient current has two components: a faster component (exponential rise) and a slower component (nearly linear rise). We attribute the faster component to Br⁻ motion to the anode followed by facilitated hole injection and the slower component to drift of other heavy ions (both cation and anion, which is difficult to distinguish). An increase in grain boundary density led to an increase in the exponential growth component of the transient current due to excess Br⁻ motion. To extract the activation energy of the ion motion, we fit the faster current response with the single-exponential function below.

$$J = A \exp\left(-\frac{t}{\tau}\right) + y_0 \quad (4.4)$$

Table 4.3 Single exponential fitting of the transient current of the 0.3 mol L⁻¹ film (Figure 4.13a). Fit with $y = A_1 \exp\left(-\frac{x}{t_1}\right) + y_0$. Data taken and analysed by myself.

Parameter fit	300K	290K	280K	270K	260K	250K	240K	230K
y0	121.52 ±	115.69 ±	106.54 ±	101.32 ±	92.24 ±	82.87 ±	71.8 ±	53.1 ±
	0.04	0.03	0.03	0.03	0.06	0.09	0.1	0.2
A1	-33.3 ±	-29.6 ±	-28.9 ±	-21.99 ±	-18.28 ±	-13.07 ±	-13.51 ±	-6.4 ±
	0.2	0.2	0.1	0.05	0.05	0.08	0.09	0.2
t1	5.32 ±	6.34 ±	8.20 ±	12.21 ±	22.9 ±	26.9 ±	26.9 ±	36 ± 2
	0.05	0.05	0.06	0.06	0.2	0.4	0.5	
R ²	0.941	0.919	0.956	0.981	0.977	0.946	0.925	0.693

Table 4.4 Single exponential fitting of the transient current of the 0.4 mol L⁻¹ film (Figure 4.13b). Fit with $y = A_1 \exp\left(-\frac{x}{t_1}\right) + y_0$. "--" represents unconverged fitting error. Data taken and analysed by myself.

Parameter fit	300K	290K	280K	270K	260K	250K	240K	230K
y0	122.73 ± 0.05	118.15 ± 0.07	103.1 ± 0.1	89.7 ± 0.3	82.02 ± 0.03	76.67 ± 0.03	60.67 ± --	55.90 ± 0.01
A1	-18.93 ± 0.05	-16.58 ± 0.06	-13.37 ± 0.09	-6.5 ± 0.2	-3.56 ± 0.04	-1.73 ± 0.04	-- ± --	-1.20 ± 0.09
t1	16.8 ± 0.1	19.0 ± 0.2	28.6 ± 0.5	39 ± 3	15.1 ± 0.5	16 ± 1	13.33 ± --	1.7 ± 0.2
R ²	0.970	0.948	0.939	0.630	0.611	0.316	0	0.080

Table 4.5 Single exponential fitting of the transient current of the 0.5 mol L⁻¹ film (Figure 4.13c). Fit with $y = A_1 \exp\left(-\frac{x}{t_1}\right) + y_0$. "--" represents unconverged fitting error. Data taken and analysed by myself.

Parameter fit	300K	290K	280K	270K	260K	250K	240K	230K
y0	82.9 ± 0.3	69.9 ± 0.4	71541.67 ± --	47.81 ± 0.01	38.04 ± 0.01	35.37 ± 0.03	25.3 ± 0.7	19.5 ± 0.2
A1	-18.9 ± 0.3	-10.2 ± 0.4	-71486.34 ± --	-0.80 ± 0.09	-0.91 ± 0.07	0.99 ± 0.03	1.0 ± 0.7	-0.3 ± 0.2
t1	64 ± 2	66 ± 3	2276129.53 ± --	1.5 ± 0.2	1.9 ± 0.2	19 ± 2	93 ± 82	48 ± 38
R ²	0.972	0.896	0.453	0.037	0.084	0.228	0.054	0.018

Fitting parameters are summarized in Table 4.3 – 4.5. When the temperature is high and the concentration of films is low, the model's fit converged. However, at low temperatures and higher concentration films, especially the 0.5 mol L⁻¹ film, the fittings did not converge. This

is due to the heavily impeded exponential growth and the almost linear increase in current (Figure 4.13c). Therefore, we cannot extract a time constant from low temperatures in the 0.4 mol L⁻¹ film and all curves in the 0.5 mol L⁻¹ film.

To extract the ion motion activation energy, we fit the available time constant with the following equation¹⁵²

$$K = \frac{1}{\tau} \propto \sigma = C \exp\left(-\frac{E_a}{k_B T}\right) \quad (4.5)$$

In Equation 4.5, K is the rate at which the current increases in the initial faster part of the transient current response, τ is the time constant from Equation (4.4), σ is ionic conductivity, C is a constant coefficient, E_a is the activation energy for ion migration, k_B is the Boltzmann constant and T is temperature. To extract the activation energy, I conducted linear fittings on $\ln(K)$ versus $(k_B T)^{-1}$ (Figure 4.13d). The slopes of the linear fit give the activation energy. Due to the diminished exponential growth component discussed above, only the activation energy for 0.3 mol L⁻¹ and 0.4 mol L⁻¹ films (using the four high temperature curves for 0.4 mol L⁻¹) were extracted. The low temperature data points for the 0.3 mol L⁻¹ film deviate more from the fitted trend line due to the uncertainties in fitting the nearly-linear initial current transients. The data from the 0.5 mol L⁻¹ film did not fit an exponential decay model, and this agrees with an increase in the activation energy barrier for ion migration. The activation energies in the other two films (0.17 ± 0.04 eV for 0.3 mol L⁻¹; 0.21 ± 0.05 eV for 0.4 mol L⁻¹) are consistent with the analysis that ionic transport through grain boundaries and therefore ionic diffusion is prominent in films grown from lower concentration precursor solutions (with higher densities of grain boundaries). In contrast, Cs₂AgBiBr₆ single crystals have been reported to have an activation energy of 0.348 eV,¹¹³ suggesting that ion migration in Cs₂AgBiBr₆ single crystals is indeed more difficult. It is noted that whilst the film thickness changes across the three different samples, the resulting changes in the internal electric field would not influence the values of the activation energy barriers obtained. This is because the activation energy barrier is determined from an Arrhenius plot that depends on the change in time constant with temperature in each film (slope of $\ln(1/\tau)$ against $1/k_B T$), instead of the absolute value of the time constant itself. Another way of looking at this is that the activation energy barrier is primarily affected by the local environment the ions are in,^{153,154} and changes in the internal electric field by a factor of two would not influence the mechanism of ion migration. The changes in activation energy would therefore reflect the effects of a change in grain boundary

density. Therefore, I conclude that grain boundaries are indeed the main channels for ion movement in $\text{Cs}_2\text{AgBiBr}_6$ thin films.

Finally, It is noted that up to now, most works investigating carrier transport in halide double perovskites have used spectroscopy-based techniques, such as time resolved microwave conductivity (TRMC) or time resolved terahertz spectroscopy (TRTS).^{78,79,155} By achieving halide double perovskite FETs with current modulation at room temperature, we provide important insights into the macroscopic carrier transport mechanisms of thin films that account for the effects of point and extended defects. This information is complementary to that obtained from spectroscopy-based methods, which measure the local mobility of photo-excited carriers. Beyond providing insights into the role of grain boundaries on the ion migration dynamics, as discussed above, the FET measurements also show carrier transport to be intrinsically limited by a thermally-activated hopping-based mechanism,^{156,157} in which the field-effect mobility increases as a function of temperature once the effects of gate screening by ionic defects is minimized (Figure 4.9b). In contrast, previous TRMC measurements have suggested carrier transport in $\text{Cs}_2\text{AgBiBr}_6$ and related materials to be band-like, in which mobility decreases with increasing temperature.^{78,79} Further work is needed to resolve these differences between local and macroscopic electronic measurements of carrier transport, which could be influenced by the point defects that accumulate at grain boundaries (through direct carrier trapping,⁷⁷ or through self-trapping due to the influence of the defects on the interactions between carriers and acoustic phonons),^{89,158,159} or due to the inherent energetic disorder in the material. FET measurements of double perovskites could play an important role in shedding light on the underlying mechanisms for this thermally activated hopping behaviour.

4.5 Conclusions

In summary, by tuning the grain size, I achieved a direct evaluation of the effect of grain boundary density on charge-carrier and ion transport in $\text{Cs}_2\text{AgBiBr}_6$ thin films. I found that grain boundaries are the dominant non-radiative recombination sites and also the main channels for ion migration. Furthermore, the first p-type halide double perovskite field-effect transistor (FET) developed in this work brings new insights into carrier transport and ion migration. Whilst previous spectroscopy measurements have suggested band-like transport in $\text{Cs}_2\text{AgBiBr}_6$, these FET measurements showed carrier transport to be intrinsically limited by a thermally activated hopping mechanism, which helps to explain the low mobilities found in $\text{Cs}_2\text{AgBiBr}_6$. Taken together, these results reveal grain boundaries to be one of the major causes of the

discrepancy between the promising optoelectronic properties reported in single crystals and the more limited performance achieved in Cs₂AgBiBr₆ thin films. This work therefore shows how grain boundaries could mask the true potential of new compounds and the importance of addressing the effects of grain boundaries in the exploration of new compounds in thin film devices to prevent false negatives. This could be achieved using the systematic characterization approach developed in this work. Addressing the role of defects at grain boundaries, such as through passivation, will be essential for the further development of the halide double perovskite family in efficient thin film devices, including solar cells, photoelectrochemical cells and radiation detectors.

Contributions

This chapter is based on a published paper: “Li, Z.; Senanayak, S. P.; Dai, L.; Kusch, G.; Shivanna, R.; Zhang, Y.; Pradhan, D.; Ye, J.; Huang, Y.; Sirringhaus, H.; Oliver, R. A.; Greenham, N. C.; Friend, R. H.; Hoye, R. L. Z. Understanding the Role of Grain Boundaries on Charge-Carrier and Ion Transport in Cs₂AgBiBr₆ Thin Films. *Adv. Funct. Mater.* 2021, 2104981. <https://doi.org/10.1002/adfm.202104981>”.¹⁶⁰ I synthesized the Cs₂AgBiBr₆ double perovskite thin films, tuned the grain size, and performed XRD, SEM, UV-Visible Spectrophotometry and transient current measurements. Zewei Li analysed most of the data (in the case of TFT, with the help of Satyaprasad P. Senanayak) and wrote the manuscript. Satyaprasad P. Senanayak and Dipika Pradhan made the TFT and performed the mobility and impedance measurements. Linjie Dai performed the TAS measurements. Gunnar Kusch performed the CL measurements. Ravichandran Shivanna helped with the discussion about transient current data analysis. Youcheng Zhang and Ravichandran Shivanna helped with the transient current measurements. Junzhi Ye and Yi-Teng Huang helped with the discussion about carrier lifetime analysis. Henning Sirringhaus, Rachel A. Oliver and Neil C. Greenham contributed to the discussion and helped comment on the manuscript. Richard H. Friend supervised Zewei Li and contributed to the discussion. Robert L. Z. Hoye conceived of the project and supervised the work.

5 Bandgap Lowering in Mixed Alloys of $\text{Cs}_2\text{Ag}(\text{Sb}_x\text{Bi}_{1-x})\text{Br}_6$ Double Perovskite Thin Films

After revealing the effect of grain boundaries, one of the critical limitations of $\text{Cs}_2\text{AgBiBr}_6$ is its wide bandgap, which restricts its photoconversion efficiency. Previous literature has shown that its bandgap can be reduced through alloying with Sb^{3+} , but Sb-rich alloys are difficult to synthesize owing to the high formation energy of $\text{Cs}_2\text{AgSbBr}_6$ itself. In this chapter, I developed a solution-based route to synthesize $\text{Cs}_2\text{Ag}(\text{Sb}_x\text{Bi}_{1-x})\text{Br}_6$ thin films over the entire alloying range. The mixed alloys (with x between 0.5 and 0.9) demonstrate smaller bandgaps than the pure Sb- and Bi- based compounds. Through band-alignment characterization and computations, I propose that the bandgap lowering in the mixed alloys arises from the type II band alignment between $\text{Cs}_2\text{AgBiBr}_6$ and $\text{Cs}_2\text{AgSbBr}_6$, as well as the non-linear mixing of orbitals between Bi and Sb. This work demonstrates the underlying mechanisms for the bandgap lowering phenomenon, which is also seen in Pb-Sn perovskites. It further illustrates a general approach to achieve bandgap reduction and highlight that bandgap lowering may be found in other double perovskite alloys by pairing together materials forming a type II band alignment.

5.1 Introduction

The wide bandgap (2.1–2.3 eV) and its indirect nature are limiting the potential of $\text{Cs}_2\text{AgBiBr}_6$ for photovoltaic and photocatalytic applications.^{59,65,161–164} People have achieved a smaller and more direct bandgap by alloying with Tl, but this is more toxic than Pb.^{61,165} Alloying $\text{Cs}_2\text{AgBiBr}_6$ with the substantially less toxic Sb was also shown to be effective, but led to a smaller reduction in bandgap than Tl alloying.^{78,124,166} In part, this was because the Sb-based double perovskite itself ($\text{Cs}_2\text{AgSbBr}_6$) has a wide bandgap of 1.9–2.1 eV.^{64,167} Another factor was that only a maximum of 37.5% Sb could be introduced through powder melt synthesis, limiting the extent of bandgap reduction.¹²⁴ Interestingly, mixed $\text{Cs}_2\text{Ag}(\text{Sb}_x\text{Bi}_{1-x})\text{Br}_6$ alloys exhibit a non-linear reduction in the bandgap, i.e., bandgap bowing, with increasing Sb content.^{124,166} Bandgap bowing has also been found in Pb/Sn perovskite alloys, and, in this case, the bowing is pronounced such that the mixed alloy exhibits a smaller bandgap than either of the pure Pb- or Sn-based compounds.^{120–122} An important question would be whether a similar phenomenon occurs in $\text{Cs}_2\text{Ag}(\text{Sb}_x\text{Bi}_{1-x})\text{Br}_6$ alloys.

Until now, knowledge about the extent of bandgap bowing in Sb-Bi double perovskite alloys and whether the mixed compositions could exhibit a smaller bandgap than the pure compounds are still not known. This will require the full composition range in $\text{Cs}_2\text{Ag}(\text{Sb}_x\text{Bi}_{1-x})\text{Br}_6$ alloys to be characterized. However, phase-pure $\text{Cs}_2\text{AgSbBr}_6$ is challenging to synthesize, particularly in thin film form. This is because of the high formation energy of $\text{Cs}_2\text{AgSbBr}_6$ and the small ionic radius of Sb^{3+} relative to Bi^{3+} .¹⁶⁸ Recently, Liu *et al.* synthesized thin films of $\text{Cs}_2\text{Ag}(\text{Sb}_x\text{Bi}_{1-x})\text{Br}_6$ alloys by dipping their substrates in a heated solution of the precursor salts in dimethyl sulfoxide (DMSO).¹⁶⁶ But they were only able to achieve up to 75% Sb alloying and were not able to synthesize the pure Sb-based compound. Colloidal nanocrystal synthesis routes have been found to be more successful in growing less thermodynamically favoured compounds (*e.g.*, iodide-based double perovskites, which have a positive heat of formation). Yang *et al.* recently developed a route to grow $\text{Cs}_2\text{AgSbBr}_6$ nanocrystals.¹⁶⁸ But they did not concentrate on the bandgap bowing as they characterized the bandgap. And bandgaps of nanocrystals are determined not only by their intrinsic band structure, but also extrinsic factors like the nanocrystal size. Therefore, it is desirable to achieve phase-pure $\text{Cs}_2\text{AgSbBr}_6$ as bulk thin films, which do not have carriers confined within individual grains, as is the case for nanocrystals bound with long-chain ligands.

In this work, I developed a solution-based route to synthesize the entire composition range of Sb-Bi double perovskite alloys in thin film form. I found that the mixed alloys have a lower bandgap than the pure Bi- and Sb-based double perovskites, with similar pronounced nonlinear bandgap behaviour found in lead-tin perovskite alloys.^{120–122} Through X-ray diffraction (XRD) and Rutherford Backscattering Spectrometry (RBS), I found all films to be phase-pure. The thin film composition in the bulk matches the ratio of elements in the precursor solution. I used Photothermal Deflection Spectroscopy (PDS) to accurately determine the variation trend of bandgap and electronic disorder in Sb-Bi double perovskite alloys with different compositions. The electronic structure and band positions were calculated by Density Functional Theory (DFT) to help understand the origins of the bandgap lowering mechanism.

5.2 Synthesis and verification of composition

$\text{Cs}_2\text{Ag}(\text{Sb}_x\text{Bi}_{1-x})\text{Br}_6$ thin films were grown by solution processing. The CsBr, AgBr, SbBr₃ and BiBr₃ precursors were mixed according to their stoichiometric ratio in DMSO with a concentration of 0.5 mol·L⁻¹. The precursors for $\text{Cs}_2\text{AgBiBr}_6$ (CsBr, AgBr and BiBr₃) can be dissolved in DMSO from room temperature to 100 °C. The precursors for $\text{Cs}_2\text{AgSbBr}_6$ (CsBr,

AgBr and SbBr₃) must be dissolved at room temperature, as opposed to 180 °C in literature,¹⁶⁶ and can only be spined for a limited time. Otherwise, the precursor solution will become cloudy, implying the presence of precipitation. Also, in contrast to the dipping method used by Liu *et al.*,¹⁶⁶ a lower annealing temperature and shorter annealing time were used (details in the Experimental Chapter), which may have contributed to the successful synthesis of phase-pure Cs₂AgSbBr₆. Photographs of the films (approx. 200 nm thickness in all cases) are shown in Figure 5.1a, and the mixed compositions showed a deeper colour.

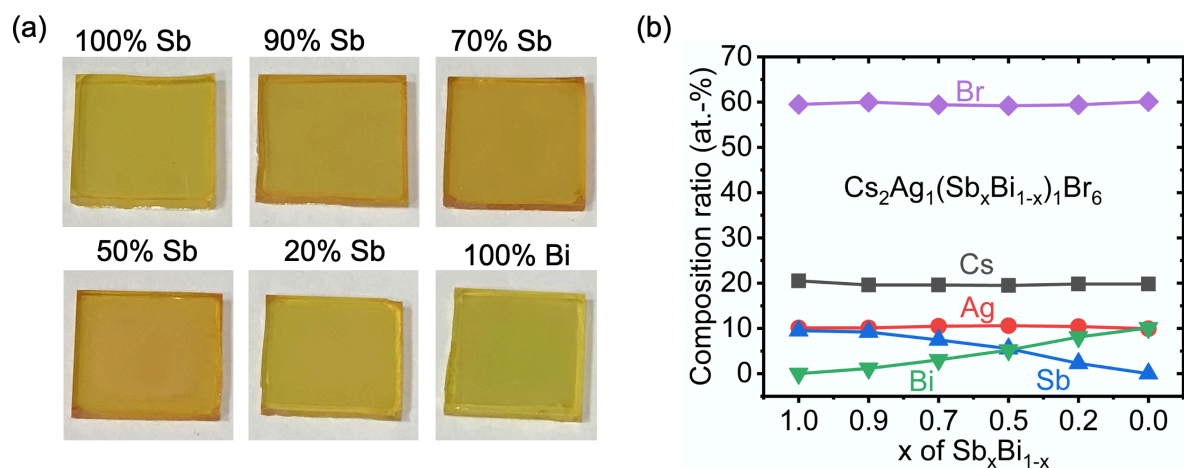


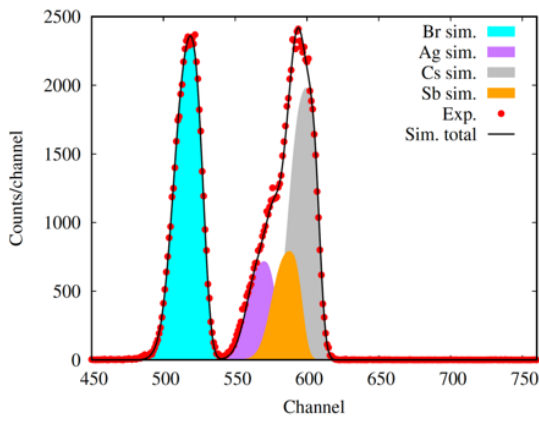
Figure 5.1 (a) Photographs of the Cs₂Ag(Sb_xBi_{1-x})Br₆ films on glass under ambient lighting, with a thickness of approximately 200 nm. The Sb percentage labelled is that in the precursor solution. (b) Measurement of the bulk composition of Cs₂Ag(Sb_xBi_{1-x})Br₆ films with Rutherford Backscattering Spectrometry (fitting in Figure 5.2). Films synthesised and photo taken by myself; data in Figure 5.1b taken by Mari Napari, Mikko Laitinen and Jaakko Julin.

To determine the bulk composition of the films, RBS measurements (Figure 5.1b and Table 5.1) were performed. It was found that the Sb/Bi ratio from the RBS measurements matched the stoichiometry in the precursor solution, deviating from the nominal precursor stoichiometry by up to 2.1 percentage points (Table 5.1). The fitting and statistical uncertainties are high with low Sb concentration because the Sb RBS peak is buried between two other peaks (Ag and Cs, Figure 5.2). These discrepancies could be either due to uncertainties in the RBS measurement or errors in preparing the precursor solution. Overall, these measurements indicate the bulk composition to match the precursor stoichiometry in the solution. However, we cannot exclude the presence of phase-impurities in the films below the percent-level.

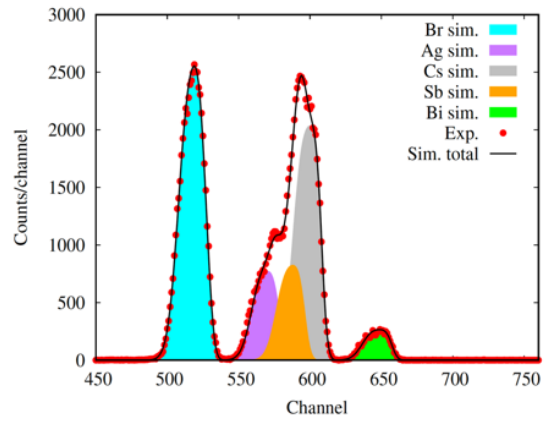
Table 5.1 Quantification of the bulk composition of $Cs_2Ag(Sb_xBi_{1-x})Br_6$ thin films by RBS. Data taken and analysed by Mari Napari, Mikko Laitinen and Jaakko Julin.

Nominal Sb/(Sb+Bi) in precursor solution	RBS					Sb/(Sb+Bi) in film
	Cs/at.-%	Ag/at.-%	Sb/at.-%	Bi/at.-%	Br/at.-%	
100%	20.5	10.1	9.5	0	59.5	100%
90%	19.6	10.1	9.2	1.2	60.0	88.5%
70%	19.6	10.5	7.5	3.2	59.4	70.1%
50%	19.5	10.6	5.5	5.2	59.2	51.4%
20%	19.8	10.4	2.3	8.1	59.4	22.1%
0%	19.8	10.0	0	10.1	60.1	0%

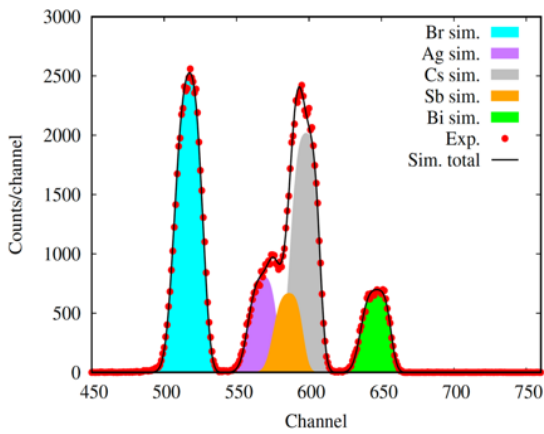
100% Sb on Si substrate



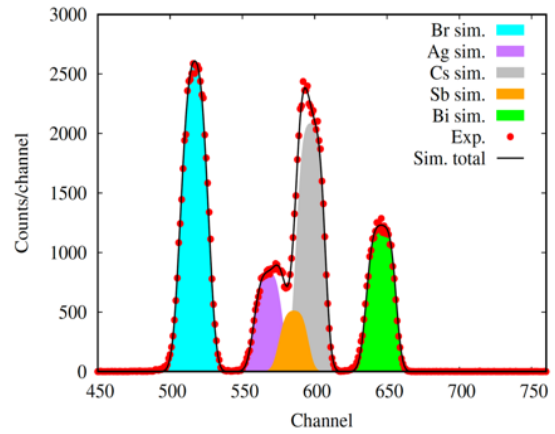
90% Sb on Si substrate



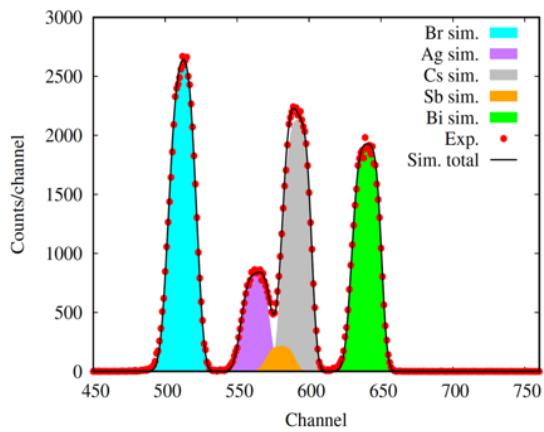
70% Sb on Si substrate



50% Sb on Si substrate



20% Sb on Si substrate



100% Bi on Si substrate

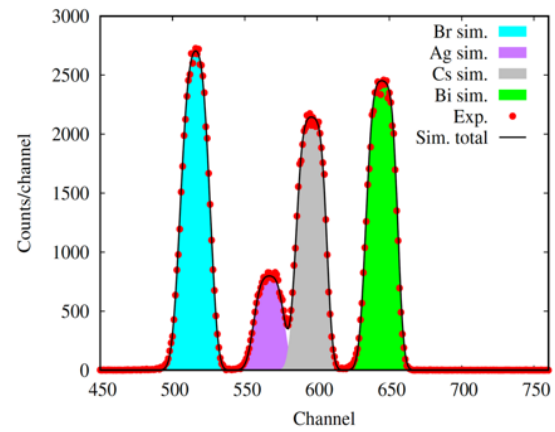


Figure 5.2 Rutherford Backscattering Spectrometry measurements for $Cs_2Ag(Sb_xBi_{1-x})Br_6$ films deposited on silicon substrates, along with the fits used to determine the composition. The “X% Sb/Bi on Si substrate” are the nominal values of the precursor solution used to deposit the films. Data taken and analysed by Mari Napari, Mikko Laitinen and Jaakko Julin.

5.3 Crystal structure and phase purity

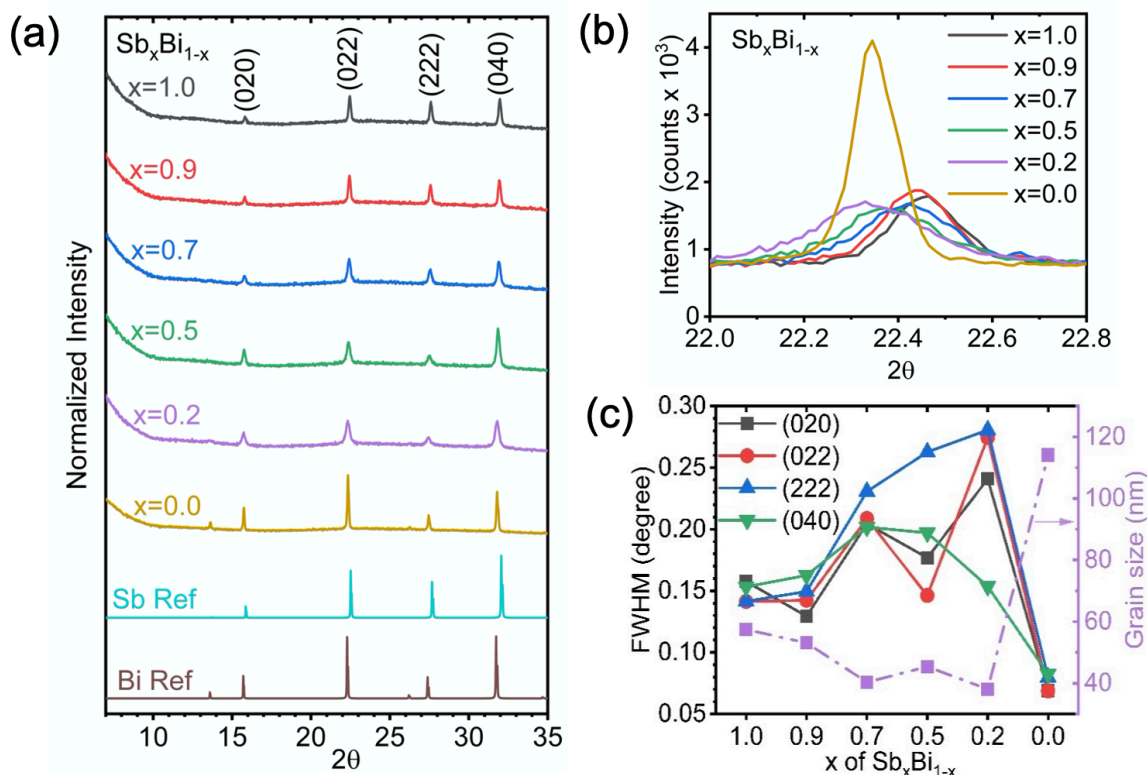


Figure 5.3 (a) XRD pattern of the $Cs_2Ag(Sb_xBi_{1-x})Br_6$ films over the composition series. The reference patterns of $Cs_2AgSbBr_6$ and $Cs_2AgBiBr_6$ calculated from their crystallographic information files are denoted as *Sb Ref* and *Bi Ref* respectively.^{12,15} (b) Full width half maximum (FWHM) of the (022) peak for different compositions. (c) FWHM of different diffraction peaks and the average grain size calculated using the Scherrer equation for different compositions. Data taken and analysed by myself.

I characterized the phase-purity of the films through XRD measurements (Figure 5.3a). $Cs_2AgSbBr_6$ and $Cs_2AgBiBr_6$ have the same cubic structure and space group ($Fm\bar{3}m$). The lattice constants were found to be 11.2 Å for $Cs_2AgSbBr_6$ and 11.3 Å for $Cs_2AgBiBr_6$, with a continuous variation between these extremes through the alloying range, as could be seen from the continuous shift in peak positions (Figure 5.3b and Figure 5.6d). In the process of synthesizing $Cs_2AgSbBr_6$ and $Cs_2AgBiBr_6$, we can often see phase impurities of $Cs_3Bi_2Br_9$ and $Cs_3Sb_2Br_9$. Both impurities have almost the same diffraction patterns with their double perovskite counterparts, but one of the main differences is a peak from $Cs_3Bi_2Br_9$ at 8.95°, or from $Cs_3Sb_2Br_9$ at 9.10°.¹⁶⁹ Neither impurity peaks were found to be present here. However, these XRD measurements were taken with a 1D linescan, and it is possible that the impurity

peaks were hidden due to preferred orientation. Therefore, XRD measurements with a 2D detector were performed to check if there are any hidden peaks (Figure 5.4). I synthesized the double perovskite thin films over the whole alloying range and intentionally induced a $\text{Cs}_3(\text{Bi,Sb})_2\text{Br}_9$ phase impurity to the films with 50% Sb. From the 2D XRD patterns, we can see that the diffraction peak should be detectable by the 1D linescan if it is present because it is in the plane of a 1D linescan. Therefore, the absence of phase-impurities in the 1D XRD patterns in Figure 5.3a shows the films to be phase-pure.

It is noticed that although the diffraction patterns showed no peak splitting, the full width at half maximum (FWHM) of the pure Sb-based double perovskite and mixed alloys were larger than the Bi-based double perovskite (Figure 5.3b&c). This could either be due to smaller grains or small amounts of phase segregation that could not be resolved. Scanning Electron Microscopy (SEM) measurements of the films showed that the Sb-based double perovskites and mixed alloys have smaller and less well-defined grains than the pure Bi-based double perovskite (Figure 5.5), consistent with the larger FWHM in the diffraction patterns of Sb containing films. These XRD and SEM measurements, together with the RBS measurements matching the stoichiometry of the precursor solutions, indicate that the alloys are homogeneous.

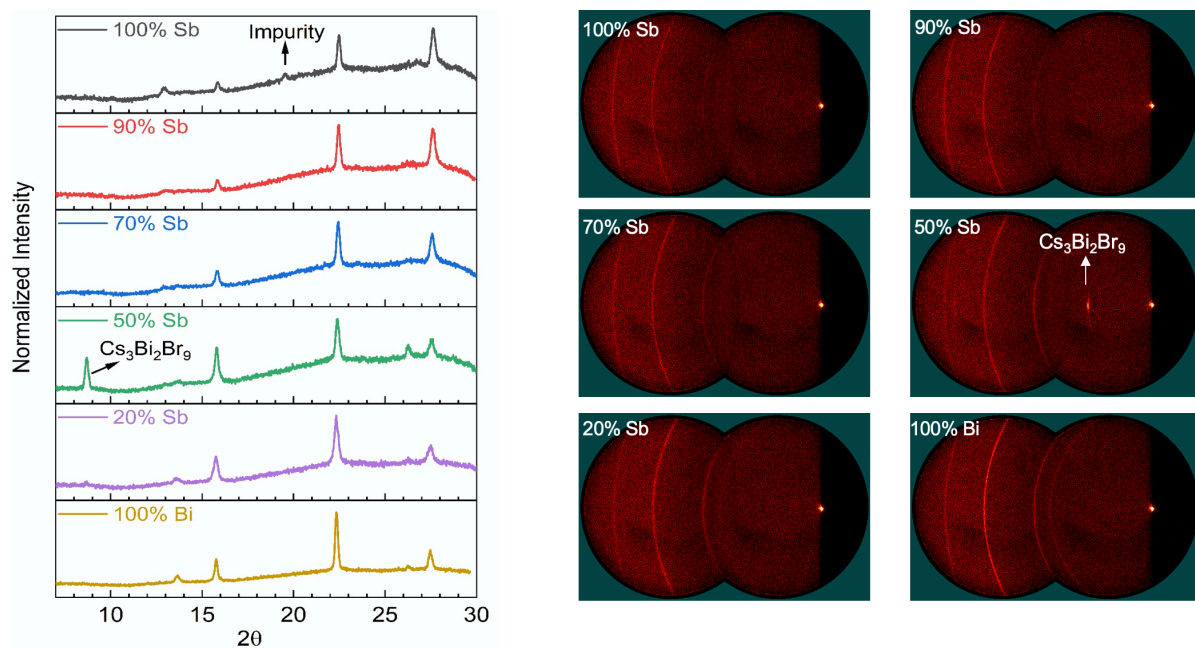


Figure 5.4 2D XRD of $\text{Cs}_2\text{Ag}(\text{Sb}_x\text{Bi}_{1-x})\text{Br}_6$ thin films, characterized on glass. The 8.9° peak of $\text{Cs}_3\text{Bi}_2\text{Br}_9$ at the 2D scan matches well with the peak in 1D linescan. Data taken by Robert G. Palgrave and analysed by myself.

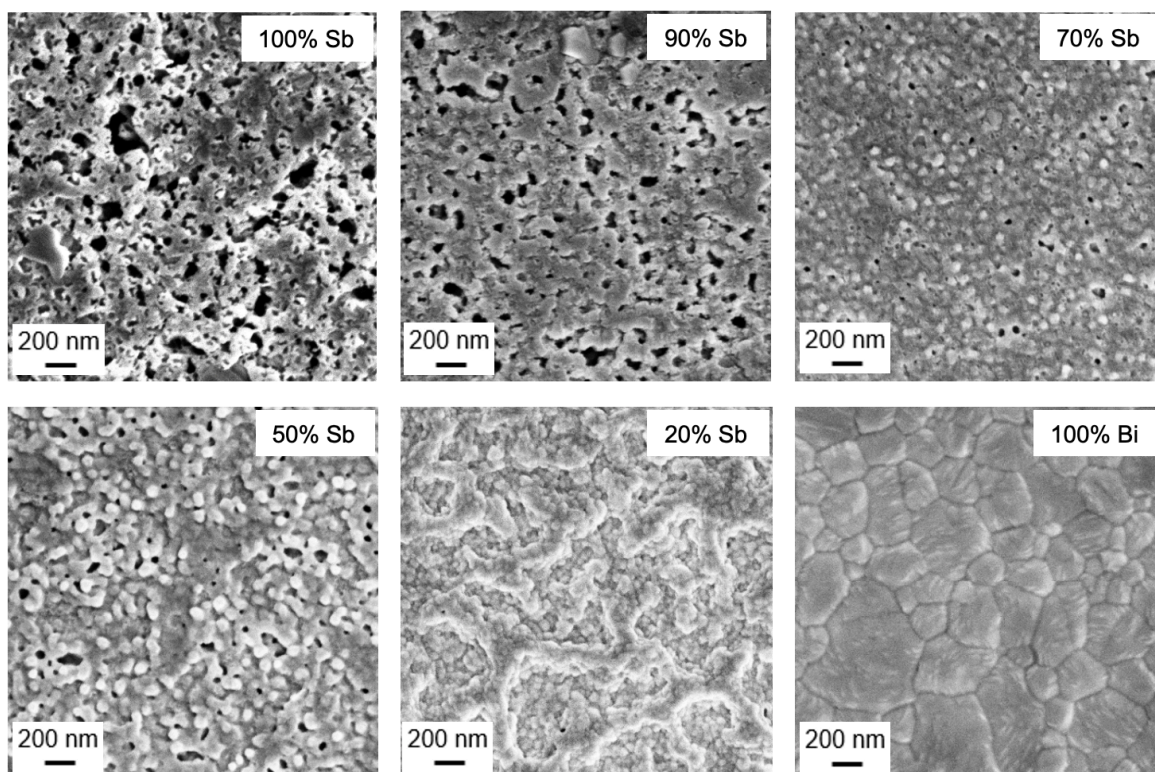


Figure 5.5 SEM of $Cs_2Ag(Sb_xBi_{1-x})Br_6$ thin films, characterized on glass. Only the $Cs_2AgBiBr_6$ exhibits a large grain size and good morphology. Data taken and analysed by myself.

5.4 Absorption, bandgap and band positions

Standard optical transmittance and reflectance measurements (using a UV-visible spectrophotometer with an integrating sphere) were used to determine the absorption coefficient of the double perovskite thin films (Figure 5.6a). All films showed a slow increase in the absorption coefficient for photon energies >2 eV, before rising sharply to $>10^5$ cm^{-1} at >2.6 eV. An absorption coefficient exceeding 10^5 cm^{-1} at >2.6 eV is characteristic of a direct band-to-band transition. Both $Cs_2AgBiBr_6$ and $Cs_2AgSbBr_6$ have indirect bandgaps due to the effects of the Ag d orbitals at the band-edges, and their alloys are also expected to have indirect bandgaps.⁶¹ Therefore, to determine the indirect bandgap, I investigated the absorption onset in the lower photon energy range (*i.e.*, between 2–2.6 eV), leaving the discussion of the absorption in the higher photon energy range to later in this chapter. I observed that the alloys with 70%–90% Sb showed a lower-energy absorption onset than the pure Sb- and Bi-based films. However, the indirect bandgaps resulted in the absorption coefficients being small close to the band-edge, making it difficult to accurately determine the bandgap from standard transmittance and reflectance measurements. Therefore, we performed PDS measurements,

which are sensitive to the absorbance 3–4 orders below the band-edge (operating details in the Experimental Chapter).

The feature of high sensitivity to low absorbance in PDS measurement makes its signal saturates for high absorbance at >2.6 eV (Figure 5.6b), and the peaks in the absorption coefficient seen in Figure 5.6a are not observed in the PDS measurements plotted on a semi-logarithmic scale. The normalized absorbance from PDS measurements at the band edge (in the range of 2–2.3 eV) is approximately 3 orders of magnitude lower than the absorbance at 2.6 eV, where the absorption coefficient is $>10^5$ cm^{-1} (Figure 5.6a). Thus, the absorption coefficient at the band edge should be on the order of 10^2 cm^{-1} . Silicon, which is a typical indirect bandgap material, has an absorption coefficient of 10^2 cm^{-1} at the band edge.^{170,171}

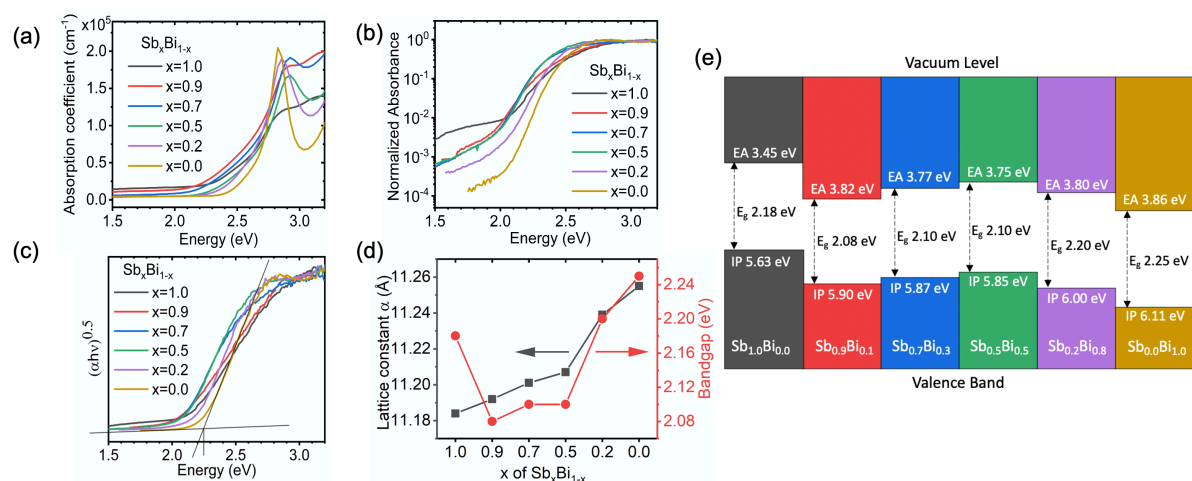


Figure 5.6 Measurements of the bandgap of $\text{Cs}_2\text{Ag}(\text{Sb}_x\text{Bi}_{1-x})\text{Br}_6$ films. (a) Absorption coefficient determined from transmittance and reflectance measurements of films deposited on glass substrates. (b) Normalized absorbance measured by PDS for films deposited on quartz substrates. (c) Tauc plot from PDS measurements. (d) Bandgap and lattice parameter of double perovskite films plotted against the Sb content in the precursor solution. The lattice parameter was acquired by fitting the XRD measurements (Figure 5.3a). The bandgap was obtained from the Tauc plot constructed from the PDS data in part c. (e) Band positions of $\text{Cs}_2\text{Ag}(\text{Sb}_x\text{Bi}_{1-x})\text{Br}_6$ compounds measured by ultraviolet and X-ray photoemission spectroscopy. Data in Figure 5.6(a)(d) taken by myself; data in Figure 5.6(b)(c) taken by Mojtaba Abdi-Jalebi and Zahra Andaji-Garmaroudi; data in Figure 5.6(e) taken by Mark A. Isaacs; all analysed by myself.

From Figure 5.6b we can see the double perovskites with x ranging from 0 to 0.7 have similar slopes in their absorption onsets when plotted on a semi-logarithmic scale. For $x = 0.9$ and the pure Sb-based compound, the slopes are shallower. Increasing the fraction of Sb (x) from 0

(pure Bi) to 0.5 reveals a red-shift in the absorption onset. The double perovskites with $x = 0.7$ and $x = 0.9$ all have similar absorption onsets to the material with $x = 0.5$. These mixed alloys with $x = 0.5$ – 0.9 all have absorption onsets that are red-shifted to the pure Sb-based compound, as well as the pure Bi-based compound. Therefore, alloys with 50–90% Sb demonstrate smaller bandgaps than either of the pure end double perovskites.

To extract numerical values of the bandgap and quantify their variation with composition, I fitted the PDS absorbance data using a Tauc plot, which is a plot of $(\alpha h\nu)^{1/n}$ against $h\nu$. The rationale can be seen from Equation 5.1

$$(\alpha h\nu)^{\frac{1}{n}} = A(h\nu - E_g) \quad (5.1)$$

where α is the absorption coefficient, h is Planck's constant, ν is the photon frequency, A is a proportionality constant, E_g is the bandgap, and $n = 2$ for an indirect bandgap.^{170,171} Therefore, by plotting $(\alpha h\nu)^{0.5}$ against $(h\nu)$, the bandgap can be extracted from the intercept between the tangents fit to the absorption onset and background (Figure 5.6c). It should be noted that the bandgap is obtained from the intersection of the tangents fit to the absorption onset and background, rather than the intersection of the absorption onset and x axis. This is because many semiconductors, including $\text{Cs}_2\text{AgSbBr}_6$ investigated here, have sub-bandgap states which will lead to a slight rise in the absorption signal before their absorption onset. For these materials, taking the intersection between the tangent to the absorption onset and x axis will underestimate the true optical bandgap. In addition, what is important is the trend in bandgaps, and we used the same fitting procedure to guarantee a consistent series of bandgap values that we can compare between each other. From these Tauc plots, the system exhibits significant bandgap bowing (Figure 5.6d). The compound with $x = 0.9$ demonstrated the lowest bandgap of 2.08 eV, smaller than the bandgap of $\text{Cs}_2\text{AgSbBr}_6$ (2.18 eV) and $\text{Cs}_2\text{AgBiBr}_6$ (2.25 eV). It is noticed that bandgaps extracted from a Tauc plot can be affected by the absorbance at the band-edge and the steepness of the absorption onset. $\text{Cs}_2\text{AgBiBr}_6$ (and $\text{Cs}_2\text{AgSbBr}_6$) thin films have very low absorbance at the band-edge due to the indirect bandgap and the low quantity of material (film thickness about 200 nm). Therefore, their bandgaps extracted from Tauc plots have tended to be higher than the bandgaps extracted in single crystals or powders, which have a significantly larger quantity of material to absorb at the band-edge.^{59,67,79,124,166} In addition, it is possible that the lower bandgap value extracted for the mixed alloy with $x = 0.9$ than for materials with $x = 0.5$ and $x = 0.7$ (both 2.10 eV) were due to errors in the fitting process, which may have arisen in part from the lower slope in the absorption onset of the material with $x =$

0.9. Nevertheless, we emphasize that from the Tauc plots, the compounds with $x = 0.5$ – 0.9 all have smaller bandgaps than the pure Bi- and Sb-based compounds, and that this comparison is valid because all materials are thin films with similar thickness. The trend in bandgap values is consistent with our analysis of the PDS absorbance measurements in Figure 5.6b. This is also consistent with the bandgap trend we extracted from the Tauc plots (Figure 5.7) based on the absorption coefficient measurements (Figure 5.6a). In addition, the bandgap lowering was smooth, with no switch in the bandgap from indirect to direct. This bandgap lowering behaviour is similar to the Pb-Sn perovskite system and has not been previously observed in Sb-Bi double perovskites. The maximum reduction in bandgap (170 meV) compared to $\text{Cs}_2\text{AgBiBr}_6$ is larger than if the alloy system had obeyed Vegard’s law and was constrained by the bandgap of $\text{Cs}_2\text{AgSbBr}_6$ (70 meV).

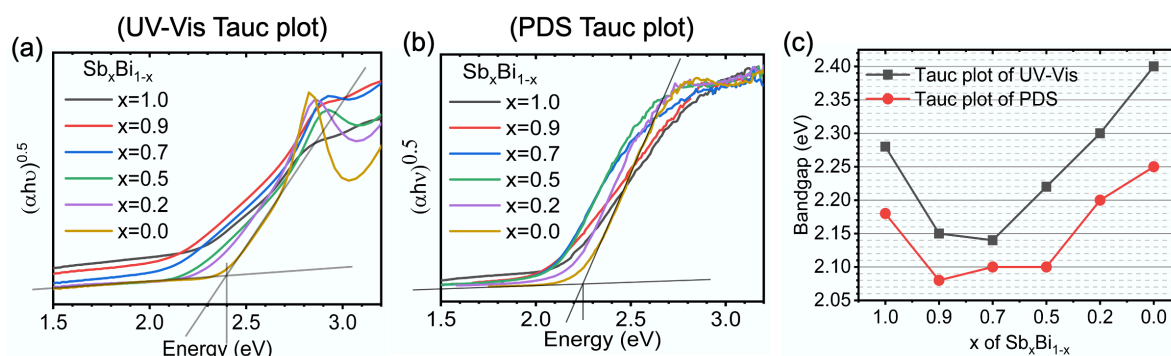


Figure 5.7 (a) Tauc plot of $\text{Cs}_2\text{Ag}(\text{Sb}_x\text{Bi}_{1-x})\text{Br}_6$ thin films on glass based on the absorption coefficient measured by UV-visible spectrophotometry. (b) Tauc plot from PDS measurements of $\text{Cs}_2\text{Ag}(\text{Sb}_x\text{Bi}_{1-x})\text{Br}_6$ thin films on quartz. (c) Bandgaps extract from the Tauc plots in a and b. Only fitting of $\text{Cs}_2\text{AgBiBr}_6$ is given as examples in (a) and (b). The thickness of the $\text{Cs}_2\text{Ag}(\text{Sb}_x\text{Bi}_{1-x})\text{Br}_6$ films were approximately 200 nm in all cases. Data taken and analysed by myself.

In addition, we measured the band positions of $\text{Cs}_2\text{Ag}(\text{Sb}_x\text{Bi}_{1-x})\text{Br}_6$ over the full composition range through photoemission spectroscopy (PES; Figure 5.6e and Table 5.2). The work function was determined by linear fitting of the secondary-electron cut-off of the ultraviolet photoemission spectra (UPS). The valence band to Fermi level offset ($E_F - \text{VB}$) was determined by fitting the leading-edge of the X-ray photoemission spectroscopy (XPS) data. These were fit by the least-squares method to the leading edge of calculated XPS plots to determine the $E_F - \text{VB}$ value. The ionization potential was determined from the work function and $E_F - \text{VB}$ measurements. The electron affinity was calculated by subtracting the bandgap measured by

PDS from the ionization potential. The fitted spectra are given in Figures 5.8-5.14. These measurements showed that when alloying Bi into $\text{Cs}_2\text{AgSbBr}_6$, the electron affinity increased from 3.45 eV to ~ 3.8 eV and remained at approximately this value for the mixed alloys, which is similar to the electron affinity of $\text{Cs}_2\text{AgBiBr}_6$ (3.86 eV). The ionization potential also increased when adding Bi to $\text{Cs}_2\text{AgSbBr}_6$, but to a lesser extent than the change in the electron affinity, hence the reduction in the bandgap. The ionization potential remained at approximately 5.9 eV for $x = 0.9$ down to $x = 0.5$, before increasing to 6.11 eV for $x = 0$ (Figure 5.6e). The larger variation of electron affinity when alloying Bi into $\text{Cs}_2\text{AgSbBr}_6$ may partly arise from the stronger spin-orbit coupling introduced by the heavier element-Bi. Overall, the band positions of the $\text{Cs}_2\text{Ag}(\text{Sb}_x\text{Bi}_{1-x})\text{Br}_6$ alloys are compatible with the common charge transport layers for photovoltaic devices.¹⁷² But like most other Bi-based compounds,¹⁷³ $\text{Cs}_2\text{Ag}(\text{Sb}_x\text{Bi}_{1-x})\text{Br}_6$ has high ionization potentials. Achieving high open-circuit voltages will therefore require the development of hole transport layers with high work functions.

Table 5.2 Band positions of the $\text{Cs}_2\text{Ag}(\text{Sb}_x\text{Bi}_{1-x})\text{Br}_6$ films determined from the photoemission spectroscopy and photothermal deflection spectroscopy measurements. Data taken by Mark A. Isaacs and analysed by myself.

Nominal Sb/(Sb+Bi) in precursor solution	Workfunction (eV)	$E_F - \text{VB}$ (eV)	Bandgap (eV)	Ionization potential (eV)	Electron affinity (eV)
100%	4.82	0.81	2.18	5.63	3.45
90%	5.09	0.81	2.08	5.90	3.82
70%	5.05	0.82	2.10	5.87	3.77
50%	5.04	0.81	2.10	5.85	3.75
20%	4.89	1.11	2.20	6.00	3.80
0%	4.90	1.21	2.25	6.11	3.86

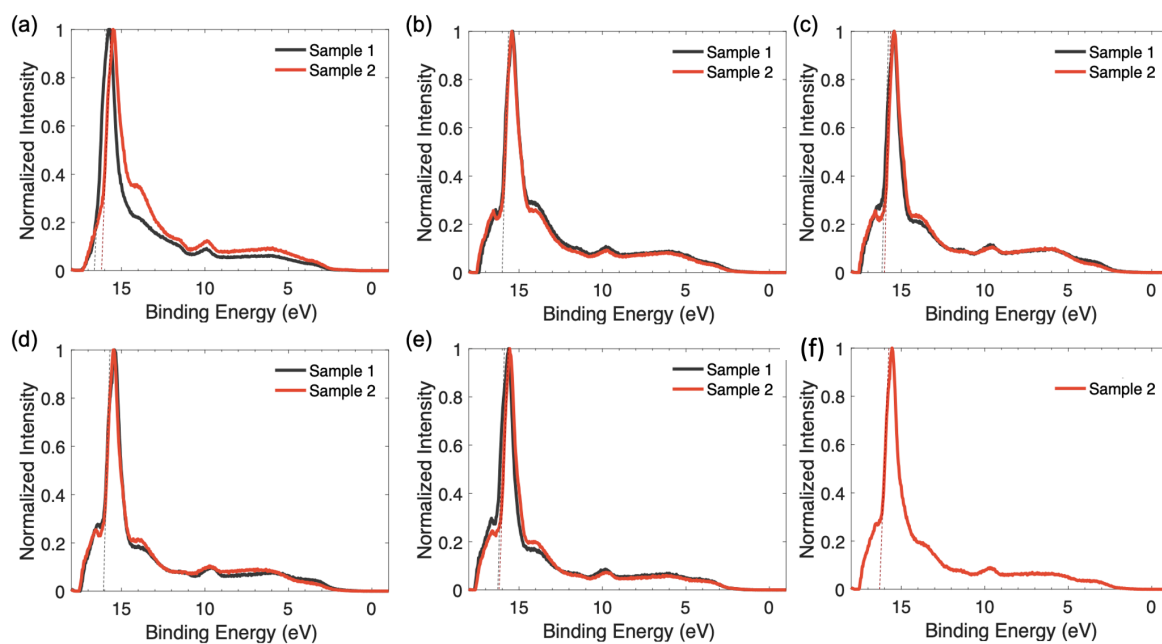


Figure 5.8 Ultraviolet photoemission spectroscopy measurements of (a) $\text{Cs}_2\text{AgSbBr}_6$, (b) $\text{Cs}_2\text{AgSb}_{0.9}\text{Bi}_{0.1}\text{Br}_6$, (c) $\text{Cs}_2\text{AgSb}_{0.7}\text{Bi}_{0.3}\text{Br}_6$, (d) $\text{Cs}_2\text{AgSb}_{0.5}\text{Bi}_{0.5}\text{Br}_6$, (e) $\text{Cs}_2\text{AgSb}_{0.2}\text{Bi}_{0.8}\text{Br}_6$, (f) $\text{Cs}_2\text{AgBiBr}_6$ thin films deposited on ITO/glass substrates. Data taken by Mark A. Isaacs and analysed by myself.

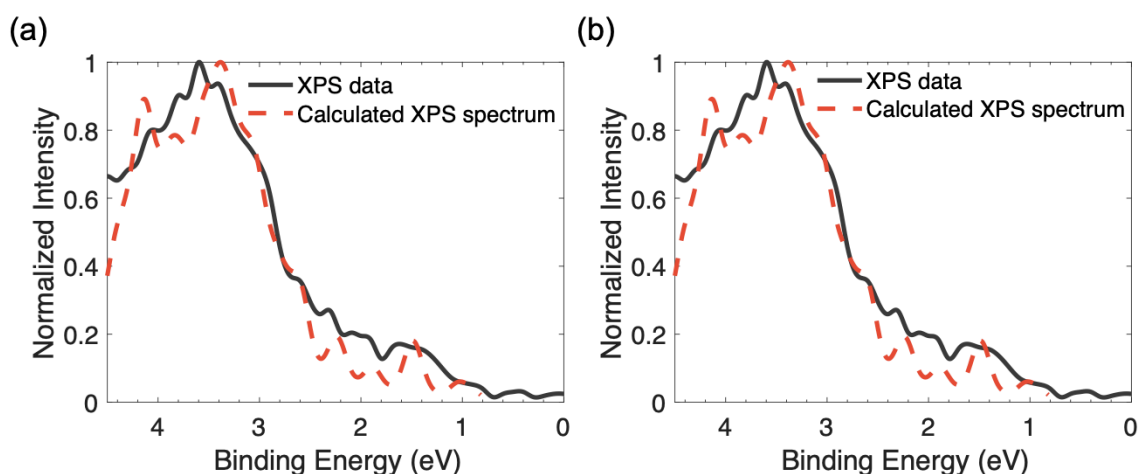


Figure 5.9 XPS measurements of samples (a) 1 and (b) 2 of $\text{Cs}_2\text{AgSbBr}_6$ thin film deposited on ITO/glass. The $E_F - V_B$ value that gave the best fit of the calculated XPS spectrum to the measured data was 0.81 eV. The calculated XPS spectrum was for $\text{Cs}_2\text{AgSbBr}_6$. Data taken by Mark A. Isaacs and analysed by myself.

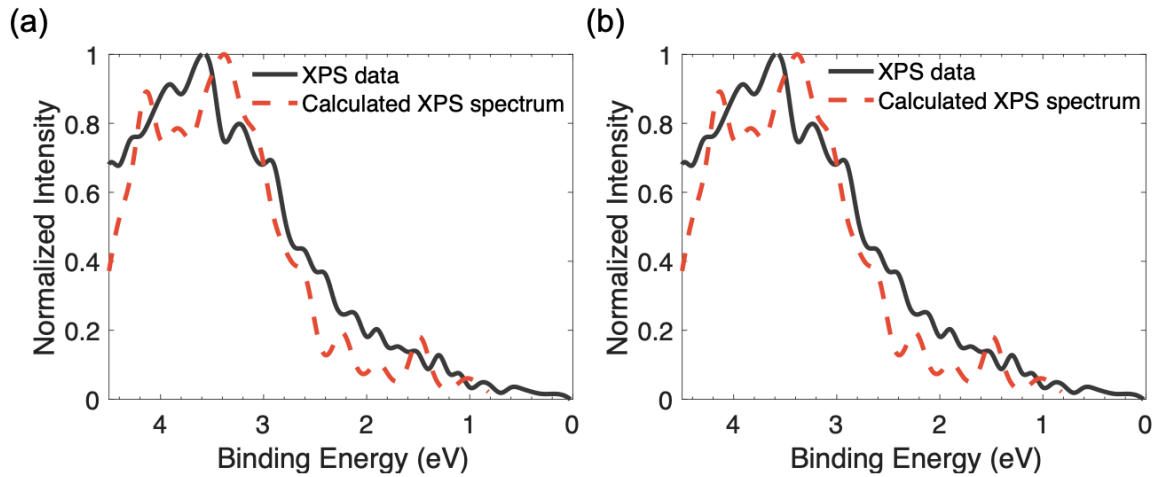


Figure 5.10 XPS measurements of samples (a) 1 and (b) 2 of $\text{Cs}_2\text{AgSb}_{0.9}\text{Bi}_{0.1}\text{Br}_6$ thin film deposited on ITO/glass. The $E_F - V_B$ value that gave the best fit of the calculated XPS spectrum to the measured data was 0.81 eV. The calculated XPS spectrum was for $\text{Cs}_2\text{AgSbBr}_6$. Data taken by Mark A. Isaacs and analysed by myself.

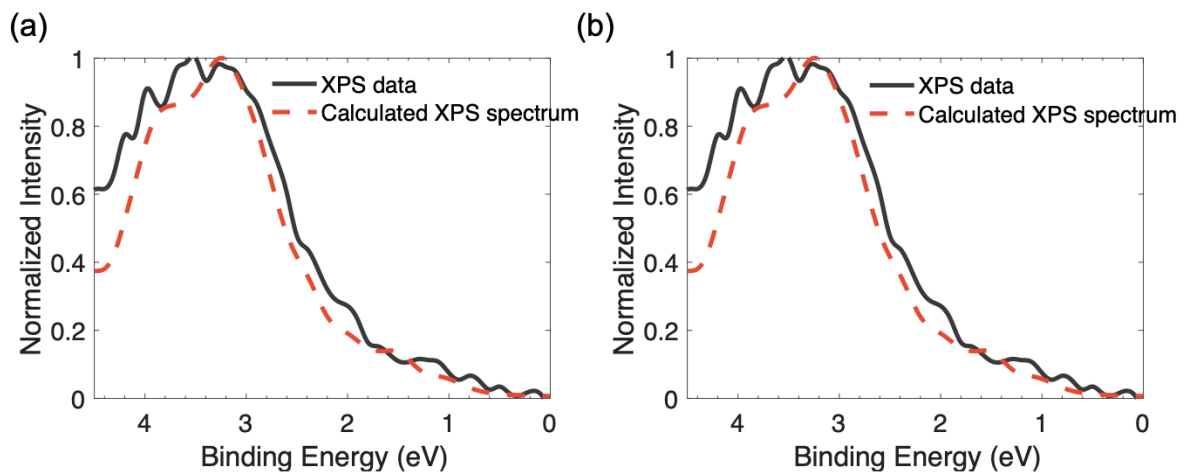


Figure 5.11 XPS measurements of samples (a) 1 and (b) 2 of $\text{Cs}_2\text{AgSb}_{0.7}\text{Bi}_{0.3}\text{Br}_6$ thin film deposited on ITO/glass. The $E_F - V_B$ value that gave the best fit of the calculated XPS spectrum to the measured data was 0.82 eV. The calculated XPS spectrum was for $\text{Cs}_2\text{AgSb}_{0.75}\text{Bi}_{0.25}\text{Br}_6$. Data taken by Mark A. Isaacs and analysed by myself.

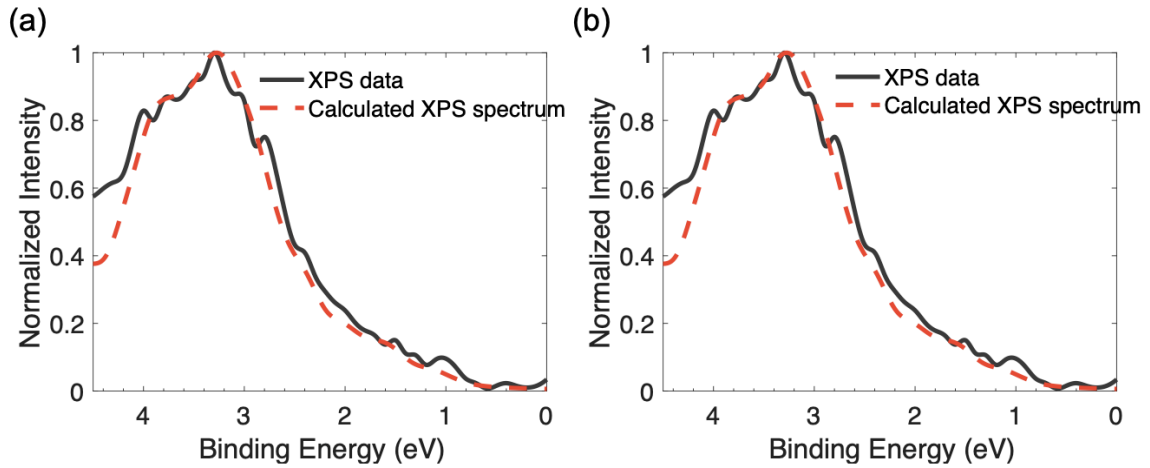


Figure 5.12 XPS measurements of samples (a) 1 and (b) 2 of $\text{Cs}_2\text{AgSb}_{0.50}\text{Bi}_{0.50}\text{Br}_6$ thin film deposited on ITO/glass. The $E_F - V_B$ value that gave the best fit of the calculated XPS spectrum to the measured data was 0.81 eV. The calculated XPS spectrum was for the $\text{Cs}_2\text{AgSb}_{0.50}\text{Bi}_{0.50}\text{Br}_6$ supercell with the diagonally-similar arrangement of octahedra (Figure 5.18). Data taken by Mark A. Isaacs and analysed by myself.

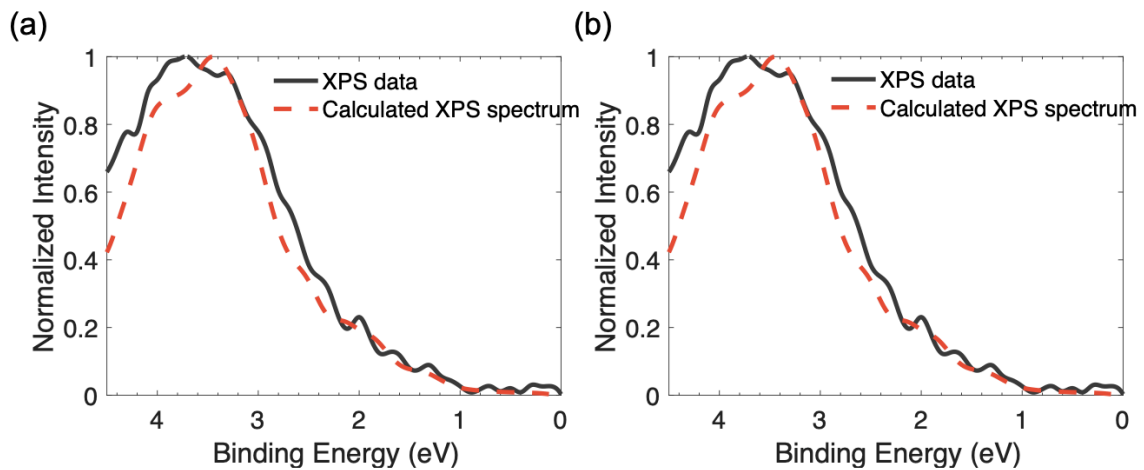


Figure 5.13 XPS measurements of samples (a) 1 and (b) 2 of $\text{Cs}_2\text{AgSb}_{0.2}\text{Bi}_{0.8}\text{Br}_6$ thin film deposited on ITO/glass. The $E_F - V_B$ value that gave the best fit of the calculated XPS spectrum to the measured data was 1.11 eV. The calculated XPS spectrum was for $\text{Cs}_2\text{AgSb}_{0.12}\text{Bi}_{0.88}\text{Br}_6$. Data taken by Mark A. Isaacs and analysed by myself.

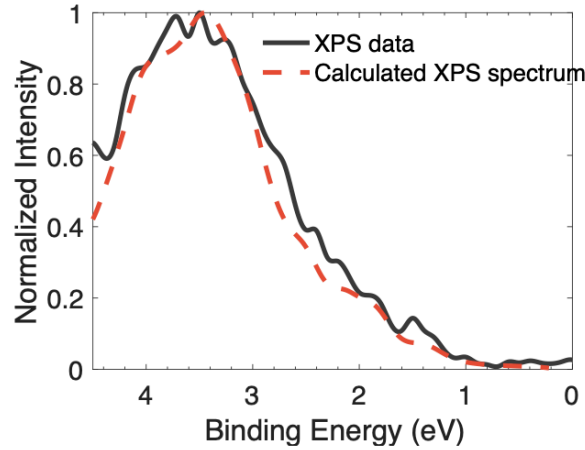


Figure 5.14 XPS measurements of $\text{Cs}_2\text{AgBiBr}_6$ thin film deposited on ITO/glass. The $E_F - V_B$ value that gave the best fit of the calculated XPS spectrum to the measured data was 1.21 eV. The calculated XPS spectrum was for $\text{Cs}_2\text{AgBiBr}_6$. Data taken by Mark A. Isaacs and analysed by myself.

5.5 Electronic structure and bandgap lowering mechanism

To understand the atomistic origin of the bandgap lowering in the Sb-Bi double perovskites, calculations of the electronic structure were performed. The band structure and density of states for pure Sb and Bi double perovskites are shown in Figure 5.15a-d. In agreement with previous literature, as well as our optical measurements in Figure 5.6, both $\text{Cs}_2\text{AgSbBr}_6$ and $\text{Cs}_2\text{AgBiBr}_6$ were found to have an indirect bandgap,^{61,124,167} with the valence band maximum (VBM) located at the **X** point and the conduction band minimum (CBM) at the **L** point in reciprocal space. Using relativistic hybrid density functional theory (HSE06 including spin-orbit coupling), the indirect bandgap and first direct transition of $\text{Cs}_2\text{AgSbBr}_6$ were calculated to be 1.37 and 2.60 eV, respectively. Analysis of the electron band orbital character revealed the conduction band states to be dominated by anti-bonding Sb 5p - Br 4p interactions, while the valence band states dominated by Sb 5s, Ag 4d and Br 4p orbital interactions. The Cs^+ cations act as spectator ions, as noted in literature,¹⁷⁴ with a relatively large nearest-neighbour-ion distance to Br^- .

Likewise, the indirect bandgap and direct transition of $\text{Cs}_2\text{AgBiBr}_6$ were calculated to be 1.77 and 2.49 eV, respectively. Due to the stronger spin-orbit coupling of the Bi 6p orbitals, the direct bandgap of $\text{Cs}_2\text{AgBiBr}_6$ is slightly reduced from that of $\text{Cs}_2\text{AgSbBr}_6$, despite a larger fundamental gap. Similarly, the conduction band states are dominated by anti-bonding

interactions between the trivalent pnictogen cation (Bi 6p) and the halide anion (Br 4p) orbitals, while the valence band states primarily arise from Bi 6s, Ag 4d and Br 4p orbital interactions. Notably, the larger band gap of $\text{Cs}_2\text{AgBiBr}_6$ relative to $\text{Cs}_2\text{AgSbBr}_6$ is an interesting exception to the typical trend of decreasing bandgap upon atomic substitution with heavier members from the same periodic group, which has been observed for other perovskite materials.^{64,175,176}

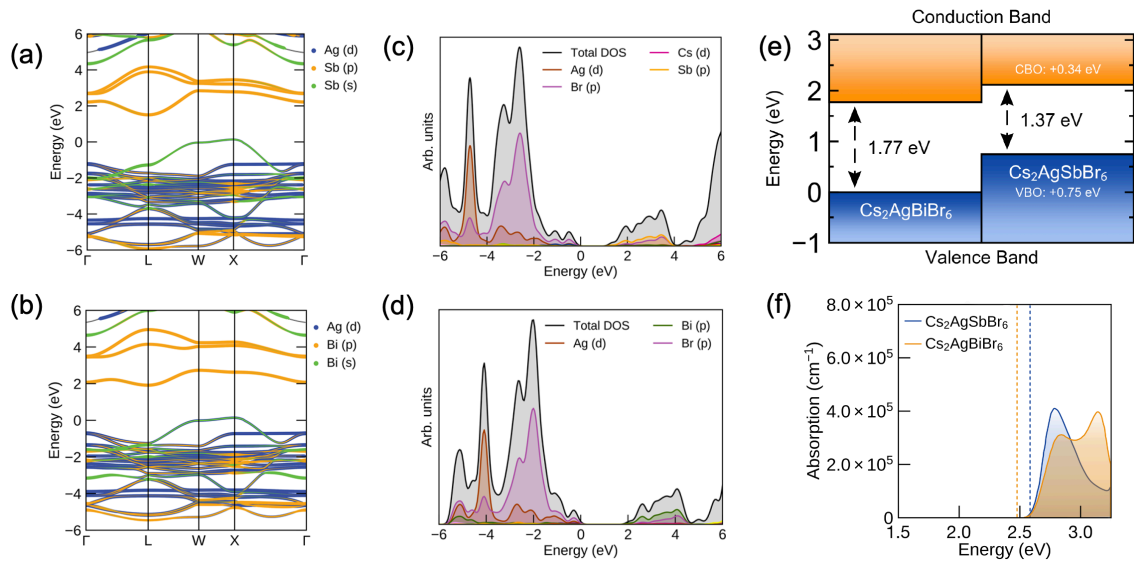


Figure 5.15 (a) Orbital-projected band structure of $\text{Cs}_2\text{AgSbBr}_6$. (b) Orbital-projected band structure of $\text{Cs}_2\text{AgBiBr}_6$. (c) Electronic density of states of $\text{Cs}_2\text{AgSbBr}_6$. (d) Electronic density of states of $\text{Cs}_2\text{AgBiBr}_6$. (e) Electron band alignment of $\text{Cs}_2\text{AgSbBr}_6$ and $\text{Cs}_2\text{AgBiBr}_6$. CBO = Conduction Band Offset, VBO = Valence Band Offset. (f) Calculated optical absorption plots of $\text{Cs}_2\text{AgSbBr}_6$ (blue) and $\text{Cs}_2\text{AgBiBr}_6$ (orange). Dashed vertical lines indicate the positions of optical absorption onset, corresponding to the direct band transitions of 2.60 eV for $\text{Cs}_2\text{AgSbBr}_6$ and 2.49 eV for $\text{Cs}_2\text{AgBiBr}_6$. Note that only vertical transitions are accounted for in this calculation, and the absorption from indirect transitions are not shown. Calculations made by Seán R. Kavanagh.

To delve closer to the origin of bandgap lowering, the ‘natural’ band offset of the two double perovskite materials was calculated following the alignment procedure of Butler *et al.*¹⁷⁷, with the resulting electron band alignment diagram shown in Figure 5.15e. The investigations indicate a Type II ‘staggered gap’ alignment, with a valence band offset (VBO) of 0.75 eV and a conduction band offset (CBO) of 0.34 eV ($\text{Cs}_2\text{AgSbBr}_6$ above $\text{Cs}_2\text{AgBiBr}_6$ in both cases). Typically, the energies of valence electrons become less negative as one moves down a group in the periodic table, corresponding to a decrease in ionization energies. However, for Bi^{3+} and Sb^{3+} , this is not the case, with the Bi^{3+} 6s² lone pair being lower in energy than the Sb^{3+} 5s²

lone pair.¹⁷⁸ This is a result of the relativistic contraction of the Bi 6s orbital, due to its large atomic number, resulting in a more localized, lower-energy valence s orbital, compared to Sb 5s.¹⁷⁹ Consequently, the more-diffuse, higher-energy Sb 5s² lone-pair has a stronger interaction with the Ag 4d and Br 4p orbitals, due to a reduced energy separation of the bonding orbitals (Figure 5.16). This produces both greater dispersion in the valence band and a higher VBM, as shown in Figure 5.15e.

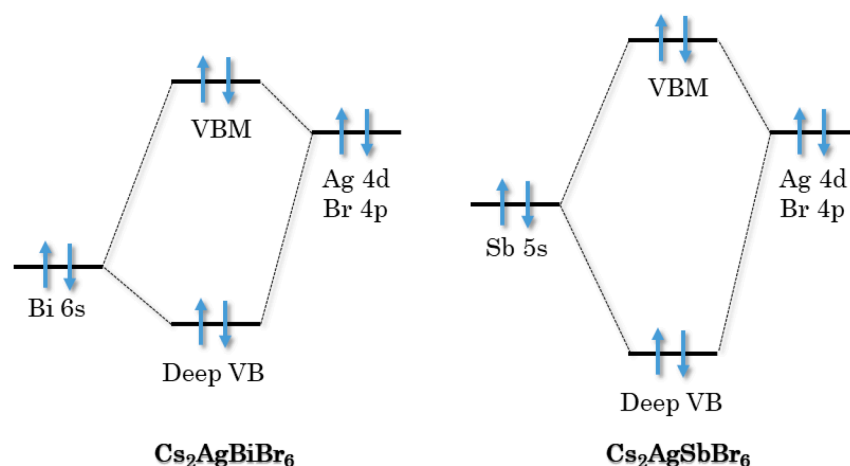


Figure 5.16 Schematic molecular orbital diagram demonstrating the effect of cationic lone-pair interactions on the VBM position. Calculation made by Seán R. Kavanagh.

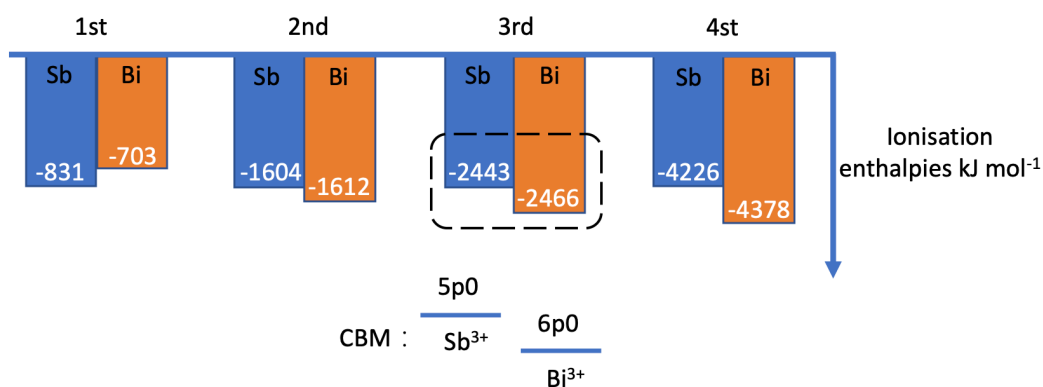


Fig 5.17 Schematic ionisation energy diagram showing that the third ionization energy gives a better estimate for the unoccupied p orbitals.¹⁸⁰

In a similar manner, the elevated position of the CBM in Cs₂AgSbBr₆ can be understood by considering the ionization energies and ionic orbital energies. While the first ionization energy of Sb is indeed larger than that of Bi, the third ionization energy (corresponding to the removal of a p electron from Sb²⁺/Bi²⁺) is in fact 0.3 eV lower for Sb than for Bi,¹⁷⁸ indicating higher energy cationic p states (Figure 5.17). When the pnictogen elements are in the +3 oxidation

state, as is the case in these materials, the third ionization energy provides an improved estimate for the energy of the unoccupied p orbitals. Hence, we argue that, in the +3 formal charge state, the Sb valence p orbitals are in fact higher in energy than those of Bi, suggesting a higher energy CBM for $\text{Cs}_2\text{AgSbBr}_6$, as witnessed in our investigations.

The origins of bandgap bowing in semiconductor alloys are typically due to chemical effects (*e.g.*, differences in electronegativity), local size-mismatch effects or changes in the lattice parameter.^{181–183} For the Pb-Sn perovskite alloy system, Im *et al.* attributed bandgap bowing to the combined effect of spin-orbit coupling and composition-induced phase change.¹²⁰ Snaith and co-workers proposed that the short range ordering of preferred atomic scale clusters allow the bandgap of the mixed alloy to be below that of both pure compounds.¹²¹ In contrast, Stevanović and co-workers found that the strong nonlinearity in bandgap was primarily due to the mismatch in energy between s and p atomic orbitals of Pb and Sn.¹²² The Pb-Sn alloys have a higher VBM dominated by Sn-5s and I-5p orbitals and lower CBM dominated by Pb-6p and I-5p orbitals. They found that spin-orbit coupling, structure changes and short-range ordering did not have a significant effect on bandgap bowing and proposed that a homogeneous structure would have improved stability over a structure with short range ordering.

In the case of $\text{Cs}_2\text{Ag}(\text{Sb}_x\text{Bi}_{1-x})\text{Br}_6$, we propose that the Type II staggered gap alignment between the pure compounds allows for the non-linear mixing of electronic states such that bandgaps lower than that of either pure material are obtained (Figure 5.15e). Upon addition of Bi to the pure Sb double perovskite, the conduction band will be lowered because the CBM wavefunction amplitude is preferentially allocated to the Bi sites, producing a ‘Bi-like’, lower-energy conduction band state. The presence of Bi will also enhance spin-orbit coupling, further reducing the energy of the CBM. On the other hand, the highest energy valence band state will remain ‘Sb-like’, with greater wavefunction amplitude at the Sb sites yielding a VBM only slightly below that of the pure Sb material. This mixing of electronic states in the alloys to produce a low-energy CBM, dominated by Bi-Br interactions, and a high-energy VBM, dominated by Sb-Ag-Br interactions, produces bandgaps in the double perovskite alloys which are lower than that of either pure material. Indeed, this prediction is supported by electronic structure calculations for the alloys (assuming a uniform atomic distribution), which show reduced bandgaps due to the expected orbital mixing at the band edges (Figures 5.18-5.20, Table 5.3). These predictions are further supported by the experimentally-determined band positions of the $\text{Cs}_2\text{Ag}(\text{Sb}_x\text{Bi}_{1-x})\text{Br}_6$ compounds (Figure 5.6e), which show the electron

affinities of the mixed alloys to be close to $\text{Cs}_2\text{AgBiBr}_6$. The ionization potentials of the mixed alloys with $x = 0.5\text{--}0.9$ are in between those of the pure compounds. This accounts for the reduction in their bandgap compared to $\text{Cs}_2\text{AgBiBr}_6$. The reduction in the bandgaps of the $x = 0.5\text{--}0.9$ mixed alloys compared to $\text{Cs}_2\text{AgSbBr}_6$ are due to the increase in ionization potential being smaller than the increase in electron affinity when Bi is added to $\text{Cs}_2\text{AgSbBr}_6$, as discussed earlier.

As the alloy mixing parameter x approaches extreme values ($x \rightarrow 0$ or $x \rightarrow 1$), the ability of the band extrema states to simultaneously adopt Bi and Sb character is diminished, hence the bandgap increases toward the pure double perovskite values. Therefore, we propose that this orbital-mixing behaviour, facilitated by the Type II bandgap alignment, is the origin of the non-linear, non-monotonic variation in bandgap with composition in the Sb-Bi double perovskite system.

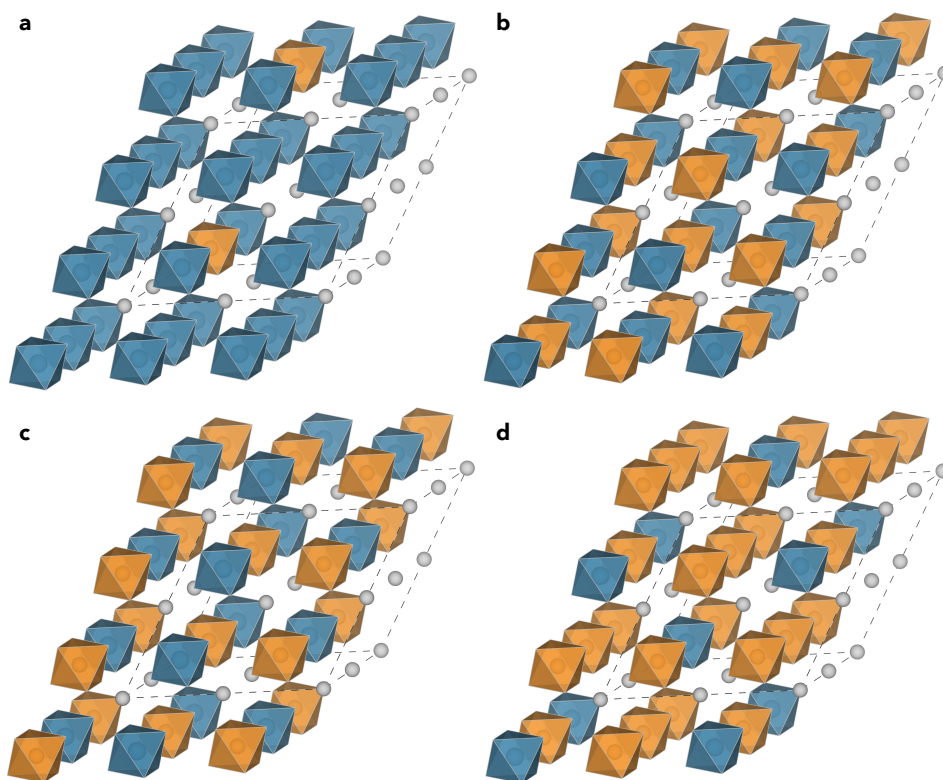


Figure 5.18 Structures used for the investigation of alloy electronic properties, corresponding to (a) $\text{Cs}_2\text{AgSb}_{0.125}\text{Bi}_{0.875}\text{Br}_6$, (b,c) $\text{Cs}_2\text{AgSb}_{0.5}\text{Bi}_{0.5}\text{Br}_6$ (in two possible arrangements) and (d) $\text{Cs}_2\text{AgSb}_{0.75}\text{Bi}_{0.25}\text{Br}_6$. Sb-based octahedra are coloured orange, Bi-based octahedra are coloured blue, and Ag atoms in silver. Br anions located at octahedral corners, and Cs cations omitted for clarity. Calculation made by Seán R. Kavanagh.

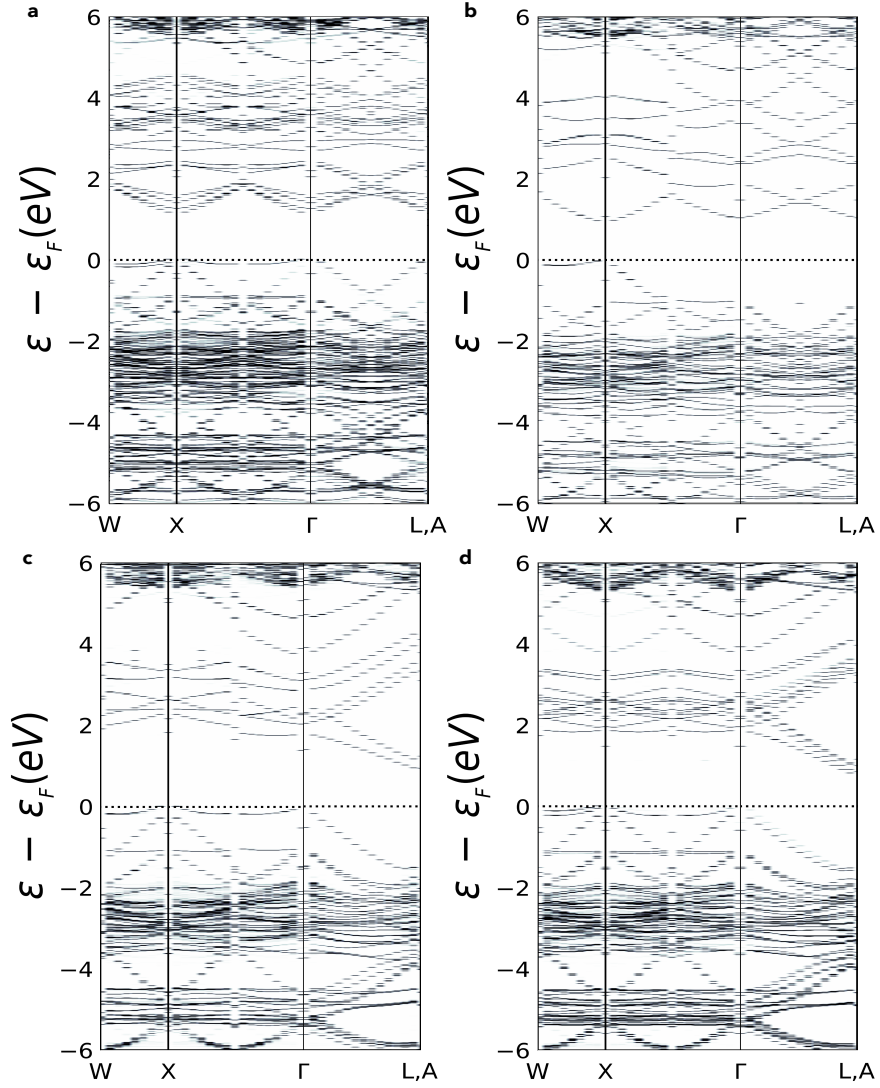


Figure 5.19 Symmetry-weighted unfolded band structures of the simulated alloy materials, for (a) $\text{Cs}_2\text{AgSb}_{0.125}\text{Bi}_{0.875}\text{Br}_6$, (b,c) $\text{Cs}_2\text{AgSb}_{0.5}\text{Bi}_{0.5}\text{Br}_6$ (in the two arrangements shown in Figure 5.18) and (d) $\text{Cs}_2\text{AgSb}_{0.75}\text{Bi}_{0.25}\text{Br}_6$. Fermi level set to match the VBM in each case. Slight discontinuities in the unfolded band structures are due to broken symmetry relations (between the alloy supercells and the original $Fm\bar{3}m$ space group primitive cell) – leading to band splitting and inequivalent directions in reciprocal space, and reduced \mathbf{k} -point sampling density – due to computational limitations. Corresponding electronic density of states and bandgaps provided in Figure 5.20 and Table 5.3 below. Calculation made by Seán R. Kavanagh.

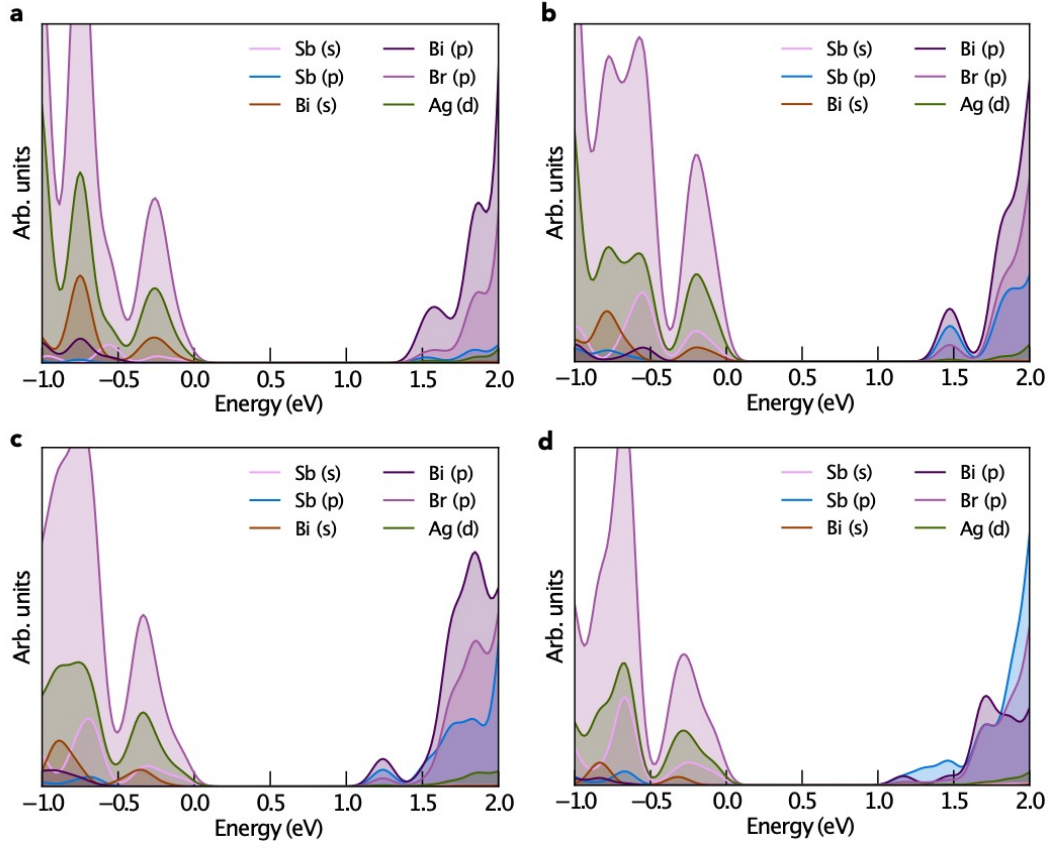


Figure 5.20 Orbital-projected electronic density of states of the simulated alloy materials, for (a) $\text{Cs}_2\text{AgSb}_{0.125}\text{Bi}_{0.875}\text{Br}_6$, (b,c) $\text{Cs}_2\text{AgSb}_{0.5}\text{Bi}_{0.5}\text{Br}_6$ (in the two arrangements shown in Figure 5.18) and (d) $\text{Cs}_2\text{AgSb}_{0.75}\text{Bi}_{0.25}\text{Br}_6$. VBM set to 0 in each case. In each case, the VBM is composed of Ag d, Br p and Sb/Bi s orbital character, while the CBM primarily arises from Sb/Bi p – Br p interactions, in agreement with the prediction that non-linear orbital mixing at the band edges is the source of the experimentally-observed bandgap lowering. Calculation made by Seán R. Kavanagh.

Table 5.3 Calculated bandgaps for both the pure and alloy materials, in units of electronvolts. Calculation made by Seán R. Kavanagh.

x for	0	0.125	0.5 (Figure 5.18b)	0.5 (Figure 5.18c)	0.75	1.0
$\text{Cs}_2\text{AgSb}_x\text{Bi}_{1-x}\text{Br}_6$						
Fundamental Bandgap (eV)	1.77	1.18	0.97	0.94	0.82	1.37

Another possible contribution to bandgap bowing is volume deformation, whereby variation in the lattice constant upon alloying results in non-linear transformation of the electronic structure.¹²² This mechanism, however, more commonly dominates in alloys involving more chemically-distinct materials than is the case here. Moreover, due to the small positive bandgap deformation potentials calculated for the Sb and Bi compounds ($\Delta E_g \sim 0.02$ eV), we rule out this mechanism. Relative to the experimentally observed bowing (~ 0.1 eV, Figure 5.6d), volume distortion alone is not the origin of bandgap bowing in this alloy system.

This bandgap lowering mechanism from the Type II bandgap alignment can be illustrated with Equation 5.2 and the schematics below (Figure 5.21&5.22).

$$E_g = xE_a + (1 - x)E_b - bx(1 - x) \quad (5.2)$$

E_a is the bandgap of material a, E_b is bandgap of material b, E_g is the bandgap of the mixed alloy, x the composition ratio of material a, and b is the bowing parameter. The bandgap of an alloy usually comprises two parts: a linear part and a bowing part. The bowing parameter is usually positive, with the three common reasons discussed above (chemical effect, local size mismatch effects and changes in the lattice parameter). Therefore, the final mixed alloy bandgap bends downwards. As is discussed above, the bowing mechanism in our system is chemical effect, which is the nonlinear mixing of atomic orbitals due to the electronegativity difference. For example, if we have two materials with Type I alignment (Figure 5.21), we can imagine two extreme conditions. In the first condition, when these two materials are quite chemically similar, the energy orbitals of the alloys will mix nearly perfectly. This will lead to the linear variation of the bandgap (the dotted linear line in Figure 5.22) . In the other extreme condition, if these two materials are chemically distinct, the bands do not mix at all. What happens is like the CBM and VBM of material a are inserted into the gap region of material b . Thus, the bandgap will be the same as material a (Figure 5.21). The reality will be a compromise between these two extreme conditions. So, we have a bowing deviation from the linear trend (the shallow curved solid line in Figure 5.22). This situation is for Type I alignment. We can also have type II alignment, which is our case. The linear condition is the same. However, in the other extreme condition, when the two materials are quite chemically different, and the orbitals do not mix. The mixed alloy will have CBM of material b and VBM of material a as its band edge. It will have a bandgap equals to E_{\min} (Figure 5.21). Again, the reality is a compromise. It can be like the deep curved solid line in Figure 5.22. We need to know that this type II alignment can also have the shallow bowing curve, as long as the two materials are

similar. It is just only in type II alignment, the mixed alloy can have a bandgap smaller than either pure material, requiring the bowing parameter larger than the bandgap difference of the two constituent materials. This is exactly our case. In the mixed alloy, the VBM wavefunction preferentially allocate to the Sb site, and the CBM wavefunction preferentially allocate to the Bi site, leading to a smaller bandgap in the mixed alloys.



Figure 5.21 Schematic diagram showing Type I and Type II band alignment.

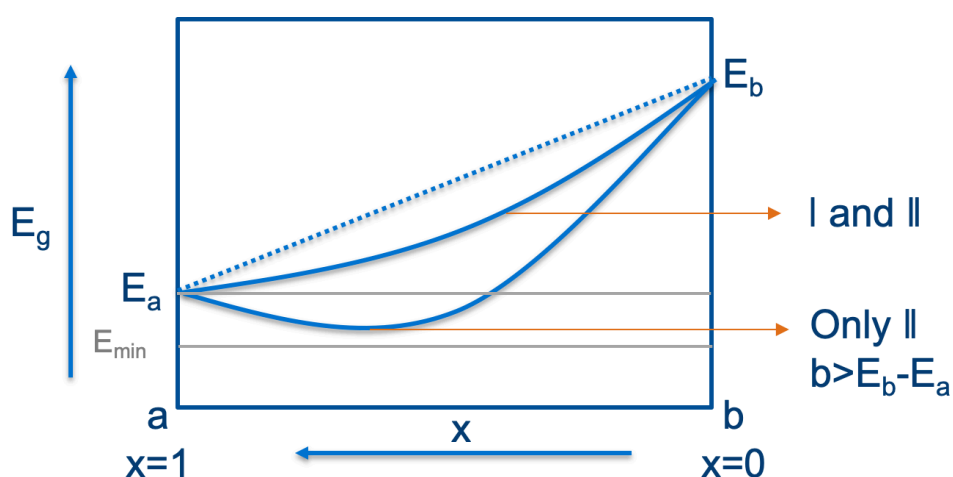


Figure 5.22 Schematic diagram demonstrating possible bandgap variations in mixed semiconductor alloys with Type I and Type II band alignment.

Finally, we return to discuss the sharp peak in the absorption coefficient of the films at >2.6 eV (Figure 5.6a). This is especially evident for $\text{Cs}_2\text{AgBiBr}_6$. Previous work attributed the sharp absorption peak in $\text{Cs}_2\text{AgBiBr}_6$ to an exciton associated with the direct transition.^{78,80,94,141,184} However, there is also the possibility that these features in the pure compounds and mixed alloys are due to a narrow density of states at the band-edges. To explore this possibility, we computed the absorption spectra for $\text{Cs}_2\text{AgSbBr}_6$ and $\text{Cs}_2\text{AgBiBr}_6$ without excitonic effects (Figure 5.15f). These spectra were broadened by convoluting with a Gaussian peak with a FWHM of 0.15 eV. For both materials, the calculated absorption spectra exhibit peaks at 2.8 eV, in agreement with the experimental measurements. These peaks arise from the relatively-

weak dispersion of the electron bands at the CBM and VBM of the materials (Figure 5.15a, b), yielding peaks in both the density of states (Figure 5.15c, d) and thus the optical absorption (Figure 5.15f). This strongly suggests that the peaks observed in the experimental UV-visible measurements are the result of direct transitions between the relatively-flat electron bands. That said, the exciton binding energy of $\text{Cs}_2\text{AgBiBr}_6$ was calculated to be 167 meV within effective mass theory, which is sufficiently large that stable exciton formation is possible in these systems.

Curiously, the computed absorption spectrum for $\text{Cs}_2\text{AgSbBr}_6$ shows a distinct absorption peak (Figure 5.15f), whereas the measured peak from UV-visible spectrophotometry became less distinct with increasing Sb content, until there was barely an observable peak for the pure Sb-based compound (Figure 5.6a). This may have been due a ‘smearing out’ of the absorption peak due to structural disorder.^{185–187} We calculated the absorption spectra for the pure Sb-based compound convoluted with Gaussian peaks with wider FWHM (0.2 eV, 0.3 eV, 0.4 eV; Figure 5.23). These show that the peak becomes indistinguishable when broadening is large, as witnessed experimentally and consistent with the PDS measurements. Thus, peak broadening as a result of disorder leads to the observed ‘smeared-out’ absorption spectrum in Figure 5.6a.

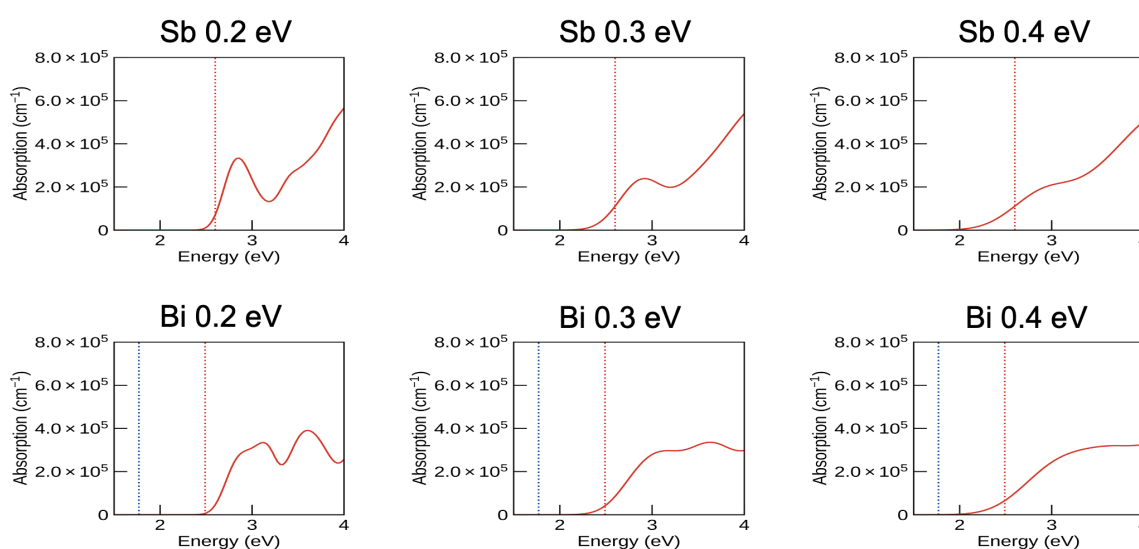


Figure 5.23 Calculated optical absorption with higher Gaussian broadening (indicated in the energy values in the title), resulting in smeared out peaks. Dashed vertical red line indicates the calculated position of the optical gap. Calculation made by Seán R. Kavanagh.

5.6 Conclusions

In conclusion, I successfully synthesized phase-pure $\text{Cs}_2\text{AgSbBr}_6$ thin films, as well as $\text{Cs}_2\text{Ag}(\text{Sb}_x\text{Bi}_{1-x})\text{Br}_6$ with x varying over the full compositional range. In doing so, I found that the mixed double perovskites with x between 0.5 and 0.9 to have the smallest bandgaps, lower than those of the pure compounds. From the electronic band alignment, I found that the origin of bandgap bowing in this double perovskite alloy is due to chemical rather than structural effects. The Type II band alignment between $\text{Cs}_2\text{AgBiBr}_6$ and $\text{Cs}_2\text{AgSbBr}_6$, in combination with non-linear mixing of the electronic states, results in the alloy having smaller bandgaps than either pure material. This work demonstrates a novel route to reduce the bandgap of $\text{Cs}_2\text{AgBiBr}_6$ and $\text{Cs}_2\text{AgSbBr}_6$, which could be generalized to other halide double perovskites. That is, we propose that alloys formed from compounds with a Type II band alignment, and which are alloying chemically-similar elements, could exhibit similar bandgap lowering. This may prove crucial for improving the suitability of halide double perovskites for photovoltaic and photocatalytic applications.

Contributions

This Chapter is based on a published paper: “Li, Z.; Kavanagh, S. R.; Napari, M.; Palgrave, R.; Abdi-Jalebi, M.; Andaji-Garmaroudi, Z.; Davies, D.; Laitinen, M.; Julin, J.; Isaacs, M. A.; Friend, R.; Scanlon, D. O.; Walsh, A.; Hoye, R. L. Z. Bandgap Lowering in Mixed Alloys of $\text{Cs}_2\text{Ag}(\text{Sb}_x\text{Bi}_{1-x})\text{Br}_6$ Double Perovskite Thin Films. *J. Mater. Chem. A* **2020**, *8* (41), 21780–21788. <https://doi.org/10.1039/d0ta07145e>.”⁶⁶ I synthesized the Sb-Bi double perovskite thin films, optimized the morphology, and performed 1D XRD, SEM and UV-Visible Spectrophotometry measurements. Seán R. Kavanagh performed the theoretical calculations and analyzed the results, along with Daniel W. Davies, David O. Scanlon and Aron Walsh. Zewei Li and Seán R. Kavanagh wrote the manuscript. Zewei Li analyzed most of the data (in case of RBS, with the help of Mari Napari). Mari Napari analyzed the RBS results, which were collected by Mikko Laitinen and Jaakko Julin. Robert G. Palgrave measured the 2D XRD data. Mojtaba Abdi-Jalebi and Zahra Andaji-Garmaroudi measured the PDS data. Mark A. Isaacs performed the PES measurements. Richard H. Friend supervised Zewei Li and contributed to the discussion. Robert L. Z. Hoye conceived of the project and supervised the work.

6 Investigating the Limiting Factors for the Performance of $\text{Cs}_2\text{Ag}(\text{Sb}_x\text{Bi}_{1-x})\text{Br}_6$ Double Perovskite Solar Cell

A reduction in the bandgap of $\text{Cs}_2\text{AgBiBr}_6$ was achieved through alloying with Sb in Chapter 5. In this chapter, I investigate the influence of Sb alloying on the photovoltaic performance of halide double perovskite thin films. Despite Sb alloying lowering the bandgap, I find that this leads to a strong decrease in the power conversion efficiency of the photovoltaic devices. Through photothermal deflection spectroscopy and steady-state photoluminescence measurements, I demonstrate that Sb alloying introduces sub-bandgap states, especially a weak luminescent state at 1.55 eV. Transient absorption spectroscopy measurements show that the dual photoinduced absorption peaks on either side of the ground state bleach in the $\text{Cs}_2\text{AgBiBr}_6$ sample gradually disappear as the Sb content is increased. I propose that Sb alloying introduces new defect states in $\text{Cs}_2\text{AgBiBr}_6$, thus deteriorating the performance of the mixed alloy solar cells.

6.1 Introduction

I showed in Chapter 5 that the bandgap of $\text{Cs}_2\text{AgBiBr}_6$ can be reduced by alloying with Sb, and the mixed alloys, $\text{Cs}_2\text{Ag}(\text{Sb}_x\text{Bi}_{1-x})\text{Br}_6$ ($x=0.5-0.9$), have smaller bandgaps than either of the pure compounds. This new class of double perovskite alloys with lower bandgaps are appealing for a wide range of optoelectronic applications, including photocatalysts,^{163,164} indoor photovoltaics (1.9 eV ideal bandgap),^{188,189} and top-cells in tandems (1.7-1.9 eV ideal bandgap).¹⁹⁰ In particular, $\text{Cs}_2\text{Ag}(\text{Sb}_{0.9}\text{Bi}_{0.1})\text{Br}_6$, with a bandgap of 2.08 eV, has a bandgap that is closest to being suitable for top-cells in tandem photovoltaics, or photocathodes for water splitting.

In this chapter, I investigate the performance of double perovskite solar cells with $\text{Cs}_2\text{Ag}(\text{Sb}_x\text{Bi}_{1-x})\text{Br}_6$ as the single absorbing layer. I start with device optimization, mainly through improving the double perovskite thin film morphology. But I found that alloying with Sb lowers the device performance. I then investigated the limiting factors with PDS, steady state photoluminescence and transient absorption measurements. I finish this chapter by discussing the implications and future pathways to overcoming these limitations.

6.2 Morphology optimization and device performance

In this work, I developed an n-i-p structured solar cell with the following architecture: glass/FTO/compact TiO₂/mesoporous TiO₂/double perovskite/PTAA/Au. To realize a solar cell device, the absorber layer must be compact without large pinholes, which would otherwise lead to device shunting. The double perovskite morphology with direct spin coating on FTO/compact TiO₂/mesoporous TiO₂ has many large pinholes (Figure 6.1), and devices made from these morphologies were indeed shunted.

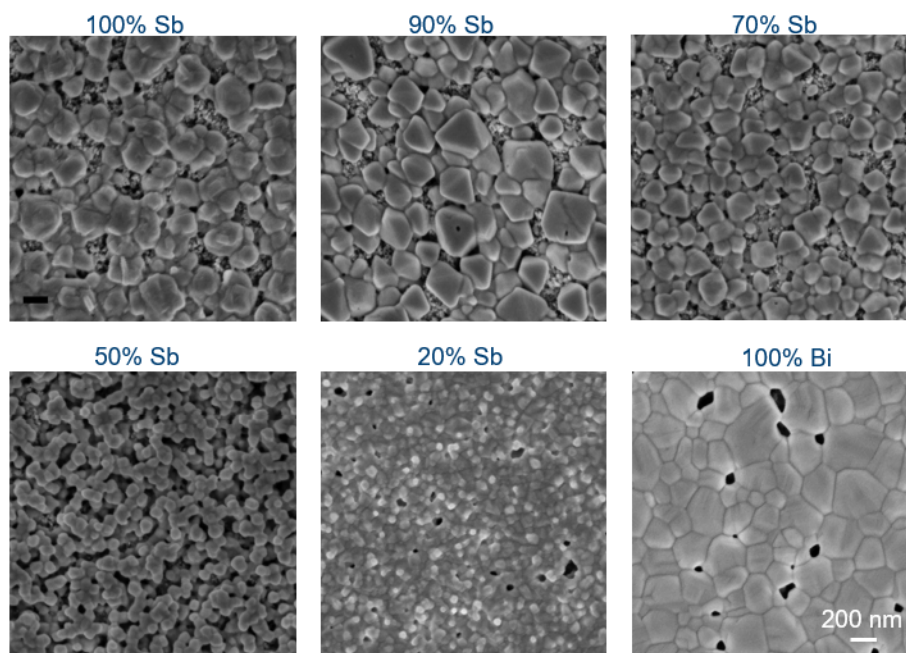


Figure 6.1 Scanning electron micrographs of $Cs_2Ag(Sb_xBi_{1-x})Br_6$ thin films grown from precursor solutions with different compositions on glass/FTO/compact TiO₂/mesoporous TiO₂/double perovskite structure. Magnification in all cases was the same, and the scalebar shown is applicable to all micrographs. Data taken and analysed by myself.

To eliminate the pinholes and optimise film morphology, I investigated the antisolvent method, which involves dropping a certain amount of antisolvent (in which the double perovskite has low solubility) onto the film surface during spin coating in order to induce rapid supersaturation and therefore achieve a high nucleation density.^{191,192} The nuclei form within a narrow time window and grow together. According to the LaMer diagram, this would lead to a more uniform distribution of grain sizes.¹⁴⁰ Therefore, the grain sizes will be more uniform and the morphology more compact. Nevertheless, morphology optimisation with this method involves many variables to tune, including the antisolvent type, and dropping time, amount, height and

speed. Among the different antisolvent options (ethanol, chloroform, chlorobenzene, toluene), I found toluene has the best effect. Pinholes for the double perovskite films containing Sb were eliminated with toluene as antisolvent (Figure 6.2). $\text{Cs}_2\text{Ag}(\text{Sb}_{0.9}\text{Bi}_{0.1})\text{Br}_6$ was chosen among the mixed alloys because it has the lowest bandgap in the alloy series (refer to Chapter 5). $\text{Cs}_2\text{AgSbBr}_6$ and $\text{Cs}_2\text{AgBiBr}_6$ serve as references for comparison. There are still some pinholes in $\text{Cs}_2\text{AgBiBr}_6$ thin films, but even the $\text{Cs}_2\text{AgBiBr}_6$ thin films without antisolvent still work in devices. This may be due to these pinholes being so small that they can be masked by the PTAA deposited on top later.

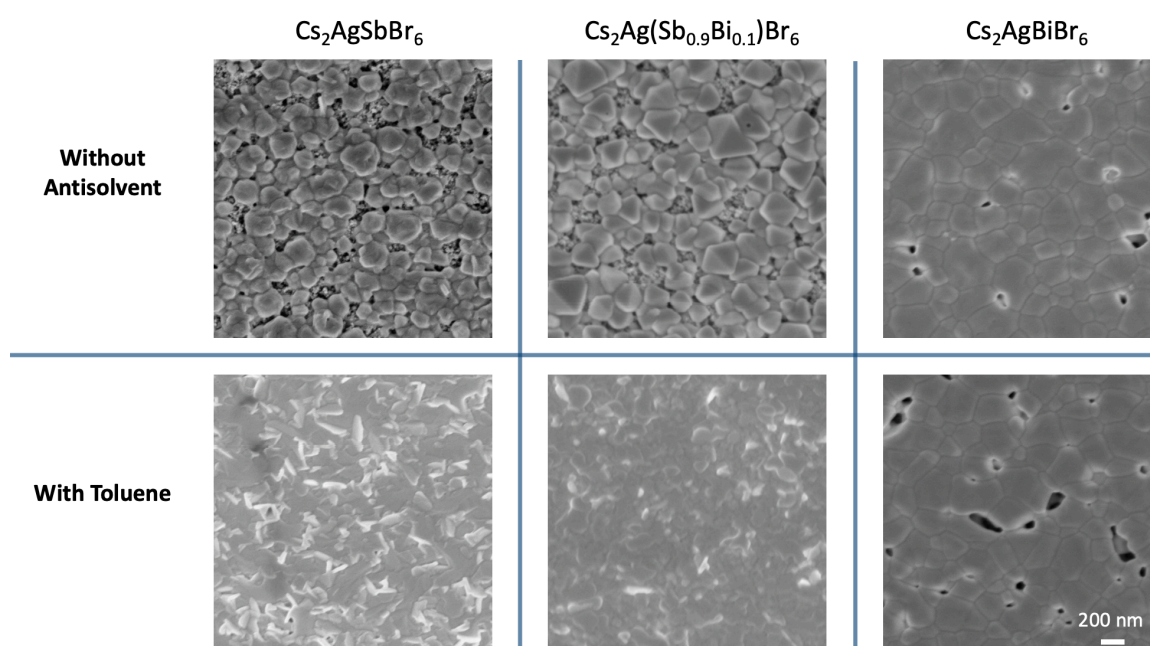


Figure 6.2 Morphology optimization with the antisolvent method. Scanning electron micrographs of $\text{Cs}_2\text{Ag}(\text{Sb}_x\text{Bi}_{1-x})\text{Br}_6$ thin films grown from precursor solutions with different compositions on FTO/compact TiO_2 /mesoporous TiO_2 /double perovskite structure. Magnification in all cases was the same, and the scalebar shown is applicable to all micrographs. Data taken and analysed by myself.

Working solar cell devices were realised on these pinhole-free double perovskite films. The device with $\text{Cs}_2\text{Ag}(\text{Sb}_{0.9}\text{Bi}_{0.1})\text{Br}_6$ as the absorbing layer was expected to have the highest efficiency since it has the lowest bandgap. However, I found that alloying with Sb deteriorates the performance of $\text{Cs}_2\text{AgBiBr}_6$ solar cells (Figure 6.3a). A reduction in the open-circuit voltage (V_{OC}) by 0.7 eV was observed for both pure $\text{Cs}_2\text{AgSbBr}_6$ and $\text{Cs}_2\text{Ag}(\text{Sb}_{0.9}\text{Bi}_{0.1})\text{Br}_6$ solar cells compared to $\text{Cs}_2\text{AgBiBr}_6$ photovoltaics. The short circuit current density (J_{sc}) also decreased as the Sb concentration increased. From the dark J - V curves (Figure 6.3b), solar cells

with Sb display current density (at -0.2 V) approximately 10^2 times higher than the pure Bi device, indicating a higher leakage current. This may be due to the worse morphologies of double perovskite films containing Sb. Consistent with the trends in photovoltaic performance, the EQEs were also lower with Sb alloying (Figure 6.3c). The peak at 2.8 eV for $\text{Cs}_2\text{AgBiBr}_6$ is from either the resonant exciton or a narrow density of states in the conduction band as discussed in Chapter 5. Figure 6.3d shows the EQE curves on a log-linear scale. This confirms that $\text{Cs}_2\text{Ag}(\text{Sb}_{0.9}\text{Bi}_{0.1})\text{Br}_6$ has the lowest bandgap, due to its lowest absorption onset.

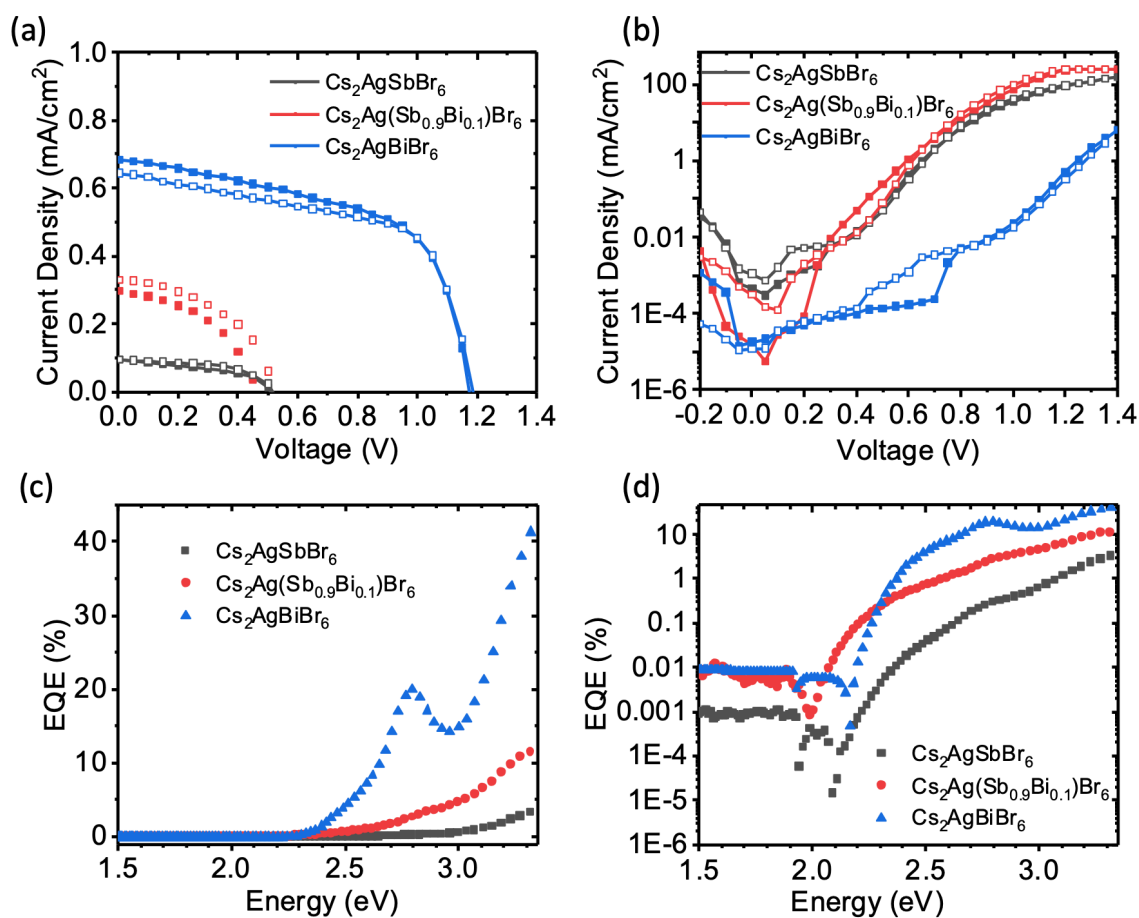


Figure 6.3 Device performance. Typical J - V curves of the double perovskite solar cells under illumination (a) and in dark condition (b). Solid square for forward bias and open square for reversed bias. EQE curves of the devices in linear scale (c) and in log scale (d). Device structure: FTO/compact TiO_2 /mesoporous TiO_2 /double perovskite/PTAA/Au. Data taken and analysed by myself.

6.3 Absorption, photoluminescence and transient absorption

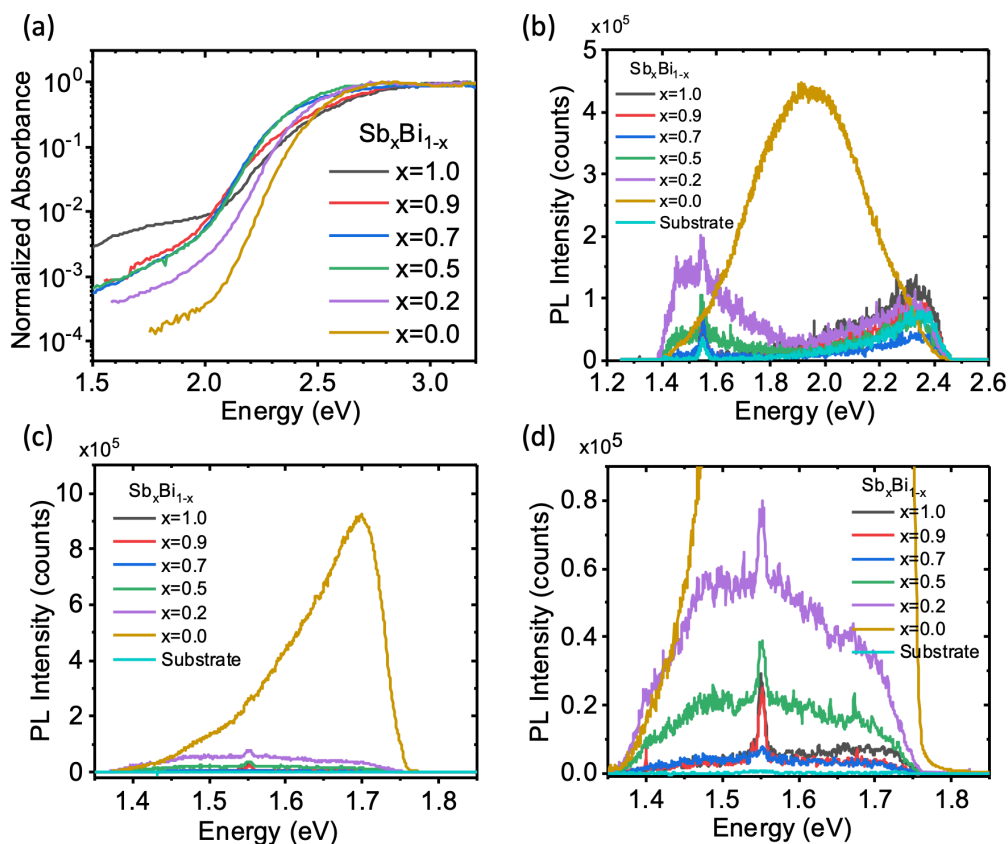


Figure 6.4 (a) Normalized absorbance measured by PDS for $\text{Cs}_2\text{Ag}(\text{Sb}_x\text{Bi}_{1-x})\text{Br}_6$ films deposited on quartz substrates. Data from Chapter 5. Photoluminescence of the $\text{Cs}_2\text{Ag}(\text{Sb}_x\text{Bi}_{1-x})\text{Br}_6$ films deposited on glass substrate. Excitation at 400nm (3.11 eV), 1mw. Detector centred at 1.78 eV (700nm) for (b), and detector centred at 1.38 eV (900 nm) for (c) and (d). (d) Enlargement of (c). Measurements for (b) and (c) were conducted on different set of samples. Data in Figure 6.4 (a) taken by Mojtaba Abdi-Jalebi and Zahra Andaji-Garmaroudi; data in Figure 6.4 (b)-(d) taken by myself; all analysed by myself.

To detect the factors that limit the performance of Sb containing solar cells, double perovskite films were investigated through absorption and luminescence measurements. Figure 6.4a shows the PDS absorption data from last chapter. As the Sb concentration is increased, the absorption below the bandgap also increased, indicating the introduction of sub-bandgap states through Sb alloying. This is further confirmed by the slopes of the absorption onset for $\text{Cs}_2\text{AgSbBr}_6$ and $\text{Cs}_2\text{Ag}(\text{Sb}_{0.9}\text{Bi}_{0.1})\text{Br}_6$ being shallower than the other compositions, and therefore having a larger Urbach energy. For the Sb-substituted double perovskites, the main PL peak intensity is also much lower than that of $\text{Cs}_2\text{AgBiBr}_6$ (Figure 6.4b), and a relatively

weak PL peak emerges at 1.55 eV. The sharp peak at 1.55 eV (800 nm), which is also present on the glass substrates, is from the excitation laser source. After subtracting this sharp peak for the samples, we can still see the broad peak on these Sb-mixed alloys, indicating it is indeed from the double perovskite samples. Interestingly, the intensity is reduced with increasing Sb concentrations and almost vanished for pure $\text{Cs}_2\text{AgSbBr}_6$ double perovskites. It is noted that the asymmetric profile is due to the cut-off from the detector at 1.4 eV. Photoluminescence in Figure 6.4c was conducted on a different set of samples, with the detector centred at lower energy. The whole PL ranges can be seen, which are more symmetric. I attribute this sub-bandgap PL peak to originate from a colour centre, which involves an intermediate band formed within the bandgap with 1.55 eV from either the conduction band or valence band due to the high concentration of sub-bandgap states.⁸⁰ Nevertheless, this weak PL peak at 1.55 eV verifies the introduction of sub-bandgap states by alloying Sb with $\text{Cs}_2\text{AgBiBr}_6$. This sub-bandgap peak was also reported in literature.¹²⁴ For the peak at 2.3 eV, it can be observed on both samples and substrates with similar intensities. Therefore, I propose this high-energy PL peak is not necessarily from the double perovskite film itself, but may originate from extrinsic factors specific to the measurement and is visible in these plots only due to the low PL intensity from the sample.

To understand how charge-carrier lifetime changes with composition, I further performed transient absorption spectroscopy measurements. Pure $\text{Cs}_2\text{AgBiBr}_6$ shows a GSB peak at 2.8 eV surrounded by two PIA peaks (Figure 6.5f), similar to what we observed in Chapter 4. This profile feature was attributed to the broadening of the direct exciton transition introduced by carrier-exciton scattering.^{89,94} It is notice that with higher Sb concentration, the GSB peak intensity increases, while the two adjacent PIA peaks gradually vanish and turn into GSB peaks (Figure 6.5a-e).

Before in Chapter 5, we have seen from steady-state absorption measurements (with a UV-Vis spectrophotometer) that the peak at 2.8 eV gradually decreases with increasing Sb concentration (Figure 5.6a). These two observations are consistent with each other that this sharp peak at 2.8 eV is from excitons. Because the exciton binding energy is lower in Sb-double perovskite (from calculation, Table 6.1), with higher Sb concentration, this sharp peak in absorption figure decreases, and the signature of carrier-exciton scattering in TA measurements also becomes only GSB signals from the density of states in the conduction band. Whilst the dissociation of excitons to free carriers is beneficial to improved photovoltaic performance,

this may be countered by the increased loss in V_{OC} that would come about due to increased disorder, as well as the new sub-bandgap state that forms with the addition of Sb.

It is noted that an alternative explanation for the absorption peak at 2.8 eV is from a high density of states in the conduction band and the smearing peaks in Sb mixed alloys is due to the increased disorder, as discussed in Chapter 5. Following this possibility, the origin of the PIA peaks in $Cs_2AgBibr_6$ still needs to be determined.

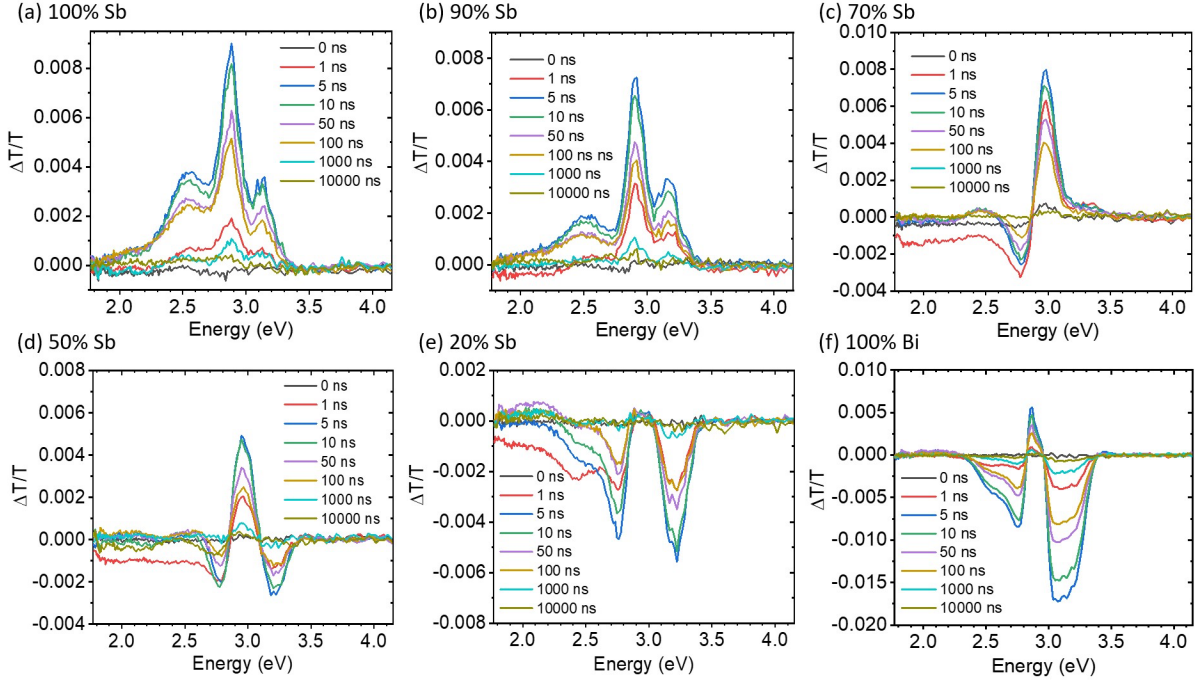


Figure 6.5 $\Delta T/T$ spectra for the transient absorption measurement of the $Cs_2Ag(Sb_xBi_{1-x})Br_6$ thin films. (a) $Cs_2AgSbBr_6$, (b) $Cs_2Ag(Sb_{0.9}Bi_{0.1})Br_6$, (c) $Cs_2Ag(Sb_{0.7}Bi_{0.3})Br_6$, (d) $Cs_2Ag(Sb_{0.5}Bi_{0.5})Br_6$, (e) $Cs_2Ag(Sb_{0.2}Bi_{0.8})Br_6$, (f) $Cs_2AgBiBr_6$. The excitation wavelength was 355 nm (3.5 eV) for laser pulses with a pulse length less than 1 ns at a repetition rate of 1 kHz and fluence of $50 \mu J cm^{-2} pulse^{-1}$. Data taken by Sachin Dev Verma and analysed by myself.

The optical exciton binding energies were determined from the calculated values for the effective masses (Table 6.2), with the effective mass approximation:¹⁹³

$$E_{ex,opt} = \left(\frac{m^*}{m_0 \epsilon_\infty^2} \right) R_H \quad (6.1)$$

Where $m^* = \frac{m_e m_h}{m_e + m_h}$ is the reduced effective mass, m_0 is the electronic mass, R_H is the Rydberg constant and ϵ_∞ is the optical dielectric constant.

Table 6.1 Calculated dielectric constants and optical exciton binding energies ($E_{ex,opt}$) of $Cs_2AgSbBr_6$ and $Cs_2AgBiBr_6$. Calculation made by Seán R. Kavanagh.

Material	ϵ_{ionic}	ϵ_{∞}	$\epsilon_0 = \epsilon_{ionic} + \epsilon_{\infty}$	$E_{ex,opt}$
$Cs_2AgSbBr_6$	8.87	4.82	13.69	124 meV
$Cs_2AgBiBr_6$	8.16	4.60	12.76	167 meV

Table 6.2 Calculated effective mass values for $Cs_2AgSbBr_6$ and $Cs_2AgBiBr_6$ in units of electron mass, using non-parabolic fitting of the band structures. Calculation made by Seán R. Kavanagh.

Material	$m_h^{\Gamma-X}$	m_h^{X-W}	m_e^{W-L}	$m_e^{L-\Gamma}$
$Cs_2AgSbBr_6$	0.15	0.62	0.26	0.32
$Cs_2AgBiBr_6$	0.18	0.61	0.31	0.45

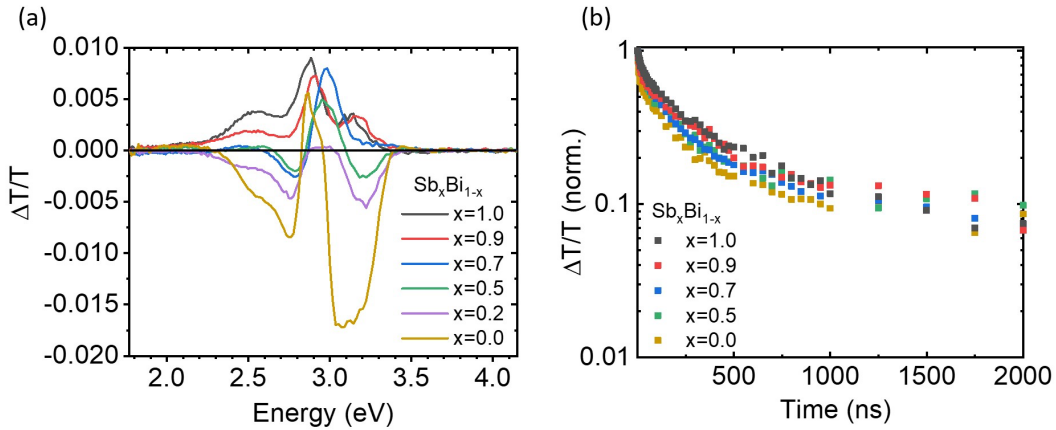


Figure 6.6 Transient absorption measurement of the $Cs_2Ag(Sb_xBi_{1-x})Br_6$ thin films. (a) $\Delta T/T$ spectra at 5 ns. (b) Normalized kinetics of the main ground state bleach (GSB) for $Cs_2AgSbBr_6$ (2.89 eV), $Cs_2Ag(Sb_{0.9}Bi_{0.1})Br_6$ (2.89 eV), $Cs_2Ag(Sb_{0.7}Bi_{0.3})Br_6$ (2.96 eV), $Cs_2Ag(Sb_{0.5}Bi_{0.5})Br_6$ (2.96 eV), $Cs_2AgBiBr_6$ (2.86 eV). The excitation wavelength was 355 nm for laser pulses with a pulse length less than 1 ns at a repetition rate of 1 kHz and fluence of $50 \mu J cm^{-2} pulse^{-1}$. Data taken by Sachin Dev Verma and analysed by myself.

Figure 6.6a is the $\Delta T/T$ spectra at 5 ns for the whole alloying range. It clearly shows that the two PIA peaks are turning into GSB peaks as the Sb composition increases. Figure 6.6b shows the kinetics of the main GSB peak (2.8~2.9 eV) for the mixed alloys. The kinetic profiles of all the compositions follow the same trend. The lifetimes characterized by TA do not decrease (or even increase) with higher Sb concentration, even though we have seen that Sb alloying introduces sub-bandgap states to $\text{Cs}_2\text{AgBiBr}_6$ and lowers its PL intensity. In addition, we also notice that in each composition, the kinetics of the GSB and PIA peaks display similar profiles (Figure 6.7). This means that these different GSB and PIA peaks originate from the same excited-state carriers. Similar to the TA measurements in Chapter 4 (Figure 4.3), any GSB at wavelengths longer than 550 nm was not observed. I attributed this to a combination of two effects: i) the weak absorption at the indirect bandgap and ii) the neighbouring PIA peak covering any weak GSB that may exist there.

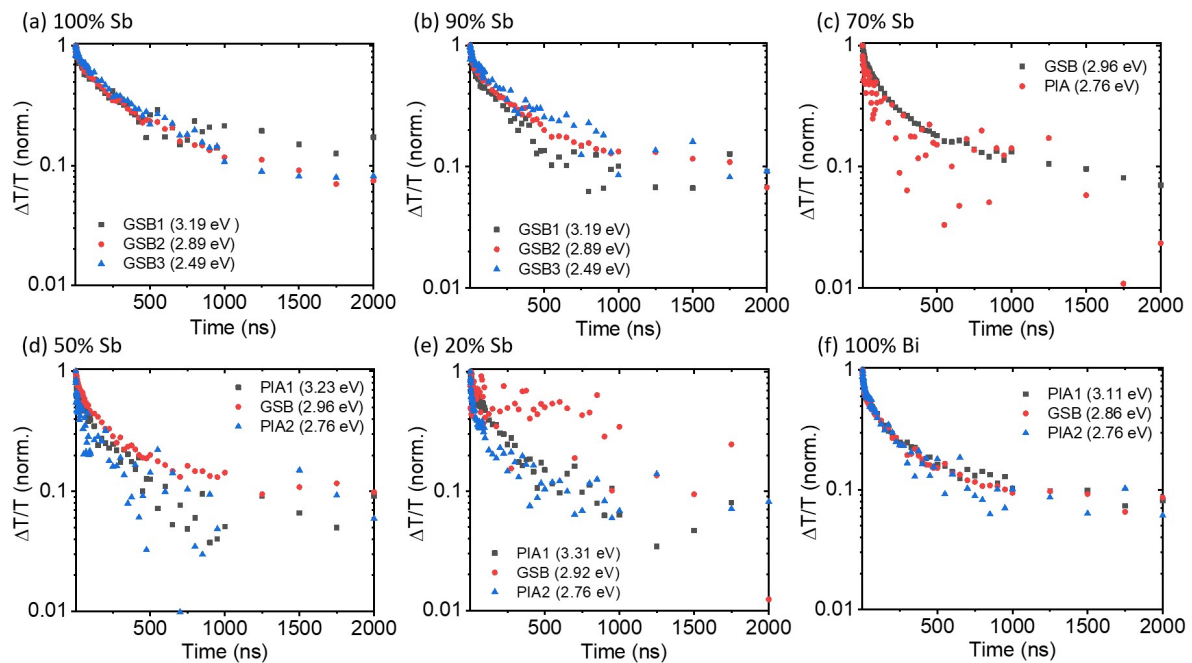


Figure 6.7 Normalised kinetics of the ground state bleach (GSB) and photoinduced absorption (PIA) for the transient absorption measurement of the $\text{Cs}_2\text{Ag}(\text{Sb}_x\text{Bi}_{1-x})\text{Br}_6$ thin films. (a) $\text{Cs}_2\text{AgSbBr}_6$, (b) $\text{Cs}_2\text{Ag}(\text{Sb}_{0.9}\text{Bi}_{0.1})\text{Br}_6$, (c) $\text{Cs}_2\text{Ag}(\text{Sb}_{0.7}\text{Bi}_{0.3})\text{Br}_6$, (d) $\text{Cs}_2\text{Ag}(\text{Sb}_{0.5}\text{Bi}_{0.5})\text{Br}_6$, (e) $\text{Cs}_2\text{Ag}(\text{Sb}_{0.2}\text{Bi}_{0.8})\text{Br}_6$, (f) $\text{Cs}_2\text{AgBiBr}_6$. The excitation wavelength was 355 nm for laser pulses with a pulse length less than 1 ns at a repetition rate of 1 kHz and fluence of $50 \mu\text{J cm}^{-2} \text{ pulse}^{-1}$. Data taken by Sachin Dev Verma and analysed by myself.

6.4 Conclusions and future work

6.4.1 Characterization of the sub-bandgap states

It has been shown in this chapter that Sb alloying introduces sub-bandgap states to the $\text{Cs}_2\text{AgBiBr}_6$ double perovskite, one of which luminesces at 1.55 eV. To further verify the positions of those defect states, I plan to characterise the devices with photo induced current transient spectroscopy (PICTS), which is a variant of deep-level transient spectroscopy (DLTS). DLTS is a capacitance-based technique where defects are characterized by observation of thermal emission of carriers from deep states within the depletion region of a diode by means of a capacitive transient.¹⁹⁴ However, it is particularly problematic in high-resistivity materials (as the case for $\text{Cs}_2\text{AgBiBr}_6$ double perovskite¹¹³), which may have low carrier density (hence a long dielectric relaxation time) as well as low carrier mobility (hence a long transit time).¹⁹⁵ Therefore, charges are not readily available in the semiconductor for defect-level filling and need to be transported over a finite distance. However, in PICTS, light excitation is used to disturb the occupancy of carriers in defect states. PICTS measurements allow the determination of the defect parameters, such as volumetric concentration, energy depth and capture cross-section, for each of the defect levels present.¹⁹⁵ Therefore, it can reveal information about defects in both $\text{Cs}_2\text{AgBiBr}_6$ and its Sb alloys. Together with PICTS, we can then confirm that Sb alloying introduces defect states and thus deteriorate the solar cell performance.

6.4.2 Identification of the sub-bandgap states

The next step is to identify the origin of the luminescent sub-bandgap states. Since we notice from SEM that the morphology (how well ordered the grains are and what the grain size is) of the Sb containing films are worse than the pure Bi double perovskite, the defect states introduced by the grain boundaries is one possibility for the sub-bandgap states. To test this hypothesis, I can optimise the morphology further by antisolvent method and solvent annealing method. I can then observe whether the optoelectronic properties improve with better morphology. However, beyond optimising the ordering of the grains and grain boundary density, the exact defect states causing the colour centre still needs to be determined. This may be elucidated using defect calculations. However, the double perovskite is a highly complex system with high levels of disorder that would be very computationally expensive to simulate.

The PL intensity from the luminescent sub-bandgap state at 1.55 eV decreases with higher Sb ratio and finally vanishes in the pure Sb double perovskite. This suggests that the luminescent peak is not intrinsically from the pure Sb-based double perovskite, but a disturbance to the electronic structure of the pure Bi double perovskite. To further verify this 1.55 PL peak is from defect states, we can perform excitation power dependent PL measurement. Sb alloying may also introduce symmetry forbidden transition to the double perovskite system.¹⁹⁶ Further theoretical analysis can be performed to understand this possibility.

Previous works have reported that mixed Sb-Bi double perovskite alloys with high Sb contents have marginally lower stability. For example, Liu *et al.* found that $\text{Cs}_2\text{Ag}(\text{Sb}_x\text{Bi}_{1-x})\text{Br}_6$ thin films with $x = 0.75$ had AgBr and CsAgBr₂ decomposition products after 4 h annealing at 250 °C.¹⁶⁶ Therefore, another hypothesis is that the increasing sub-bandgap states with more Sb alloying is due to phase impurities with <1% concentration that cannot be detected by XRD. A closer analysis by TEM, along with TEM-EDX or electron energy loss spectroscopy (EELS) may identify whether these small phase impurities occur.¹⁹⁷

6.4.3 Mitigation of the sub-bandgap states

To eliminate the defects, a wide range of methods, such as adding additives in the precursors, surface passivation and mixing with 2D counterparts, have been reported.^{198,199} These can also be performed to further improve the optoelectronic properties and the device performance of $\text{Cs}_2\text{AgBiBr}_6$ and its Sb mixed alloys.

Contributions

Sachin Dev Verma measured the TA data. Seán R. Kavanagh performed the theoretical calculations. I collected all the other data and analysed all the data.

7 Conclusions and Outlook

In this thesis, I investigated the optoelectronic properties of $\text{Cs}_2\text{AgBiBr}_6$ double perovskite for solar cell applications. To fulfil the research objectives posed at the beginning of this thesis, I firstly investigated the role of grain boundaries on charge-carrier and ion transport in $\text{Cs}_2\text{AgBiBr}_6$ thin films. I subsequently studied the effect of Sb alloying on the bandgap of $\text{Cs}_2\text{AgBiBr}_6$ and investigated the underlying mechanism for the bandgap variation with composition. Finally, I examined whether Sb alloying can help to improve the efficiencies of $\text{Cs}_2\text{AgBiBr}_6$ solar cells and identified the factors limiting the performance.

For the first project, I found that grain boundaries are the dominant nonradiative recombination sites and also the main channel for ion transport in thin films. By developing the first halide double perovskite field-effect transistor (FET), I obtained insights into the macroscopic transport of carriers and ions over the entire film. This contrasts to the information obtained from spectroscopic measurements, which have been the most common methods to study carrier transport, and which can only probe local mobility and are dominated by the most mobile carrier. Thus, whilst previous spectroscopy measurements have suggested band-like transport in $\text{Cs}_2\text{AgBiBr}_6$,^{78,79} the FET results show that carrier transport within the bulk material is intrinsically limited by a thermally-activated hopping mechanism.

This project illustrates the role that grain boundaries have in $\text{Cs}_2\text{AgBiBr}_6$, and shows the critical need to develop passivation strategies at grain boundaries in order to mitigate nonradiative recombination and ion migration. In addition, the demonstration that the carrier mobility in this material is intrinsically limited motivates future efforts to identify the underlying cause, whether it is due to carrier trapping in tail states, or the formation of small polarons due to the coupling of carriers to acoustic phonons. This is the next important step that could provide insights to guide the identification of more promising materials in the halide double perovskite family.

For the second project, I studied the bandgap lowering mechanism in mixed alloys of $\text{Cs}_2\text{Ag}(\text{Sb}_x\text{Bi}_{1-x})\text{Br}_6$ double perovskite thin films. I achieved the complete mixing of Sb in the Bi site in thin films for the first time, allowing the synthesis of phase-pure $\text{Cs}_2\text{Ag}(\text{Sb}_x\text{Bi}_{1-x})\text{Br}_6$ with x continuously varying over the entire composition range. This has not been achieved before in thin films because $\text{Cs}_2\text{AgSbBr}_6$ has a high formation energy. In doing so, I revealed that the mixed alloy Sb-Bi double perovskites have lower bandgaps than the pure compounds. The reduction in the bandgap of $\text{Cs}_2\text{AgBiBr}_6$ achieved through alloying is 170 meV, which is

more than double the bandgap lowering achievable (70 meV) if the alloy bandgaps were constrained to between those of $\text{Cs}_2\text{AgBiBr}_6$ and $\text{Cs}_2\text{AgSbBr}_6$. I identified the origin of this unexpected bandgap lowering through first-principles calculations. It is found that the pure Sb- and Bi-based double perovskites form a Type II band alignment. Non-linear mixing of the atomic orbitals from Bi^{3+} and Sb^{3+} leads to the mixed alloys adopting a smaller bandgap than the pure compounds.

To date, most double perovskite thin films have bandgaps well above 2 eV,²⁰⁰ which is too wide for practical applications in photovoltaics or photocatalysis. This work suggests that bandgap lowering could be more broadly found in other halide double perovskite alloys composed of compounds forming a Type II band alignment, opening up a ‘design rule’ for tuning the bandgap to lower values that are ideal for a wide range of optoelectronic applications. These include photocatalysts and indoor photovoltaics (~ 2 eV ideal bandgap),^{188,189} top-cells in tandems (1.7-1.9 eV ideal bandgap),¹⁹⁰ and others. In addition, the unusual bandgap lowering behavior I discover here is important for understanding bandgap bowing across different alloy systems.

Finally, I investigated the factors limiting the performance of photovoltaics based on $\text{Cs}_2\text{Ag}(\text{Sb}_x\text{Bi}_{1-x})\text{Br}_6$ double perovskites. I found that Sb alloying introduces sub-bandgap states to the $\text{Cs}_2\text{AgBiBr}_6$ double perovskite, one of which luminesces at 1.55 eV. These sub-bandgap states cause substantial losses on the V_{OC} and J_{SC} of $\text{Cs}_2\text{Ag}(\text{Sb}_x\text{Bi}_{1-x})\text{Br}_6$ solar cells. To finish this project, future work includes characterizing the thin films to determine important characteristics of its defects, such as the energy levels, concentration of defects and their capture cross-sections. This could be done through PICTS measurements. Next, the origin of the defect states still needs to be determined and likely requires detailed high-resolution TEM measurements coupled with simulations of the grain boundaries of the double perovskites. Finally, I will investigate how these sub-bandgap states could be mitigated to improve the performance of $\text{Cs}_2\text{Ag}(\text{Sb}_x\text{Bi}_{1-x})\text{Br}_6$ solar cells. There are many passivation strategies for lead-halide perovskites that could be utilized. Introducing additives to the precursor solution and mixing with 2D-structured double perovskites are some promising routes.

Overall, the findings gained in this thesis about $\text{Cs}_2\text{AgBiBr}_6$ double perovskite provides both physical understanding and engineering guides to improve its optoelectronic properties. With appropriate strategies to mitigate the defect states in thin films, $\text{Cs}_2\text{AgBiBr}_6$ double perovskite

and its Sb alloys have potentials for applications in a wide range of fields, such as photocatalysts, indoor photovoltaics, top-cells in tandems and radiation detectors.

References

- (1) Koebrich, S.; Bowen, T.; Sharpe, A. 2018 Renewable Energy Data Book. **2018**, 149.
- (2) Green, M. A. Commercial Progress and Challenges for Photovoltaics. *Nat. Energy* **2016**, *1* (1), 15015. <https://doi.org/10.1038/nenergy.2015.15>.
- (3) Fraunhofer ISE. Current and Future Cost of Photovoltaics. Long-Term Scenarios for Market Development, System Prices and LCOE of Utility-Scale PV Systems. *Agora Energiewende* **2015**.
- (4) Kurtz, S.; Atwater, H.; Rockett, A.; Buonassisi, T.; Honsberg, C.; Benner, J. Solar Research Not Finished. *Nat. Photonics* **2016**, *10* (3), 141–142. <https://doi.org/10.1038/nphoton.2016.16>.
- (5) Needleman, D. B.; Poindexter, J. R.; Kurchin, R. C.; Peters, I. M.; Wilson, G.; Buonassisi, T. Economically Sustainable Scaling of Photovoltaics to Meet Climate Targets. *Energy Environ. Sci.* **2016**, *9*, 2122–2129. <https://doi.org/10.1039/C6EE00484A>.
- (6) McMeekin, D. P.; Sadoughi, G.; Rehman, W.; Eperon, G. E.; Saliba, M.; Hörantner, M. T.; Haghighirad, A.; Sakai, N.; Korte, L.; Rech, B.; Johnston, M. B.; Herz, L. M.; Snaith, H. J. A Mixed-Cation Lead Mixed-Halide Perovskite Absorber for Tandem Solar Cells. *Science*. **2016**, *351* (6269), 151–155. <https://doi.org/10.1126/science.aad5845>.
- (7) Best Research-Cell Efficiency Chart | Photovoltaic Research | NREL <https://www.nrel.gov/pv/cell-efficiency.html> (accessed Jul 10, 2021).
- (8) Vidal, R.; Alberola-Borràs, J. A.; Habisreutinger, S. N.; Gimeno-Molina, J. L.; Moore, D. T.; Schloemer, T. H.; Mora-Seró, I.; Berry, J. J.; Luther, J. M. Assessing Health and Environmental Impacts of Solvents for Producing Perovskite Solar Cells. *Nat. Sustain.* **2021**, *4* (3), 277–285. <https://doi.org/10.1038/s41893-020-00645-8>.
- (9) de Wild-Scholten, M. J.; Wambach, K.; Alsema, E. A.; Jäger-Waldau, A. Implications of European Environmental Legislation for Photovoltaic Systems. In *20th European Photovoltaic Solar Energy Conference*; 2005; pp 3143–3147.
- (10) Moody, N.; Sesena, S.; deQuilettes, D. W.; Dou, B. D.; Swartwout, R.; Buchman, J.

- T.; Johnson, A.; Eze, U.; Brenes, R.; Johnston, M.; Haynes, C. L.; Bulović, V.; Bawendi, M. G. Assessing the Regulatory Requirements of Lead-Based Perovskite Photovoltaics. *Joule* **2020**, *4* (5), 970–974. <https://doi.org/10.1016/j.joule.2020.03.018>.
- (11) Sze, S. M.; Ng, K. K. *Physics of Semiconductor Devices*; John Wiley and Sons, 2006. <https://doi.org/10.1002/0470068329>.
- (12) Würfel, P. *Physics of Solar Cells: From Principles to New Concepts*; John Wiley and Sons, 2007. <https://doi.org/10.1002/9783527618545>.
- (13) Shockley, W.; Queisser, H. J. Detailed Balance Limit of Efficiency of P-N Junction Solar Cells. *J. Appl. Phys.* **1961**, *32* (3), 510–519. <https://doi.org/10.1063/1.1736034>.
- (14) Smith, D. D.; Cousins, P. J.; Masad, A.; Waldhauer, A.; Westerberg, S.; Johnson, M.; Tu, X.; Dennis, T.; Harley, G.; Solomon, G.; Rim, S.; Shepherd, M.; Harrington, S.; Defensor, M.; Leygo, A.; Tomada, P.; Wu, J.; Pass, T.; Ann, L.; Smith, L.; Bergstrom, N.; Nicdao, C.; Tipones, P.; Vicente, D. Generation III High Efficiency Lower Cost Technology: Transition to Full Scale Manufacturing. *Conf. Rec. IEEE Photovolt. Spec. Conf.* **2012**, 1594–1597. <https://doi.org/10.1109/PVSC.2012.6317899>.
- (15) Polman, A.; Knight, M.; Garnett, E. C.; Ehrler, B.; Sinke, W. C. Photovoltaic Materials: Present Efficiencies and Future Challenges. *Science*. **2016**, *352* (6283), aad4422. <https://doi.org/10.1126/science.aad4424>.
- (16) Peters, I. M.; Buonassisi, T. Economically Sustainable Scaling of Photovoltaics to Meet Climate Targets. *Energy Environ. Sci.* **2016**, *9*, 2122–2129. <https://doi.org/10.1039/C6EE00484A>.
- (17) Fortunato, E.; Barquinha, P.; Martins, R. Oxide Semiconductor Thin-Film Transistors: A Review of Recent Advances. *Adv. Mater.* **2012**, *24* (22), 2945–2986. <https://doi.org/10.1002/adma.201103228>.
- (18) Knipp, D. Introduction to Electronic Devices [http://www.faculty.jacobs-university.de/dknipp/c300331/Lectures/6 Field Effect Transistors.pdf](http://www.faculty.jacobs-university.de/dknipp/c300331/Lectures/6%20Field%20Effect%20Transistors.pdf) (accessed Jul 31, 2021).
- (19) Senanayak, S. P.; Yang, B.; Thomas, T. H.; Giesbrecht, N.; Huang, W.; Gann, E.; Nair, B.; Goedel, K.; Guha, S.; Moya, X.; McNeill, C. R.; Docampo, P.; Sadhanala, A.; Friend, R. H.; Sirringhaus, H. Understanding Charge Transport in Lead Iodide

- Perovskite Thin-Film Field-Effect Transistors. *Sci. Adv.* **2017**, *3* (1), e1601935. <https://doi.org/10.1126/sciadv.1601935>.
- (20) Sirringhaus, H. Device Physics of Solution-Processed Organic Field-Effect Transistors. *Adv. Mater.* **2005**, *17* (20), 2411–2425. <https://doi.org/10.1002/adma.200501152>.
- (21) Sirringhaus, H.; Bird, M.; Richards, T.; Zhao, N. Charge Transport Physics of Conjugated Polymer Field-Effect Transistors. *Adv. Mater.* **2010**, *22* (34), 3893–3898. <https://doi.org/10.1002/adma.200902857>.
- (22) Kagan, C. R.; Mitzi, D. B.; Dimitrakopoulos, C. D. Organic-Inorganic Hybrid Materials as Semiconducting Channels in Thin-Film Field-Effect Transistors. *Science*. **1999**, *286* (5441), 945–947. <https://doi.org/10.1126/science.286.5441.945>.
- (23) Radisavljevic, B.; Kis, A. Mobility Engineering and a Metal-Insulator Transition in Monolayer MoS₂. *Nat. Mater.* **2013**, *12* (9), 815–820. <https://doi.org/10.1038/nmat3687>.
- (24) Dong, Q.; Fang, Y.; Shao, Y.; Mulligan, P.; Qiu, J.; Cao, L.; Huang, J. Electron-Hole Diffusion Lengths > 175 Micrometers in Solution-Grown CH₃NH₃PbI₃ Single Crystals. *Science*. **2015**, *347* (6225), 967–970. <https://doi.org/10.1126/science.aaa5760>.
- (25) Dequilettes, D. W.; Koch, S.; Burke, S.; Paranjli, R. K.; Shropshire, A. J.; Ziffer, M. E.; Ginger, D. S. Photoluminescence Lifetimes Exceeding 8 Microseconds and Quantum Yields Exceeding 30% in Hybrid Perovskite Thin Films by Ligand Passivation. *ACS Energy Lett.* **2016**, *1* (2), 438–444. <https://doi.org/10.1021/acsenerylett.6b00236>.
- (26) Braly, I. L.; Dequilettes, D. W.; Pazos-Outón, L. M.; Burke, S.; Ziffer, M. E.; Ginger, D. S.; Hillhouse, H. W. Hybrid Perovskite Films Approaching the Radiative Limit with over 90% Photoluminescence Quantum Efficiency. *Nat. Photonics* **2018**, *12* (6), 355–361. <https://doi.org/10.1038/s41566-018-0154-z>.
- (27) Yang, X.; Zhang, X.; Deng, J.; Chu, Z.; Jiang, Q.; Meng, J.; Wang, P.; Zhang, L.; Yin, Z.; You, J. Efficient Green Light-Emitting Diodes Based on Quasi-Two-Dimensional Composition and Phase Engineered Perovskite with Surface Passivation. *Nat. Commun.* **2018**, *9* (1), 570. <https://doi.org/10.1038/s41467-018-02978-7>.

- (28) Stranks, S. D.; Hoyer, R. L. Z.; Di, D.; Friend, R. H.; Deschler, F. The Physics of Light Emission in Halide Perovskite Devices. *Adv. Mater.* **2019**, *31* (47), 1803336. <https://doi.org/10.1002/adma.201803336>.
- (29) Jung, H. S.; Park, N. G. Perovskite Solar Cells: From Materials to Devices. *Small* **2015**, *11* (1), 10–25. <https://doi.org/10.1002/sml.201402767>.
- (30) Stoumpos, C. C.; Malliakas, C. D.; Kanatzidis, M. G. Semiconducting Tin and Lead Iodide Perovskites with Organic Cations: Phase Transitions, High Mobilities, and Near-Infrared Photoluminescent Properties. *Inorg. Chem.* **2013**, *52* (15), 9019–9038. <https://doi.org/10.1021/ic401215x>.
- (31) Noel, N. K.; Stranks, S. D.; Abate, A.; Wehrenfennig, C.; Guarnera, S.; Haghighirad, A. A.; Sadhanala, A.; Eperon, G. E.; Pathak, S. K.; Johnston, M. B.; Petrozza, A.; Herz, L. M.; Snaith, H. J. Lead-Free Organic-Inorganic Tin Halide Perovskites for Photovoltaic Applications. *Energy Environ. Sci.* **2014**, *7* (9), 3061–3068. <https://doi.org/10.1039/c4ee01076k>.
- (32) Pellet, N.; Gao, P.; Gregori, G.; Yang, T. Y.; Nazeeruddin, M. K.; Maier, J.; Grätzel, M. Mixed-Organic-Cation Perovskite Photovoltaics for Enhanced Solar-Light Harvesting. *Angew. Chem. Int. Ed.* **2014**, *53* (12), 3151–3157. <https://doi.org/10.1002/anie.201309361>.
- (33) Sadhanala, A.; Deschler, F.; Thomas, T. H.; Dutton, E.; Goedel, K. C.; Hanusch, F. C.; Lai, M. L.; Steiner, U.; Bein, T.; Docampo, P.; Cahen, D.; Friend, R. H. Preparation of Single-Phase Films of $\text{CH}_3\text{NH}_3\text{Pb}(\text{I}_{1-x}\text{Br}_x)_3$ with Sharp Optical Band Edges. *J. Phys. Chem. Lett.* **2014**, *5* (15), 2501–2505. <https://doi.org/10.1021/jz501332v>.
- (34) Stranks, S. D.; Eperon, G. E.; Grancini, G.; Menelaou, C.; Alcocer, M. J. P.; Leijtens, T.; Herz, L. M.; Petrozza, A.; Snaith, H. J. Electron-Hole Diffusion Lengths Exceeding 1 Micrometer in an Organometal Trihalide Perovskite Absorber. *Science*. **2013**, *342* (18), 341–344. <https://doi.org/10.1126/science.1243982>.
- (35) Lin, Q.; Armin, A.; Nagiri, R. C. R.; Burn, P. L.; Meredith, P. Electro-Optics of Perovskite Solar Cells. *Nat. Photonics* **2015**, *9* (2), 106–112. <https://doi.org/10.1038/nphoton.2014.284>.
- (36) Miyata, A.; Mitioglu, A.; Plochocka, P.; Portugall, O.; Wang, J. T.-W.; Stranks, S. D.;

- Snaith, H. J.; Nicholas, R. J. Direct Measurement of the Exciton Binding Energy and Effective Masses for Charge Carriers in an Organic-Inorganic Tri-Halide Perovskite. *Nat. Phys.* **2015**, *11* (7), 582–587. <https://doi.org/10.1038/nphys3357>.
- (37) Deschler, F.; Price, M.; Pathak, S.; Klintberg, L. E.; Jarausch, D. D.; Higler, R.; Hüttner, S.; Leijtens, T.; Stranks, S. D.; Snaith, H. J.; Atatüre, M.; Phillips, R. T.; Friend, R. H. High Photoluminescence Efficiency and Optically Pumped Lasing in Solution-Processed Mixed Halide Perovskite Semiconductors. *J. Phys. Chem. Lett.* **2014**, *5* (8), 1421–1426. <https://doi.org/10.1021/jz5005285>.
- (38) Saba, M.; Cadelano, M.; Marongiu, D.; Chen, F.; Sarritzu, V.; Sestu, N.; Figus, C.; Aresti, M.; Piras, R.; Geddo Lehmann, A.; Cannas, C.; Musinu, A.; Quochi, F.; Mura, A.; Bongiovanni, G. Correlated Electron-Hole Plasma in Organometal Perovskites. *Nat. Commun.* **2014**, *5*, 5049. <https://doi.org/10.1038/ncomms6049>.
- (39) Richter, J. M.; Abdi-Jalebi, M.; Sadhanala, A.; Tabachnyk, M.; Rivett, J. P. H.; Pazos-Outón, L. M.; Gödel, K. C.; Price, M.; Deschler, F.; Friend, R. H. Enhancing Photoluminescence Yields in Lead Halide Perovskites by Photon Recycling and Light Out-Coupling. *Nat. Commun.* **2016**, *7*, 13941. <https://doi.org/10.1038/ncomms13941>.
- (40) Pazos-Outón, L. M.; Xiao, T. P.; Yablonovitch, E. Fundamental Efficiency Limit of Lead Iodide Perovskite Solar Cells. *J. Phys. Chem. Lett.* **2018**, *9* (7), 1703–1711. <https://doi.org/10.1021/acs.jpcclett.7b03054>.
- (41) Bowman, A. R.; Anaya, M.; Greenham, N. C.; Stranks, S. D. Quantifying Photon Recycling in Solar Cells and Light-Emitting Diodes: Absorption and Emission Are Always Key. *Phys. Rev. Lett.* **2020**, *125* (6), 67401. <https://doi.org/10.1103/PhysRevLett.125.067401>.
- (42) Yin, W.-J.; Shi, T.; Yan, Y. Unusual Defect Physics in CH₃NH₃PbI₃ Perovskite Solar Cell Absorber. *Appl. Phys. Lett.* **2014**, *104*, 063903. <https://doi.org/10.1063/1.4864778>.
- (43) Yin, W.-J.; Yang, J.-H.; Kang, J.; Yan, Y.; Wei, S.-H. Halide Perovskite Materials for Solar Cells: A Theoretical Review. *J. Mater. Chem. A* **2015**, *3*, 8926–8942. <https://doi.org/10.1039/C4TA05033A>.
- (44) Brandt, R. E.; Poindexter, J. R.; Gorai, P.; Kurchin, R. C.; Hoye, R. L. Z.; Nienhaus,

- L.; Wilson, M. W. B.; Polizzotti, J. A.; Sereika, R.; Žaltauskas, R.; Lee, L. C.; Macmanus-Driscoll, J. L.; Bawendi, M.; Stevanović, V.; Buonassisi, T. Searching for “Defect-Tolerant” Photovoltaic Materials: Combined Theoretical and Experimental Screening. *Chem. Mater.* **2017**, *29* (11), 4667–4674. <https://doi.org/10.1021/acs.chemmater.6b05496>.
- (45) Zakutayev, A.; Caskey, C. M.; Fioretti, A. N.; Ginley, D. S.; Vidal, J.; Stevanovic, V.; Tea, E.; Lany, S. Defect Tolerant Semiconductors for Solar Energy Conversion. *J. Phys. Chem. Lett.* **2014**, *5* (7), 1117–1125. <https://doi.org/10.1021/jz5001787>.
- (46) Huang, Y. T.; Kavanagh, S. R.; Scanlon, D. O.; Walsh, A.; Hoye, R. L. Z. Perovskite-Inspired Materials for Photovoltaics and beyond-from Design to Devices. *Nanotechnology* **2021**, *32* (13), 132004. <https://doi.org/10.1088/1361-6528/abcf6d>.
- (47) Abdi-Jalebi, M.; Andaji-Garmaroudi, Z.; Cacovich, S.; Stavrakas, C.; Philippe, B.; Richter, J. M.; Alsari, M.; Booker, E. P.; Hutter, E. M.; Pearson, A. J.; Lilliu, S.; Savenije, T. J.; Rensmo, H.; Divitini, G.; Ducati, C.; Friend, R. H.; Stranks, S. D. Maximizing and Stabilizing Luminescence from Halide Perovskites with Potassium Passivation. *Nature* **2018**, *555* (7697), 497–501. <https://doi.org/10.1038/nature25989>.
- (48) Doherty, T. A. S.; Winchester, A. J.; Macpherson, S.; Johnstone, D. N.; Pareek, V.; Tennyson, E. M.; Kosar, S.; Kosasih, F. U.; Anaya, M.; Abdi-Jalebi, M.; Andaji-Garmaroudi, Z.; Wong, E. L.; Madéo, J.; Chiang, Y. H.; Park, J. S.; Jung, Y. K.; Petoukhoff, C. E.; Divitini, G.; Man, M. K. L.; Ducati, C.; Walsh, A.; Midgley, P. A.; Dani, K. M.; Stranks, S. D. Performance-Limiting Nanoscale Trap Clusters at Grain Junctions in Halide Perovskites. *Nature* **2020**, *580* (7803), 360–366. <https://doi.org/10.1038/s41586-020-2184-1>.
- (49) Tiep, N. H.; Ku, Z.; Fan, H. J. Recent Advances in Improving the Stability of Perovskite Solar Cells. *Adv. Energy Mater.* **2016**, *6* (3), 1501420. <https://doi.org/10.1002/aenm.201501420>.
- (50) Navas, J.; Sánchez-Coronilla, A.; Gallardo, J. J.; Martín, E. I.; Hernández, N. C.; Alcántara, R.; Fernández-Lorenzo, C.; Martín-Calleja, J. Revealing the Role of Pb²⁺ in the Stability of Organic-Inorganic Hybrid Perovskite CH₃NH₃(Pb_{1-x}Cdx)I₃: An Experimental and Theoretical Study. *Phys. Chem. Chem. Phys.* **2015**, *17* (37), 23886–23896. <https://doi.org/10.1039/c5cp04009d>.

- (51) Qin, C.; Matsushima, T.; Fujihara, T.; Potscavage, W. J.; Adachi, C. Degradation Mechanisms of Solution-Processed Planar Perovskite Solar Cells: Thermally Stimulated Current Measurement for Analysis of Carrier Traps. *Adv. Mater.* **2016**, *28* (3), 466–471. <https://doi.org/10.1002/adma.201502610>.
- (52) Leijtens, T.; Eperon, G. E.; Pathak, S.; Abate, A.; Lee, M. M.; Snaith, H. J. Overcoming Ultraviolet Light Instability of Sensitized TiO₂ with Meso-Structured Organometal Tri-Halide Perovskite Solar Cells. *Nat. Commun.* **2013**, *4*, 2885. <https://doi.org/10.1038/ncomms3885>.
- (53) Li, X.; Ibrahim Dar, M.; Yi, C.; Luo, J.; Tschumi, M.; Zakeeruddin, S. M.; Nazeeruddin, M. K.; Han, H.; Grätzel, M. Improved Performance and Stability of Perovskite Solar Cells by Crystal Crosslinking with Alkylphosphonic Acid ω -Ammonium Chlorides. *Nat. Chem.* **2015**, *7* (9), 703–711. <https://doi.org/10.1038/nchem.2324>.
- (54) Bush, K. A.; Palmstrom, A. F.; Yu, Z. J.; Boccard, M.; Cheacharoen, R.; Mailoa, J. P.; McMeekin, D. P.; Hoye, R. L. Z.; Bailie, C. D.; Leijtens, T.; Peters, I. M.; Minichetti, M. C.; Rolston, N.; Prasanna, R.; Sofia, S.; Harwood, D.; Ma, W.; Moghadam, F.; Snaith, H. J.; Buonassisi, T.; Holman, Z. C.; Bent, S. F.; McGehee, M. D. 23.6%-Efficient Monolithic Perovskite/Silicon Tandem Solar Cells With Improved Stability. *Nat. Energy* **2017**, *2* (4), 17009. <https://doi.org/10.1038/nenergy.2017.9>.
- (55) Mei, A.; Li, X.; Liu, L.; Ku, Z.; Liu, T.; Rong, Y.; Xu, M.; Hu, M.; Chen, J.; Yang, Y.; Grätzel, M.; Han, H. A Hole-Conductor-Free, Fully Printable Mesoscopic Perovskite Solar Cell with High Stability. *Science*. **2014**, *345* (6194), 295–298. <https://doi.org/10.1126/science.1254763>.
- (56) Grancini, G.; Zimmermann, I.; Mosconi, E.; Martineau, D.; Nabey, S. One-Year Stable Perovskite Solar Cells by 2D/3D Interface Engineering. *Nat. Commun.* **2017**, *8*, 15684. <https://doi.org/10.1038/ncomms15684>.
- (57) Li, J.; Cao, H. L.; Jiao, W. Bin; Wang, Q.; Wei, M.; Cantone, I.; Lü, J.; Abate, A. Biological Impact of Lead from Halide Perovskites Reveals the Risk of Introducing a Safe Threshold. *Nat. Commun.* **2020**, *11*, 310. <https://doi.org/10.1038/s41467-019-13910-y>.
- (58) Yang, S.; Fu, W.; Zhang, Z.; Chen, H.; Li, C.-Z. Recent Advances in Perovskite Solar

- Cells: Efficiency, Stability and Lead-Free Perovskite. *J. Mater. Chem. A* **2017**, *5* (23), 11462–11482. <https://doi.org/10.1039/C7TA00366H>.
- (59) Slavney, A. H.; Hu, T.; Lindenberg, A. M.; Karunadasa, H. I. A Bismuth-Halide Double Perovskite with Long Carrier Recombination Lifetime for Photovoltaic Applications. *J. Am. Chem. Soc.* **2016**, *138* (7), 2138–2141. <https://doi.org/10.1021/jacs.5b13294>.
- (60) Wei, F.; Deng, Z.; Sun, S.; Zhang, F.; Evans, D. M.; Kieslich, G.; Tominaka, S.; Carpenter, M. A.; Zhang, J.; Bristowe, P. D.; Cheetham, A. K. Synthesis and Properties of a Lead-Free Hybrid Double Perovskite: (CH₃NH₃)₂AgBiBr₆. *Chem. Mater.* **2017**, *29* (3), 1089–1094. <https://doi.org/10.1021/acs.chemmater.6b03944>.
- (61) Savory, C. N.; Walsh, A.; Scanlon, D. O. Can Pb-Free Halide Double Perovskites Support High-Efficiency Solar Cells? *ACS Energy Lett.* **2016**, *1* (5), 949–955. <https://doi.org/10.1021/acsenergylett.6b00471>.
- (62) Wei, F.; Deng, Z.; Sun, S.; Xie, F.; Kieslich, G.; Evans, D. M.; Carpenter, M. A.; Bristowe, P.; Cheetham, T. The Synthesis, Structure and Electronic Properties of a Lead-Free Hybrid Inorganic-Organic Double Perovskite (MA)₂KBiCl₆ (MA = Methylammonium). *Mater. Horizons* **2016**, *3*, 328–332. <https://doi.org/10.1039/C6MH00053C>.
- (63) Xiao, Z.; Meng, W.; Wang, J.; Yan, Y. Thermodynamic Stability and Defect Chemistry of Bismuth-Based Lead-Free Double Perovskites. *ChemSusChem* **2016**, *6*, 2628–2633. <https://doi.org/10.1002/cssc.201600771>.
- (64) Volonakis, G.; Filip, M. R.; Haghighirad, A. A.; Sakai, N.; Wenger, B.; Snaith, H. J.; Giustino, F. Lead-Free Halide Double Perovskites via Heterovalent Substitution of Noble Metals. *J. Phys. Chem. Lett.* **2016**, *7* (7), 1254–1259. <https://doi.org/10.1021/acs.jpcclett.6b00376>.
- (65) McClure, E. T.; Ball, M. R.; Windl, W.; Woodward, P. M. Cs₂AgBiX₆ (X = Br, Cl): New Visible Light Absorbing, Lead-Free Halide Perovskite Semiconductors. *Chem. Mater.* **2016**, *28* (5), 1348–1354. <https://doi.org/10.1021/acs.chemmater.5b04231>.
- (66) Li, Z.; Kavanagh, S. R.; Napari, M.; Palgrave, R.; Abdi-Jalebi, M.; Andaji-Garmaroudi, Z.; Davies, D.; Laitinen, M.; Julin, J.; Isaacs, M. A.; Friend, R.; Scanlon,

- D. O.; Walsh, A.; Hoye, R. L. Z. Bandgap Lowering in Mixed Alloys of Cs₂Ag(SbxBi_{1-x})Br₆ Double Perovskite Thin Films. *J. Mater. Chem. A* **2020**, *8* (41), 21780–21788. <https://doi.org/10.1039/d0ta07145e>.
- (67) Hoye, R. L. Z.; Eyre, L.; Wei, F.; Brivio, F.; Sadhanala, A.; Sun, S.; Li, W.; Zhang, K. H. L.; MacManus-Driscoll, J. L.; Bristowe, P. D.; Friend, R. H.; Cheetham, A. K.; Deschler, F. Fundamental Carrier Lifetime Exceeding 1 Microsecond in Cs₂AgBiBr₆ Double Perovskite. *Adv. Mater. Interfaces* **2018**, *5*, 1800464. <https://doi.org/10.1002/admi.201800464>.
- (68) Zhao, Y.; Cruse, K.; Abdelsamie, M.; Ceder, G.; Sutter-Fella, C. M. Synthetic Approaches for Thin-Film Halide Double Perovskites. *Matter* **2021**, *4* (6), 1801–1831. <https://doi.org/10.1016/j.matt.2021.03.009>.
- (69) Xiao, Z.; Meng, W.; Wang, J.; Mitzi, D. B.; Yan, Y. Searching for Promising New Perovskite-Based Photovoltaic Absorbers: The Importance of Electronic Dimensionality. *Mater. Horizons* **2017**, *4* (2), 206–216. <https://doi.org/10.1039/c6mh00519e>.
- (70) Li, T.; Zhao, X.; Yang, D.; Du, M. H.; Zhang, L. Intrinsic Defect Properties in Halide Double Perovskites for Optoelectronic Applications. *Phys. Rev. Appl.* **2018**, *10* (4), 041001. <https://doi.org/10.1103/PhysRevApplied.10.041001>.
- (71) Kang, J.; Wang, L. W. High Defect Tolerance in Lead Halide Perovskite CsPbBr₃. *J. Phys. Chem. Lett.* **2017**, *8* (2), 489–493. <https://doi.org/10.1021/acs.jpcllett.6b02800>.
- (72) Jin, H.; Debroye, E.; Keshavarz, M.; Scheblykin, I. G.; Roeffaers, M. B. J.; Hofkens, J.; Steele, J. A. It's a Trap! On the Nature of Localised States and Charge Trapping in Lead Halide Perovskites. *Mater. Horizons* **2020**, *7* (2), 397–410. <https://doi.org/10.1039/c9mh00500e>.
- (73) Buin, A.; Pietsch, P.; Xu, J.; Voznyy, O.; Ip, A. H.; Comin, R.; Sargent, E. H. Materials Processing Routes to Trap-Free Halide Perovskites. *Nano Lett.* **2014**, *14* (11), 6281–6286. <https://doi.org/10.1021/nl502612m>.
- (74) Slavney, A. H.; Leppert, L.; Saldivar Valdes, A.; Bartesaghi, D.; Savenije, T. J.; Neaton, J. B.; Karunadasa, H. I. Small-Band-Gap Halide Double Perovskites. *Angew. Chem. Int. Ed.* **2018**, *57*, 12765–12770. <https://doi.org/10.1002/anie.201807421>.

- (75) Igbari, F.; Wang, R.; Wang, Z. K.; Ma, X. J.; Wang, Q.; Wang, K. L.; Zhang, Y.; Liao, L. S.; Yang, Y. Composition Stoichiometry of Cs₂AgBiBr₆ Films for Highly Efficient Lead-Free Perovskite Solar Cells. *Nano Lett.* **2019**, *19* (3), 2066–2073. <https://doi.org/10.1021/acs.nanolett.9b00238>.
- (76) Longo, G.; Mahesh, S.; Buizza, L. R. V.; Wright, A. D.; Ramadan, A. J.; Abdi-Jalebi, M.; Nayak, P. K.; Herz, L. M.; Snaith, H. J. Understanding the Performance-Limiting Factors of Cs₂AgBiBr₆ Double-Perovskite Solar Cells. *ACS Energy Lett.* **2020**, *5* (7), 2200–2207. <https://doi.org/10.1021/acsenerylett.0c01020>.
- (77) Delor, M.; Slavney, A. H.; Wolf, N. R.; Filip, M. R.; Neaton, J. B.; Karunadasa, H. I.; Ginsberg, N. S. Carrier Diffusion Lengths Exceeding 1 Micrometer despite Trap-Limited Transport in Halide Double Perovskites. *ACS Energy Lett.* **2020**, *5* (5), 1337–1345. <https://doi.org/10.1021/acsenerylett.0c00414>.
- (78) Hutter, E. M.; Gélvez-Rueda, M. C.; Bartesaghi, D.; Grozema, F. C.; Savenije, T. J. Band-Like Charge Transport in Cs₂AgBiBr₆ and Mixed Antimony-Bismuth Cs₂Ag(Bi_{1-x}Sbx)Br₆ Halide Double Perovskites. *ACS Omega* **2018**, *3* (9), 11655–11662. <https://doi.org/10.1021/acsomega.8b01705>.
- (79) Bartesaghi, D.; Slavney, A. H.; Gélvez-Rueda, M. C.; Connor, B. A.; Grozema, F. C.; Karunadasa, H. I.; Savenije, T. J. Charge Carrier Dynamics in Cs₂AgBiBr₆ Double Perovskite. *J. Phys. Chem. C* **2018**, *122* (9), 4809–4816. <https://doi.org/10.1021/acs.jpcc.8b00572>.
- (80) Zelewski, S. J.; Urban, J. M.; Surrente, A.; Maude, D. K.; Kuc, A.; Schade, L.; Johnson, R. D.; Dollmann, M.; Nayak, P. K.; Snaith, H. J.; Radaelli, P.; Kudrawiec, R.; Nicholas, R. J.; Plochocka, P.; Baranowski, M. Revealing the Nature of Photoluminescence Emission in the Metal-Halide Double Perovskite Cs₂AgBiBr₆. *J. Mater. Chem. C* **2019**, *7* (27), 8350–8356. <https://doi.org/10.1039/c9tc02402f>.
- (81) Wright, A. D.; Buizza, L. R. V.; Savill, K. J.; Longo, G.; Snaith, H. J.; Johnston, M. B.; Herz, L. M. Ultrafast Excited-State Localization in Cs₂AgBiBr₆ Double Perovskite. *J. Phys. Chem. Lett.* **2021**, *12* (13), 3352–3360. <https://doi.org/10.1021/acs.jpcllett.1c00653>.
- (82) Franchini, C.; Reticcioli, M.; Setvin, M.; Diebold, U. Polarons in Materials. *Nat. Rev. Mater.* **2021**, *6*, 560–586. <https://doi.org/10.1038/s41578-021-00289-w>.

- (83) Neukirch, A. J.; Nie, W.; Blancon, J. C.; Appavoo, K.; Tsai, H.; Sfeir, M. Y.; Katan, C.; Pedesseau, L.; Even, J.; Crochet, J. J.; Gupta, G.; Mohite, A. D.; Tretiak, S. Polaron Stabilization by Cooperative Lattice Distortion and Cation Rotations in Hybrid Perovskite Materials. *Nano Lett.* **2016**, *16* (6), 3809–3816. <https://doi.org/10.1021/acs.nanolett.6b01218>.
- (84) Li, S.; Luo, J.; Liu, J.; Tang, J. Self-Trapped Excitons in All-Inorganic Halide Perovskites: Fundamentals, Status, and Potential Applications. *J. Phys. Chem. Lett.* **2019**, *10* (8), 1999–2007. <https://doi.org/10.1021/acs.jpcllett.8b03604>.
- (85) Buizza, L. R. V.; Herz, L. M. Polarons and Charge Localization in Metal-Halide Semiconductors for Photovoltaic and Light-Emitting Devices. *Adv. Mater.* **2021**, *33*, 2007057. <https://doi.org/10.1002/adma.202007057>.
- (86) Devreese, J. T.; Alexandrov, A. S. Fröhlich Polaron and Bipolaron: Recent Developments. *Reports Prog. Phys.* **2009**, *72*, 066501. <https://doi.org/10.1088/0034-4885/72/6/066501>.
- (87) Williams, R. T.; Song, K. S. The Self-Trapped Exciton. *J. Phys. Chem. Solids* **1990**, *51* (7), 679–716. [https://doi.org/10.1016/0022-3697\(90\)90144-5](https://doi.org/10.1016/0022-3697(90)90144-5).
- (88) Stoneham, A. M.; Gavartin, J.; Shluger, A. L.; Kimmel, A. V.; Muñoz Ramo, D.; Rønnow, H. M.; Aepli, G.; Renner, C. Trapping, Self-Trapping and the Polaron Family. *J. Phys. Condens. Matter* **2007**, *19*, 255208. <https://doi.org/10.1088/0953-8984/19/25/255208>.
- (89) Wu, B.; Ning, W.; Xu, Q.; Manjappa, M.; Feng, M.; Ye, S.; Fu, J.; Lie, S.; Yin, T.; Wang, F.; Goh, T. W.; Harikesh, P. C.; Tay, Y. K. E.; Shen, Z. X.; Huang, F.; Singh, R.; Zhou, G.; Gao, F.; Sum, T. C. Strong Self-Trapping by Deformation Potential Limits Photovoltaic Performance in Bismuth Double Perovskite. *Sci. Adv.* **2021**, *7* (8), eabd3160. <https://doi.org/10.1126/sciadv.abd3160>.
- (90) Kim, S.; Márquez, J. A.; Unold, T.; Walsh, A. Upper Limit to the Photovoltaic Efficiency of Imperfect Crystals from First Principles. *Energy Environ. Sci.* **2020**, *13* (5), 1481–1491. <https://doi.org/10.1039/d0ee00291g>.
- (91) Whalley, L. D.; van Gerwen, P.; Frost, J. M.; Kim, S.; Hood, S. N.; Walsh, A. Giant Huang–Rhys Factor for Electron Capture by the Iodine Interstitial in Perovskite Solar

- Cells. *J. Am. Chem. Soc.* **2021**, *143* (24), 9123–9128.
<https://doi.org/10.1021/jacs.1c03064>.
- (92) Smith, M. D.; Connor, B. A.; Karunadasa, H. I. Tuning the Luminescence of Layered Halide Perovskites. *Chem. Rev.* **2019**, *119* (5), 3104–3139.
<https://doi.org/10.1021/acs.chemrev.8b00477>.
- (93) Steele, J. A.; Puech, P.; Keshavarz, M.; Yang, R.; Banerjee, S.; Debroye, E.; Kim, C. W.; Yuan, H.; Heo, N. H.; Vanacken, J.; Walsh, A.; Hofkens, J.; Roeffaers, M. B. J. Giant Electron-Phonon Coupling and Deep Conduction Band Resonance in Metal Halide Double Perovskite. *ACS Nano* **2018**, *12* (8), 8081–8090.
<https://doi.org/10.1021/acsnano.8b02936>.
- (94) Kentsch, R.; Scholz, M.; Horn, J.; Schlettwein, D.; Oum, K.; Lenzer, T. Exciton Dynamics and Electron-Phonon Coupling Affect the Photovoltaic Performance of the Cs₂AgBiBr₆ Double Perovskite. *J. Phys. Chem. C* **2018**, *122* (45), 25940–25947.
<https://doi.org/10.1021/acs.jpcc.8b09911>.
- (95) Miyata, K.; Atallah, T. L.; Zhu, X. Y. Lead Halide Perovskites: Crystal-Liquid Duality, Phonon Glass Electron Crystals, and Large Polaron Formation. *Sci. Adv.* **2017**, *3*, e1701469. <https://doi.org/10.1126/sciadv.1701469>.
- (96) Yang, B.; Chen, J.; Yang, S.; Hong, F.; Sun, L.; Han, P.; Pullerits, T.; Deng, W.; Han, K. Lead-Free Silver-Bismuth Halide Double Perovskite Nanocrystals. *Angew. Chem. Int. Ed.* **2018**, *57* (19), 5359–5363. <https://doi.org/10.1002/anie.201800660>.
- (97) Biega, R.-I.; Filip, M. R.; Leppert, L.; Neaton, J. B. Chemically-Localized Resonant Excitons in Silver-Pnictogen Halide Double Perovskites. *J. Phys. Chem. Lett.* **2021**, *12* (8), 2057–2063. <https://doi.org/10.1021/acs.jpcclett.0c03579>.
- (98) Dey, A.; Richter, A. F.; Debnath, T.; Huang, H.; Polavarapu, L.; Feldmann, J. Transfer of Direct to Indirect Bound Excitons by Electron Intervalley Scattering in Cs₂AgBiBr₆ Double Perovskite Nanocrystals. *ACS Nano* **2020**, *14* (5), 5855–5861.
<https://doi.org/10.1021/acsnano.0c00997>.
- (99) Kim, J.; Lee, S. H.; Lee, J. H.; Hong, K. H. The Role of Intrinsic Defects in Methylammonium Lead Iodide Perovskite. *J. Phys. Chem. Lett.* **2014**, *5* (8), 1312–1317. <https://doi.org/10.1021/jz500370k>.

- (100) Yin, W. J.; Shi, T.; Yan, Y. Unique Properties of Halide Perovskites as Possible Origins of the Superior Solar Cell Performance. *Adv. Mater.* **2014**, *26* (27), 4653–4658. <https://doi.org/10.1002/adma.201306281>.
- (101) Walsh, A.; Scanlon, D. O.; Chen, S.; Gong, X. G.; Wei, S. H. Self-Regulation Mechanism for Charged Point Defects in Hybrid Halide Perovskites. *Angew. Chem. Int. Ed.* **2015**, *54* (6), 1791–1794. <https://doi.org/10.1002/anie.201409740>.
- (102) Eames, C.; Frost, J. M.; Barnes, P. R. F.; O'Regan, B. C.; Walsh, A.; Islam, M. S. Ionic Transport in Hybrid Lead Iodide Perovskite Solar Cells. *Nat. Commun.* **2015**, *6*, 7497. <https://doi.org/10.1038/ncomms8497>.
- (103) Yuan, Y.; Chae, J.; Shao, Y.; Wang, Q.; Xiao, Z.; Centrone, A.; Huang, J. Photovoltaic Switching Mechanism in Lateral Structure Hybrid Perovskite Solar Cells. *Adv. Energy Mater.* **2015**, *5*, 1500615. <https://doi.org/10.1002/aenm.201500615>.
- (104) Yuan, Y.; Huang, J. Ion Migration in Organometal Trihalide Perovskite and Its Impact on Photovoltaic Efficiency and Stability. *Acc. Chem. Res.* **2016**, *49* (2), 286–293. <https://doi.org/10.1021/acs.accounts.5b00420>.
- (105) Futscher, M. H.; Lee, J. M.; McGovern, L.; Muscarella, L. A.; Wang, T.; Haider, M. I.; Fakharuddin, A.; Schmidt-Mende, L.; Ehrler, B. Quantification of Ion Migration in CH₃NH₃PbI₃ Perovskite Solar Cells by Transient Capacitance Measurements. *Mater. Horizons* **2019**, *6* (7), 1497–1503. <https://doi.org/10.1039/c9mh00445a>.
- (106) Senocrate, A.; Moudrakovski, I.; Kim, G. Y.; Yang, T. Y.; Gregori, G.; Grätzel, M.; Maier, J. The Nature of Ion Conduction in Methylammonium Lead Iodide: A Multimethod Approach. *Angew. Chem. Int. Ed.* **2017**, *56* (27), 7755–7759. <https://doi.org/10.1002/anie.201701724>.
- (107) Walsh, A.; Stranks, S. D. Taking Control of Ion Transport in Halide Perovskite Solar Cells. *ACS Energy Lett.* **2018**, *3* (8), 1983–1990. <https://doi.org/10.1021/acsenergylett.8b00764>.
- (108) Shao, Y.; Fang, Y.; Li, T.; Wang, Q.; Dong, Q.; Deng, Y.; Yuan, Y.; Wei, H.; Wang, M.; Gruverman, A.; Shield, J.; Huang, J. Grain Boundary Dominated Ion Migration in Polycrystalline Organic-Inorganic Halide Perovskite Films. *Energy Environ. Sci.* **2016**, *9* (5), 1752–1759. <https://doi.org/10.1039/c6ee00413j>.

- (109) Yun, J. S.; Seidel, J.; Kim, J.; Soufiani, A. M.; Huang, S.; Lau, J.; Jeon, N. J.; Seok, S. Il; Green, M. A.; Ho-Baillie, A. Critical Role of Grain Boundaries for Ion Migration in Formamidinium and Methylammonium Lead Halide Perovskite Solar Cells. *Adv. Energy Mater.* **2016**, *6*, 1600330. <https://doi.org/10.1002/aenm.201600330>.
- (110) Xing, J.; Wang, Q.; Dong, Q.; Yuan, Y.; Fang, Y.; Huang, J. Ultrafast Ion Migration in Hybrid Perovskite Polycrystalline Thin Films under Light and Suppression in Single Crystals. *Phys. Chem. Chem. Phys.* **2016**, *18* (44), 30484–30490. <https://doi.org/10.1039/c6cp06496e>.
- (111) Reid, O. G.; Yang, M.; Kopidakis, N.; Zhu, K.; Rumbles, G. Grain-Size-Limited Mobility in Methylammonium Lead Iodide Perovskite Thin Films. *ACS Energy Lett.* **2016**, *1* (3), 561–565. <https://doi.org/10.1021/acsenergylett.6b00288>.
- (112) DeQuilettes, D. W.; Jariwala, S.; Burke, S.; Ziffer, M. E.; Wang, J. T. W.; Snaith, H. J.; Ginger, D. S. Tracking Photoexcited Carriers in Hybrid Perovskite Semiconductors: Trap-Dominated Spatial Heterogeneity and Diffusion. *ACS Nano* **2017**, *11* (11), 11488–11496. <https://doi.org/10.1021/acsnano.7b06242>.
- (113) Pan, W.; Wu, H.; Luo, J.; Deng, Z.; Ge, C.; Chen, C.; Jiang, X.; Yin, W. J.; Niu, G.; Zhu, L.; Yin, L.; Zhou, Y.; Xie, Q.; Ke, X.; Sui, M.; Tang, J. Cs₂AgBiBr₆ Single-Crystal X-Ray Detectors with a Low Detection Limit. *Nat. Photonics* **2017**, *11* (11), 726–732. <https://doi.org/10.1038/s41566-017-0012-4>.
- (114) Ghasemi, M.; Zhang, L.; Yun, J. H.; Hao, M.; He, D.; Chen, P.; Bai, Y.; Lin, T.; Xiao, M.; Du, A.; Lyu, M.; Wang, L. Dual-Ion-Diffusion Induced Degradation in Lead-Free Cs₂AgBiBr₆ Double Perovskite Solar Cells. *Adv. Funct. Mater.* **2020**, *30*, 2002342. <https://doi.org/10.1002/adfm.202002342>.
- (115) Yang, B.; Pan, W.; Wu, H.; Niu, G.; Yuan, J. H.; Xue, K. H.; Yin, L.; Du, X.; Miao, X. S.; Yang, X.; Xie, Q.; Tang, J. Heteroepitaxial Passivation of Cs₂AgBiBr₆ Wafers with Suppressed Ionic Migration for X-Ray Imaging. *Nat. Commun.* **2019**, *10*, 1989. <https://doi.org/10.1038/s41467-019-09968-3>.
- (116) Yang, J.; Zhang, P.; Wei, S.-H. Band Structure Engineering of Cs₂AgBiBr₆ Perovskite through Order–Disordered Transition: A First-Principle Study. *J. Phys. Chem. Lett.* **2018**, *9* (1), 31–35. <https://doi.org/10.1021/acs.jpcclett.7b02992>.

- (117) Ji, F.; Klarbring, J.; Wang, F.; Ning, W.; Wang, L.; Yin, C.; Figueroa, J. S. M.; Christensen, C. K.; Etter, M.; Ederth, T.; Sun, L.; Simak, S.; Abrikosov, I.; Gao, F. Lead-Free Halide Double Perovskite Cs₂AgBiBr₆ with Decreased Bandgap. *Angew. Chem. Int. Ed.* **2020**, *59* (35), 15191–15194. <https://doi.org/10.1002/anie.202005568>.
- (118) Li, Q.; Wang, Y.; Pan, W.; Yang, W.; Zou, B.; Tang, J.; Quan, Z. High-Pressure Band-Gap Engineering in Lead-Free Cs₂AgBiBr₆ Double Perovskite. *Angew. Chem. Int. Ed.* **2017**, *56* (50), 15969–15973. <https://doi.org/10.1002/anie.201708684>.
- (119) Hao, F.; Stoumpos, C. C.; Chang, R. P. H.; Kanatzidis, M. G. Anomalous Band Gap Behavior in Mixed Sn and Pb Perovskites Enables Broadening of Absorption Spectrum in Solar Cells. *J. Am. Chem. Soc.* **2014**, *136* (22), 8094–8099. <https://doi.org/10.1021/ja5033259>.
- (120) Im, J.; Stoumpos, C. C.; Jin, H.; Freeman, A. J.; Kanatzidis, M. G. Antagonism between Spin-Orbit Coupling and Steric Effects Causes Anomalous Band Gap Evolution in the Perovskite Photovoltaic Materials CH₃NH₃(Sn_{1-x}Pb_x)I₃. *J. Phys. Chem. Lett.* **2015**, *6* (17), 3503–3509. <https://doi.org/10.1021/acs.jpcclett.5b01738>.
- (121) Eperon, G. E.; Leijtens, T.; Bush, K. A.; Prasanna, R.; Green, T.; Wang, J. T. W.; McMeekin, D. P.; Volonakis, G.; Milot, R. L.; May, R.; Palmstrom, A.; Slotcavage, D. J.; Belisle, R. A.; Patel, J. B.; Parrott, E. S.; Sutton, R. J.; Ma, W.; Moghadam, F.; Conings, B.; Babayigit, A.; Boyen, H. G.; Bent, S.; Giustino, F.; Herz, L. M.; Johnston, M. B.; McGehee, M. D.; Snaith, H. J. Perovskite-Perovskite Tandem Photovoltaics with Optimized Band Gaps. *Science*. **2016**, *354* (6314), 861–865. <https://doi.org/10.1126/science.aaf9717>.
- (122) Goyal, A.; McKechnie, S.; Pashov, D.; Tumas, W.; Schilfgaard, M. Van; Stevanović, V. Origin of Pronounced Nonlinear Band Gap Behavior in Lead-Tin Hybrid Perovskite Alloys. *Chem. Mater.* **2018**, *30* (11), 3920–3928. <https://doi.org/10.1021/acs.chemmater.8b01695>.
- (123) Slavney, A. H.; Leppert, L.; Bartesaghi, D.; Gold-Parker, A.; Toney, M. F.; Savenije, T. J.; Neaton, J. B.; Karunadasa, H. I. Defect-Induced Band-Edge Reconstruction of a Bismuth-Halide Double Perovskite for Visible-Light Absorption. *J. Am. Chem. Soc.* **2017**, *139* (14), 5015–5018. <https://doi.org/10.1021/jacs.7b01629>.
- (124) Du, K. Z.; Meng, W.; Wang, X.; Yan, Y.; Mitzi, D. B. Bandgap Engineering of Lead-

- Free Double Perovskite Cs₂AgBiBr₆ through Trivalent Metal Alloying. *Angew. Chem. Int. Ed.* **2017**, *56* (28), 8158–8162. <https://doi.org/10.1002/anie.201703970>.
- (125) Berera, R.; van Grondelle, R.; Kennis, J. T. M. Ultrafast Transient Absorption Spectroscopy: Principles and Application to Photosynthetic Systems. *Photosynth. Res.* **2009**, *101*, 105–118. <https://doi.org/10.1007/s11120-009-9454-y>.
- (126) Drouin, D.; Couture, A. R.; Joly, D.; Tastet, X.; Aimez, V.; Gauvin, R. CASINO V2.42 - A Fast and Easy-to-Use Modeling Tool for Scanning Electron Microscopy and Microanalysis Users. *Scanning* **2007**, *29* (3), 92–101. <https://doi.org/10.1002/sca.20000>.
- (127) Peña, F. de la; Fauske, V. T.; Burdet, P.; Prestat, E.; Jokubauskas, P.; Nord, M.; Ostasevicius, T.; MacArthur, K. E.; Sarahan, M. Hyperspy/Hyperspy v1.4.1. 2018. <https://doi.org/10.5281/ZENODO.1469364>.
- (128) Lecture 9 Ion-surface interactions https://physics.uwo.ca/~lgonchar/courses/p9826/Lecture9_Ion_RBS_Impl_partI.pdf (accessed Aug 30, 2021).
- (129) Mayer, M. *SIMNRA User 's Guide*; 2017.
- (130) Yang, X.; Chen, Y.; Liu, P.; Xiang, H.; Wang, W.; Ran, R.; Zhou, W.; Shao, Z. Simultaneous Power Conversion Efficiency and Stability Enhancement of Cs₂AgBiBr₆ Lead-Free Inorganic Perovskite Solar Cell through Adopting a Multifunctional Dye Interlayer. *Adv. Funct. Mater.* **2020**, *30* (23), 2001557. <https://doi.org/10.1002/adfm.202001557>.
- (131) Greul, E.; Petrus, M. L.; Binek, A.; Docampo, P.; Bein, T. Highly Stable, Phase Pure Cs₂AgBiBr₆ Double Perovskite Thin Films for Optoelectronic Applications. *J. Mater. Chem. A* **2017**, *5*, 19972–19981. <https://doi.org/10.1039/c7ta06816f>.
- (132) Wang, M.; Zeng, P.; Bai, S.; Gu, J.; Li, F.; Yang, Z.; Liu, M. High-Quality Sequential-Vapor-Deposited Cs₂AgBiBr₆ Thin Films for Lead-Free Perovskite Solar Cells. *Sol. RRL* **2018**, *2* (12), 1800217. <https://doi.org/10.1002/solr.201800217>.
- (133) Xiao, Z.; Meng, W.; Wang, J.; Yan, Y. Thermodynamic Stability and Defect Chemistry of Bismuth-Based Lead-Free Double Perovskites. *ChemSusChem* **2016**, *9* (18), 2628–2633. <https://doi.org/10.1002/cssc.201600771>.

- (134) Visoly-Fisher, I.; Cohen, S. R.; Gartsman, K.; Ruzin, A.; Cahen, D. Understanding the Beneficial Role of Grain Boundaries in Polycrystalline Solar Cells from Single-Grain-Boundary Scanning Probe Microscopy. *Adv. Funct. Mater.* **2006**, *16* (5), 649–660. <https://doi.org/10.1002/adfm.200500396>.
- (135) Leite, M. S.; Abashin, M.; Lezec, H. J.; Gianfrancesco, A. G.; Talin, A. A.; Zhitenev, N. B. Mapping the Local Photoelectronic Properties of Polycrystalline Solar Cells through High Resolution Laser-Beam-Induced Current Microscopy. *IEEE J. Photovoltaics* **2014**, *4* (1), 311–316. <https://doi.org/10.1109/JPHOTOV.2013.2284860>.
- (136) Durose, K.; Asher, S. E.; Jaegermann, W.; Levi, D.; McCandless, B. E.; Metzger, W.; Moutinho, H.; Paulson, P. D.; Perkins, C. L.; Sites, J. R.; Teeter, G.; Terheggen, M. Physical Characterization of Thin-Film Solar Cells. *Prog. Photovoltaics Res. Appl.* **2004**, *12*, 177–217. <https://doi.org/10.1002/pip.542>.
- (137) Chopra, K. L.; Paulson, P. D.; Dutta, V. Thin-Film Solar Cells: An Overview. *Prog. Photovoltaics Res. Appl.* **2004**, *12*, 69–92. <https://doi.org/10.1002/pip.541>.
- (138) Moseley, J.; Al-Jassim, M. M.; Kuciauskas, D.; Moutinho, H. R.; Paudel, N.; Guthrey, H. L.; Yan, Y.; Metzger, W. K.; Ahrenkiel, R. K. Cathodoluminescence Analysis of Grain Boundaries and Grain Interiors in Thin-Film CdTe. *IEEE J. Photovoltaics* **2014**, *4* (6), 1671–1679. <https://doi.org/10.1109/JPHOTOV.2014.2359732>.
- (139) Nicoara, N.; Manaligod, R.; Jackson, P.; Hariskos, D.; Witte, W.; Sozzi, G.; Menozzi, R.; Sadewasser, S. Direct Evidence for Grain Boundary Passivation in Cu(In,Ga)Se₂ Solar Cells through Alkali-Fluoride Post-Deposition Treatments. *Nat. Commun.* **2019**, *10*, 3980. <https://doi.org/10.1038/s41467-019-11996-y>.
- (140) Dunlap-Shohl, W. A.; Zhou, Y.; Padture, N. P.; Mitzi, D. B. Synthetic Approaches for Halide Perovskite Thin Films. *Chem. Rev.* **2019**, *119* (5), 3193–3295. <https://doi.org/10.1021/acs.chemrev.8b00318>.
- (141) Schade, L.; Wright, A. D.; Johnson, R. D.; Dollmann, M.; Wenger, B.; Nayak, P. K.; Prabhakaran, D.; Herz, L. M.; Nicholas, R.; Snaith, H. J.; Radaelli, P. G. Structural and Optical Properties of Cs₂AgBiBr₆ Double Perovskite. *ACS Energy Lett.* **2019**, *4* (1), 299–305. <https://doi.org/10.1021/acsenerylett.8b02090>.
- (142) Peán, E. V.; Dimitrov, S.; De Castro, C. S.; Davies, M. L. Interpreting Time-Resolved

- Photoluminescence of Perovskite Materials. *Phys. Chem. Chem. Phys.* **2020**, *22* (48), 28345–28358. <https://doi.org/10.1039/d0cp04950f>.
- (143) Guthrey, H.; Moseley, J. A Review and Perspective on Cathodoluminescence Analysis of Halide Perovskites. *Adv. Energy Mater.* **2020**, *10* (26), 1903840. <https://doi.org/10.1002/aenm.201903840>.
- (144) Groudeva-Zotova, S.; Jacob, W.; Von Keudell, A. Secondary Electron Emission Coefficient of C:H and Si:C Thin Films and Some Relations to Their Morphology and Composition. *Diam. Relat. Mater.* **1996**, *5* (10), 1087–1095. [https://doi.org/10.1016/0925-9635\(96\)00535-3](https://doi.org/10.1016/0925-9635(96)00535-3).
- (145) Zhang, N.; Cao, M.; Cui, W. Z.; Hu, T. C. Effect of Rough Surface Morphology on Secondary Electron Emission from Metal Surface. *Jpn. J. Appl. Phys.* **2017**, *56* (7), 075802. <https://doi.org/10.7567/JJAP.56.075802>.
- (146) Karl, N. Charge Carrier Transport in Organic Semiconductors. *Synth. Met.* **2003**, *133–134*, 649–657. [https://doi.org/10.1016/S0379-6779\(02\)00398-3](https://doi.org/10.1016/S0379-6779(02)00398-3).
- (147) Wang, J.; Senanayak, S. P.; Liu, J.; Hu, Y.; Shi, Y.; Li, Z.; Zhang, C.; Yang, B.; Jiang, L.; Di, D.; Ievlev, A. V.; Ovchinnikova, O. S.; Ding, T.; Deng, H.; Tang, L.; Guo, Y.; Wang, J.; Xiao, K.; Venkateshvaran, D.; Jiang, L.; Zhu, D.; Siringhaus, H. Investigation of Electrode Electrochemical Reactions in CH₃NH₃PbBr₃ Perovskite Single-Crystal Field-Effect Transistors. *Adv. Mater.* **2019**, *31* (35), 1902618. <https://doi.org/10.1002/adma.201902618>.
- (148) Senanayak, S. P.; Abdi-Jalebi, M.; Kamboj, V. S.; Carey, R.; Shivanna, R.; Tian, T.; Schweicher, G.; Wang, J.; Giesbrecht, N.; Di Nuzzo, D.; Beere, H. E.; Docampo, P.; Ritchie, D. A.; Fairen-Jimenez, D.; Friend, R. H.; Siringhaus, H. A General Approach for Hysteresis-Free, Operationally Stable Metal Halide Perovskite Field-Effect Transistors. *Sci. Adv.* **2020**, *6* (15), eaaz4948. <https://doi.org/10.1126/sciadv.aaz4948>.
- (149) Choi, H. H.; Cho, K.; Frisbie, C. D.; Siringhaus, H.; Podzorov, V. Critical Assessment of Charge Mobility Extraction in FETs. *Nat. Mater.* **2018**, *17*, 2–7. <https://doi.org/10.1038/nmat5035>.
- (150) Bandiello, E.; Ávila, J.; Gil-Escrig, L.; Tekelenburg, E.; Sessolo, M.; Bolink, H. J. Influence of Mobile Ions on the Electroluminescence Characteristics of

- Methylammonium Lead Iodide Perovskite Diodes. *J. Mater. Chem. A* **2016**, *4* (47), 18614–18620. <https://doi.org/10.1039/C6TA06854E>.
- (151) Zhang, H.; Lin, H.; Liang, C.; Liu, H.; Liang, J.; Zhao, Y.; Zhang, W.; Sun, M.; Xiao, W.; Li, H.; Polizzi, S.; Li, D.; Zhang, F.; He, Z.; Choy, W. C. H. Organic-Inorganic Perovskite Light-Emitting Electrochemical Cells with a Large Capacitance. *Adv. Funct. Mater.* **2015**, *25* (46), 7226–7232. <https://doi.org/10.1002/adfm.201502962>.
- (152) Dong, Q.; Mendes, J.; Lei, L.; Seyitliyev, D.; Zhu, L.; He, S.; Gundogdu, K.; So, F. Understanding the Role of Ion Migration in the Operation of Perovskite Light-Emitting Diodes by Transient Measurements. *ACS Appl. Mater. Interfaces* **2020**, *12* (43), 48845–48853. <https://doi.org/10.1021/acsami.0c14269>.
- (153) Futscher, M. H.; Gangishetty, M. K.; Congreve, D. N.; Ehrler, B. Quantifying Mobile Ions and Electronic Defects in Perovskite-Based Devices with Temperature-Dependent Capacitance Measurements: Frequency vs Time Domain. *J. Chem. Phys.* **2020**, *152* (4), 044202. <https://doi.org/10.1063/1.5132754>.
- (154) McGovern, L.; Koschany, I.; Grimaldi, G.; Muscarella, L. A.; Ehrler, B. Grain Size Influences Activation Energy and Migration Pathways in MAPbBr₃ Perovskite Solar Cells. *J. Phys. Chem. Lett.* **2021**, *12* (9), 2423–2428. <https://doi.org/10.1021/acs.jpcclett.1c00205>.
- (155) Yin, Y.; Tian, W.; Leng, J.; Bian, J.; Jin, S. Carrier Transport Limited by Trap State in Cs₂AgBiBr₆ Double Perovskites. *J. Phys. Chem. Lett.* **2020**, *11*, 6956–6963. <https://doi.org/10.1021/acs.jpcclett.0c01817>.
- (156) Horowitz, B. G. Organic Field-Effect Transistors. *Adv. Mater.* **1998**, *10*, 365–377. [https://doi.org/10.1002/\(SICI\)1521-4095\(199803\)10:5<365::AID-ADMA365>3.0.CO;2-U](https://doi.org/10.1002/(SICI)1521-4095(199803)10:5<365::AID-ADMA365>3.0.CO;2-U).
- (157) Horowitz, G.; Hajlaoui, M. E.; Hajlaoui, R. Temperature and Gate Voltage Dependence of Hole Mobility in Polycrystalline Oligothiophene Thin Film Transistors. *J. Appl. Phys.* **2000**, *87* (9 I), 4456–4463. <https://doi.org/10.1063/1.373091>.
- (158) Smith, M. D.; Karunadasa, H. I. White-Light Emission from Layered Halide Perovskites. *Acc. Chem. Res.* **2018**, *51* (3), 619–627. <https://doi.org/10.1021/acs.accounts.7b00433>.

- (159) Swift, M.; Janotti, A.; Van De Walle, C. G. Small Polarons and Point Defects in Barium Cerate. *Phys. Rev. B* **2015**, *92*, 214114. <https://doi.org/10.1103/PhysRevB.92.214114>.
- (160) Li, Z.; Senanayak, S. P.; Dai, L.; Kusch, G.; Shivanna, R.; Zhang, Y.; Pradhan, D.; Ye, J.; Huang, Y.; Sirringhaus, H.; Oliver, R. A.; Greenham, N. C.; Friend, R. H.; Hoye, R. L. Z. Understanding the Role of Grain Boundaries on Charge-Carrier and Ion Transport in Cs₂AgBiBr₆ Thin Films. *Adv. Funct. Mater.* **2021**, 2104981. <https://doi.org/10.1002/adfm.202104981>.
- (161) Filip, M. R.; Hillman, S.; Haghighirad, A. A.; Snaith, H. J.; Giustino, F. Band Gaps of the Lead-Free Halide Double Perovskites Cs₂BiAgCl₆ and Cs₂BiAgBr₆ from Theory and Experiment. *J. Phys. Chem. Lett.* **2016**, *7* (13), 2579–2585. <https://doi.org/10.1021/acs.jpcclett.6b01041>.
- (162) Huang, H.; Pradhan, B.; Hofkens, J.; Roeffaers, M. B. J.; Steele, J. A. Solar-Driven Metal Halide Perovskite Photocatalysis: Design, Stability, and Performance. *ACS Energy Lett.* **2020**, *5* (4), 1107–1123. <https://doi.org/10.1021/acsenerylett.0c00058>.
- (163) Zhang, Z.; Liang, Y.; Huang, H.; Liu, X.; Li, Q.; Chen, L.; Xu, D. Stable and Highly Efficient Photocatalysis with Lead-Free Double-Perovskite of Cs₂AgBiBr₆. *Angew. Chem. Int. Ed* **2019**, *58* (22), 7263–7267. <https://doi.org/10.1002/anie.201900658>.
- (164) Zhou, L.; Xu, Y. F.; Chen, B. X.; Kuang, D. Bin; Su, C. Y. Synthesis and Photocatalytic Application of Stable Lead-Free Cs₂AgBiBr₆ Perovskite Nanocrystals. *Small* **2018**, *14* (11), 1703762. <https://doi.org/10.1002/sml.201703762>.
- (165) Slavney, A. H.; Leppert, L.; Bartesaghi, D.; Gold-Parker, A.; Toney, M. F.; Savenije, T. J.; Neaton, J. B.; Karunadasa, H. I. Defect-Induced Band-Edge Reconstruction of a Bismuth-Halide Double Perovskite for Visible-Light Absorption. *J. Am. Chem. Soc.* **2017**, *139* (14), 5015–5018. <https://doi.org/10.1021/jacs.7b01629>.
- (166) Liu, Y.; Zhang, L.; Wang, M.; Zhong, Y.; Huang, M.; Long, Y.; Zhu, H. Bandgap-Tunable Double-Perovskite Thin Films by Solution Processing. *Mater. Today* **2019**, *28*, 25–30. <https://doi.org/10.1016/j.mattod.2019.04.023>.
- (167) Wei, F.; Deng, Z.; Sun, S.; Hartono, N. T. P.; Seng, H. L.; Buonassisi, T.; Bristowe, P. D.; Cheetham, A. K. Enhanced Visible Light Absorption for Lead-Free Double

- Perovskite Cs₂AgSbBr₆. *Chem. Commun.* **2019**, 55 (26), 3721–3724.
<https://doi.org/10.1039/c9cc01134j>.
- (168) Yang, B.; Hong, F.; Chen, J.; Tang, Y.; Yang, L.; Sang, Y.; Xia, X.; Guo, J.; He, H.; Yang, S.; Deng, W.; Han, K. Colloidal Synthesis and Charge-Carrier Dynamics of Cs₂Ag(Sb_{1-y}Bi_y)X₆ (X: Br, Cl; 0 ≤ y ≤ 1) Double Perovskite Nanocrystals. *Angew. Chem. Int. Ed* **2019**, 58 (8), 2278–2283. <https://doi.org/10.1002/anie.201811610>.
- (169) Gao, M.; Zhang, C.; Lian, L.; Guo, J.; Xia, Y.; Pan, F.; Su, X.; Zhang, J.; Li, H.; Zhang, D. Controlled Synthesis and Photostability of Blue Emitting Cs₃Bi₂Br₉ Perovskite Nanocrystals by Employing Weak Polar Solvents at Room Temperature. *J. Mater. Chem. C* **2019**, 7 (12), 3688–3695. <https://doi.org/10.1039/c9tc00400a>.
- (170) Sweenor, D. E.; O’Leary, S. K.; Foutz, B. E. On Defining the Optical Gap of an Amorphous Semiconductor: An Empirical Calibration for the Case of Hydrogenated Amorphous Silicon. *Solid State Commun.* **1999**, 110 (5), 281–286.
[https://doi.org/doi.org/10.1016/S0038-1098\(99\)00049-6](https://doi.org/doi.org/10.1016/S0038-1098(99)00049-6).
- (171) Mok, T. M.; O’Leary, S. K. The Dependence of the Tauc and Cody Optical Gaps Associated with Hydrogenated Amorphous Silicon on the Film Thickness: An Experimental Limitations and the Impact of Curvature in the Tauc and Cody Plots. *J. Appl. Phys.* **2007**, 102 (11), 113525. <https://doi.org/10.1063/1.2817822>.
- (172) Shin, S. S.; Lee, S. J.; Seok, S. Il. Metal Oxide Charge Transport Layers for Efficient and Stable Perovskite Solar Cells. *Adv. Funct. Mater.* **2019**, 29, 1900455.
<https://doi.org/10.1002/adfm.201900455>.
- (173) Lee, L. C.; Huq, T. N.; Macmanus-Driscoll, J. L.; Hoyer, R. L. Z. Research Update: Bismuth-Based Perovskite-Inspired Photovoltaic Materials. *APL Mater.* **2018**, 6 (8), 084502. <https://doi.org/10.1063/1.5029484>.
- (174) Stamplecoskie, K. G.; Manser, J. S.; Kamat, P. V. Dual Nature of the Excited State in Organic-Inorganic Lead Halide Perovskites. *Energy Environ. Sci.* **2015**, 8 (1), 208–215. <https://doi.org/10.1039/c4ee02988g>.
- (175) Hao, F.; Stoumpos, C. C.; Cao, D. H.; Chang, R. P. H.; Kanatzidis, M. G. Lead-Free Solid-State Organic-Inorganic Halide Perovskite Solar Cells. *Nat. Photonics* **2014**, 8 (6), 489–494. <https://doi.org/10.1038/nphoton.2014.82>.

- (176) Tang, L. C.; Chang, C. S.; Huang, J. Y. Electronic Structure and Optical Properties of Rhombohedral CsGeI₃ Crystal. *J. Phys. Condens. Matter* **2000**, *12* (43), 9129–9143. <https://doi.org/10.1088/0953-8984/12/43/303>.
- (177) Butler, K. T.; Hendon, C. H.; Walsh, A. Electronic Chemical Potentials of Porous Metal–Organic Frameworks. *J. Am. Chem. Soc.* **2014**, *136* (7), 2703–2706. <https://doi.org/10.1021/ja4110073>.
- (178) Lide, D. R. *CRC Handbook of Chemistry and Physics, 84th Edition*; CRC Press: Florida, 2003; Vol. Chapter 10. <https://doi.org/10.1021/ja0336372>.
- (179) Pyykkö, P. Relativistic Effects in Structural Chemistry. *Chem. Rev.* **1988**, *88* (3), 563–594. <https://doi.org/10.1021/cr00085a006>.
- (180) The periodic table of the elements by WebElements <https://www.webelements.com/> (accessed Jun 9, 2021).
- (181) Wei, S. H.; Zunger, A. Band Gaps and Spin-Orbit Splitting of Ordered and Disordered (Al_xGa_{1-x})As and Ga(As_xSb_{1-x}) Alloys. *Phys. Rev. B* **1989**, *39* (5), 3279–3304. <https://doi.org/10.1103/PhysRevB.39.3279>.
- (182) Moon, C. Y.; Wei, S. H.; Zhu, Y. Z.; Chen, G. D. Band-Gap Bowing Coefficients in Large Size-Mismatched II-VI Alloys: First-Principles Calculations. *Phys. Rev. B* **2006**, *74* (23), 233202. <https://doi.org/10.1103/PhysRevB.74.233202>.
- (183) Mattila, T.; Wei, S. H.; Zunger, A. Localization and Anticrossing of Electron Levels in GaAs_{1-x}N_x Alloys. *Phys. Rev. B* **1999**, *60*, R11245–R11248. <https://doi.org/10.1103/PhysRevB.60.R11245>.
- (184) Gao, W.; Ran, C.; Xi, J.; Jiao, B.; Zhang, W.; Wu, M.; Hou, X.; Wu, Z. High-Quality Cs₂AgBiBr₆ Double Perovskite Film for Lead-Free Inverted Planar Heterojunction Solar Cells with 2.2% Efficiency. *ChemPhysChem* **2018**, *19* (14), 1696–1700. <https://doi.org/10.1002/cphc.201800346>.
- (185) Savchenko, S. S.; Weinstein, I. A. Inhomogeneous Broadening of the Exciton Band in Optical Absorption Spectra of InP/ZnS Nanocrystals. *Nanomaterials* **2019**, *9* (5), 716. <https://doi.org/10.3390/nano9050716>.
- (186) Weinstein, I. A.; Zatsepin, A. F.; Kortov, V. S. Effects of Structural Disorder and Urbach’s Rule in Binary Lead Silicate Glasses. *J. Non. Cryst. Solids* **2001**, *279* (1),

- 77–87. [https://doi.org/10.1016/S0022-3093\(00\)00396-3](https://doi.org/10.1016/S0022-3093(00)00396-3).
- (187) Butté, R.; Lahourcade, L.; Uzdavinyis, T. K.; Callsen, G.; Mensi, M.; Glauser, M.; Rossbach, G.; Martin, D.; Carlin, J. F.; Marcinkevičius, S.; Grandjean, N. Optical Absorption Edge Broadening in Thick InGaN Layers: Random Alloy Atomic Disorder and Growth Mode Induced Fluctuations. *Appl. Phys. Lett.* **2018**, *112* (3), 032106. <https://doi.org/10.1063/1.5010879>.
- (188) Mathews, I.; Kantareddy, S. N.; Buonassisi, T.; Peters, I. M. Technology and Market Perspective for Indoor Photovoltaic Cells. *Joule* **2019**, *3* (6), 1415–1426. <https://doi.org/10.1016/j.joule.2019.03.026>.
- (189) Murphy, A. B.; Barnes, P. R. F.; Randeniya, L. K.; Plumb, I. C.; Grey, I. E.; Horne, M. D.; Glasscock, J. A. Efficiency of Solar Water Splitting Using Semiconductor Electrodes. *Int. J. Hydrogen Energy* **2006**, *31* (14), 1999–2017. <https://doi.org/10.1016/j.ijhydene.2006.01.014>.
- (190) Todorov, T.; Gunawan, O.; Guha, S. A Road towards 25% Efficiency and beyond: Perovskite Tandem Solar Cells. *Mol. Syst. Des. Eng.* **2016**, *1* (4), 370–376. <https://doi.org/10.1039/c6me00041j>.
- (191) Lee, K. M.; Lin, C. J.; Liou, B. Y.; Yu, S. M.; Hsu, C. C.; Suryanarayanan, V.; Wu, M. C. Selection of Anti-Solvent and Optimization of Dropping Volume for the Preparation of Large Area Sub-Module Perovskite Solar Cells. *Sol. Energy Mater. Sol. Cells* **2017**, *172*, 368–375. <https://doi.org/10.1016/j.solmat.2017.08.010>.
- (192) Bruening, K.; Tassone, C. J. Antisolvent Processing of Lead Halide Perovskite Thin Films Studied by: In Situ X-Ray Diffraction. *J. Mater. Chem. A* **2018**, *6* (39), 18865–18870. <https://doi.org/10.1039/c8ta06025h>.
- (193) Böer, K. W.; Pohl, U. W. *Semiconductor Physics*; Springer International Publishing, 2015.
- (194) Miller, G. L.; Lang, D. V.; Kimerling, L. C. Capacitance Transient Spectroscopy. **1977**, *7*, 377–448. <https://doi.org/10.1146/annurev.ms.07.080177.002113>.
- (195) Pecunia, V.; Zhao, J.; Kim, C.; Tuttle, B. R.; Mei, J.; Li, F.; Peng, Y.; Huq, T.; Hoye, R. L. Z.; Kelly, N. D.; Dutton, S. E.; Xia, K.; MacManus-Driscoll, J.; Sringhaus, H. Assessing the Impact of Defects on Lead-Free Perovskite-Inspired Photovoltaics via

- Photo-Induced Current Transient Spectroscopy. *Adv. Energy Mater.* **2021**, *11* (22), 2003968. <https://doi.org/10.1002/aenm.202003968>.
- (196) Luo, J.; Wang, X.; Li, S.; Liu, J.; Guo, Y.; Niu, G.; Yao, L.; Fu, Y.; Gao, L.; Dong, Q.; Zhao, C.; Leng, M.; Ma, F.; Liang, W.; Wang, L.; Jin, S.; Han, J.; Zhang, L.; Etheridge, J.; Wang, J.; Yan, Y.; Sargent, E. H.; Tang, J. Efficient and Stable Emission of Warm-White Light from Lead-Free Halide Double Perovskites. *Nature* **2018**, *563* (7732), 541–545. <https://doi.org/10.1038/s41586-018-0691-0>.
- (197) Huang, Y. C.; Tsao, C. S.; Cho, Y. J.; Chen, K. C.; Chiang, K. M.; Hsiao, S. Y.; Chen, C. W.; Su, C. J.; Jeng, U. S.; Lin, H. W. Insight into Evolution, Processing and Performance of Multi-Length-Scale Structures in Planar Heterojunction Perovskite Solar Cells. *Sci. Rep.* **2015**, *5*, 13657. <https://doi.org/10.1038/srep13657>.
- (198) Chen, X.; Cheng, S.; Xiao, L.; Sun, H. Identifying, Understanding and Controlling Defects and Traps in Halide Perovskites for Optoelectronic Devices: A Review. *J. Phys. D. Appl. Phys.* **2020**, *53*, 373001. <https://doi.org/10.1088/1361-6463/ab9134>.
- (199) Gao, F.; Zhao, Y.; Zhang, X.; You, J. Recent Progresses on Defect Passivation toward Efficient Perovskite Solar Cells. *Adv. Energy Mater.* **2020**, *10*, 1902650. <https://doi.org/10.1002/aenm.201902650>.
- (200) Creutz, S. E.; Crites, E. N.; De Siena, M. C.; Gamelin, D. R. Colloidal Nanocrystals of Lead-Free Double-Perovskite (Elpasolite) Semiconductors: Synthesis and Anion Exchange to Access New Materials. *Nano Lett.* **2018**, *18* (2), 1118–1123. <https://doi.org/10.1021/acs.nanolett.7b04659>.